To the Graduate Council:

I am submitting herewith a dissertation written by Zheng Rong Xu entitled "Measurements of Small Deformation Associated with Water Uptake by Polymers; Single Fiber Behavior in Epoxy Resin Undergoing Water Uptake; Moisture Induced Degradation of Electronic Materials." I have examined the final copy of this dissertation for form and content and recommend that it be accepted in partial fulfillment of the requirements for the degree of Doctor of Philosophy, with a major in Materials Science and Engineering.

K H G. Ashbee

Ken H. G. Ashbee, Major Professor

We have read this dissertation
and recommend its acceptance:

W. T. Becker

C R Brooke

Marian L. Hansen

Accepted for the Council:

Lewinkel

Vice Provost
and Dean of The Graduate School

MEASUREMENTS OF SMALL DEFORMATION ASSOCIATED WITH WATER UPTAKE BY POLYMERS; Single Fiber Behavior in Epoxy Resin Undergoing Water Uptake; Moisture Induced Degradation of Electronic Materials

A Dissertation
Presented for the
Doctor of Philosophy
Degree
The University of Tennessee, Knoxville

Zheng Rong Xu
August 1991

Copyright © 1991

by

ZHENG RONG XU

All rights reserved

DEDICATION

This disseration is dedicated to my parents, Mr. Fu Sheng Xu,

許福森

and Mrs. Zi Fen Dai Xu,

戴芝芬

my wife, Ming Hua,

余明華

and my Daughter, Donna.

許冬妮

ACKNOWLEDGMENTS

The author wishes to express his profound appreciation to his advisor, Dr. K. H. G. Ashbee, for the privilege of working with him, as well as his support, advice and encouragement.

The author also wishes to thank Dr. W. Becker, Dr. C. R. Brooks and Dr. M. G. Hanson for taking the time and the efforts as members of his dissertation committee to review the manuscript and for their inputs to its contents and organization.

The author is grateful to the Department of Materials Science and Engineering, UTK, the Boeing Tennessee and Martin Marietta Laboratory for supporting with a graduate research assistantship through out the research work.

The author wishes to thank his laboratory colleagues Dr. David Tossell, James Brewster and Steve Joslin for the fruitful discussion and suggestion.

The author is deeply indebted to his parents for their understanding and strong support. Finally, and most importantly, the author would like to thank his wife, Ming Hua She, for her constant support and encouragement through out his graduate study period.

ABSTRACT

Composite materials are prone to degradation under a variety of influences. Investigation of single fiber behavior in epoxy resin undergoing water uptake, of the effects on moisture induced degradation of surface treatment of fiber and of post-curing of polymer coatings on electronic packages, together with the development of new experimental techniques, including techniques for measurements of small displacements and for measurement of optical birefringence , have been completed and are reported in this thesis.

The mathematical analysis of a new method of optical caustic foci developed here to measure small displacement, of up to 10 nm, is reliable. The new technique has been successfully used to measure dimensional changes accompanying water uptake by model composites and polymer coatings on COB components. The optical interference technique cannot be used for this purpose owing to the transparency of the coating material.

The results have shown that resin swelling associated with water uptake can overcome and exceed resin shrinkage resulting from curing, by a margin that is sufficiently large for the axial tension in some short carbon fiber composites to exceed the fiber failure strain. The durability of load transfer between matrix resin and fiber has been enhanced by surface treatments to such an extent that swelling deformations large enough to fracture fibers can be realized. The different surface treatments of fibers employed in experiments reported here have permitted different failure modes to be studied in

composites exposed to aqueous environments. These studies concern detailed investigation of stress-induced birefringence around single fibers and of fracture surfaces of test-pieces containing fiber bundles.

For proprietary coatings on electronic packages, the results presented here have identified the effects of post-curing treatments on dimensional change rates, and hence on both water uptake rates and saturated water uptake values. Two generic types of degradation intrinsic to the polymer coating technology have been observed, one being electrolytic corrosion of the underlying substrate and the other being swelling and, in some cases, peeling of the coating itself.

TABLE OF CONTENTS

CHAPTER	PAGE
I. INTRODUCTION	1
II. INTRODUCTION TO INTERFACES IN COMPOSITES	4
2.1 Fibers and matrices	5
2.2 Fiber-matrix interface	7
2.2.1 Theories of adhesion	11
2.2.2 Models for the interface between the fiber and matrix	12
2.2.3 Interface test methods	16
2.3 Effects of the interface	23
2.3.1 Effects of the interface on the elastic properties of composite materials	23
2.3.2 Effects of the interface on the fracture properties of a composite materials	30
2.3.3 Effects of the interface on the failure modes of single fiber specimen	40
III. MOISTURE INDUCED DEGRADATION	44
3.1 Introduction	44
3.2 Effects of moisture on component materials	45
3.2.1 Effects of moisture on fibers	45
3.2.2 Effects of moisture on glass transition temperature of matrix resins	45
3.2.3 Microcracking in the matrix due to water uptake	48
3.3 Swelling Stresses due to non-uniform water uptake	48

3.3.1 Moisture diffusion 48

3.3.2 Volumetric swelling of matrix polymers 55

3.3.3 Swelling stresses due to non-uniform water uptake 58

3.4 Loss of load transfer in fiber reinforced resin 62

3.4.1 Load transfer mechanism 62

3.4.2 Durability of interfacial bonding 66

3.4.3 Loss of load transfer in fiber reinforced resins 66

3.5 Moisture induced degradation of the properties of composites 70

3.6 Current methods for study of moisture induced degradation of composites 70

IV. INTRODUCTION OF PROTECTIVE COATING ON ELECTRONIC MATERIALS 75

4.1 Introduction 75

4.2 Moisture induced degradation of protective coatings on electronic materials 75

V. EXPERIMENTAL PROCEDURE AND MATERIALS 81

5.1 The specimens 81

5.2 The experimental set-up 87

5.3 Measurement of water uptake 93

5.4 Determination of the optical fast and slow axes in the specimen 93

5.5 Measurement of optical-stress coefficient 95

5.6 The measurement of stress birefringence 98

5.7 The measurement of small deformation associated with water uptake 98

5.8 Estimation of stresses 99

5.9 Theoretical treatments 100

5.9.1 The redistribution of stresses due to debonding 100

5.9.2 Two-dimension model 102

5.9.3 Moisture expansion coefficient 104

VI. MEASUREMENT OF STRESS-INDUCED BIREFRINGENCE 107

6.1 Introduction to photoelasticity 107

6.1.1 The stress optic law in two dimensions 107

6.1.2 Measurement of optical retardation 108

6.2 Poincaré sphere analysis 118

6.3 A new method to measure stresses in specimen 128

VII. MEASUREMENT OF SMALL DEFORMATION 135

7.1 Introduction 135

7.2 Optical interferometry 137

7.2.1 Theory of interferometry 137

7.2.2 Two-beam interference 137

7.2.3 Multiple-beam interference 140

7.2.4 Moire optical interference technique 142

7.2.5 Interferometric "strain gauge" 147

7.3 Optical caustic foci 147

7.3.1 The fundamentals of caustic theory 151

7.3.2 The application of causticS. 156

7.3.3 A new method to measure small deformation 158

7.3.4 Application to the measurement of dimensional changes 173

VIII. RESULTS AND DISCUSSION 201

8.1 Water uptake 201

8.1.1 Dimensional changes of epoxy resin during

fabrication and during water uptake 201

8.1.2 The changes in state of stress of epoxy resin due to volumetric swelling associated with water uptake 204

8.1.3 Moisture expansion and water uptake by a model composite 206

8.2 Effects of water uptake on stress-optical coefficient of epoxy resin 218

8.3 Durability of interfacial bonding 225

8.3.1 Stress induced birefringence patterns 225

8.3.2 Shear stress distribution and occurrence of debonding 227

8.3.3 Effects of different surface treatment of fibers on the durability of interfacial bonding 232

8.4 Effects of different surface treatment of fibers on surface energy of interfacial debonding cracks 234

8.5 Microcracking of matrix resin 237

8.6 Fracture of fibers 240

8.6.1 Deformation of fiber due to matrix swelling associated with water uptake 240

8.6.2 Stress distribution of around a single fiber..... 249

8.6.3 Birefringence observation of fiber fracture and identification of the failure modes 264

8.6.4 Fiber pull-out length..... 278

8.6.5 Discussion..... 278

8.7 Protective coating 285

8.7.1 Volumetric swelling of substrate associated with water uptake 286

8.7.2 Volumetric swelling of coatings 288

8.7.3 Failure modes of coating and substrate 301

IX. CONCLUSIONS 312

LIST OF REFERENCES 317
APPENDICES 325
Appendix A 326
Appendix B 329
Appendix C 332
VITA 338

LIST OF TABLES

TABLE		PAGE
2.1	Typical properties of fibers used in composite materials	8
2.2	Typical properties of polymer resins used in composite materials	9
2.3	Comparison of the strength of Interfacial bonding using different approaches	24
2.4	Failure modes of single-filament-resin specimen	41
3.1	In plane shear (=45° tension) test results for dry and wet AS/3501-5A Laminates (Source: Laurities et al. 1979)	71
5.1	Specimens of Chip-on-board (COB)	89
7.1	Methods of small deformation measurement	136
7.2	The advantages and limitations of optical caustic focus measurement as a method for measuring small displacement	178

LIST OF FIGURES

FIGURE		PAGE
2.1.	Schematic presentation of the interfacial region between fiber and matrix	13
2.2	Schematic presentation of the components of the interfacial region between fiber and matrix	14
2.3	Schematic arrangement for pullout test	17
2.4	Fiber configuration and illustration of fiber fragmentation process during determination of interfacial shear strength	20
2.5	Schematic diagram of the micro-indentation method whereby a single fiber or a group of fiber is compressed for measuring interfacial shear strength	22
2.6	Deformation of a unidirectional laminate due to a tensile load in the fiber direction when there is a perfect fiber-matrix bond	26
2.7	The effect of elastic properties of interfacial region (500nm) on the longitudinal modulus of the carbon/epoxy composite	28
2.8	Deformation of a unidirectional laminate due to a tensile load in the direction perpendicular to the fiber axis. A perfect fiber-matrix bond is assumed	29
2.9	The effects of elastic properties of interfacial region (500nm) on the transverse modulus of the composites with different fiber volume fractions	31
2.10	The mechanism of debonding (Outwater& Murphy Model)	34
2.11	The schematic presentation of the mechanism of fiber pull-out	36
2.12	Debonding according to Cook/Gordon where the tensile component in the stress field ahead of the crack causes interfacial failure before the crack reaches the fiber	38

2.13 The stress precipitating fracture, σ_y, and the stress parallel to the length of the crack, σ_x, both normalized to the remotely applied stress 39

3.1 Glass transition temperature as a function of absorbed moisture. (Source: Browning et al. 1977) 47

3.2 Moisture weight gain (%) vs time$^{1/2}$ of 3502 epoxy coupons subjected to various stress levels at constant humidity of 97% and at temperature of 40°C. (Source: Henson et al. 1987) 52

3.3 Maximal levels of moisture weight gain (%) attained in 3502 epoxy samples after 5 weeks of exposure to humidity under various stress levels. Conditions same as in Figure 3.2. (Source: Henson et al. 1987) 53

3.4 Relative moisture absorption (%) in epoxy coupons vs time. Samples immersed in distilled water under various levels of compressive stress. (Source: Yaniv et al. 1987) 54

3.5 The dependence of the moisture weight gain on the load direction respect with the direction of fiber. (source: Marom 1981) 56

3.6 Water uptake (upper row) and associated in-plane stress distribution (lower row), as a function of time of exposure to an aqueous environment. (Source: Ashbee 1989) 60

3.7 The schematic presentation of the mechanism of load transfer (shear lag theory) 64

3.8 The schematic presentation of the mechanism of load transfer (slip theory) 67

3.9 Osmotic-pressure-filled pockets at fiber interface (Source: Ashbee 1969) 69

3.10 Shear strength distribution for E-glass/Epon 828 before (filled bars) and after 0.5 hour exposure to water at 88°C (open bars). (Source: Miller et al 1987) 74

4.1 Corroded surface of an electronic package..... 77

4.2 Polymer coating peeled away from the substrate 78

4.3 Typical moisture–absorption curves for some polymers used as protective coating. (Source: Licabi 1970) 79

5.1 Schematic of thin film specimens containing either single short carbon fiber or no fibers 82

5.2 A small furnace used for fabrication of specimens 83

5.3 A set-up for water immersion test 85

5.4 Schematic of cylindrical specimen containing a single glass fiber at the axial direction of the cylinder 86

5.5 An as-received specimen coated with transparent polymer .. 88

5.6 Schematic of tensile specimen containing a bundle of carbon fibers 90

5.7 Nikon polarizing microscope (a) with a Brace-Köhler compensator (b) and a Sénarmont compensator (c) 91

5.8 Optical system used to generate and record interference fringe pattern and caustic foci 94

5.9 Schematic of showing how the optical fast and slow axes can be detected 96

5.10 A sample holder for stress-optical coefficient measurement 97

5.11 Single fiber composite specimen. (a) unstressed, (b) stressed and debonded at the ends of the fiber, and (c) the interfacial shear stress, τ, and the fiber axial stress, σ 101

5.12 Tensile stress trajectories in the matrix. (Source: Tyson et al. 1965) 103

5.13 Transformation of a 2-dimensional axial section of conic symmetry into one of elliptical symmetry 105

6.1 A stressed photoelastic specimen in a plane polariscope 109

6.2 Plane-polarized light, with polarization vector **A**, entering a birefringent specimen 111

6.3 Absorbing and transmitting characteristics of an analyzer ... 113

6.4 Superposition of retardation exhibited by specimen and compensator 116

6.5 Projection of the **E** vector helix 119

6.6 Poincaré sphere construction 120

6.7 Effects of retardation on elliptically polarized light can be seen by rotating through angle $\delta\theta=\psi$ about the axis **LJ** 125

6.8 Poincaré sphere analysis of retardation measured by Sénarmont method 127

6.9 Total birefringence are generated by the polarized light through a cylinder from a_1 to a_2 131

6.10 A cylinder consists of a large number of concentric rings such that the total birefringence along a path of light is the sum of contributions of individual rings 133

7.1 Schematic of two-beam interference 139

7.2 Schematic of multiple-beam interference 141

7.3 The complementary function $[1-\mathbf{A}(\theta)]$ 143

7.4 (a) Two-beam interference generated between a cover slip adhering to a specimen and an optical flat. (b) Multiple-beam interference generated between a light reflective surface coated with transparent polymer and an optical flat 145

7.5 Schematic of optical system developed to measure radial deformation of fiber in specimen immersed in distilled water. The light source is the same as in Figure 5.8 148

7.6 Schematic of the generation of the three sets of the interference fringes 149

7.7 The point focus of paraxial optics 150

7.8 Spherical aberration for a lens. The envelope of the refracted rays is called a caustic. (Source: Hecht [2]) 152

7.9 Formation of caustics in a cup of coffee. (a) the caustic rosette formed in a cup of coffee; (b) a ray diagram showing how the sharp, bright curves are generated 153

7.10 Geometrical relationship between incident ray and reflected ray in 3-dimensions 154

7.11 Geometric interpretation of the formation of a caustic, cf. Figure 7.10 157

7.12 The caustic geometry associated with a surface deformed from flat to cylindrical shape 159

7.13 Showing how, in this case, the sinusoidal shape of the second differential of the reflecting surface in (b) may be deduced from the relative positions of the cusps in the caustic focus (a) 165

7.14 The different geometries of the caustic foci corresponding to the increment of center displacement of the reflecting surface. The position of cusp point migrates towards the specimen surface with increasing center displacement 166

7.15 Generation of surface profile from a caustic focus by iteration 168

7.16 Comparison of the inverted surface profile obtained from caustic foci measurement and its true surface profile 171

7.17 The effect on surface profile determination of an error, $\Delta x = \pm 20$ μm, made in measurement of the position of a caustic focus 172

7.18 Surface profiles obtained by inverting the caustic focus shown in Figure 7.17 174

7.19 The deviation of experimentally determined surface profile at various sites, that is caused by the measurement error shown in Figure 7.16 175

7.20 The change, with increments of reflecting surface deformation, of x-axis co-ordinate of the caustic focus 176

7.21 Displacement of a cusp in a caustic focus as a function of deformation of the reflecting surface 177

7.22 Schematic of a caustic focus in the form of a conical surface of high light intensity that is everywhere tangential to the rays reflected by a deformed cover slip bonded to the end of a self-stressed uniaxial composite 180

7.23 Three sections through a caustic focus (bright star-shaped contrast and associated rings at the center of the field of view) formed by light reflected from the deformed cover slip bonded to one end of a uniaxial composite that has been self-stressed by immersing in distilled water for 250 hours at 50°C. The less bright family of concentric fringes extending over the whole of the field of view are Newton's rings resulting from interference in the water gap between the cover slip and the optical flat 181

7.24 Same as Figure 7.23 but for immersion in distilled water for 264 hours at 25°C 182

7.25 Vertical section through the caustic focus recorded in Figure 7.23 183

7.26 Vertical section through the caustic focus recorded in Figure 7.24. Note that the virtual part of the caustic has been measured 184

7.27 Cover slip displacement deduced from the measured caustic geometry presented in Figure 7.24 185

7.28 Cover slip displacement deduced from the measured caustic geometry presented in Figure 7.25 186

7.29 Showing how the size of the caustic changes with increasing time of immersion in water at 25°C 187

7.30 The build-up of stress at the center of the cover slip during immersion in water at 25°C 188

7.31 The reflected ray diagrams that form caustic foci. The two examples shown here are associated with the different surface geometries, cf. Figure 7.32 190

7.32 Showing the vastly different shape of caustic focus that results from very small differences in profile of the reflecting surface. Note that the 2nd differential is also markedly changed 191

7.33 Computer simulation showing the propagation of rays through a transparent coating that has a smoothly curved edge 192

7.34 Propagation of a ray striking the specimen at normal incidence 193

7.35 The geometry used to deduce Equation (7-35) 196

7.36 The computer generated ray diagram (a) and corresponding caustic focus (b) formed by the protective coating 197

7.37 Change of caustic associated with uniform swelling of coating during water uptake 198

8.1 Schematic of the shrinkage of epoxy after curing and the measurement of linear dimensional change 202

8.2 Linear dimensional changes of the net epoxy resin during immersion in distilled water at boiling temperature. Measurements were made at room temperature 203

8.3 The time needed for specimens to change from a state of compression to tension at point near the fiber end 205

8.4 Moire fringe loops created by superimposing on the initial interference pattern, the same pattern photographed at subsequent intervals during water immersion at 24.6°C 207

8.5 Normal displacement measured across a diameter in Figure 8.4 211

8.6 Volumetric swelling versus immersion time 212

8.7 Volumetric swelling versus square root of immersion time 213

8.8 The linear relationship between volumetric swelling and water content 216

8.9 Experimental data fitted to Fick's law using the diffusion coefficient evaluated from the measurement of volumetric swelling 219

8.10 Retardation measured versus tensile stress applied uniaxially on a specimen of neat epoxy resin 221

8.11 Retardation measurement of another specimen 222

8.12 The patterns of stress-induced birefringence around a single fiber totally embedded in a film of epoxy resin. (a). viewed at 0° to the polarizer axes, and (b). at 45° to the axes 226

8.13 The patterns of stress-induced birefringence change after immersion in boiling water. (a) before and (b) after water immersion 228

8.14 The retardation increases as immersion time increases..... 229

8.15 Typical retardation measurements made near fiber ends at points along a radial direction from a fiber totally embedded in epoxy resin and immersed in boiling water 230

8.16 The magnitude of the stress in the epoxy resin acting parallel to the fiber axis 231

8.17 Fiber **B**. Optical retardation changes close to the interface during boiling water uptake 233

8.18 Fiber **C**. Optical retardation changes close to the interface during boiling water uptake 235

8.19 The immersion time needed for specimens containing each of fibers **A**, **B**, **C**, **D** and **E** to debond 236

8.20 The relationships between the length of interfacial failure and water uptake time for different fibers..... 238

8.21 The interfacial fracture surface energies, normalized to that for fiber **C**, for specimens with fibers of different surface treatments 239

8.22 Penny-shaped crack in epoxy resin due to osmotic pressure generated by the diffused water 241

8.23 Crack in epoxy resin around a inclusion due to the mismatch between them. (a) initial; (b) after 10.5 hours immersion in boiling water; (c) an inclusion embedded in epoxy shown in (b); (d) an inclusion viewed at a polarizing microscope 242

8.24 Optic interferometry from a single fiber in a thin film..... 245

8.25 Changes in the patterns of interference fringes during water uptake. The same specimen as Figure 8.24 but after (a) 150 h. and (b) 500 h of water immersion at 25°C 246

8.26 The measured displacements permitting calculation of the fiber radial displacement resulting from deformation of the epoxy resin during water uptake 247

8.27 The geometry of a specimen 248

8.28 Measured displacements for another specimen. The legends are uased in the same way as in Figure 8.26 250

8.29 Thickness of the swollen region versus immersion time 253

8.30 Rate of advance of the swollen resin versus the immersion time 254

8.31 Graphically differentiation of the displacement W(r) for 58 hours immersion see Figure 8.5 255

8.32 Maximum and minimum deviants obtained by regression method and compared with graphical and analytical methods 258

8.33 Radial stress distribution generated by graphical differentiation from displacement curves in Figure 8.5. (a). 0.5, (b). 4.5, (c). 20 and (d). 58 hours 259

8.34 The sequence pattern of stress-induced birefringence of fiber **B** during water immersion, viewed at 45° to the polarizer axes 265

8.35 The sequence pattern of stress-induced birefringence of fiber **C** during water immersion, viewed at 45° to the polarizer axes 266

8.36 Fiber **B** Optical retardation measured through the resin adjacent to the interface and the corresponding interfacial shear stress, plotted as a function of both fiber length and immersion time 268

8.37 Fiber **C** Optical retardation measured through the resin adjacent to the interface and the corresponding interfacial shear stress, plotted as a function of both fiber length and immersion time 269

8.38 (a) Schematic of failure mode observed in fiber **B**. (b) The stress birefringence observed with fiber axis at 0° and 45° to the polarizer, **P** and analyzer, **A** axes 270

8.39 The patterns of stress-induced birefringence near the fracture of fiber **B**, viewed at 0° and to 45° to the polarizer axes respectively 272

8.40 (a) Schematic of failure mode observed in fiber **C**. (b) The stress birefringence observed with fiber axis at 0° and

45° to the polarizer, **P** and analyzer, **A** axes 273

8.41 The patterns of stress-induced birefringence near the fracture of fiber **C**, viewed at 0° and to 45° to the polarizer axes respectively 274

8.42 The sequence of the fracture of single carbon fiber **B** in epoxy resin after immersion in water at boiling temperature 275

8.43 The sequence of the fracture of single carbon fiber **C** in epoxy resin after immersion in water at boiling temperature 276

8.44 The SEM observation of a fiber fracture (fiber **B**) in the matrix self-stressed by water uptake 277

8.45 Similar crack propagation from single fibers for fibers **A**, **D** and **E** 279

8.46 The SEM observation of the typical fracture surface of specimens after 14 days immersion in distilled water at boiling temperature. (a) a specimen containing a bundle of fiber **B**, (b) a specimen containing a bundle of fiber **C** 280

8.47 The distribution of the pulled-out lengths of fiber under same conditions as Figure 4.46. (a) specimens containing a bundle of fiber **B**, (b) specimens containing a bundle of fiber **C** 282

8.48 The times required for the occurrence of debonding and fracture for all five fibers 284

8.49 Schematic, showing the overall thickness change of coating and substrate. Solid lines indicate dimensions of an as-received specimen; dashed lines represent dimensions after water uptake 287

8.50 Moire fringes, **M**, for sample #2 after immersion in distilled water at 25°C for (a) 10 days and (b) 20 days 289

8.51 Moire fringes, **M**, for sample #3 after immersion in distilled water at 25°C for (a) 13 days and (b) 33 days 290

8.52 Moire fringes, **M**, for sample #5 after immersion in distilled water at 25°C for (a) 12.5 days and (b) 28.5 days 291

8.53 Sketches of the Moire fringe patterns for the samples #2, #3 and #5, photographed in Figures 8.51, 8.51 and

8.52 292

8.54 The thickness increase of the substrate during water immersion of samples #2, #3 and #5 293

8.55 Schematic of caustic focus generated by the curved edges of the coating on the COB 294

8.56 The caustic focus (bright "picture frame") generated by the curved edges of the polymer coating and observed at four different distances from the specimen surface 295

8.57 The measured caustic focus for sample #1 immersed in distilled water at 25°C 297

8.58 The measured caustic focus for sample #2 immersed in distilled water at 25°C 298

8.59 The measured caustic focus for sample #3 immersed in distilled water at 25°C 299

8.60 The measured caustic focus for sample #4 immersed in distilled water at 25°C 300

8.61 The coating surface profiles during water uptake obtained by inverting the data in Figure 8.57 302

8.62 The coating surface profiles during water uptake obtained by inverting the data in Figure 8.58 303

8.63 The coating surface profiles during water uptake obtained by inverting the data in Figure 8.59 304

8.64 The coating surface profiles during water uptake obtained by inverting the data in Figure 8.60 305

8.65 The coating thickness change due to water uptake for the different samples 306

8.66 (a) As-received specimen, and (b) after 50 days immersion in distilled water at 25°C. **B**-bubble, **C**-corrosion pit 308

8.67 X-ray analysis, (a) at a corrosion pit, (Zn and Cu are present in the specimen holder), and (b) elsewhere on the coating 309

8.68 No visible damage. (A) As-received specimen, and (b) after 50 days immersion in distilled water at 25°C 310

8.69 Polymer coating that has peeled away from the substrate 311

CHAPTER I

INTRODUCTION

Composite materials, in common with most other materials, are prone to degradation under a variety of chemical, physical, and biological influences. The significance of the degradative effects is accentuated in today's technology. There is cause for concern because the mechanical properties of such materials often deteriorate during exposure to moisture for long periods of time. Thus, for carbon fiber/epoxy resin composites, the reductions in mechanical properties include, on the order of 50% for interlaminar shear strength, 50% for compressive strength and 10% for tensile strength.

Since the structure and properties of the fiber-matrix interface play a profound role in the mechanical and physical properties of composite materials, much work has been done on fiber surface treatments, characterization and evaluation of the interface. However, physically meaningful data for the effects of fiber surface treatment on moisture induced degradation of composite materials, are hard to come by.

The principal aims of the work reported here were to investigate the effects of fiber surface treatment in carbon fiber composite materials, and of post-curing of polymer coatings on electronic packages, on moisture induced degradation, respectively. Specifically, in respect to the former, the behavior of a single fiber in epoxy resin undergoing water uptake, as well as the water diffusion

process in a model composite, the volumetric swelling of the composite, the swelling-induced stresses, the durability of interfacial bonding, and the failure modes have been investigated.

In order to facilitate this investigation, several experimental techniques new to composite materials research have been refined and developed. The Poincaré sphere construction has been used for theoretical analysis of optical retardation measurements made during the course of this work. A new method of measurement of internal stresses in the specimen, based on a paper by Porisky [1934], has been developed. A Moire technique has been refined to make use of two- and multiple-beam interferences to study the small surface displacement associated with water uptake by a model composite and by the substrate of electronic packages. Optical caustics have been exploited to develop a new method to measure small displacements of materials under a variety of conditions.

The results have shown that the internal stress generated by the volumetric resin swelling can cause the fiber to deform enough for the strain to exceed the failure strain of the fiber, i.e., the fiber fractures. This is attributed to the durability of load transfer between matrix resin and fiber having been enhanced, by the proprietary fiber coating, to such an extent that swelling deformation large enough to fracture the fiber can be realized.

In respect of coatings on electronic packages, the results have revealed the effects of post-curing treatments on the dimensional change rates, and hence, on water uptake rates, and on saturated values for water uptake.

The method of optical caustic foci developed here is recommended for investigation of mechanical deformation of microscopic interface regions.

CHAPTER II

INTRODUCTION TO INTERFACES IN COMPOSITES

That two or more materials judiciously combined will perform differently, and often more efficiently than the materials themselves, is well known. The extra degree of freedom offered by the combination of materials, such as the choice of materials, their forms, proportions, distributions, orientations and interfaces, offers an extremely useful way of developing new materials. This kind of material is known as a composite material.

There is no universally accepted definition of composite materials. Depending upon the level of definition, steel, for example, might be classified as a composite material since there are at least, from micro point of view, two materials (components) combined. A working definition of composite materials which takes into account both the structural form and the composition of the material constituents is given by [Schwartz 1984],

A composite material is a materials system composed of a mixture or combination of two or more macroconstituents differing in form and/or material composition and that are essentially insoluble in each other.

Composite materials have also been classified in many ways, depending upon the ideas and concepts that need to be identified. A useful and all-embracing classification can be given as (I). natural composite materials, such as wood, bone, muscle and other tissue; (II).

microcomposite materials, such as poly phase metallic alloy, reinforced thermoplastics; (III). macrocomposites, such as reinforced concrete beams; (IV). molecular composites.

2.1 Fibers and matrices [Hull 1981 and Schwartz 1984]

Carbon fibers Carbon fibers are about 7 to 8 mm in diameter and consist of small crystallites of "turbostratic" graphite, which is one of the allotropic forms of carbon and which closely resembles single crystal graphite. In a single graphite crystal, the carbon atoms are arranged in hexagonal arrays. The atoms in the layer or basal plane are held together by very strong covalent bonds and there are weak van der Waal forces between the layers. This means that the carbon fibers are highly anisotropic: the in-plane Young's modulus is 910 GNm^{-2} and compared with 30 GNm^{-2} normal to the plane.

Carbon fibers are characterized by a combination of light weight, high strength, and high stiffness. Their high modulus and strength depends upon the degree of preferred orientation. To obtain high modulus and strength the layer planes of the graphite have to be aligned parallel to the axis of the fiber. The modulus of carbon fibers depends upon the degree of perfection of alignment which varies considerably with the manufacturing route and conditions. The arrangement of the layer planes in the cross-section of the fiber is also important since it affects the transverse and shear properties of the fiber.

Glass fibers Glass fiber, produced from mineral glasses based on silica

(SiO_2) with additions of oxides of calcium, boron, sodium, iron, and aluminium, is usually amorphous. The strength and modulus of glass is determined primarily by the three-dimensional structure of the constituent oxides.

Organic fibers High strength and stiffness can be obtained in fully aligned polymers [Frank 1970]. Organic fibers have been developed based on this physical principle. The most successful commercial organic fiber to date is produced by Du Pont company with the trade name Kevlar.

Thermosetting resins In thermosetting polymers, such as epoxy and polyester resin, the liquid resins are converted into hard brittle solids by chemical cross-linking which leads to the formation of tightly bound three-dimensional networks of polymer chains. The most characteristic property is in response to heat since, unlike thermoplastics, they do not melt on heating. The mechanical properties depend upon the molecular unit which make up the network, and the length and density of the cross-links [Ward 1970]. Thermosetting resins are usually isotropic and are normally regarded as brittle solids.

Thermoplastics Thermoplastics, being not cross-linked, derive their strength and stiffness from the inherent properties and the very high molecular weight. This characteristic ensures that in amorphous thermoplastics there is a high concentration of molecular

entanglements, which act like cross-links, and in crystalline thermoplastics there is a high degree of molecular order and alignment. In amorphous thermoplastics heating leads to disentanglement and a change from a rigid solid to a viscous liquid. In crystalline thermoplastics heating results in melting of the crystalline phase to give an amorphous viscous liquid.

Both amorphous and crystalline polymers may have anisotropic properties depending upon the conditions during solidification. Thermoplastic matrices are normally used with short fiber reinforcement for applications in products made by injection molding.

The properties of a selection of fibers and matrices used in composite materials are tabled in Tables 2.1 and 2.2.

2.2 Fiber-matrix interface

As seen in the previous section and in Tables 2.1 and 2.2, there are large differences between the elastic properties of the matrix and fiber materials. In a composite material, they somehow have to be mechanically coupled.

As the understanding has progressed, it has become apparent that a third entity—the interface between fiber and matrix—is so important that its structure and properties play a profound role in the mechanical and physical properties of the composite. The stresses acting on the matrix are transmitted to the fiber across the interface; the large differences between the elastic and physical properties of the matrix and the fiber have to be communicated through the interface. Although a precise description of the interface is beyond

Table 2.1 [Hull 1981]

Typical Properties of Fibers Used in Composite Materials

Property	Units	Carbon PAN-based Type 1	Carbon PAN-based Type 2	E glass	Kevlar
Dia.	μm	7.0-9.7	7.6-8.6	8-14	11.9
D	$10^3 kgm^{-3}$	1.95	1.75	2.56	1.45
E_1	GNm^{-2}	390	250	76	125
E_2	GNm^{-2}	12	20	76	
YS	GNm^{-2}	2.2	2.7	1.4-2.5	2.8-3.6
ε	%	0.5	1.0	1.8-3.2	2.2-2.8
β	$10^{-6}\,°C^{-1}$	- 0.5 to -1.2 (1)	-0.1 to -0.5 (1)	4.9	-2 (1)
		7 to 12 (2)	7-12 (2)		59 (2)
H	$Wm^{-1}\,°C^{-1}$	105	24	1.04	0.04

where Dia = Diameter, D = density, E = Young's modulus, YS = Tensile strength, ε = Elongation to fracture, β = Coefficient of thermal expansion (0 °C to 100 °C), H = Thermal conductivity (parallel to fiber axis), footnote 1= Parallel to the axis of fiber, footnote 2 = Fiber radial direction.

Table 2.2 [Hull 1981]

Typical Properties of Polymer Resins Used in Composite Materials

Property	Units	Epoxy	Polyester	Polypropylene	Nylon 66	Polycarbonate
D	Mgm^{-3}	1.1-1.4	1.2-1.5	0.90	1.14	1.06-1.20
E	GNm^{-2}	3-6	2-4.5	1.0-1.4	1.4-1.8	2.2-2.4
ν		0.38-0.4	0.37-0.39	0.3	0.3	0.3
YS	MNm^{-2}	35-100	40-90	25-38	60-75	45-70
ε	%	1.6	2	>300	40-80	45-70
H	$Wm^{-1}{}^{o}C^{-1}$	0.1	0.2	0.2	0.2	0.2
β	$10^{-6}{}^{o}C^{-1}$	60	100-200	110	90	70
W_a	%	0.1-0.4	0.1-0.3	0.03	1.3	0.1

Where ν = Poisson's ratio, W_a = water absorption 24 h to 20°C, the others are same as in Table 2.1.

present knowledge, an understanding of the role of the interface in composite behavior and the ability to control the properties and behavior of the interface are as important as the understanding and control of the properties of the two primary components—fiber and matrix. The production of a well-bonded interface is still a critical factor in polymer-matrix composite fabrication. In many cases, the transverse and shear properties in the composite are limited by the properties of the interface. The chemical and mechanical stability of the composite during service is subject to reactions which occur at the interface and to the relative interfacial energy. In addition, the interface plays a very important role during fracture of composite materials. For instance, by diverting cracks through a mechanism involving interfacial delamination, a composite material consisting of two brittle phases can exhibit significant toughness.

Some appreciation of the real properties of the interface is essential for an understanding of composite material properties. The interface, for example, plays a dominant role in the fracture toughness of composite materials and in their response to aqueous and corrosive environments. Composite materials with weak interfaces have relatively low strength and stiffness but high resistance to fracture, whereas materials with strong interfaces have high strength and stiffness but are very brittle. This effect is related to the ease of debonding and pull-out of fibers from the matrix during crack propagation. On the other hand, a weak bond fosters toughness since a crack has to stop at a free surface, i.e., interfacial gap.

In this section a literature review of the nature of the bonding

between the fiber and matrix, the theories of adhesion, and the effects of the interface on the mechanical and fracture properties of composite materials will be presented.

2.2.1 Theories of adhesion

In a simple system, bonding at an interface is due to adhesion between fiber and matrix. In general, adhesion can be attributed to five different mechanisms which can occur at the interface either in isolation or in combination to produce the bond [Wake 1978].

1. Absorption and wetting. As two electrically neutral surfaces are brought sufficiently close together there is a physical attraction, which can be best understood by considering the wetting of solid surface by liquids. From the results made by Kelly [1973], it is predicted that glass and graphite with surface energies of 560 mJm^{-2} and 70 mJm^{-2} respectively will be readily wetted by polyester and epoxy resins with surface energies of 35 mJm^{-2} and 43 mJm^{-2} respectively.

2. Interdiffusion. A bond between two polymer surfaces is formed by the diffusion of the polymer molecules on one surface into the molecular network of the other surface [Raghava 1987]. The bond strength will depend upon the amount of molecular entanglement and the number of molecules involved.

3. Chemical bonding. A chemical bond is formed between a chemical group on a surface and a compatible chemical group on the other surface. The strength of the bond depends upon the number and type of bonds. This is of particular interest for fiber composite

materials since interface failure must then involve bond breakage.

4. Electrostatic attraction. Forces of attraction occur between two surfaces when one surface carries a net positive charge and the other surface a net negative charge. The strength of the interface will depend upon the charge density.

5. Mechanical adhesion. Some bonding may occur purely by the mechanical interlocking of two surfaces.

2.2.2 Models for the interface between the fiber and matrix

According to the mechanism of chemical bonding and absorption and wetting, the "interface" may be defined as an "interfacial region", as shown in Figure 2.1, where chemical bonding is formed and which exists from the outer shell of the fiber, where the local properties begin to change from the fiber bulk properties [Hopfgarten 1979] through the actual interface and into the matrix, where the local properties are again identical to the bulk properties. The complexity of this interfacial region can best be illustrated with the use of a schematic model which allows the many different characteristics of this region to be visualized as shown in Figure 2.2.

A detailed experimental program has been conducted during the last few years to measure the adhesion between graphite fiber and epoxy resin to determine the interfacial chemistry and materials properties and to quantify the locus of fiber-matrix interfacial failure under shear loadings [Drzal et al. 1982, 1983]. These investigations have shown fundamental differences in both the level of adhesion and in the interfacial failure mode for each fiber combination. The

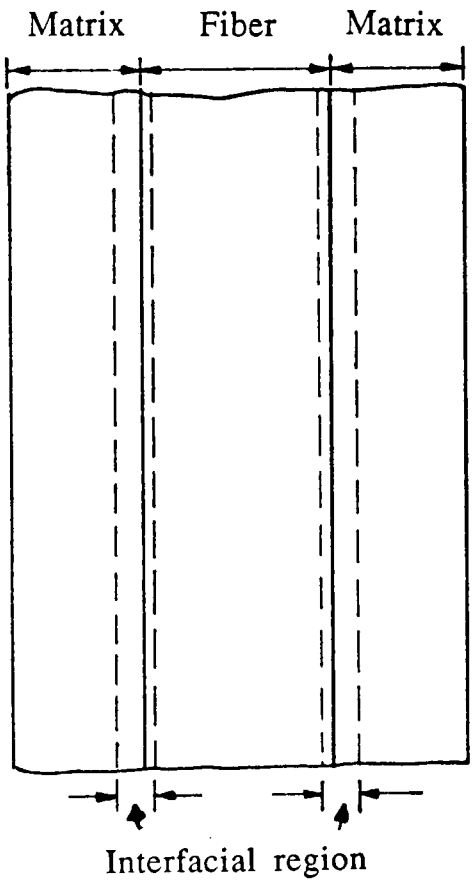


Figure 2.1. Schematic presentation of the interfacial zone between fiber and matrix.

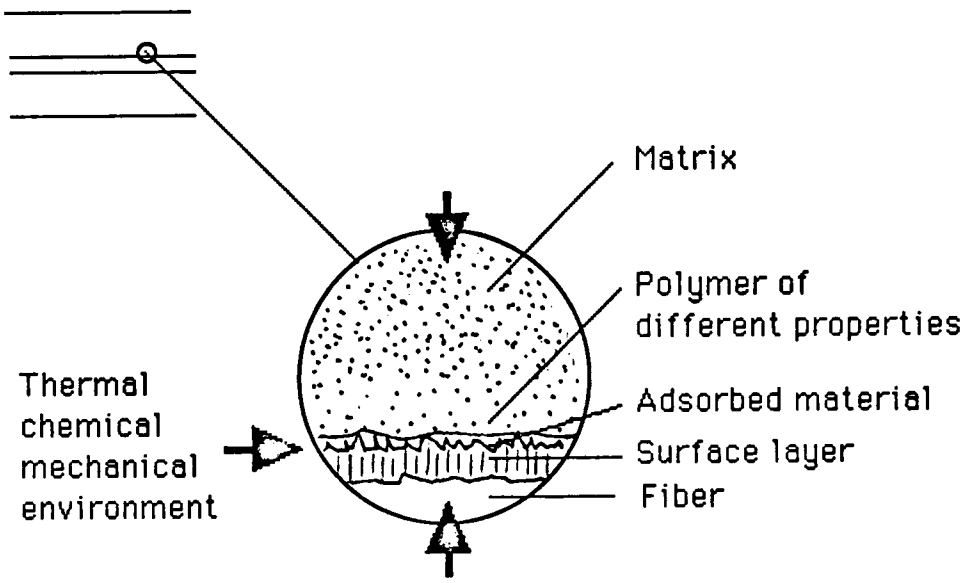


Figure 2.2 Schematic presentation of the components of the interfacial region between fiber and matrix.

adhesion level attained for surface treated and coated fibers is 30% to 100 % greater than that attained for the as-received fibers [Drzal et al. 1987].

It has been suggested that a volume of material surrounding the fiber is significantly different from the bulk matrix [Piggott 1987, Garton 1985 and Shelton 1988]. An attempt was made to determine the properties of the interface region [Drzal et al. 1983]. With finished fiber, the amine in the epoxy resin matrix diffuses into the amine free finish, at the same time it is reacting with epoxy functionalities. This would retard free diffusion and create an interfacial layer having a gradation in amine concentration decreasing that of the bulk of the resin to a very low value near the fiber surface. The measurements of the same matrix materials with varying amounts of mPDA (meta-phenylene diamine), shows that reducing amine content results in a material with a higher modulus [Drzal et al. 1983].

However, recent work has indicated that this layer may be softer than the normal matrix material. For a model composite with a single fiber embedded in an epoxy/amine matrix, this layer has been observed to be about 500 nm thick and the material had an average elastic modulus of about 1/4 of that of the normal matrix material [Williams et al. 1990].

The presence of material of higher or lower modulus itself can have an effect on the stress transfer and consequently on the interfacial shear strength. Some results showed that a material of higher modulus increases the shear stress transfer at the interface and thereby reduces the critical transfer length giving

rise to an increase in the interfacial shear strength [Kelly et al. 1965]. Mathematical relationships for a model single fiber system show that the interfacial shear strength increases with the shear or tensile modulus of the interface layer [Agarwal et al. 1979, Rosen 1965].

This layer significantly affects the elastic and fracture properties of the fiber reinforced composite, a fact that will be discussed in later sections.

2.2.3 Interface test methods

Although it is very important to have some measure of the strength of the bonding between fiber and matrix for evaluation of composite properties and for the development of well-designed interfaces, there is no satisfactory method of measuring the strength of the bonding. Most of the judgements as to bond quality are based on composite properties. Some rely on fractography of failed specimens to observe the surface and the fiber pull-out length. There are several approaches to the estimation of bond strength, one being a direct approach, and the others being derived from stress analysis.

The first approach is the single fiber pull-out test which is possible in cases where an individual fiber can be embedded in matrix in a controlled manner, and then removed without breaking the fiber. The bond strength is determined from the pull force and the bond surface area between the fiber and polymer disk (Figure 2.3). The relationship which assumes the shear stress to be uniformly distributed along the interface is as follows:

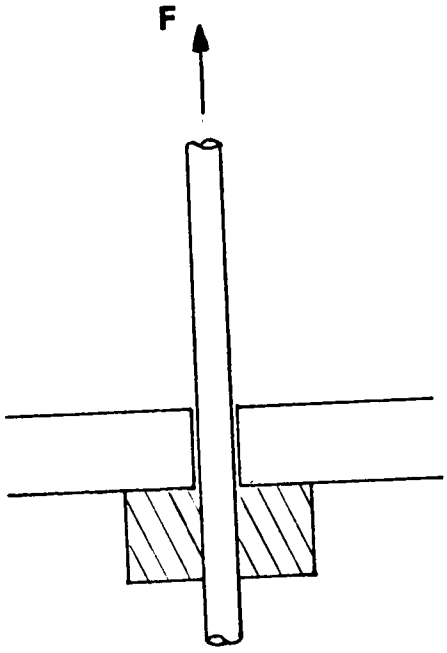


Figure 2.3 Schematic arrangement for pullout test.

$$\tau = \frac{F_p}{\pi D L} \qquad (2\text{-}1)$$

where:

τ = average shear strength of the interface,

F_p= Pull-out force,

D = fiber diameter, and

L = embedded fiber length.

This test is usually limited to materials in which the specimen can be easily cast. Techniques for casting a very thin disc [Penn and Lee 1982] or droplet [Miller 1987] around a small diameter fiber have been successful in a few cases.

In this test, the pull-out length depends on friction as well as bonding strength. Since the measured pull-out force is the sum of contribution of friction resistance and interfacial bonding strength. On the other hand, the state of stress at the fiber exit generated during pull-out testing, increases a tensile interfacial force which will affect the measurement of the interfacial shear strength. Because of these, it is not a satisfactory method of measuring the strength of the interfacial bonding.

The commonly used fiber pull-out technique, which gives rise to a direct measurement of force of debonding, has received wide usage with glass fibers but is difficult to use with the brittle and small graphite fibers. A technique used with metals was adapted [Drzal 1982] and designed to evaluate the interfacial shear strength directly.

The second approach is that a single graphite fiber is aligned axially in a tensile dogbone coupon, then the coupon is loaded in tension until the fiber fractures. As first proposed by Kelly [1970] the matrix material which has a high strain to failure can be loaded in tension. The brittle fiber encapsulated within the coupon is loaded in tension through the transfer of shear forces from the coupon operating within the fiber-matrix interface. The tensile load on the fiber builds up and exceed the fracture strength of the fiber causing it to fracture within the tensile coupon (Figure 2.4). This fiber fracturing process continues to create shorter and shorter fiber fragments until a length is reached which is no longer sufficient to support enough shear at the interface to cause further fiber fracture. This limiting length is known as the critical transfer length L_c. A simple force balance assuming ideal fiber properties and uniform distribution of load leads to the relationship

$$\tau = \frac{\sigma_f}{2} \frac{D}{L_c} \qquad (2\text{-}2)$$

where:

σ_f = the fiber fracture strength at the critical length L_c,

In practice a distribution of lengths is achieved due to the variations in fiber properties, e.g., defects, surface heterogeneities, geometric variations, etc. Therefore a statistical evaluation of the fiber

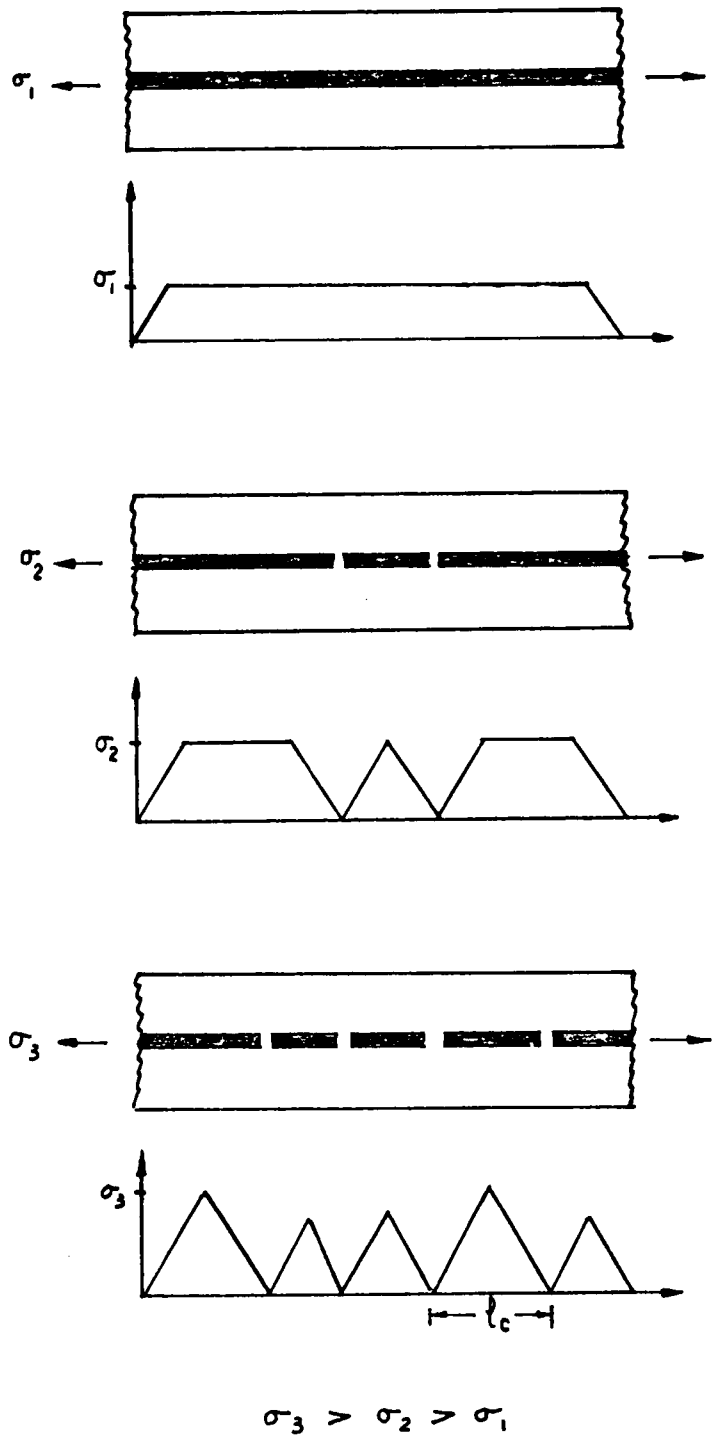


Figure 2.4 Fiber configuration and illustration of fiber fragmentation process during determination of interfacial shear stress strength.

length data must be made. This leads to a modified expression for

$$\tau = \frac{\sigma_f}{2\beta} \Gamma(1-\frac{1}{\alpha}) \qquad (2\text{-}3)$$

where:

Γ = the so-called Gamma function, and

a, b = the Weibull shape and scale factors of the two parameter of Weibull distribution [Cohen 1978].

This approach assumes that the matrix surrounding the fiber behaves as a perfectly plastic material wherein the shear stresses at the interface are considered to be constant along the short fiber critical length. Thus, the technique give rise an average value of the interfacial shear strength τ. It should be noted that, in this test, the interfacial is subjected to a net compressive stress due to Poisson's shrinkage of the matrix.

A third approach to bond characterization has been developed [Mandell et al. 1980, 1986], where a diamond-tipped microprobe is used as a indenter to push individual fibers or a groups of fibers in a composite until debonding occurs, as schematically shown in Figure 2.5. The direct result of the test is measurement of the force to produce debonding of a particular fiber. The data are then reduced to a nominal interfacial shear strength through a finite-element analysis. This technique has the advantage of reflecting actual processing conditions since the measurement is made on a real composite system. It can allow determination of interfacial bond strength during

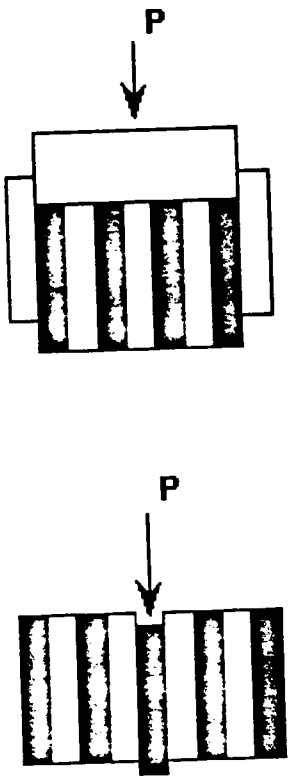


Figure 2.5 Schematic diagram of the micro-indentation method whereby a single fiber or a group of fiber is compressed for measuring interfacial shear strength

environmental exposure and even during service.

There are, however, some questions which remain unanswered regarding the nature of events taking place below the free surface, since they can significantly affect the interfacial shear stresses. A summary of the concerns to be accounted for this test is as follows: 1. Poisson's expansion of the fiber must substantially increase interfacial friction; 2. the compressional modulus, of carbon fiber for example, differs from the tensile modulus; 3. most materials densify under an indenter, e.g., see Ernsberger's elegant experiment [Ernsberger, 1968]; 4. graphite (in carbon fiber) is easily indented and plastically deformed under an indentation, but others (glass fiber for sure) fractures; 5. the effect of thermal and elastic residual stresses can significantly affect the interfacial shear strength. It should also be pointed out that artifacts may be made during the surface preparation procedure, for example, some damages created on the specimen surface during polishing procedure.

For comparison, the test results of interfacial bonding for particular fibers, measured by these three approaches, are listed in Table 2.3.

2.3 Effects of the interface

2.3.1 Effects of the interface on the elastic properties of composite materials

The elastic properties of the composite material can be calculated from the distribution of stress and strain. Because of the complexity of the calculation it is often necessary to use empirically

Table 2.3

Comparison of the Strength of
Interfacial Bonding Using Different Approaches

Approach	Fiber	Matrix	Strength(MPa)
Droplet	Carbon(Celion 3000)	Epon 828	57
Droplet	E glass	Epon 828	33
Droplet	Kevlar	Epon 828	38
Fiber fragmentation	Carbon	Epon 828	44.8 to 185.0
Micro-indentation	Carbon(Celion 6000)	System E	44 to 68

determined relations. In this section, the effects of interface on the elastic properties of unidirectional lamina will be discussed. The significance of the properties of the interface can be seen from the magnitudes of the transverse properties of the composite materials.

When a tensile or compressive load is applied parallel to the fibers in a unidirectional laminate (Figure 2.6), the strain, ε, in the matrix will be the same as the strain in the fiber and interface if the bond between the fiber and matrix is perfect. If fibers, interface and matrix deform elastically, and if ε is small, then the corresponding stresses are given approximately by,

$$\sigma_f = E_f \varepsilon_f, \quad \sigma_m = E_m \varepsilon_m, \quad \sigma_i = E_i \varepsilon_i \tag{2-4}$$

where:

σ = stresses,

E = elastic modulus,

ε = elastic strain,

subscripts f, m, i refer to fiber, matrix and interface, respectively.

For a composite material with cross sectional areas of fiber, matrix and interface, A_f, A_m and A_i, respectively, the applied load, P, can be expressed by

$$P = \sigma_f A_f + \sigma_m A_m + \sigma_i A_i$$

Since

$$\sigma_1 = E_1 \varepsilon_1, \quad A = A_f + A_m + A_i$$

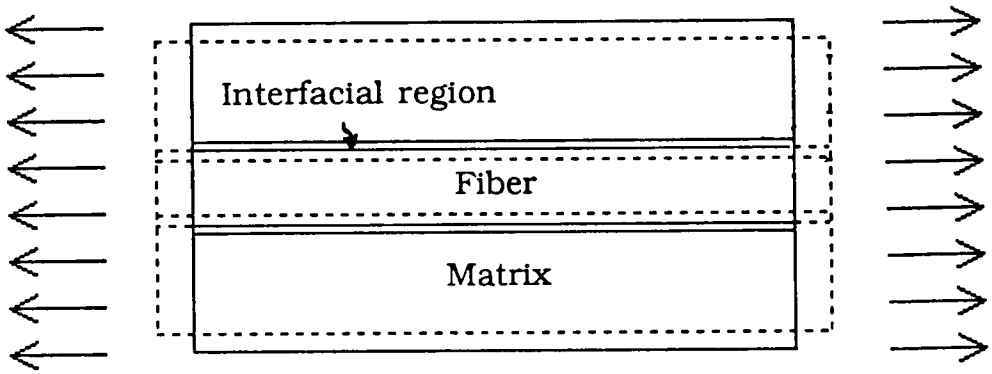


Figure 2.6 Deformation of a unidirectional laminate due to a tensile load in the fiber direction when there is a perfect fiber-matrix bond

where:

1 = the direction parallel to the fiber axis,

A = total cross sectional area.

The elastic modulus in the fiber direction can be obtained by

$$E_1 = E_f V_f + E_m V_m + E_i V_i \qquad (2\text{-}5)$$

This so–called modified "rule of mixtures" equation is obtained by adding the contribution of the interface. Figure 2.7 shows the influence of an interface, having $\frac{1}{10}$ the modulus of the matrix, on the elastic modulus parallel to the fibers of unidirectional laminate. Since the longitudinal properties of a unidirectional laminate are dominated by the properties of the fibers, the influence of the interface is evidently not significant. However, if the same kind of approach is used to predict the transverse modulus of a unidirectional lamina, E_2, the influence of the interface cannot be neglected. The simplest model of the composite material is represented in Figure 2.8 as a slice cut parallel to the fiber. The applied load transverse to the fiber acts equally on the fiber, on the interface and on the matrix and, if the assumption is made that $\sigma_f = \sigma_i = \sigma_m = \sigma_2$, the corresponding strains are

$$\varepsilon_f = \frac{\sigma_2}{E_f}, \quad \varepsilon_m = \frac{\sigma_2}{E_m}, \quad \varepsilon_i = \frac{\sigma_2}{E_i}$$

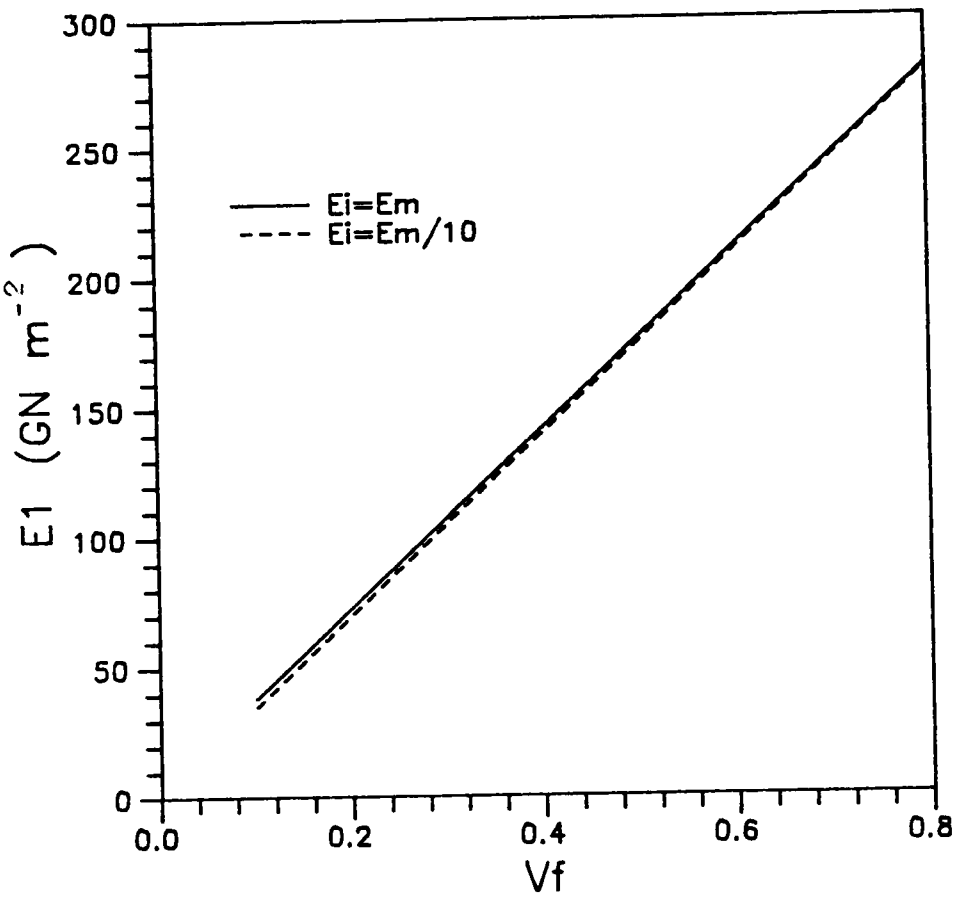


Figure 2.7 The effect of elastic properties of interfacial region (500nm) on the longitudinal modulus of the carbon/epoxy composite.

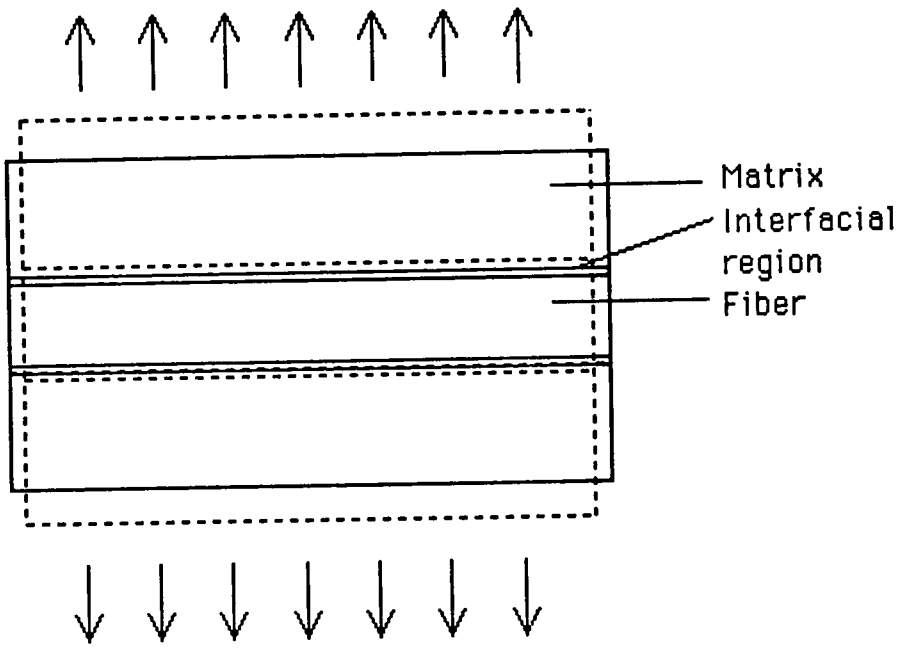


Figure 2.8 Deformation of a unidirectional laminate due to a tensile load in the direction perpendicular to the fiber axis. A perfect fiber-matrix bond is assumed.

Thus, the strain ε_2 is given by

$$\varepsilon_2 = V_f\varepsilon_f + V_i\varepsilon_i + V_m\varepsilon_m \tag{2-6}$$

Substituting these equations into $\sigma_2 = E_2\varepsilon_2$ gives

$$E_2 = \frac{E_f E_m E_i}{E_m E_i V_f + Ef Ei V_m + E_m E_f V_i} \tag{2-7}$$

This equation is plotted in Figure 2.9. The three curves represent three different cases: interfacial region of the same modulus as the matrix, of $\frac{1}{4}$ and of $\frac{1}{10}$ the modulus of the matrix. Very significant differences in the transverse elastic properties of unidirectional laminate are evident. It is concluded that the properties of the matrix in the vicinity of the reinforcing fiber are of considerable interest.

2.3.2 Effects of the interface on the fracture properties of a composite material

The fracture toughness of a composite is generally higher than the sum of the fracture toughnesses measured for its components. The reason for this is apparent since the work of fracture for a composite material is different from that of a monolithic brittle solid, the latter consisting of the fracture surface energy only. The major energy absorption mechanisms in a fiber reinforced composite include the

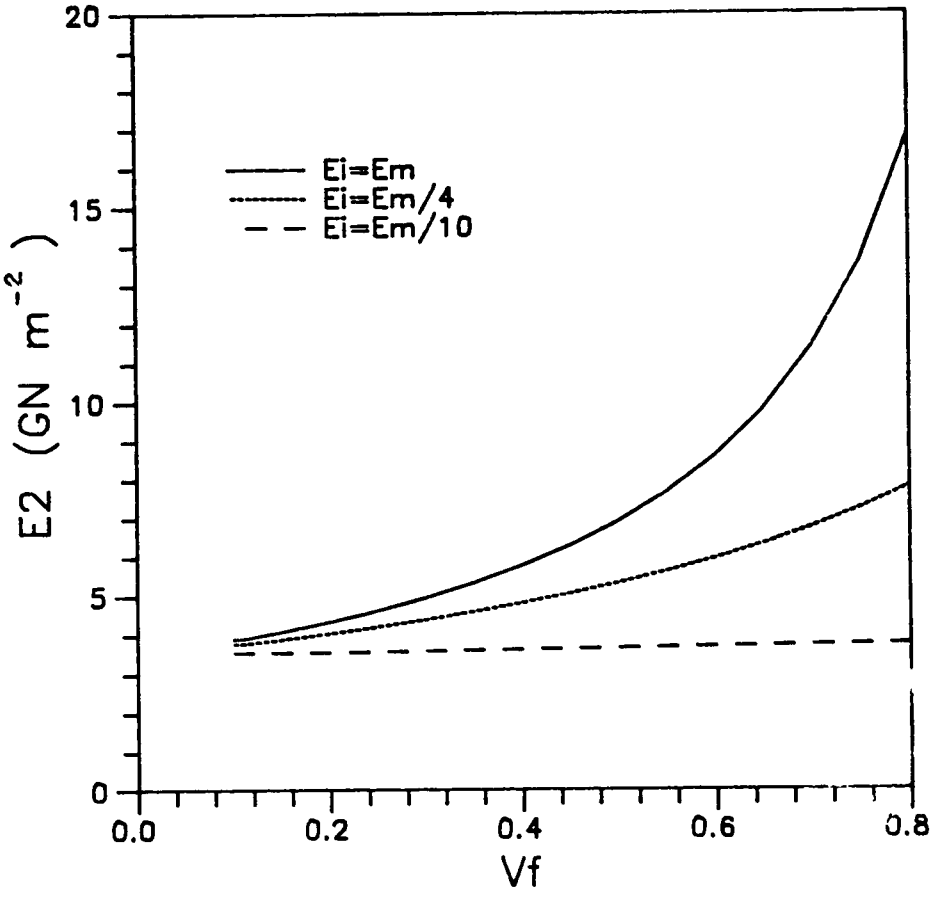


Figure 2.9 The effects of elastic properties of interfacial region (500nm) on the transverse modulus of the composites with different fiber volume fractions.

following:

a. Fiber debonding and pull-out variously known as the Cottrell [1964], Outwater-Murphy [1966] and Kelly [1973] energy absorption mechanisms.

b. Fiber deformation and fracture.

c. Matrix yielding or fracture, sometimes referred to as the Cooper-Kelly [1967] mechanism.

d. Interlaminar delamination.

e. Crack termination in a weak interface, as described by Cook and Gordon [1964].

f. Creation of fracture surface.

Of these mechanisms, mechanisms a and e, upon which the effects of interface are particularly significant, will now be discussed in more detail.

The mechanism of debonding involves a contribution made to the work of fracture by the process of debonding. In this mechanism, it is assumed that debonding of fiber and matrix can take place only after the crack has passed the fiber, i.e., it is assumed that the fracture strain of the fiber is greater than that of the matrix. This is not always true, however; sometimes the stopping of a crack at a fiber and the onset of interfacial cracking may take place simultaneously [Harris et al. 1975].

Equating the energy involved in debonding with the elastic strain energy of the debonding region of the fiber when the stress in this region reaches the failure stress, σ_f, of the fiber, Outwater and Murphy found that the work done in debonding per fiber, W_d, is given

by

$$W_d = \frac{1}{2}\frac{\sigma_f^2}{E_f} \times \text{(stressed volume)}$$

$$= \frac{1}{2}\frac{\sigma_f^2}{E_f}\frac{\pi D^2}{4} l_d \qquad (2\text{-}8)$$

where:

D = the diameter of the fiber,

E_f = the Young's modulus of the fiber, and

l_d = the debonded length, shown in Figure 2.10.

Thus if debonding occurs on N fibers for an average debonding length, L, the total strain energy dissipated as work of fracture is

$$W_d = \frac{1}{2}\frac{\sigma_f^2}{E_f}\frac{\pi D^2}{4} NL \qquad (2\text{-}9)$$

Since the volume fraction of fiber, V_f is given by,

$$V_f = \frac{N\pi d^2}{4A_c}$$

where:

A_c = the area of cross-section of the composite,

Eq. (2-9) reduces to

$$W_d = \frac{1}{2}\frac{\sigma_f^2}{E_f} V_f L A_c \qquad (2\text{-}10)$$

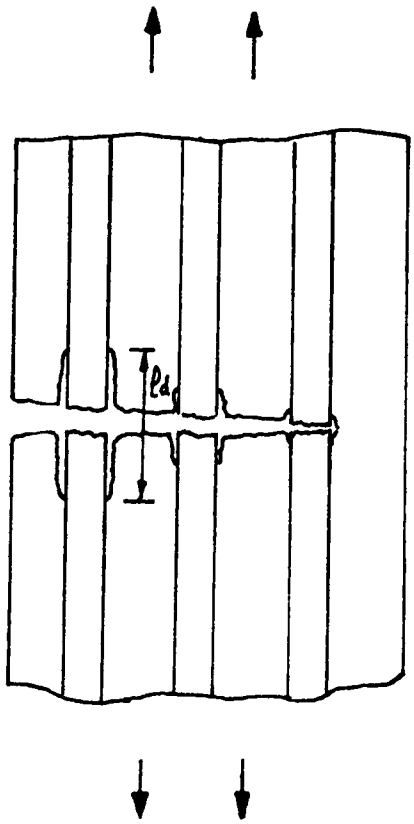


Figure 2.10 The mechanism of debonding (Outwater& Murphy Model).

Therefore the work of fracture due to debonding, γ_d, is given by

$$\gamma_d = \frac{W_d}{2A_c} = \frac{\sigma_f^2 V_f L}{4E_f} \qquad (2\text{-}11)$$

As mentioned before, this mechanism only applies when the filament fracture strain is greater that the matrix fracture strain.

Dividing the work of debonding by actual debonding area, $N\pi DL$, the fracture toughness of the fiber/matrix interface, γ_i, can be obtained as,

$$\gamma_i = \frac{W_d}{N\pi DL} = \frac{\sigma_f^2 D}{8E_f} \qquad (2\text{-}12)$$

Hence if $\gamma_i > \frac{\sigma_f^2 D}{8E_f}$, then the fiber breaks and no debonding occurs. Since γ_i is a material property, it depends upon the bond between the fiber and matrix. If the tensile strength, perpendicular to the interface, is low, then γ_i is also low and debonding becomes easier. Thus, the toughness is improved by a weak interface between the fiber and matrix.

The mechanism of pull-out simply means that fiber lengths are pulled out of the broken matrix. Assuming the stress resisting the pull-out to be τ, taken as a constant equal to the fiber-matrix interfacial strength, as shown in Figure 2.11, the work required to pull out fiber end from the matrix is given by

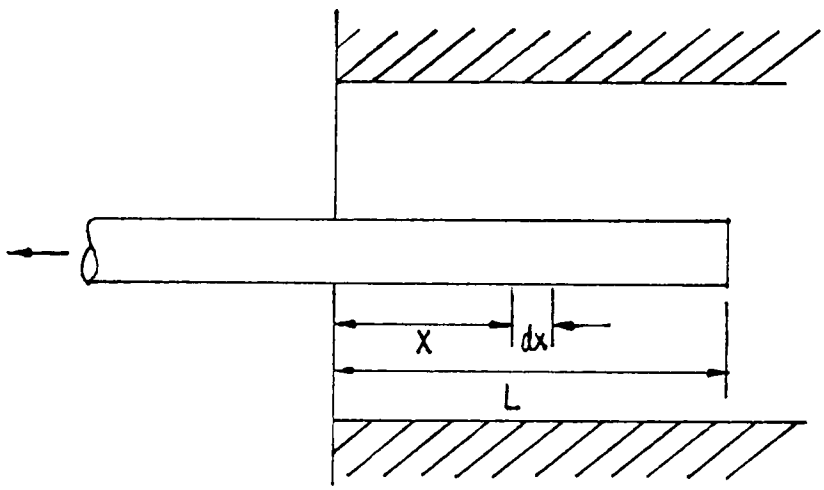


Figure 2.11 The schematic presentation of the mechanism of fiber pull-out.

$$W_p = \int_0^L \tau \pi D x \, dx = \frac{1}{2} \tau \pi D L^2 \qquad (2\text{-}13)$$

By same approach as above, the work of fracture due to pull out, γ_p, is given by

$$\gamma_p = \frac{V_f \tau L^2}{12D} \quad L \le L_c$$
$$\gamma_p = \frac{V_f \tau L_c^2}{12D} \frac{L_c}{L} \quad L \ge L_c \qquad (2\text{-}14)$$

where:

L_c = critical transfer length of a fiber,

and hence is linearly proportional to interfacial strength.

In the toughening mechanism of crack termination at a weak interface, a main or primary crack is blunted upon encountering a weak interface, as shown in Figure 2.12. If the interface is very weak, it will rupture some distance ahead of the main crack, due to a tensile component perpendicular to the fibers in the stress field ahead of a running primary crack tip, see Figure 2.13, and a secondary crack will be created. A significantly higher amount of energy is needed to initiate a new crack than the energy needed to propagate an advancing crack. Therefore, another contribution, in addition to debonding of a weak interface, to the fracture toughness of a composite material arises.

The effects of the interface on the fracture properties of composite materials can also been seen from fracture modes under

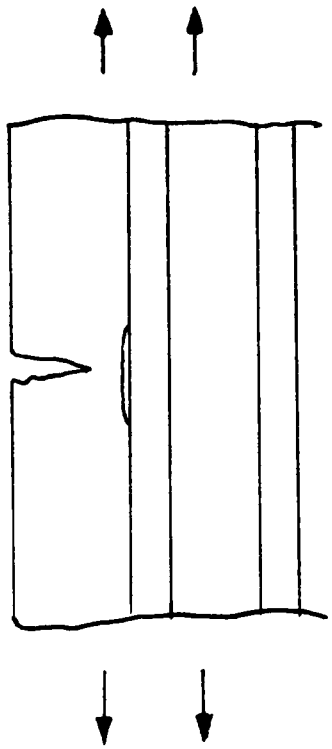


Figure 2.12 Debonding according to Cook/Gordon where the tensile component in the stress field ahead of the crack causes interfacial failure before the crack reaches the fiber.

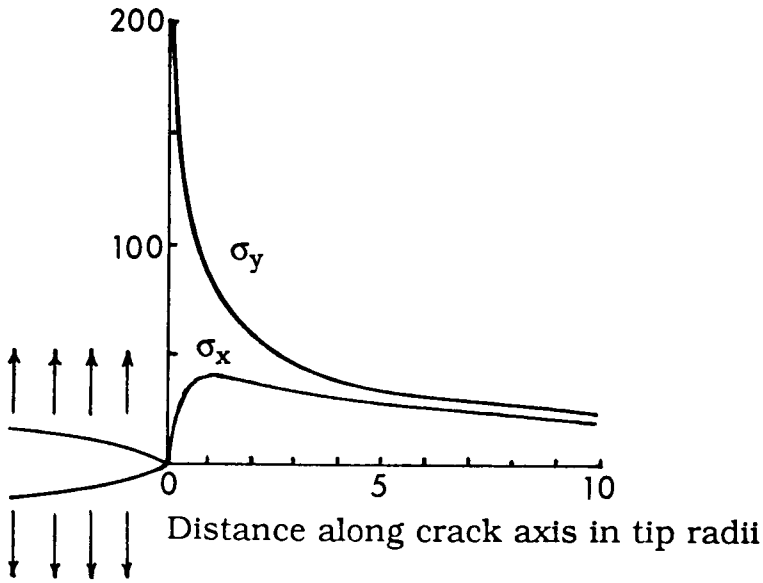


Figure 2.13 The stress precipitating fracture, σ_y, and the stress parallel to the length of the crack, σ_x, both normalized to the remotely applied stress.

same load conditions. Poor interfacial bonds easily fail, while interfacial bonds of high strength hold out and overall failure is characterized by matrix cracking.

Based upon the above energy absorption mechanisms, it can be seen that, in order to make a composite having optimum fracture toughness, compatibility between fiber, fiber coating and matrix is important. According to this, a model of a tailor-made coating and a compatible matrix has been proposed to make a controlled interface composite (Raghava 1987), in which failure modes such as fiber deformation and fracture, fiber pull-out and debonding, and interlaminar delamination occur in one fracture event.

2.3.3 Effects of interface on the failure modes of single fiber specimen

Two modes of local failure can be resolved in the fracture surfaces of composites. Unfortunately, the two modes are not easily distinguished since the failure process in composites is complicated. A single fiber test provides a useful tool for evaluating both matrix and interface characteristics. Since it is fiber that gives rise to reinforcement, fiber failure mode has significant effects on the mechanical behavior of composites. A summary of the different failure modes for single fibers reported by some researchers, are shown in Table 2.4.

Ashbee et al. [1969] studied the single fiber failure mode in glass/polyester resins and found that the interfacial debonding occurs due to the generation of osmotic pressure in water uptake tests. Debonding permits relative longitudinal movement between the fiber

Table 2.4

Failure Modes of Single-filament-resin Specimen

Workers	Results	Conditions
Ashbee et al. (1969)	1. Debonding cracks due to osmotic pressure generation 2. Indentation cracks in matrix following debonding	E glass fiber in polyester resin immersed in 100^0 C distilled water
Clarke et al. (1986)	Two failure modes 1. a single disk crack running out into resin in the same plane as the filament fracture 2. cracks run out from the interface at 45^0	Silicon carbide fiber in PMMA Loaded in tension
Drzal et al. (1982)	Three failure modes 1. frictional sliding 2. interfacial crack propagation 3. matrix crack propagation	Carbon fiber in epoxy resin loaded in tension
Mullin et al. (1968 & (1971)	Three failure modes 1. radial crack normal to fiber 2. interface debonding 3. resolved-shear-stress -induced tensile cracks in matrix	Boron-epoxy loaded in tension

and resin, thus allowing each fiber end to behave as a rigid indenter which propagates a conically shaped crack in the adjacent resin during resin shrinkage in hot water. Osmosis is the most important factor accounting for moisture induced failure in polymer matrix composites.

Clarke et al. [1986] observed two distinct types of matrix cracking behavior when a test piece consisting of a 100μm diameter silicon carbide fiber embedded in a clear PMMA (poly-methylmethacrylate) resin matrix was loaded in tension. Type I is characterized by a single disk crack running out into the resin in the same plane as the filament fracture. Type II cracks run out from the interface at 45° to the fiber axis and is attributed to matrix cracking on the plane of maximum tensile stress.

The investigations by Drzal et al. [1982] of the effects of fiber-matrix adhesion on the failure mode in a single fiber show that the different adhesion level, obtained by different surface treatment of fibers, results in significantly different failure modes. The untreated fiber exhibits the lowest level of adhesion, its interfacial shear strength being about 5.4-37.2 MPa. Failure is interfacial and is believed to be due to the shear stress induced by the single fiber test. For surface treated fibers, interfacial cracks have been observed. However, the failure mode associated with fibers which have been surface treated and coated and whose interfacial shear strength is 30 % greater than that of surface treated fibers, show a significant change from interfacial cracking to matrix cracking.

Different failure modes of single fiber, found by Mullin et al.

[1968 and 1971], were attributed to the response to the different load dynamics or to the differently modified matrices.

To summarize the observed failure modes, since the fiber is loaded by way of shear at the interface, it may do any of four things,

1. If the interfacial bond strength is sufficient, the fiber may fracture within the region of maximum tension. This may result in disk-shaped cracks in the matrix, or in inclined cracks in the matrix.
2. If the interfacial bond strength is lower but still sufficient for the fiber to be loaded to fracture, interfacial cracking after fiber fracture is possible.
3. If the interfacial bond strength is not sufficient for the fiber to be loaded to fracture, a simple debonding may occur.
4. Debonding permits relative longitudinal movement between fiber and resin, and this results in conically shaped cracks in the adjacent resin during subsequent resin shrinkage.

It is apparent from the above discussion that the properties of the interface significantly affect the fracture toughness of composite materials. For this reason the fracture toughness of a composite is generally higher than the sum of the values measured for its components.

CHAPTER III

MOISTURE INDUCED DEGRADATION

3.1 Introduction

Composite materials have been gaining wide use in commercial, military, and space applications because of their favorable performance characteristics. However, there is real concern because the mechanical properties of such materials are known to suffer when the material is exposed to moisture for long periods of time. The losses for carbon fiber/epoxy resin composites, can be of the order of 50% for interlaminar shear strength, 50% for compressive strength and 10% for tensile strength [Ashbee 1989]. Thus, it is important to have a thorough knowledge of the mechanisms of moisture transport and degradation in polymeric composite materials, as a base for understanding the deterioration of properties and also for developing improved materials. The effects of environmental factors on the properties of composite materials have been studied extensively [Springer 1980, 1984].

The apparent causes of degradation may involve several factors,

1). Degradation of the fiber-matrix interface resulting in loss of load transfer [Ashbee1969] and interfacial bond strength [Miller et al. 1987],

2). Matrix modulus and strength [Browning et al. 1977],

3). Loss of strength of the reinforced fibers due to leaching [Holland 1964, Wiederhorn et al. 1970], and stress corrosion.

Moisture absorption can take place by the following mechanisms,

1). Through the fiber-matrix interface [Marom 1977],

2). Through cracks and voids in the composite material [Ashbee 1969],

3). Through the resin (via diffusion).

This chapter will concentrate mainly on the degradation of polymer matrix composite materials by moisture absorption. Then, the established methods to investigate moisture induced degradation will be summarized.

3.2 Effects of moisture on component materials

3.2.1 Effects of moisture on fibers

A general weakening of glass strength with exposure to moisture is well cataloged [Holland 1964]. When water attacks glass, it leaches out the alkalis and, at the same time, preferentially attacks the points of high stress concentration, thus deepening the cracks and pits. The general effect of moisture on strength for exposures of 0% and 100% relative humidity is that for both an immediate and a delayed effect over several months, there is an average decrease in strength from 10 to 20 percent.

3.2.2 Effect of moisture on glass transition temperature of matrix resins

The glass transition temperature, T_g, of a polymer is defined as the temperature above which it is soft and below which it is hard [Bueche 1962]. It is an accepted theory [Bueche 1962] that at and below the glass transition temperature $\frac{1}{40}$ of the total volume of the material is free volume. If the free volume can be considered as an equivalence of Tg, then Tg can be altered by changing the free volume at a given temperature. That is, if a polymer were mixed with a miscible liquid that contains more free volume than the pure polymer, then Tg will be lowered. In particular, if it is further assumed that the free volumes are additive, then the diluent-polymer solution will contain more free volume at any given temperature than would the polymer alone. As a result, the plasticized polymer must be cooled to a lower temperature in order to reduce its free volume to $\frac{1}{40}$ of the total volume of the diluent-polymer combination. This is the kind of process which occurs when moisture is absorbed into an epoxy resin. Similar effects are observed in resin matrix composites [Browning et al. 1977]. The lowering of T_g with increasing moisture content is illustrated in Figure 3.1 for both an epoxy resin and derived graphite/epoxy composite.

In most engineering usage of fiber reinforced composites, laminate stacking geometry is chosen such that stiffness and strength are controlled by fiber modulus and strength, respectively. Thus, some matrix softening can be accommodated in such applications without serious consequences. If considerable matrix softening occurs, however, the ability of the resin to support the fiber is severely

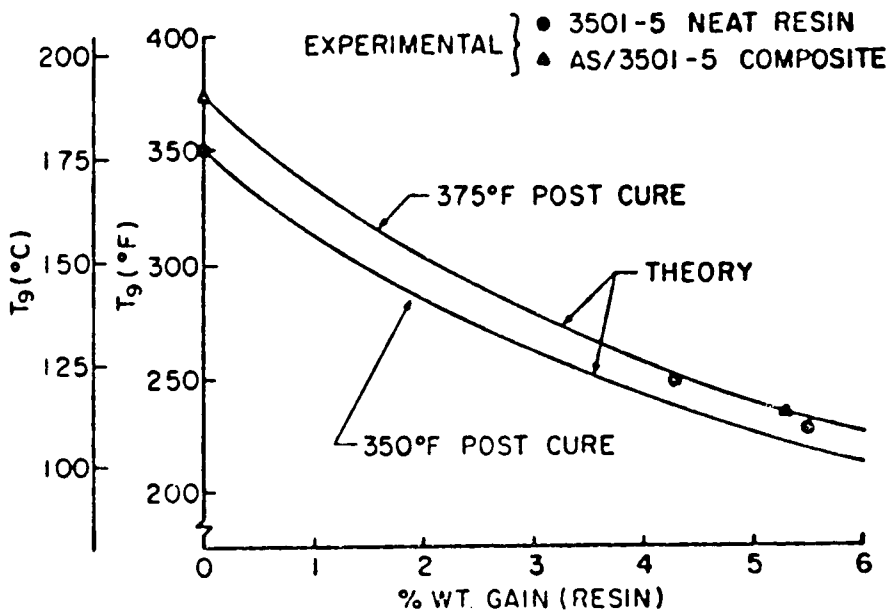


Figure 3.1 Glass transition temperature as a function of absorbed moisture. (Source: Browning et al. 1977).

reduced, along with the ability of load transfer through the matrix to the fibers. The result is a change in failure mode from fiber dominated to matrix dominated fracture. Thus, any loss in resin Tg due to moisture absorption can lead to a reduction in the useful temperature range of the composite laminate.

3.2.3 Microcracking in the matrix due to water uptake

Polymer resins, such as polyester and epoxy, usually contain water soluble constituents, dissolution of which by diffused water will create pressure differences, osmotic pressures, between the resulting solutions and the immersion water [Ashbee et al. 1967]. If the osmotic pressure exceeds the wet strength of the polymer resin, microcracking in the resin occurs, which is usually "penny" -shaped. The pressure to stabilize the formation of "penny"-shaped cracks can be estimated [Frank 1973], and is of the order of magnitude for osmotic pressure filled cracks. Measurements of the crack diameter [Sargent et al. 1984] reveal that the radial crack growth rates in epoxy resin at 70°C and 80°C are constant at 4.9×10^{-10} ms^{-1} and 1.1×10^{-9} ms^{-1}, respectively. In polyester immersed in water at 70°C and 80°C the same authors report constant crack growth rates of $5 \times 10^{-10} ms^{-1}$ and 7×10^{-11} ms^{-1}, respectively.

3.3 Swelling stresses due to non-uniform water uptake

3.3.1 Moisture diffusion

The classical simple limiting case of diffusion is described by Fick's equation, with a constant diffusion coefficient, $D_x \frac{\partial^2 c}{\partial x^2} = \frac{\partial c}{\partial t}$. Diffusion of small molecules into or through a polymer, or composite material, often follows a more complicated pattern since it depends upon many material variables. For instance, the type of fiber and matrix, the fiber orientation with respect to the concentration gradient, the temperature, the difference in water concentration between the composite material and the environment and whether the absorbed water reacts chemically with the matrix or fiber, or with the interface between fiber and matrix.

It has been reported that moisture diffusion in laminated composites can be predicted by Fick's Second Law [Shen et al. 1984]. and that for temperatures in the range 40°C to 70°C, well defined Fickian behavior is obeyed by both the pure polymer and the composite [Valentin et al. 1987]. Knowing the fiber volume fraction, V_f, and the amount of water absorbed by the pure matrix $M_m\%$, the theoretical amount of absorbed water in the composite $M_c\%$ can be deduced,

$$\frac{M_m\%}{M_c\%} = \frac{\rho_m}{\rho_c} (1 - V_f) \qquad (3\text{-}1)$$

where ρ_m and ρ_c are, respectively, the densities of the matrix and the composite. It has also been reported that for thermoplastic composites, experimental values are always lower than theoretical values. On the other hand, for thermoset composites, theoretical

values are often lower than experimental values [Dewimille and Bunsell 1982]. Thus, it is evident that the type of matrix affects the diffusion of water in composites.

Water diffusion in composite materials is also dependent on fiber orientation with respect to the concentration gradient. For continuous fibers, the transverse coefficient, D_2, can be written as [Springer and Tsai, 1967],

$$D_2 = D_m \left[1-2 \sqrt{\frac{V_f}{\pi}} \right] \qquad (3\text{-}2)$$

or the longitudinal coefficient of diffusion, D_1,[Bert and Kline,1985],

$$D_1 = D_m \left[1 - V_f \right] \qquad (3\text{-}3)$$

where:

D_m = the diffusivity of the matrix,

V_f = volume fraction of fiber.

It can also be shown that the theoretical ratio $\frac{D_1}{D_2}$ is about 2 for V_f = 40%. The diffusion coefficients in any given direction can be presented in terms of the diffusivities parallel and transverse to the fiber using the transformation relationships [Crank 1956],

$$\begin{aligned} D_{11} &= D_1 \cos^2\theta + D_2 \sin^2\theta \\ D_{12} &= (D_2 - D_1) \cos\theta \sin\theta \\ D_{22} &= D_1 \sin^2\theta + D_2 \cos^2\theta \end{aligned} \qquad (3\text{-}4)$$

Since the diffusion coefficient is a function of temperature and stress (or strain) [LeFebvre et al. 1989],

$$D = D(c, t, \sigma) \tag{3-5}$$

where:

c = constant,

t = temperature,

σ = stress,

the effects of stress on diffusion in composite are also of interest. The effect of stress can be introduced by stating, as a first approximation, that the fractional free volume of polymers is a linear function of the dilational stress component. Therefore, tensile stress is believed to increase the diffusivity of moisture in polymers. Experimental observations are consistent with this prediction. Figure 3.2 shows the percent weight gain of water vapor, maintained at 97% RH (relative humidity), by epoxy coupons that were subjected to various levels of uniaxial tensile stress [Henson and Weitsmen 1987]. The maximal levels of moisture uptake reached during the tests (which lasted about 7 weeks) are plotted vs stress in Figure 3.3. The increase of diffusivity is apparent as the tensile stress increases. The dependence of water absorption by polymers on compressive stress has also been investigated and is shown in Figure 3.4 [Yaniv and Ishai 1987]. The sorption of distilled water by epoxy coupons, when subjected to uniaxial compression, decreases as the compressive stress increases.

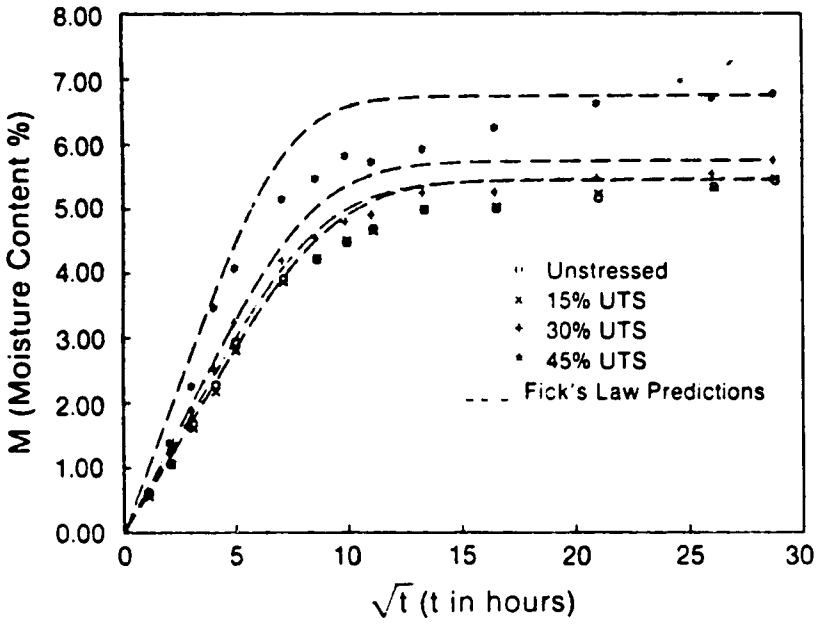


Figure 3.2 Moisture weight gain (%) vs time$^{1/2}$ of 3502 epoxy coupons subjected to various stress levels at constant humidity of 97% and at temperature of 40°C. (Source: Henson et al. 1987).

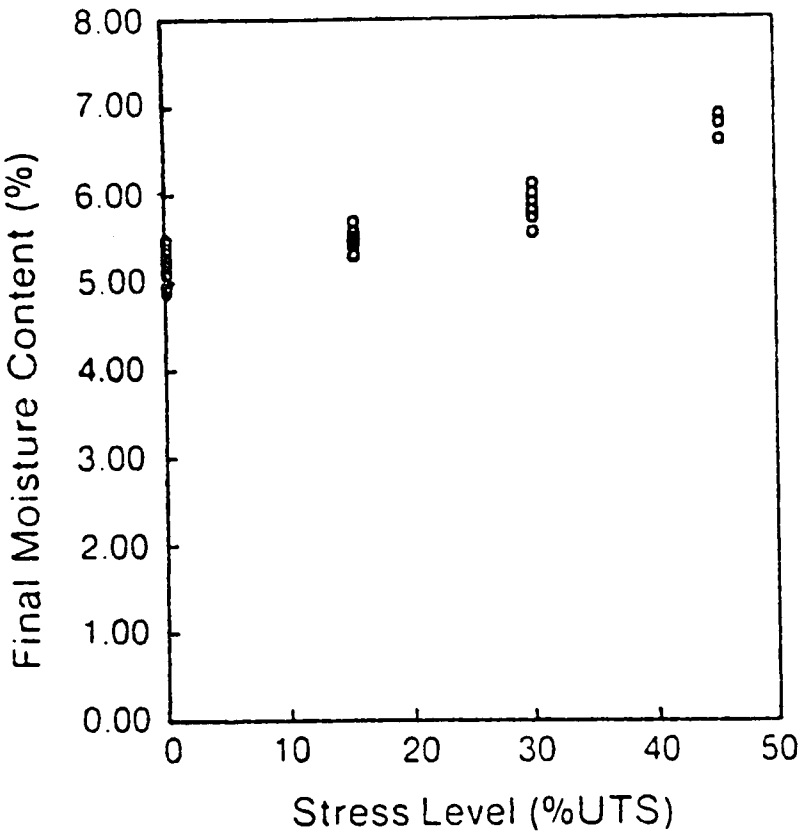


Figure 3.3 Maximal levels of moisture weight gain (%) attained in 3502 epoxy samples after 5 weeks of exposure to humidity under various stress levels. Conditions same as in Figure 3.2. (Source: Henson et al 1987).

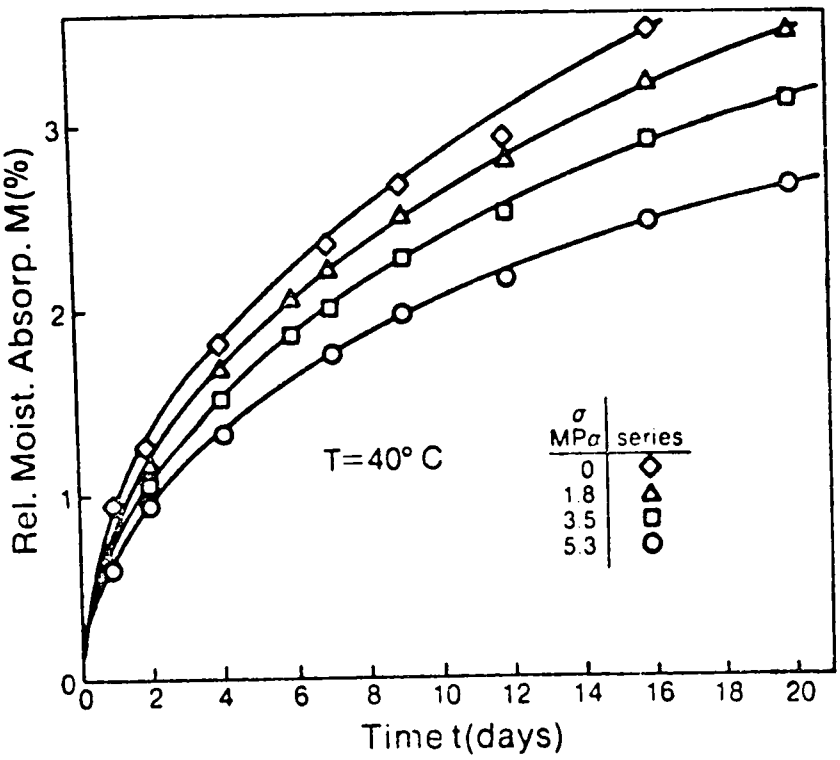


Figure 3.4 Relative moisture absorption (%) in epoxy coupons vs time. Samples immersed in distilled water under various levels of compressive stress. (Source: Yaniv et al 1987).

These experimental observations indicate the significant effects of stress on moisture diffusion in polymers. Since the diffusion mechanism depends upon the free volume within the polymer, the application of an external load is expected to affect both the rate of diffusion and its equilibrium weight gain through changing the free volume of the matrix. For example, the penetration of water into cross-ply, graphite-reinforced epoxy [Gillat et al. 1976] was shown to be highly sensitive to external load. It was found that when these materials were subjected to different stress levels, both the penetration and the equilibrium weight gain increased with increasing stress level. When a unidirectional composite specimen is loaded in tension at different angles between the the fiber direction and the load direction, the effect on water uptake depends upon the angle, transverse loading resulting in maximum effect, as shown in Figure 3.5 [Marom 1981]. In this case, the matrix undergoes maximum strain when the specimen is loaded in the transverse direction, i.e. there is maximum diffusivity for this orientation..

3.3.2 Volumetric swelling of matrix polymers

In this section, some background of thermal expansion and swelling of cured epoxy resin will be introduced.

In order to understand the experimental results, it is necessary to discuss certain theoretical concepts. "Thermal expansion" is used here to describe volumetric changes caused solely by variations in temperature at constant moisture content. "Swelling" is used to

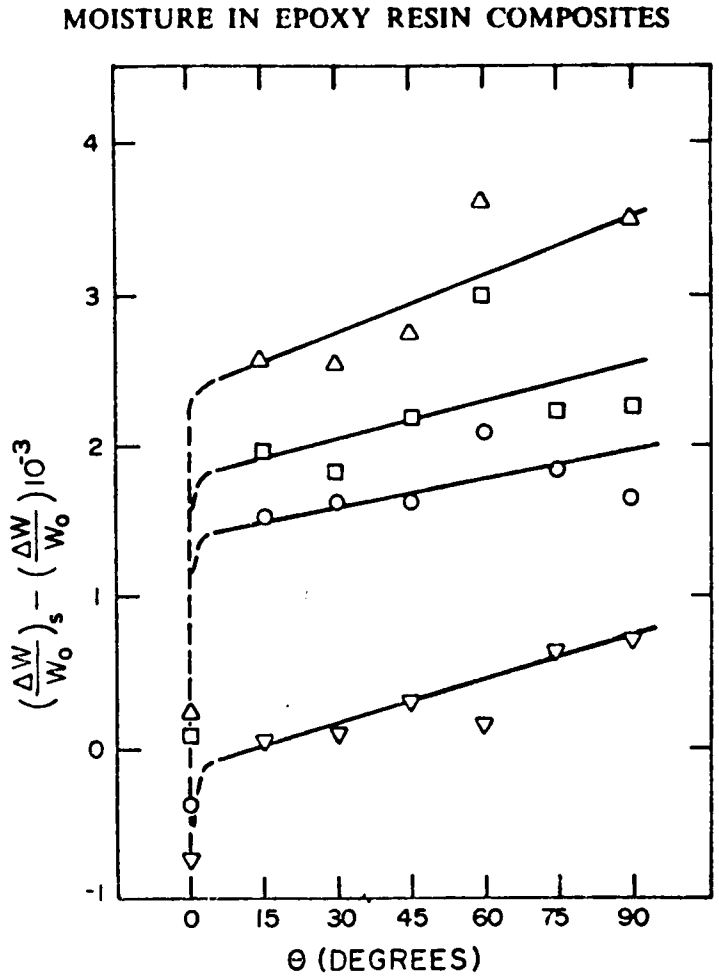


Figure 3.5 The dependence of the moisture weight gain on the load direction respect with the direction of fiber. (source: Marom 1981).

describe volumetric changes due to moisture content alone, i.e. in the absence of thermal expansion.

Thermal expansion According to the concepts presented by both Bueche [1962] and Ferry [1961], the only volume changes below T_g are of a solid-like character, involving no major structural rearrangement. Rehage and Borchard [1973] have reported that the number of hydrogen bonds is inversely dependent upon temperature. Cured epoxy resin contains polar hydroxyl groups which, because they retain a certain degree of steric freedom, are able to hydrogen bond by alightment with similar groups located on nearby segments. Consequently, one effect of temperature change is that of drawing some of the polymer segments closer together when the temperature is reduced and allowing some of the segments to move apart when the temperature is increased.

Swelling Because the water molecule is polar, it is capable of forming hydrogen bonds with hydroxyl groups, thereby disrupting interchain hydrogen bonding with the net effect of increasing the intersegmental hydrogen bond length [Kwei 1966 and Deanin 1972]. Thermodynamic arguments have shown that liquid molecules can combine with polymer molecules in the glassy state and actually become part of a glassy structure, establishing an equilibrium between the liquid and glassy phase mixture [Rehage and Borchard 1973].

Thermal expansion and swelling below T_g can be better understood through a consideration of the resin's "occupied volume" and "free volume". Occupied volume is defined as that volume, occupied by the actual mass of a molecule, plus the volume it occupies

because of thermally dependent harmonic vibration that excludes all other molecules from its domain. Occupied volume is dependent upon temperature because thermally induced motion causes each molecule (or molecular segment in the case of a cross-linked polymer) to move about its equilibrium position, thereby occupying more space than its actual mass volume [Bueche 1962]. If the molecules were packed so that their domains were in perfect contact, the occupied volume of the polymer at any temperature would exactly equal the sum of the actual mass volume of the molecules and their vibrational volume. The domains are not in perfect contact, however, and free volume is defined here as the difference between the measured volume of a polymer and the occupied volume. This difference is the result of "free space" or "voids" caused by packing irregularities [McKague et al. 1978 and Flory 1953].

It has been observed that the resulting volume of the polymer/water mixture is slightly less than the sum of the independent volumes of absorbed water and of dry polymer [Flory 1953]. Various workers [Chang et al. 1974, Paul 1969, Yasuda et al. 1971, Vieht 1965] suggest that water molecules can exist in polymeric media in two states: unbound as well as bound to the polymer molecule. It is assumed that bound water molecules, which cause swelling, are immobilized and that unbound molecules are contained in the polymer's free volume and are relatively free to migrate through the free-volume voids.

3.3.3 Swelling stresses due to non-uniform water uptake

As introduced in the previous section, in the case of water absorption the dimensional change is usually a volume expansion for epoxy resin. Absorbed water is rarely uniformly distributed in the composite material because of the effects of geometry and physical properties of the composite components. Therefore, there is a distribution of internal stress associated with water uptake, arising from both the difference in the moisture expansion of fiber and matrix and as a consequence of any constraint arising from the geometry of the composite material.

Consider in Figure 3.6 a parallel-sided slab of resin, exposed to an aqueous environment. For the sake of simplicity, any residual stress in the slab is neglected. The upper row of sketches shows the progress with time of water uptake and below that are sketches presenting the respective internal stress distribution associated with water uptake. Before the start, the water concentration, c, is zero across the thickness, and the slab is stress free. Once water uptake starts, the surface layers become saturated with water but the deeper layers are still dry. The surface swelling associated with the diffused water generates compression parallel to the slab and this requires that tension be simultaneously generated in the deeper layers. As water uptake proceeds, the stress is redistributed until it is again zero all across the thickness of the slab at uniformly saturated water uptake.

This is a most simplified case. Consider a case where there is an unswollen core in the slab. The distribution of swelling stresses will be more complicated and the largest tensile stress is the axial tension in the unswollen core. Furthermore, as the swelling front advances

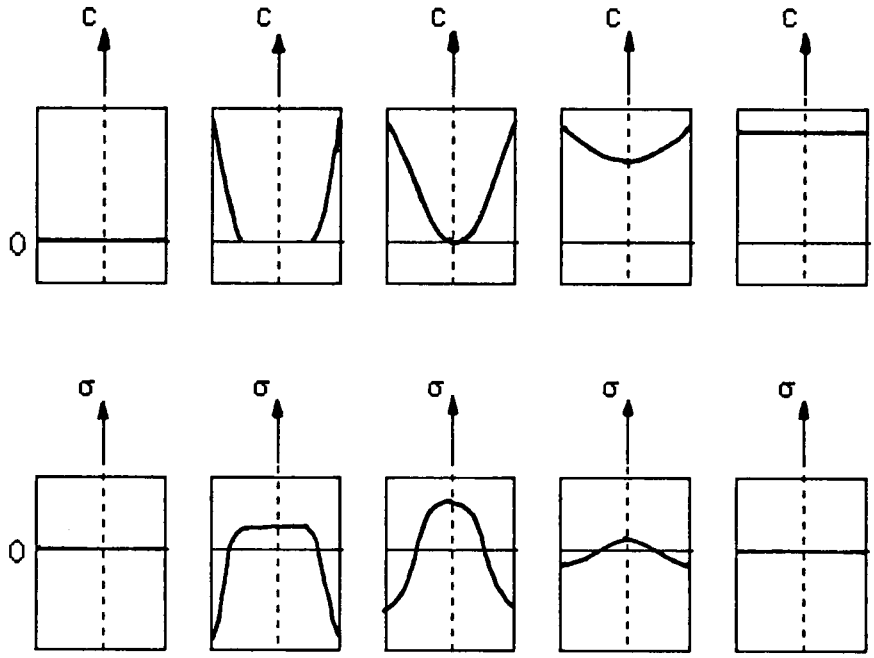


Figure 3.6 Water uptake (upper row) and associated in-plane stress distribution (lower row), as a function of time of exposure to an aqueous environment. (Source: Ashbee 1989).

inward, the calculated tensile stress using small-strain elasticity theory, increases without limit. Therefore, this increase can continue only until the tensile strength of the unswollen center is reached, at which time transverse fracture of the unswollen core is to be expected. It has been reported that a cylindrical specimen of a 5% DVB-95% styrene copolymer, fractures at the core after immersion in mehtyl ketone (MEK) at 25°C for 24.5 hr.[Alfrey et al. 1966].

Now consider a specimen of epoxy resin containing a single fiber at its center immersed in water. If a similar situation occurs, that is, the swelling stress reaches the tensile strength of the unswollen core, the fiber will fracture and this is one kind of potential damage of composite material when exposed to an aqueous environment. This particular consequence of water uptake has not been extensively realized.

Some analytical models are available for predicting the stresses in a composite system exposed to moisture. For example, an analytical model has been presented [Weitsman 1977] to analyze the debonding stresses at an interface between an adhesive layer and an adherent where the exposed edges of the adhesive absorb moisture. The results provide a satisfactory explanation to the debonding phenomena that are observed at the center of the adhesive joint as well as near the exposed edges. Some analytical models for predicting stresses in composite systems include the effect of expansional strain as a result of moisture as well as of the external load, such as for layered composite plates [Whitney 1971], and for an isolated fiber surrounded by an unbonded matrix [Whitney 1987]. An analytical prediction of the

response of both graphite/epoxy and glass/epoxy unidirectional composites to moisture uptake has been made by Adams [1979], in which, the interfacial stresses, including normal stresses and shear stresses, generated during water uptake, were calculated. These stress components are important for their effect on interfacial adhesion. The prediction of axial stress large enough to fracture fiber, was not reported.

3.4 Loss of load transfer in fiber reinforced resin

Load transfer at matrix/fiber interfaces is fundamental to the principle of fiber reinforcement. With weak interfacial bonding between fiber and matrix, the composite material may behave like a bundle of fibers; with strong interfacial bonding, the composite material may behave like a brittle monolithic solid. These alternatives have been discussed in Chapter II.

Owing to the sensitivity of interface to water uptake, moisture induced damage at the interface may be more profound than elsewhere. It is evident that, in order to optimize the level of adhesion between the fiber and matrix, the durability of interfacial bonding as well as the effects (e.g. hydrophobicity) of surface treatments must be known.

For the purpose of continuity, a brief description of the load transfer mechanisms from the matrix to the fiber is presented before reviewing on the durability of interfacial bonding.

3.4.1 Load transfer mechanism

The interactions between fibers and matrix are extremely complex. The first description, made by Cox in 1952 and now referred to as the shear lag theory, was based upon elastic interactions between fiber and matrix. Consider a fiber of length, L, embedded in a matrix of lower modulus. If the fiber is well bonded to the matrix, an applied stress on the matrix will be transferred to the fiber across the interface as illustrated in Figure 3.7.

Since the elastic modulus of the fiber is larger than that of the matrix, the strain in the fiber, in the region of the fiber ends, will be less than that in the matrix, as shown in Figure 3.7. Cox [1952] shows that, assuming both fiber and matrix to remain elastic and perfectly bonded, the tensile stress along the fiber and the shear stress at the interface, under stress applied parallel to the fiber, are given by,

$$\sigma_f = E_f \varepsilon_m \left\{ \frac{1 - \cosh\beta\left(\frac{L}{2} - x\right)}{\cosh\left(\frac{1}{2}\beta L\right)} \right\}$$

$$\tau = E_f \varepsilon_m \frac{\beta r}{2} \frac{\sinh\beta\left(\frac{L}{2} - x\right)}{\cosh\left(\frac{1}{2}\beta L\right)} \qquad (3\text{-}7)$$

where:

$$\beta = \sqrt{\frac{2G_m}{E_f r^2 \ln(R,r)}},$$

$2R$ = the interfiber spacing,

G_m = the shear modulus of the matrix, and

r = the radius,

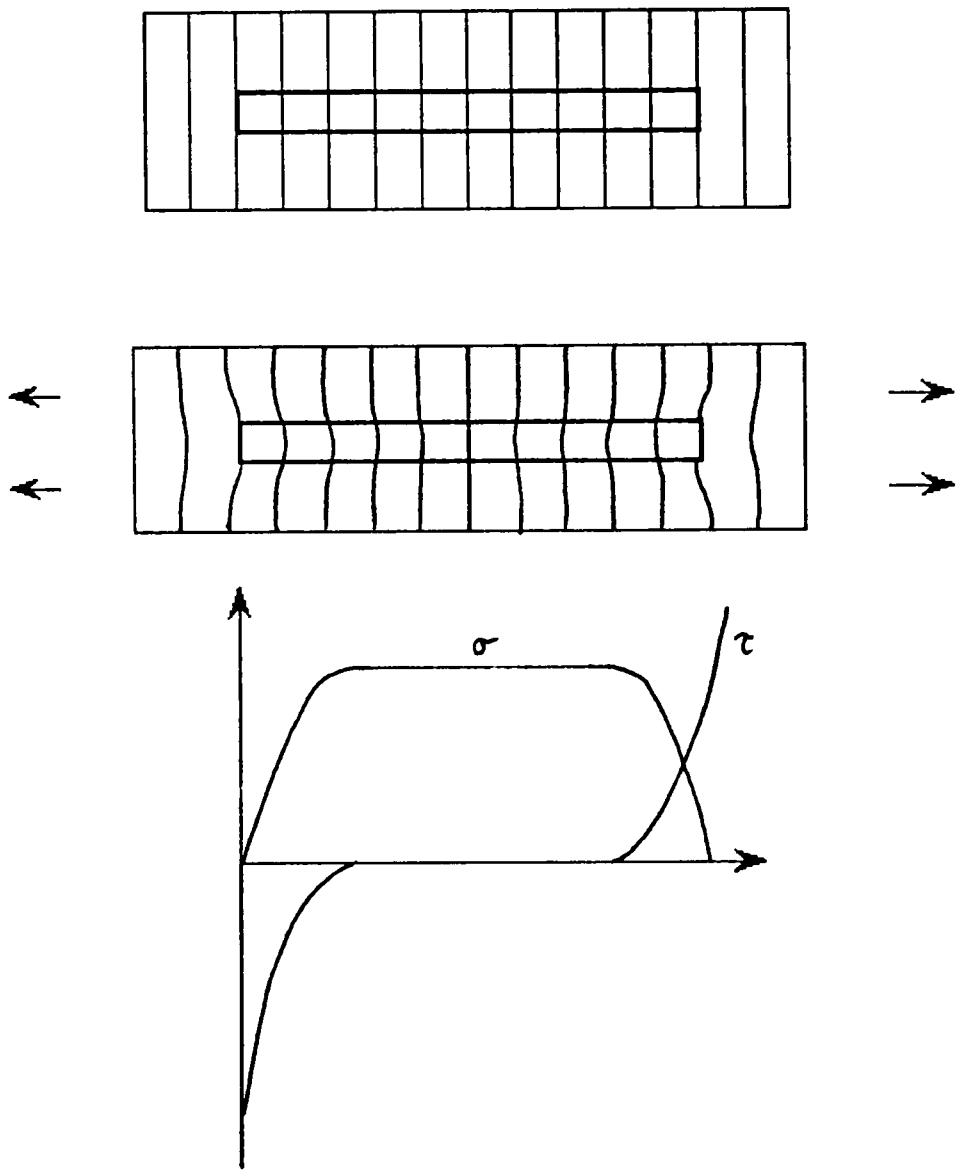


Figure 3.7 The schematic presentation of the mechanism of load transfer (shear lag theory).

L = the length,

E_f = Young's modulus, all of the fiber.

Graphical plots of Eq.(3-7) are shown in Figure 3.7. Thus, the tensile stress is zero at the fiber ends and a maximum at the center of the fiber. And, the shear stress is a maximum at the fiber ends and falls almost to zero in the center. These results indicate that there exist regions at the ends of the fiber that do not carry the full load. For this reason, the reinforcing efficiency decreases as the average length decreases.

The reinforcing efficiency is dependent not only on fiber length but also on the shear strength of the interfacial bonding. If interfacial debonding occurs at the fiber ends because of the high shear stress, the distance from the fiber end at which load transfer begins, migrates towards to the fiber center, and hence, the effective length of fiber decreases. In this way, the reinforcing efficiency decreases as interfacial debonding proceeds from the fiber ends.

In place of the shear lag theory, slip theory was proposed for metal matrix composite materials [Kelly 1965], based on matrix plasticity at the fiber surface near the fiber ends. Slip between fibers and matrix will normally take place at an interfacial shear stress which varies along the fiber length. However, in the case of metal matrices, if the fiber-matrix adhesion is perfect and if work hardening can be neglected, the shear stress will be constant in the slip regions and equal to the shear yield stress of the metal. This load transfer mechanism can also be used in frictional slip, which, in practice, usually takes place between fibers and matrix in weakly bonded

polymeric matrix composite materials. Thus slip theories are applicable to well-bonded reinforced metals, and to frictional sliding in reinforced polymers. The schematic presentation of stress distribution for the slip theory is shown in Figure 3.8 [Piggott 1980].

3.4.2 Durability of interfacial bonding

Due to the differential thermal contraction between fibers and resin, a net shrinkage of the resin on to the fibers occurs during cooling from the resin curing temperature to room temperature, and hence, the as-cast composite is self-stressed. The axial principal stress in each fiber is compressive and, for totally embedded fibers, is due to partly to the load transferred across the fiber ends and partly to the shear stress transferred across the interface between the fibers and matrix. When the composite is immersed in water, volumetric swelling takes place, as discussed previously, and this generates internal stresses which can suppress the residual stress arising from the curing procedure, and even produce a net stress, opposite in sign to that of the curing residual stress. This stress cycle, when a composite, originally dry, is exposed to an aqueous environment, will significantly affect the durability of the interfacial bonding between the fibers and matrix. For example, for a composite of carbon fiber/polyester resin exposed to boiling water, it has been observed that debonding between fiber and matrix takes place during the first few minutes [Wyatt et al. 1969].

3.4.3 Loss of load transfer in fiber reinforced resins

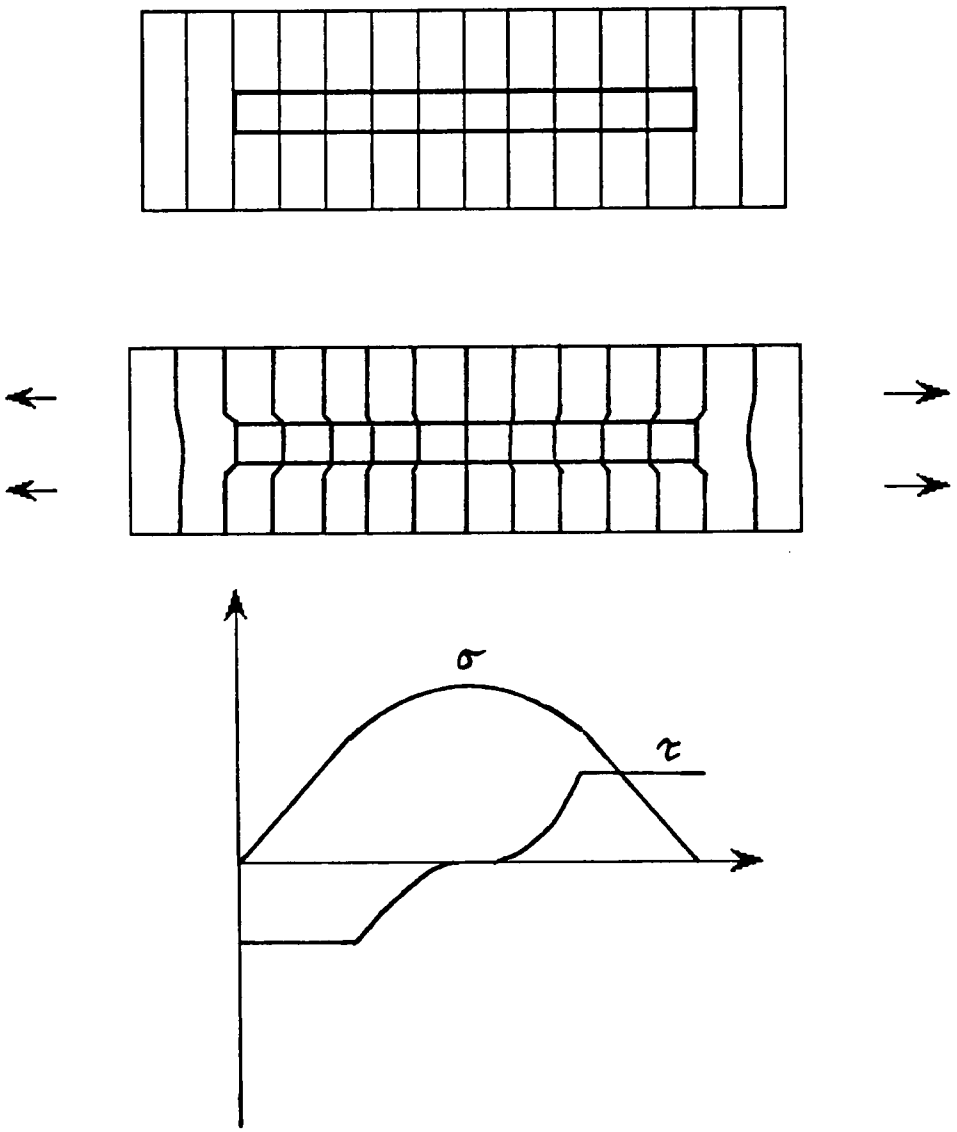


Figure 3.8 The schematic presentation of the mechanism of load transfer (slip theory).

Load transfer from matrix to fiber, can be lost when debonding between the fiber and matrix occurs. As a result, the reinforcing efficiency decreases. One important mechanism for the efficiency decrease of load transfer during service is osmosis [Ashbee and Wyatt 1969]. Water from outside diffuses through the matrix resin, dissolves water soluble material at the interface, thereby generating osmotic-pressure-filled pockets which take the form of cracks propagating into the adjacent resin. Examples of resin cracks at the fiber interface in C-glass/polyester composite are shown in Figure 3.9. In order to investigate the progress of loss of load transfer, a load transfer index was defined by Ashbee et al. [1967] when studying a composite of glass fiber and polyester resin. The fact that, for a short fiber composite in which fibers are well bonded to the matrix, the magnitude of the axial stress increases from zero at the fiber ends to a maximum at its center when the composite is loaded, allows the difference to be used as evidence that load transfer is intact. Now the optical retardation measured through a fiber diameter in a transparent glass fiber composite is due to the difference between the axial and radial principal stresses, and since the latter is approximately constant with fiber length, the diametral optical retardation should increase from the fiber ends towards the fiber center, in line with the increase in axial stress. The difference between the retardations measured at a fiber center and at each fiber ends is defined as the load transfer index. This index provides a direct indication of interfacial load transfer ability.

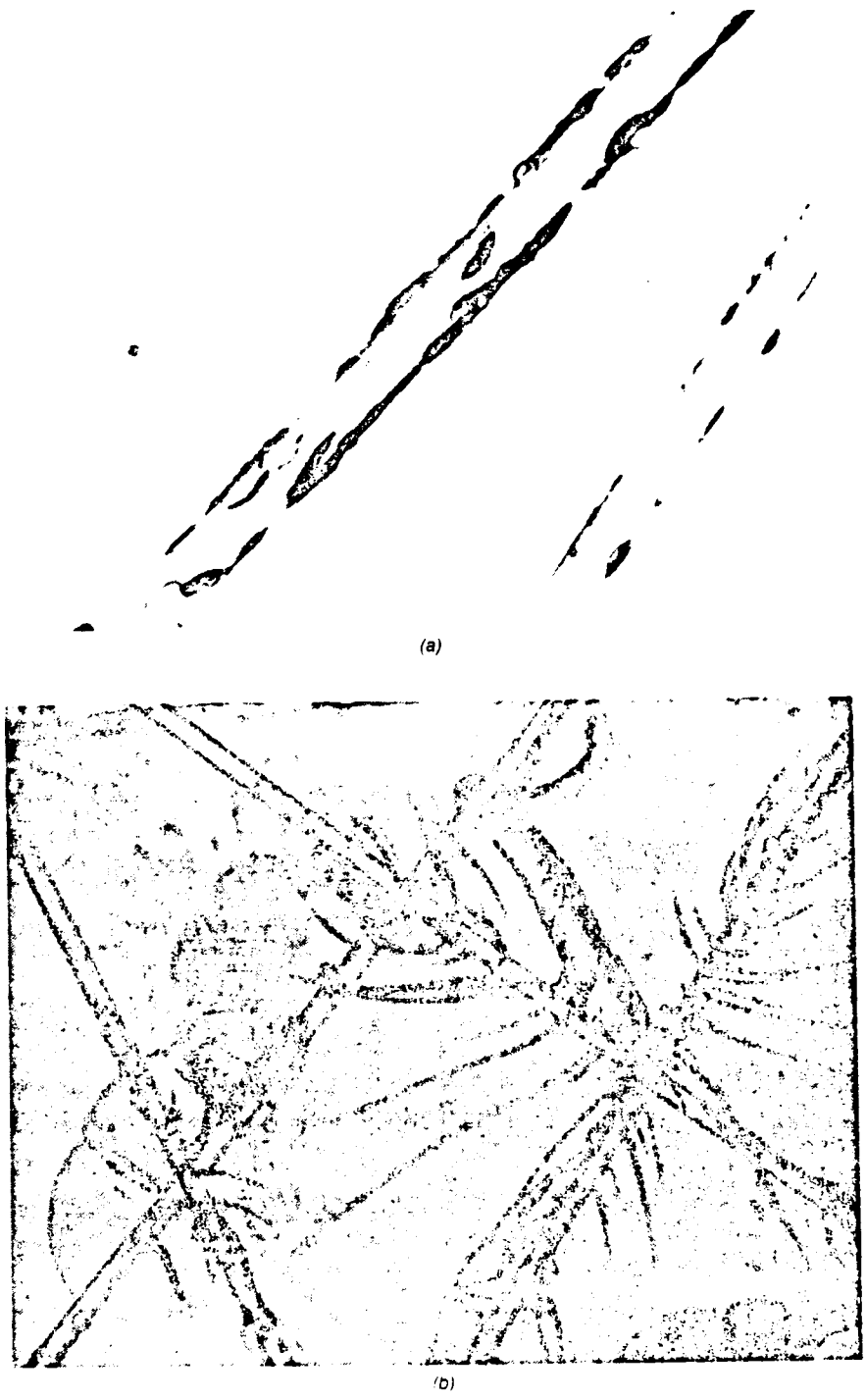


Figure 3.9 Osmotic-pressure-filled pockets at fiber interface (Source: Ashbee 1969).

3.5 Moisture induced degradation of the properties of composites

The moisture induced degradation of composites, from the micro-scale viewpoint, have been discussed in previous sections. The corresponding degradation of properties of composites on the macro-scale, is also noteworthy. Large numbers of tests have been performed by previous investigators, evaluating the effects of the environment on polymer matrix composites. The micro-mechanisms of degradation, which have been discussed, are consistent with the macro-scale test results. For instance, plane shear (45° tension) test results for dry and wet AS/3501-5A laminates (see Table 3.1) show an apparent decrease in shear strength and shear modulus, properties which are dominated by the fiber and the interface. As discussed previously, both of these locations are very sensitive to moisture pick-up from the environment.

3.6 Current methods for study of moisture induced degradation of composites

Many measurement techniques necessary for detecting moisture absorption and the associated degradation of properties have been established.

Gravimetric methods in which moisture uptake is measured in terms of the weight gain of a specimen, are most extensively used. The detection of water absorbed by carbon fiber composite material has been attempted by using microwave radiation [Carr 1986]. Since water strongly absorbs radiation in the centimeter wavelength region

Table 3.1

In Plane Shear (=45° tension) Test Results for Dry and Wet AS/3501-5A Laminates (Source: Laurities et al. 1979)

Temp °F	Max shear stress ksi		$G_{Initial\ in\ plane}$ psi X 10^{-6}		$G_{In\ plane\ at\ 20\ ksi}$ psi X 10^{-6}	
	Dry	Wet	Dry	Wet	Dry	Wet
-65	14.3	14.3	0.80	0.89	0.33	0.35
72	12.5	11.7	0.77	0.73	0.23	0.20
200	10.2	10.1	0.70	0.62	0.12	0.70
275	9.2	9.0	0.73	0.64	0.07	0.60

of the spectrum, a composite specimen after absorption produces a detectable change in attenuation.

Moisture distribution in a specimen during water uptake, which cannot be detected by any of the methods mentioned above, can be measured by X-ray diffraction and nuclear magnetic resonance. An X-ray diffraction method for detecting moisture via the changes in residual strains in crystalline filler particles, which were embedded in the matrix during layup, was developed by Predecki et al. [1984]. The results shows that the changes in diffraction peak positions are quite sensitive to environmental moisture taken up by laminates. Another experimental approach to detect moisture distribution is to use nuclear reaction [DeLasi 1984 and Whiteside 1983]. Analysis profiling of the localized moisture content is based upon exposing the specimen to D_2O, instead of H_2O, and measuring the subsequent deuterium concentration in the specimen. Published results have demonstrated that the nuclear probe is capable of determining moisture pickup in resins and composites with high sensitivity. Moisture profiles with resolution of 12μm in the direction of the concentration gradient have been measured in unidirectional graphite/epoxy composites and found to be consistent with classical diffusion theory.

Optical interference has been used to investigate swelling of CFRP specimen due to water uptake [Sargent et al. 1984]. Because of its high resolution, the swelling of the specimen associated with the amount of water uptake, can be measured very precisely.

In order to investigate the degradation of composites at the interface level, several novel experimental techniques have been

developed. For instance, photoelasticity [Ashbee 1969] has been used to monitor the onset of interfacial debonding. Ray optics, to measure the interfacial gap generated during water uptake, have also been employed [Sargent et al. 1986] to detect interfacial gaps of width 10nm. Micro pullout tests have been used to study the effects of moisture uptake on the strength of interfacial bonding, and show a significant decrease in strength after 0.5 hour exposure to water at 88°C (Figure 3.10).

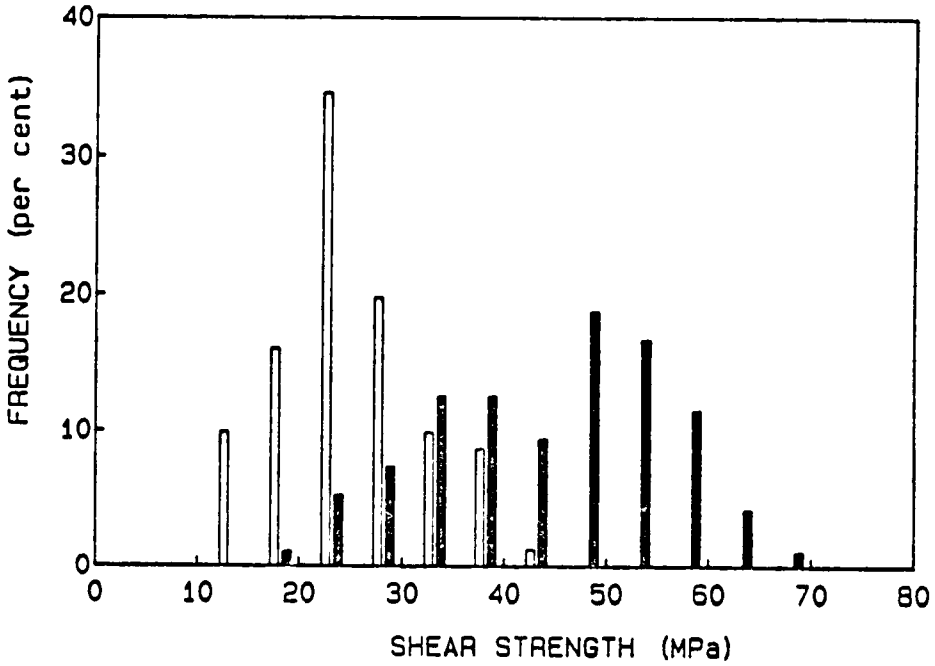


Figure 3.10 Shear strength distribution for E-glass/Epon 828 before (filled bars) and after 0.5 hour exposure to water at 88°C (open bars). (Source: Miller et al 1987).

CHAPTER IV

INTRODUCTION TO PROTECTIVE COATING ON ELECTRONIC MATERIALS

4.1 Introduction

Although coatings may serve numerous functions, the two most important functions are to provide electronic insulation and to provide protection from environmental degradation. As an environmental protection for all electronic materials, the coatings act as moisture and gas barriers to prevent corrosion and breakdown of electrical and electronic materials. Although all present polymeric coatings absorb water and are permeable to moisture and other gases to a greater or lesser degree and cannot be considered true hermetic seals, it is possible to select, and hence to tailor polymeric coatings so as to reduce moisture penetration sufficiently well for electronic packages to pass long-term storage and operational requirements.

Many kinds of polymeric coatings have been used for protection of electronic packages [Licabi 1970].

4.2 Moisture induced degradation of protective coatings on electronic materials

Failures of coatings, due to penetration of moisture, can be of three types. First, moisture mobilizes ionic contaminants within the coating or on the surface of the substrate, resulting in the commonly observed deterioration of electrical properties [Mathes 1967]. Secondly, moisture, again in the presence of impurity ions, permits electrolytic corrosion to take place [Ashbee 1989], as shown in Figure

4.1. Thirdly, moisture swells the coating and causes it to peel off the substrate [Ashbee 1989], as shown in Figure 4.2.

Because all organic coatings are permeable to moisture to varying degrees, quantitative values for their resistance to water are important. As discussed in Chapter III, water resistance may be defined in terms of three factors:

(1) the percent absorption of water by the coatings at constant temperature over a period of time,

(2) the rate of water transmission through the coating, and

(3) functioning of a coated electronic package after simulated or accelerated water uptake tests.

As mentioned above, coatings absorb water to varying degrees, the amount of water absorbed being a function of the structure of the polymeric coating and of the degree of cure. As a rule, those resin coatings containing hydrophilic polar groups such as hydroxyl or amide, or those containing low molecular weight water-soluble additives, will have high water-absorption characteristics. Also, semi-rigid coatings tend to absorb more water than highly cross-linked systems. The amount of water absorption eventually becomes constant at constant temperature for each material. In many cases, equilibrium is achieved only after one or more weeks of exposure. Some coatings exhibit a maximum water uptake value and then proceed to lose weight and reach equilibrium at an overall water uptake much lower than the maximum. This is attributed to leaching out of water soluble additives or of trapped solvents. This behavior is illustrated in Figure 4.3.

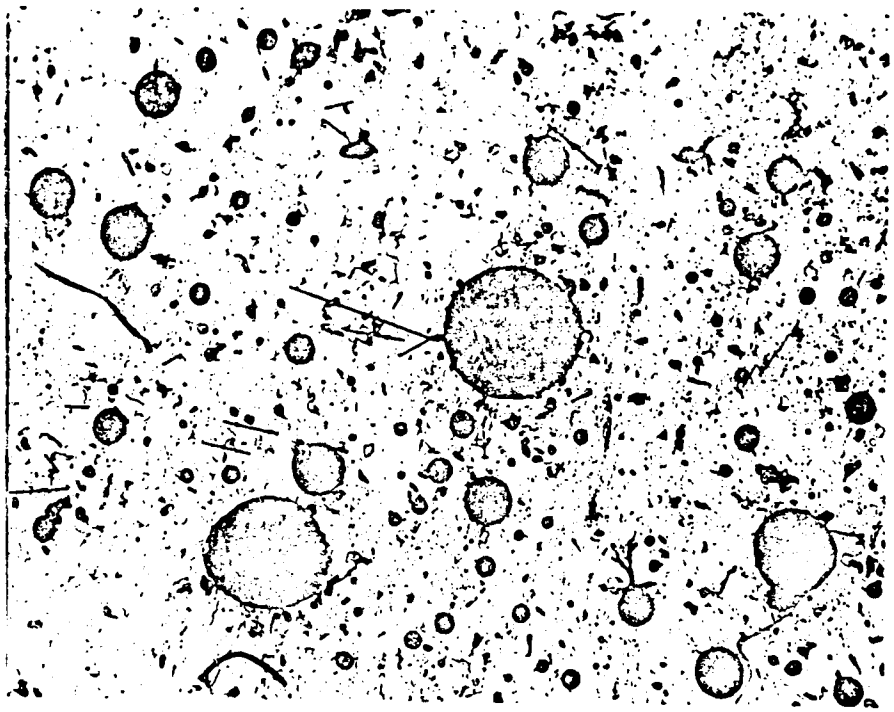


Figure 4.1 Corroded surface of an electronic package.

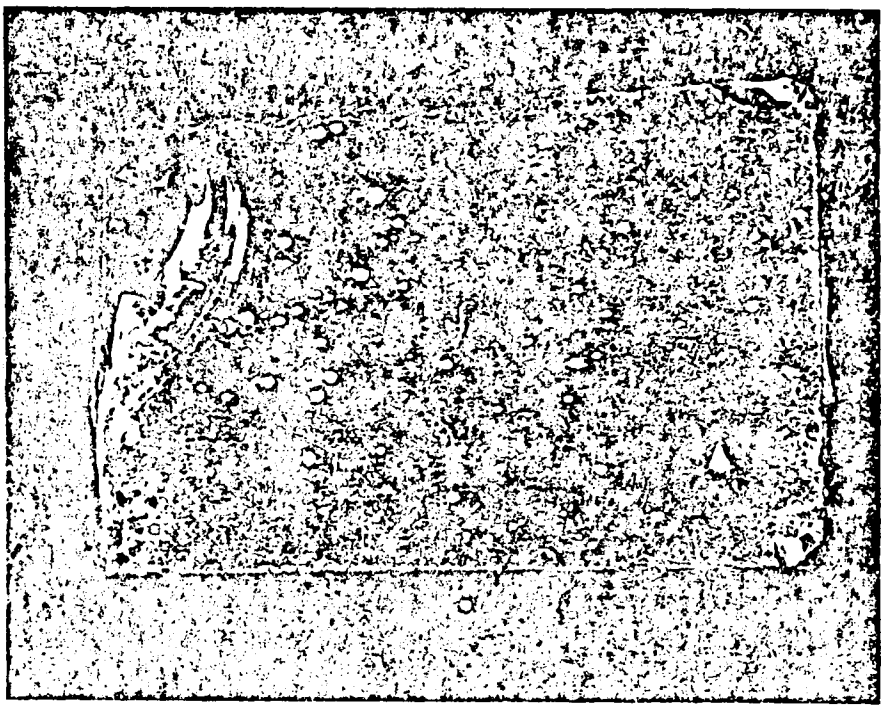


Figure 4.2 Polymer coating peeled away from the substrate.

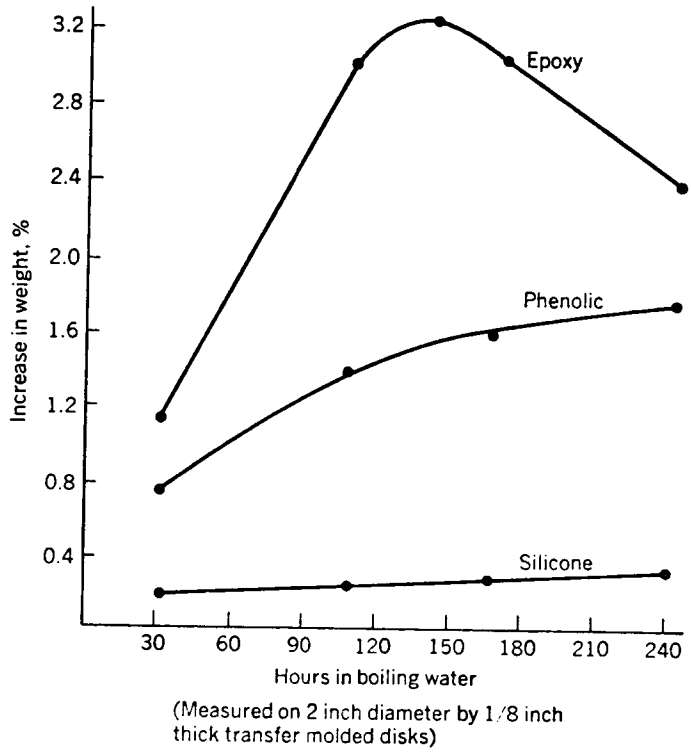


Figure 4.3 Typical moisture-absorption curves for some polymers used as protective coating. (Source: Licabi 1970).

Moisture can enter a polymeric coated electronic package by one or more mechanisms; this is similar to the state of affairs for polymeric matrix composite materials discussed in Chapter III.

1. Absorption by the polymeric coating,
2. Penetration through microcracks in the polymeric coating, or via voids that may exist in the interior of the coating, and
3. Diffusion through the polymeric coating.

The experimental methods to study water absorption of the polymeric coatings on electronic package can be classified into two types. One is the study of the pure polymers which will be used as coating materials. For instance, the polymer is immersed in water or exposed to constant humidity and temperature conditions and is weighed periodically [Kookootsedes 1967]. Measurements are continued until there is no further weight gain, i.e. until, it is presumed, the polymer no longer absorb water. Typical moisture-absorption curves for some polymers used as protective coatings are shown in Figure 4.3. Another approach is to study the polymeric coated electronic package itself. A dye penetration test, for example, has been used to determine the extent of penetration of water [Licari 1970]. Optical interference has also been used to study the swelling of substrates associated with water uptake [Ashbee 1989].

It should be pointed out that the overall amount of water absorption is not in itself a very meaningful parameter; it should be correlated with degradation effects of the coating or of the component which the coating protects. Examples of these effects include corrosion, dimensional change, delamination and loss of adhesion.

CHAPTER V

EXPERIMENTAL PROCEDURE AND MATERIALS

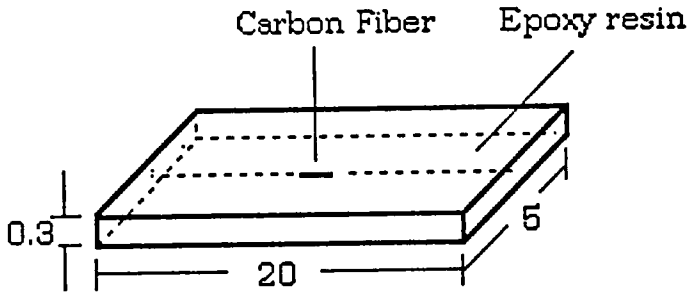
5.1 The specimens

The specimens which have been used in this study are:

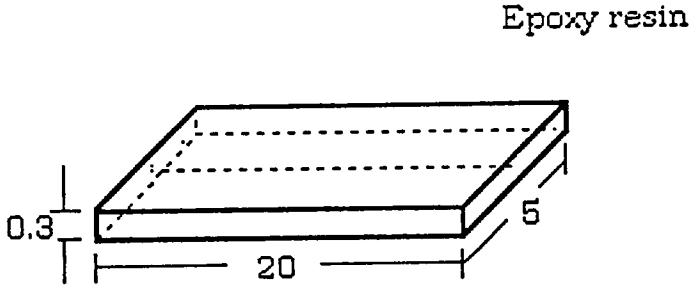
1) **A thin resin film containing a single fiber** Carbon fibers with 5 different proprietary surface treatments, designated A, B, C, D and E by Amoco Performance Products, have been studied. The fibers, of diameter about 8 μm, were chopped very carefully using a razor blade under a microscope into 1 mm lengths to be embedded in epoxy resin, ERLX-1902.

A single carbon fiber is aligned axially in a glass mold for a rectangular coupon of length 20 mm width 5 mm and thickness 300 μm, see Figure 5.1. The matrix material is poured into the cavity, and cured in situ in accordance with manufacture's recommended procedure: heating from room temperature to curing temperature 177.5°C at a heating rate of 2.5°C/min, then curing at 177.5°C for two hours; cooling from the curing temperature to room temperature at a cooling rate of 1.5°C/min. The small furnace used for specimen fabrication, see Figure 5.2, was designed to accommodate degassing during curing and temperature control. The temperature of curing cycle was controlled using a programmable temperature controller (Omega Series CN-2010). Also prepared in similar fashion were films of the same dimensions containing no fibers. These were used for measurements of overall resin dimensional changes. All samples were

A single carbon fiber coupon



Same coupon but no fiber



mm

Figure 5.1 Schematic of thin film specimens containing either single short carbon fiber or no fibers.

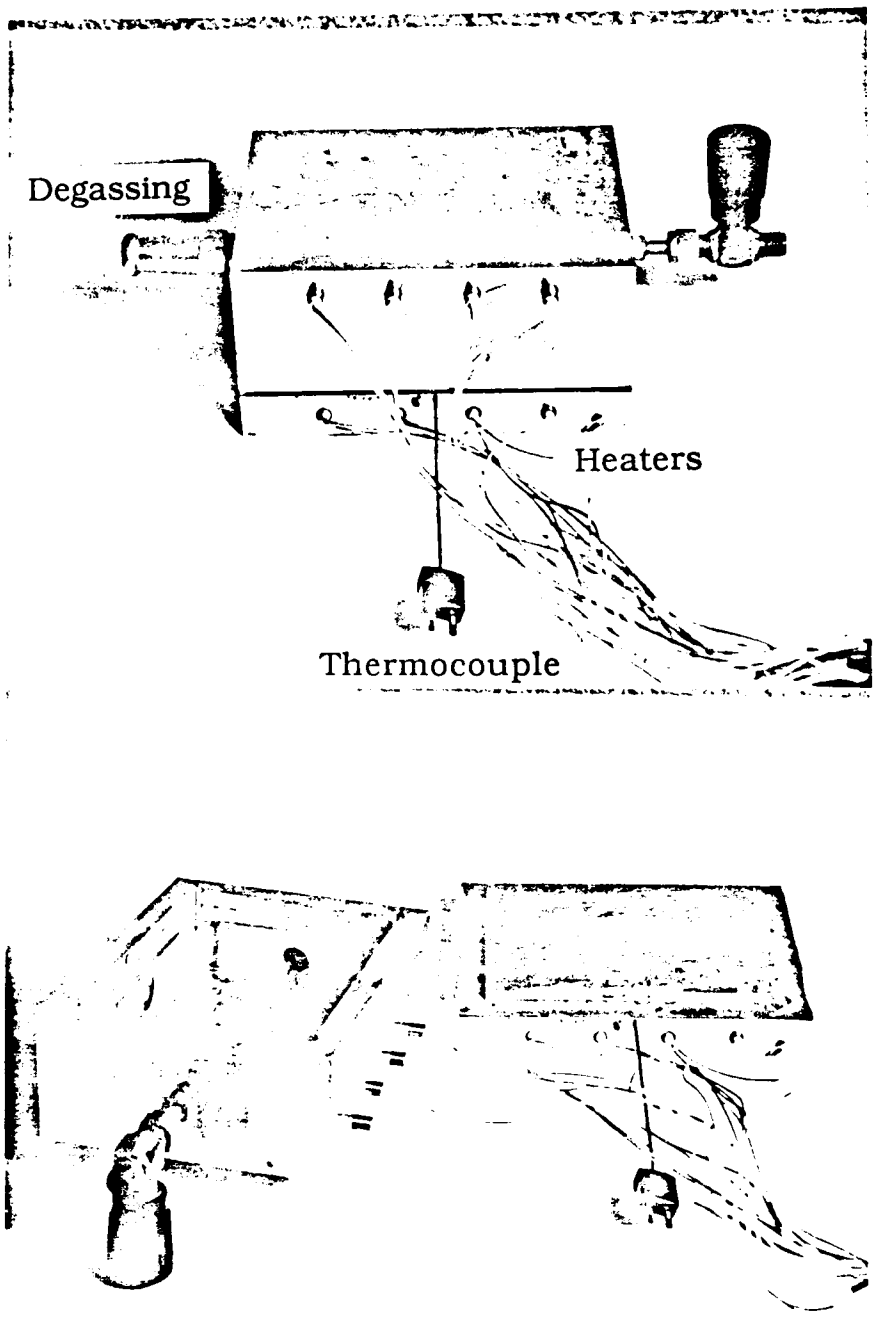


Figure 5.2 A small furnace used for fabrication of specimens.

immersed in distilled water at a temperature of 100°C. The set-up for water immersion tests is shown in Figure 5.3. The temperature of distilled water was automatically controlled by boiling it and cooling water prevented loss of distilled water by evaporation.

Specimens prepared in this way have been employed to investigate the effects of fiber surface treatment on the durability of interfacial bonding between fiber and matrix, and the consequent failure modes during water immersion tests.

Another of epoxy plate of 1mm thickness containing a single glass fiber of diameter 300μm was made to investigate the radial fiber deformation resulting from volumetric swelling of the matrix during water uptake.

2) A cylinder specimen of epoxy resin containing a single axial glass fiber The dimensions for this specimen are 38mm in length and 6 mm in diameter, the fiber diameter being 330 μm. One end of the specimen was bonded to a rigid substrate using 2-Ton Clear Epoxy. The other end of the specimen was bonded to a 150 μm thick flexible cover slip. Figure 5.4 shows a schematic of the cylindrical specimen. Specimens of this form have been used to study dimensional changes and water absorption, and the stress distribution around the single fiber.

3) **A coated silicon wafer** The samples were supplied as coated by Martin Marietta Corporate Laboratories. The substrate material had been coated with polymer coating for protection from environmental attack. The coatings were transparent. Between the coating and substrate is aluminum deposit of high reflectivity. A typical as-received

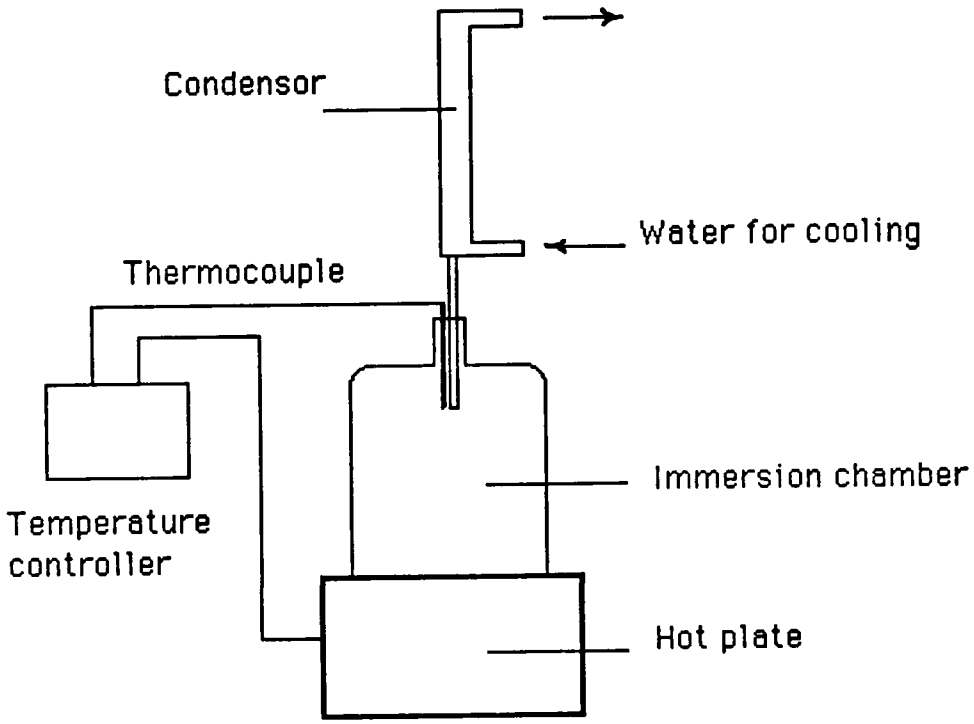


Figure 5.3 A set-up for water immersion test.

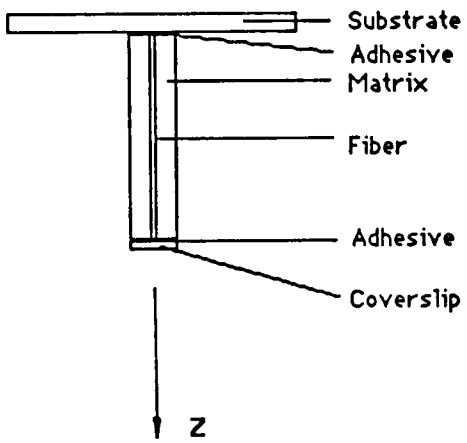


Figure 5.4 Schematic of cylindrical specimen containing a single glass fiber at the axial direction of the cylinder.

specimen is shown in Figure 5.5. Five such specimens, identified in Table 5.1, were investigated in a study of moisture induced damage, including the effects of post-curing on water uptake.

4) **A tensile test specimen containing a bundle of fibers** Figure 5.6 shows schematically a tensile specimen used for investigating the effects of surface treatment on fiber pull-out length after water immersion.

5) **A tensile test specimen containing no fibers** Specimens of the same geometry as shown in Figure 5.6 but having 0.5mm thickness were used to measure of the stress-optical coefficient of epoxy resin after water immersion.

All specimens, except the coated electronic package specimens, were made in our laboratory.

5.2 The experimental set-up

Stress-induced birefringence was observed and measured at room temperature using a Nikon polarizing microscope, Optiphot-pol, with a Brace-Köhler compensator (0.05λ) to measure small retardations, and a Sénarmont compensator (1λ) to measure large retardations, see Figure 5.7. The same Nikon microscope was also used to measure dimensional changes during water immersion.

Tensile specimens containing a bundle of carbon fibers were fractured under axial tension, after water immersion, using an INSTRON machine. A Scanning Electron Microscope was used to examine the fracture surfaces.

In same cases, the out-of-plane displacement field of a specimen

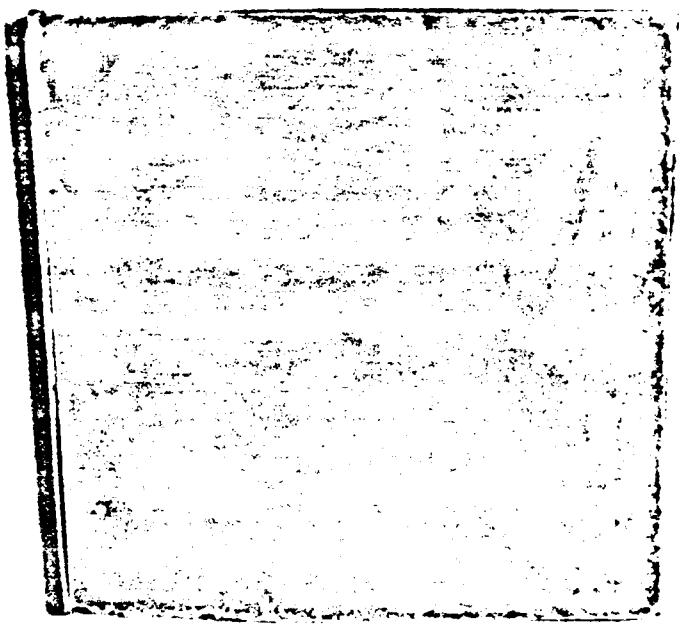


Figure 5.5 An as-received specimen coated with transparent polymer.

Table 5.1

Specimens of Chip-on-board (COB)

Specimen	Prior treatment	Investigating technique	Investigating technique
#1	11 days in humidity chamber		Caustic Foci
#2	Control Sample	Moire Fringes	Caustic Foci
#3	11 days in salt spray chamber	Moire Fringes	Caustic Foci
#4	None		Caustic Foci
#5	None	Moire Fringes	

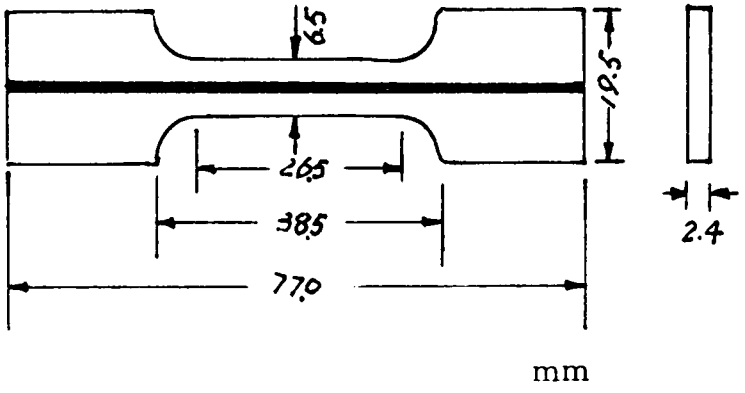


Figure 5.6 Schematic of tensile specimen containing a bundle of carbon fibers.

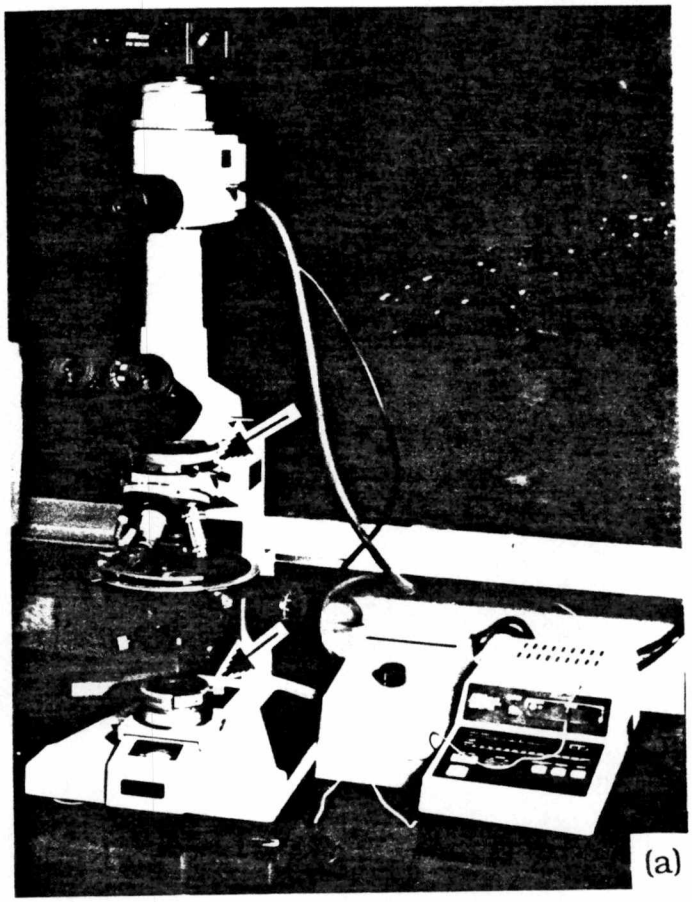


Figure 5.7 Nikon polarizing microscope (a) with a Brace-Köhler compensator (b) and a Sénarmont compensator (c).

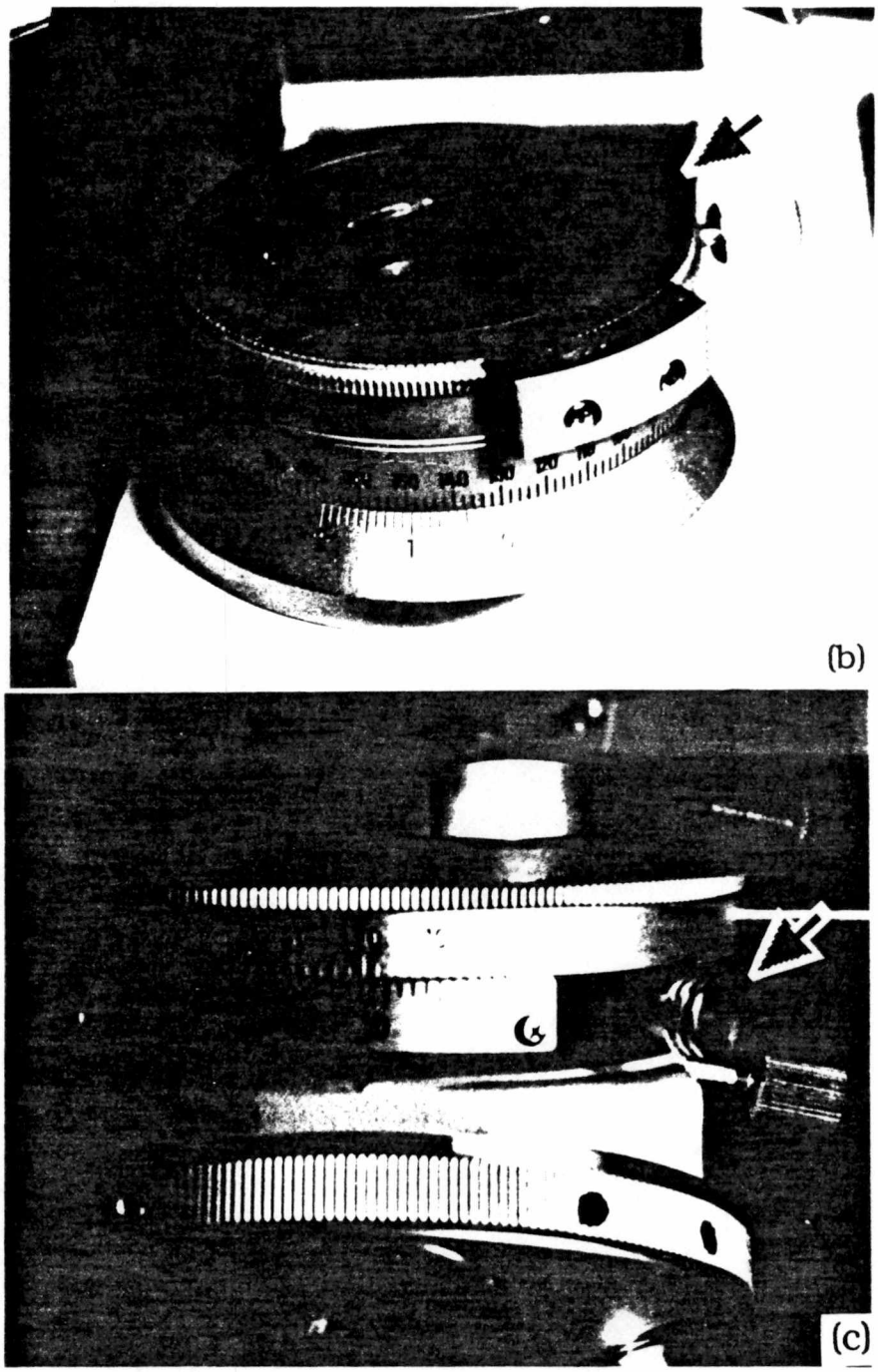


Figure 5.7 Continued.

during water immersion was periodically recorded by photographing either the optical interference fringes (Fizeau fringes) created between an optical flat and the free surface of the specimen with or without a thin glass cover slip, or by recording the caustic focus created by a beam of light reflected from the specimen surface. These fringes and caustics were generated using the optical system sketched in Figure 5.8. The laser provides monochromatic light which is expanded by a microscope objective to increase its diameter to 25 mm. This beam, after splitting by the half silvered mirror, is incident on the specimen surface. The beam reflected from the specimen surface is caused to either form caustics or to interfere with the beam reflected by the optical flat. The interference fringes or the caustics were recorded by either camera or video camera. The temperature of an environmental chamber, in which the specimen was immersed in distilled water, was controlled automatically.

5.3 Measurement of water uptake

The weight gain and the volumetric swelling or shrinkage of polymer materials give rise to the two most direct measurement methods for quantifying water uptake by polymer matrix composites or by polymer coated electronic packages.

In this research work, a Mettler H15 analytical balance capable of measuring to the nearest 0.0001g was used to measure the weight gain by composite specimens during water immersion test.

5.4 Determination of the optical fast and slow axes in the specimen

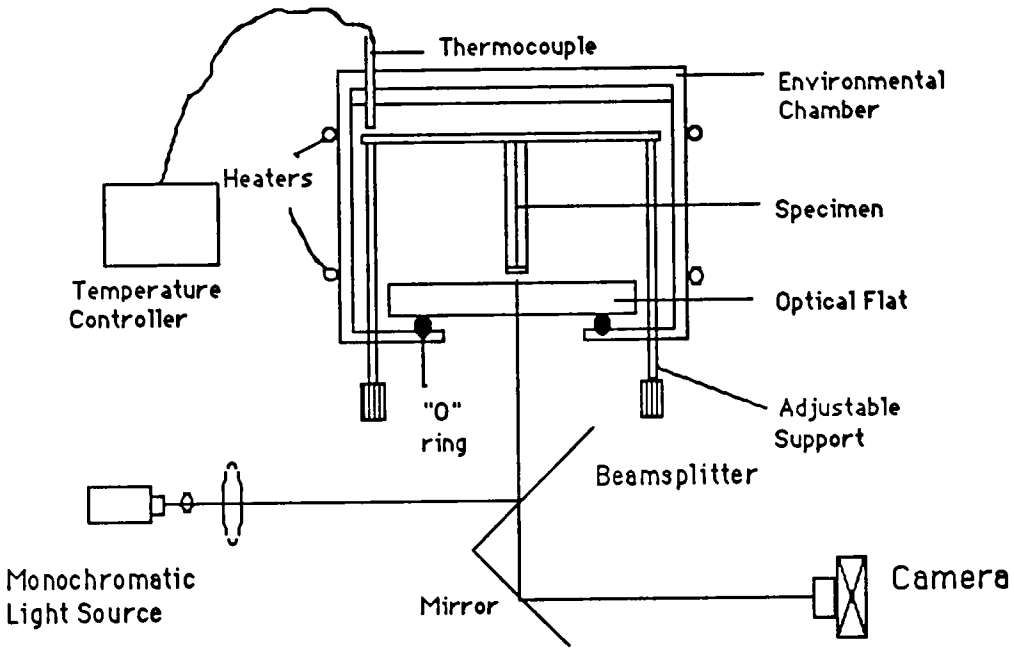


Figure 5.8 Optical system used to generate and record interference fringe pattern and caustic foci.

The procedure which has been used to determine the optical fast and slow axes is described as follows.

After making sure that the compensator is positioned with its fast and slow axes parallel to the axes of analyzer and polarizer respectively, the microscope stage is rotated to bring the field of view into extinction. Then the stage is rotated a further 45° clockwise. If the compensator plate, when rotated clockwise (for example, <45° when using a Brace-Köhler compensator, see Eq. (6-19)), re-introduces extinction, the case is that identified as (a) in Figure 5.9. If the plate has to be rotated counterclockwise to re-introduces extinction, the case is that identified as (b) in Figure 5.9.

This can be explained by the superimposition of the two birefringences generated by the specimen and the compensator plate. In order to compensate for the birefringence generated by the specimen, it is necessary to add a known birefringence with opposite directions of optical fast and slow axes to the directions of the axes of the specimen.

5.5 Measurement of optical-stress coefficient

The sample holder shown in Figure 5.10 was mounted on the microscope stage. A sample was gripped and uniaxially loaded. The applied force was measured by a load cell "Schaevitz MDTR-352L". The retardation generated by a known stress, was measured using a compensator. The relationship between retardation, Δ, and the uniaxial stress, σ, is given by [Kuske et al. 1974],

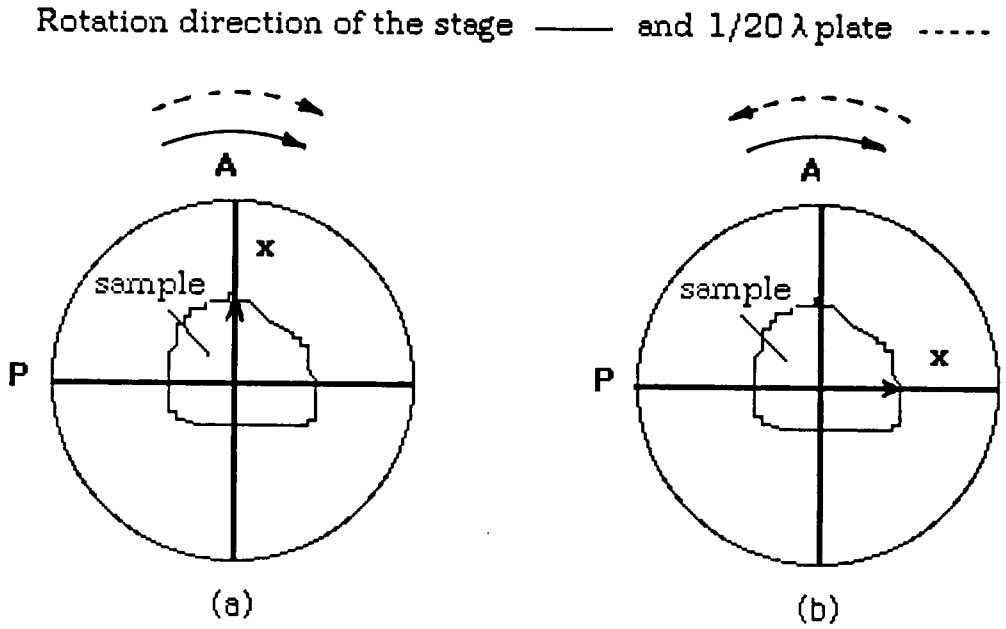


Figure 5.9 Schematic of showing how the optical fast and slow axes can be detected.

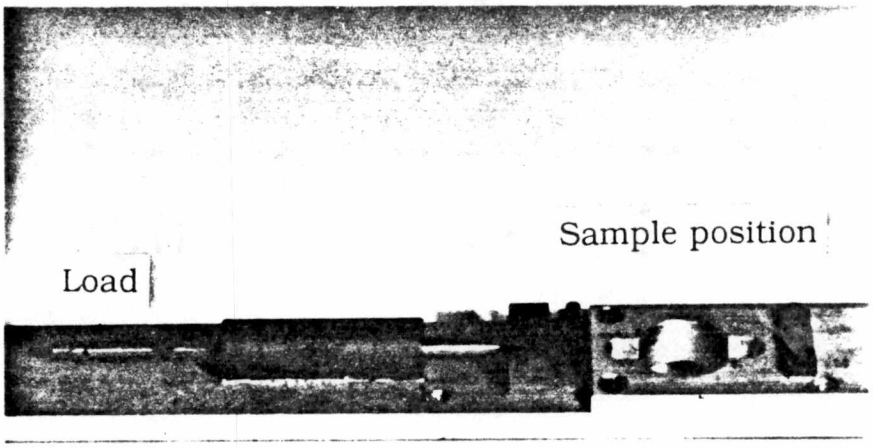


Figure 5.10 A sample holder for stress-optical coefficient measurement.

$$\Delta = \beta \sigma h \qquad (5\text{-}1)$$

where:

β = stress-optical coefficient, and

h = the thickness of the specimen.

The stress-optical coefficient of epoxy resin after water uptake was obtained by measuring the retardation, R, and stress, σ.

5.6 The measurement of stress birefringence

Epoxy resins are birefringent materials. When stress free, epoxy resin is optically isotropic; when strained or stressed, epoxy resin reveals itself as birefringent material. The overall retardation rising from the stress-induced birefringence near a single fiber has been measured using the optical compensation technique. There are two kinds of compensators used in this research work, a Brace-Köhler compensator and a Sénarmont compensator. Since the stress field around a single fiber is three dimensional, some developments for measuring stress-induced birefringence were required and these will be discussed in detail in Chapter VI.

5.7 The measurement of small deformation associated with water uptake

In order to investigate moisture-induced dimensional changes which are of very small order in most cases, it was necessary to develop techniques for their measurement. These techniques will be discussed in details in Chapter VII.

5.8 Estimation of stresses

From the displacement measurements, use of Love's analysis for the displacement field in a thin membrane deformed by a pressure drop across its faces [Love 1959], has enabled estimates to be made for the normal stresses in the glass cover slip test-pieces as follows

$$D\,\nabla^4\mathbf{W} = \frac{2Eh^3}{3(1-\gamma^2)}\,\nabla^4\mathbf{W} = -p \qquad (5\text{-}2)$$

where:

p = normal pressure,

D = flexural rigidity, given by $D = \frac{2Eh^3}{3(1-\gamma^2)}$,

E = Young's Modulus (70 GPa),

2h = thickness (0.150mm),

W = axial displacement,

γ = Poison's ratio (0.3), all of the cover slip.

Love's equation is valid in thin plates for normal displacements that are sufficiently small for lateral stretching of the plate to be ignored. The cover slip used in the z-axis deformation of a cylindrical specimen with large length/radius ratio conforms to these criteria.

Mathematically, the configuration of axial circular symmetry lends itself to analysis in cylindrical polar coordinates (r,θ,z) and the operator ∇^4 becomes

$$\frac{\partial^4}{\partial r^4} + \frac{2}{r}\frac{\partial^3}{\partial r^3} - \frac{1}{r^2}\frac{\partial^2}{\partial r^2} + \frac{1}{r^3}\frac{\partial}{\partial r} \qquad (5\text{-}3)$$

there being no dependence on θ (axial circular symmetry) nor z (thin plate).

Therefore, by graphically differentiating four times, the measured displacement curves yield the normal axial stress. The bending moment proportional to the secondary differential, can also be estimated.

When using caustics, the stress distribution can be calculated from measurement of the caustic profile. Since the profile of a caustic is related to the second differential of displacement of the reflecting surface, see later, it is evident that the bending moment of the surface then can be obtained directly from the caustic. By differentiating twice, the stress distribution in the reflecting surface can be estimated.

5.9 Theoretical treatments

In this section, some theoretical treatments as well as some assumptions used in this work will be discussed.

5.9.1 The redistribution of stresses due to debonding

As discussed in Chapter III, perfect bonding between the fiber and matrix is usually assumed when the stress distribution in the fiber and interface is analyzed theoretically. Since the shear stress reaches a maximal value at or near the fiber ends, interfacial debonding will normally first take place at or near the ends of the fiber. Consider a case with debonding at the fiber ends, as shown in Figure 5.11. When debonding occurs, this will move the location at which load transfer

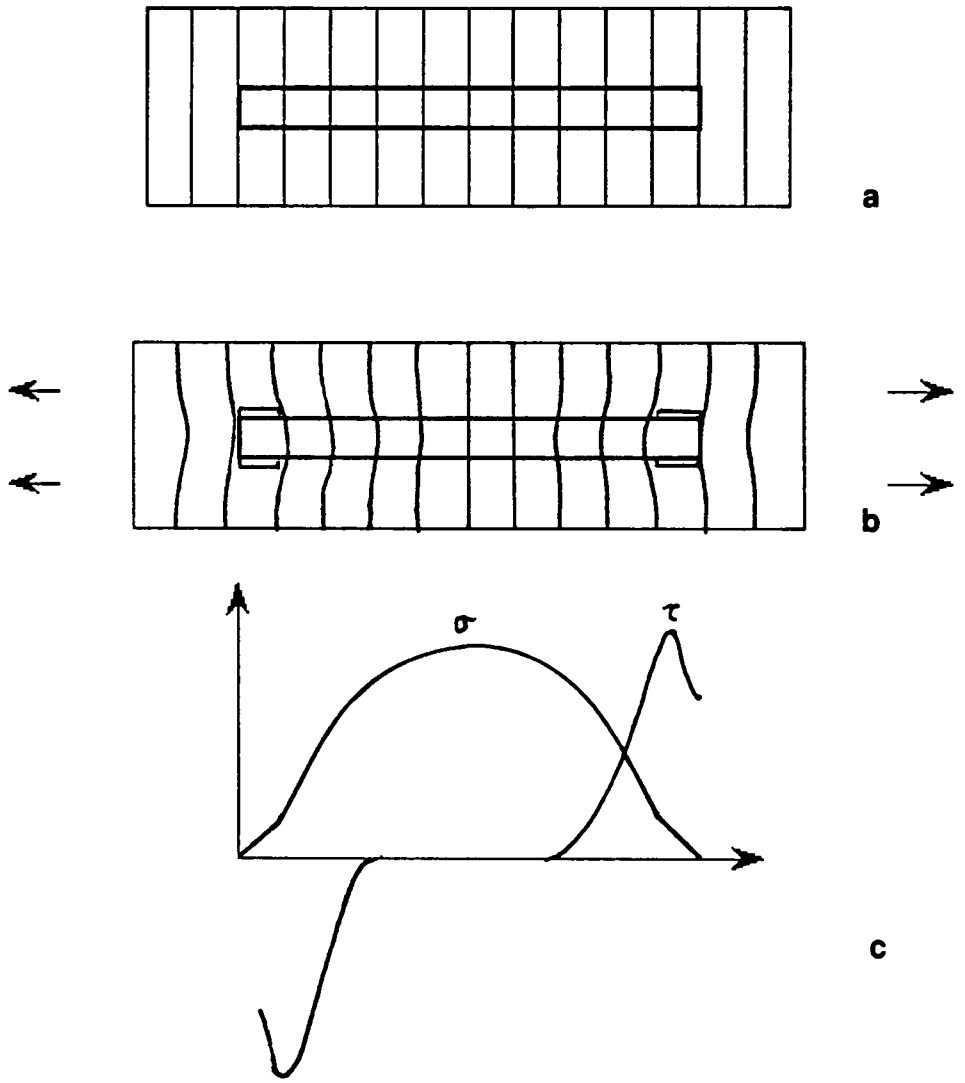


Figure 5.11 Single fiber composite specimen. (a) unstressed, (b) stressed and debonded at the ends of the fiber, and (c) the interfacial shear stress, τ, and the fiber axial stress, σ.

begins. This in turn will affect the stress distribution around the fiber. Assuming the shear lag theory [Cox 1952] is applicable, the stress distribution after debonding can be expected to be of the form shown in Figure 5.11(c). It can been seen that the shear stress distribution along the interface is significantly changed from that for perfect bonding. It is evident that, If the change in distribution of shear stress can be measured, then the progress of interfacial debonding can be monitored. This idea has been developed to investige the durability of interfacial bonding between carbon fiber, with different surface treatments, and epoxy resin, and for investigating the subsequent fiber failure modes.

5.9.2 Two-dimensional model

Since the birefringence pattern, generated around a single fiber embedded in epoxy resin and arising from the lack of correspondence between thermal contraction and moisture expansion, is of cylinder-like symmetry, a two-dimensional model can be employed for its analysis.

The tensile stress distribution around a single fiber embedded in a resin matrix under uniaxial loading, was determined by Tyson and Davies [1965] from a photoelastic investigation (Figure 5.12). In Figure 5.12, the direction of the principal stress (here it is tensile) is tangential to the trajectories at a given location. The figure shows that the tensile stress trajectories around the fiber end can be considered to have conic symmetry. According to our preliminary investigation, when a specimen is immersed in water, the stress birefringence

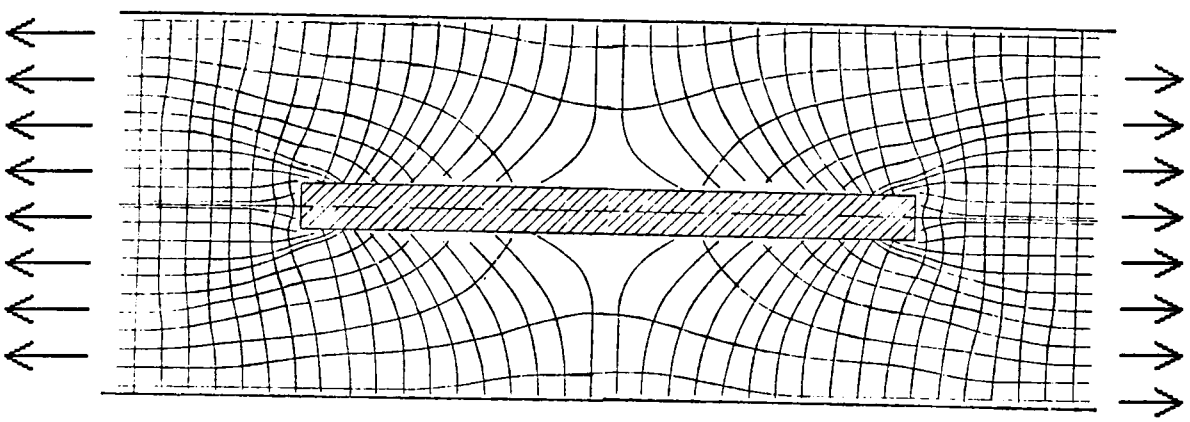


Figure 5.12 Tensile stress trajectories in the matrix.
(Source: Tyson et al. 1965).

generated due to swelling is largest near the fiber ends but rapidly disappears as we move in the direction perpendicular to the fiber axis, falling to zero within a distance of a few or ten fiber diameters from the fiber axis. Thus, by far the largest contribution to the observed stress birefringence is due to the stress near the interface. Furthermore, since the stress direction trajectories hereabouts change direction very slow, say by 10° from the fiber axis out to where the birefringence disappears, the stress field can be approximated to one of circular symmetry. Consider one half of the cone of symmetry. If a coordinate system is chosen in which one axis is parallel to the conic line, see Figure 5.13, this can be transformed into elliptic symmetry with $\frac{a}{b} = \cos\theta$. Since θ is very small, $a \approx b$. This allows us to develop a photoelastic technique based on Poritsky's paper [1934] to measure the shear stress and its distribution, and thus, to monitor the progress of interfacial debonding. This development will be discussed in Chapter VI.

5.9.3 Moisture expansion coefficient

As discussed in Chapter III, the dimensional changes of a specimen arising from water uptake, at a constant temperature and pressure, is a linear function of weight of water absorbed. It has been noted by Hahn [1976], that the swelling strain, ε, is associated with moisture absorption according to the relationship,

$$\varepsilon = 0, \text{ when } c \leq c_o \tag{5-4}$$

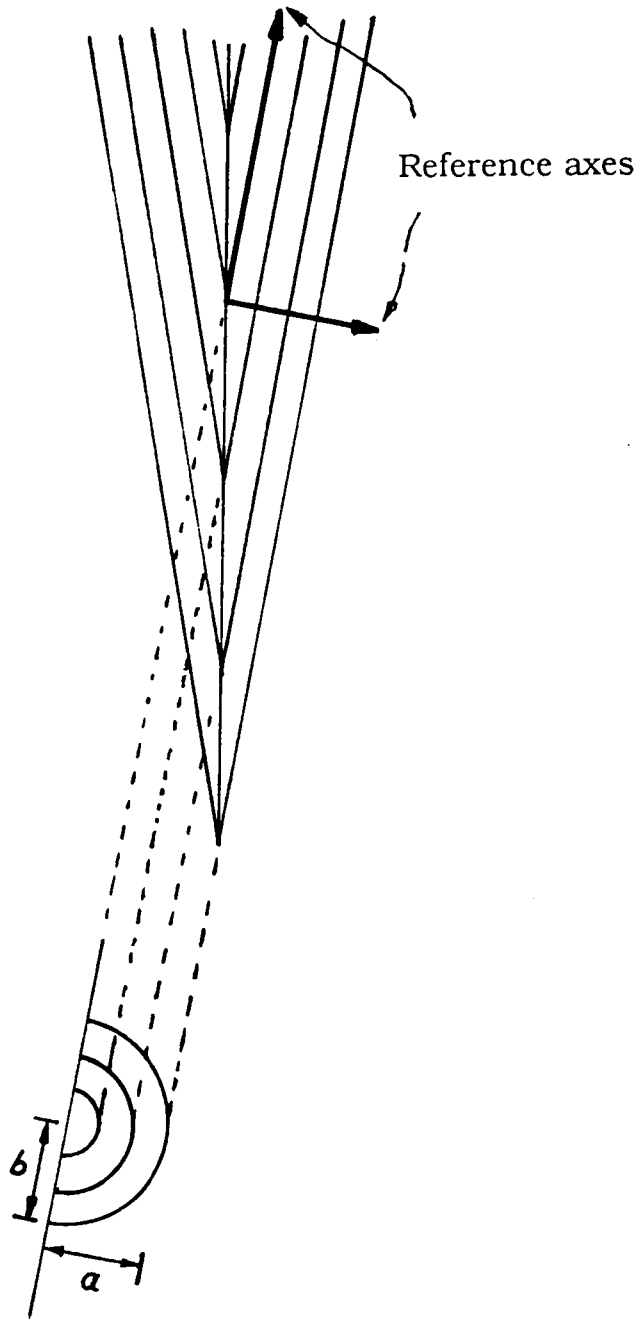


Figure 5.13 Transformation of a 2-dimensional axial section of conic symmetry into one of elliptical symmetry.

$$\varepsilon = b(c - c_o), \text{ when } c \geq c_o$$

where:

c = overall moisture concentration,

c_o = a threshold moisture concentration, and

b = the moisture expansion coefficient.

It is evident from the relationship given by Eq.(5-4), that the amount of moisture absorption and its distribution can be obtained by measuring the dimensional changes if the moisture expansion coefficient of the material under study is known.

CHAPTER VI

MEASUREMENT OF STRESS-INDUCED BIREFRINGENCE

Most of unfilled epoxy resins exhibit birefringence. When stress free, they are optically isotropic; when stressed, they are optically anisotropic with optical axes, the fast and slow axes, coinciding with the principal axes of stress. This allows us to use photoelasticity to study the state of stress in epoxy matrix composites. As a part of the present research, the application of photoelasticity to composite materials has been developed. A Poincare sphere analysis has been used to evolve the methods of optical retardation measurement used in this research. In addition, a new method, which permits semi-quantitative measurement of shear stress at the interface between the fiber and resin, has been developed.

In this chapter, the theory of photoelasticity will be briefly introduced. Then our two developments will be discussed in detail.

6.1 Introduction to photoelasticity

6.1.1 The stress optic law in two dimensions.

When a two-dimensional photoelastic specimen is in the unstressed state, it exhibits an index of refraction, n_o, which is the same at all points in the specimen. When load is applied to the specimen so as to induce a two-dimensional state of stress, its optical properties change. The specimen becomes doubly refracting; the principal axes of stress at any point become the fast and slow axes, as

shown in Figure 6.1. The consequence is that the index of refraction of the specimen is changed in relation to the stress system applied. It is this unusual optical property upon which the foundation of photoelasticity is based.

The theory which relates the changes in the index of refraction to the state of stress is due to Maxwell[1853]. The classical description of the stress optic law is given by,

$$\Delta = \beta (\sigma_1 - \sigma_2) t \qquad (6\text{-}1)$$

where:

Δ = the relative retardation,

β = the relative stress-optical coefficient,

t = the thickness of the specimen,

σ_1, σ_2 = the principal stresses.

The relative retardation, Δ, is linearly proportional to the difference in the principal stresses $(\sigma_1 - \sigma_2)$. The relative stress-optical coefficient, β, is a material property, i.e. it is a characteristic of the material employed as photoelastic specimen.

It is evident from Eq.(6-1) that the shear stress, equal to half the principal stress difference $(\sigma_1 - \sigma_2)$ in the two dimensional case can be determined if the relative retardation can be measured.

6.1.2 Measurement of optical retardation

It has been established that, for a photoelastic material, the principal stress difference $(\sigma_1 - \sigma_2)$ can be determined at any point in a

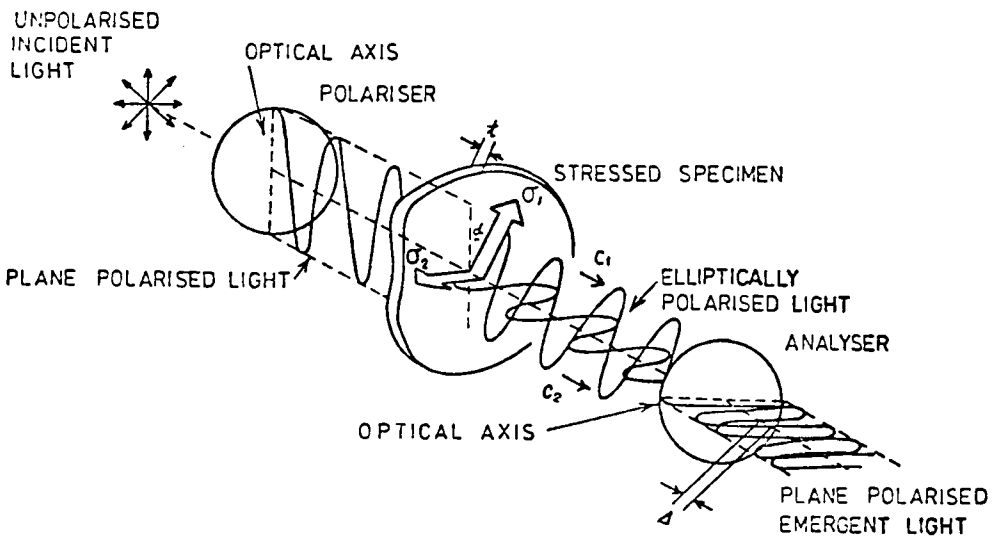


Figure 6.1 A stressed photoelastic specimen in a plane polariscope.

two dimensional stress field. In this section, the fundamental principles of retardation measurement will be introduced.

A material in which light propagates with a velocity dependent upon its plane of polarization is said to possess birefringence or optical anisotropy. For birefringent materials, there exists, in general, in a plane perpendicular to the propagation direction, a maximum and a minimum refractive index on mutually perpendicular axes, and these axes are referred to as the fast and slow axes respectively. Referring to Figure 6.1, suppose the transmission of light along fast axis **1** proceeds at velocity c_1 and along slow axis **2** at velocity c_2, and $c_1 > c_2$.

If a specimen is placed in a field of plane-polarized light such that the light vector **A**, $\mathbf{A} = k \sin(\omega t)$, makes an angle α with axis **1** (the fast axis), then it can be resolved into components $\mathbf{A}_1$ and $\mathbf{A}_2$ along axes **1** and **2** (Figure 6.2). The magnitudes of the individual components $\mathbf{A}_1$ and $\mathbf{A}_2$ are given by,

$$\mathbf{A}_1 = \mathbf{A}\cos\alpha = k \sin\omega t \cos\alpha = k \cos\alpha \sin[\frac{2\pi}{\lambda}(z-c_1 t)]$$
$$\mathbf{A}_2 = \mathbf{A}\sin\alpha = k \sin\omega t \sin\alpha = k \sin\alpha \sin[\frac{2\pi}{\lambda}(z-c_2 t)] \qquad (6\text{-}2)$$

Because of the difference between velocities c_1 and c_2, the two components will emerge from the specimen at different times, i.e., one component is retarded in time relative to the other. This retardation is best visualized by considering the relative phase shift between the two components,

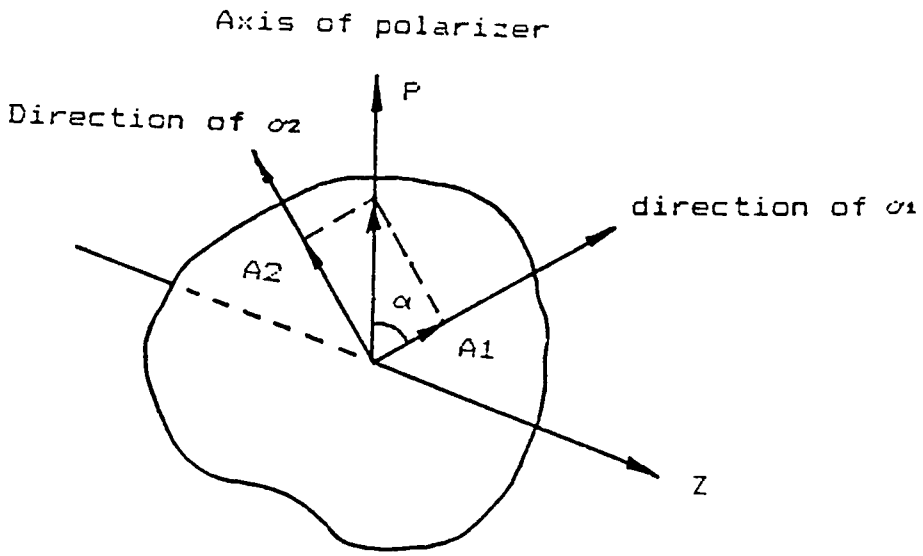


Figure 6.2 Plane-polarized light, with polarization vector **A**, entering a birefringent specimen.

$$\Delta = \frac{2\pi h}{\lambda}(n_1 - n_2) \qquad (6\text{-}3)$$

where:

n_1, n_2 = the indices of refraction along axes **1** and **2**, respectively.

Now consider first the case of a self-stressed specimen inserted into the field of a plane polariscope as illustrated in Figure 6.1. The light emerges from a polarizer and propagates through the specimen and then through the analyzer.

The light emerges from the polarizer in a plane-polarized state. It is then transmitted by the specimen as shown in Figure 6.2. When the two components emerge from the specimen, they are out of phase because of the stress birefringence. The relative phase difference between the two components is given by Eq.(6-3).

If this relative phase difference is divided equally between the two components $\mathbf{A}_1$ and $\mathbf{A}_2$, the amplitudes of the light vector components become,

$$\mathbf{A'}_1 = k \cos\alpha \sin\left(\omega t + \frac{\Delta}{2}\right)$$
$$\mathbf{A'}_2 = k \sin\alpha \sin\left(\omega t - \frac{\Delta}{2}\right) \qquad (6\text{-}4)$$

They now enter the analyzer, in the manner shown in Figure 6.3, in which components $\mathbf{A'}_1$ and $\mathbf{A'}_2$ are resolved into horizontal

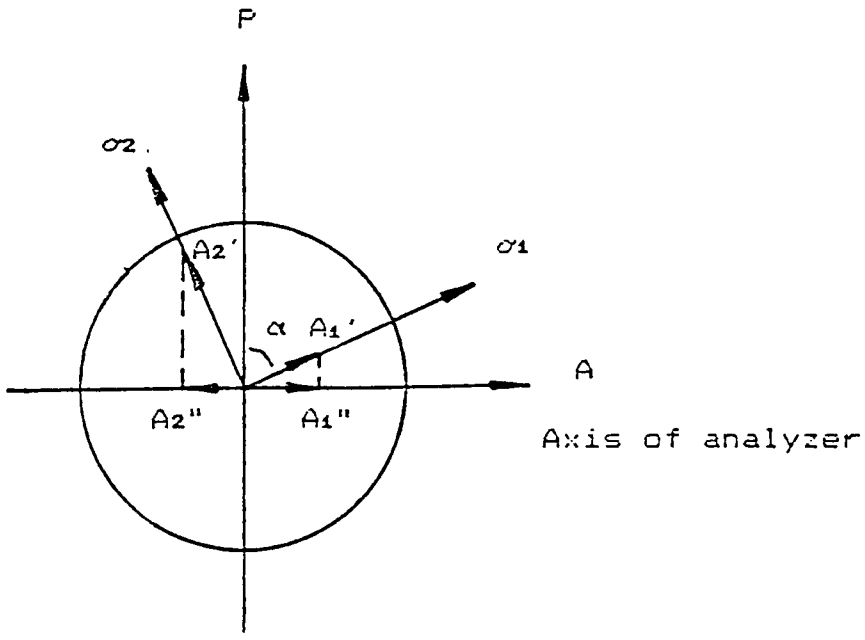


Figure 6.3 Absorbing and transmitting characteristics of an analyzer.

components $\mathbf{A''}_1$ and $\mathbf{A''}_2$ and into vertical components, the latter being absorbed because of the linear polarizing characteristics of the analyzer plate. The horizontal components are superimposed and result in an emerging light beam with polarization vector **A** and amplitude

$$\mathbf{A} = \mathbf{A''}_2 - \mathbf{A''}_1 = \mathbf{A'}_2 \cos\alpha - \mathbf{A'}_1 \sin\alpha \tag{6-5}$$

Substituting Eq.(6-4) into Eq. (6-5), we find,

$$\mathbf{A} = k \sin\alpha \cos\alpha \left[\sin(\omega t - \frac{\Delta}{2}) - \sin(\omega t + \frac{\Delta}{2}) \right] \tag{6-6}$$

Through the use of suitable trigonometric identities, Eq.(6-6) can be reduced to,

$$\mathbf{A} = - k \sin 2\alpha \cos\omega t \sin\frac{\Delta}{2} \tag{6-7}$$

The intensity of light recorded by the eye is proportional to the square of the amplitude of the light emerging from the analyzer and hence the intensity of the emerging light, I, is,

$$I = k^2 \sin^2 2\alpha \sin^2\frac{\Delta}{2} \cos^2\omega t \tag{6-8}$$

The circular frequency ω is so high (i.e., of order of 10 rad/sec) that neither the eye nor any commercial high speed photographic

equipment can detect the periodic extinction (when $\omega t = \frac{(2n+1)\pi}{2}$). So for static photoelastic applications this effect can be completely ignored and Eq.(6-8) can be rewritten as

$$I = k^2 \sin^2 2\alpha \sin^2 \frac{\Delta}{2} \qquad (6\text{-}9)$$

Examination of Eq.(6-9) shows that extinction, i.e., I = 0, can be achieved in two different ways, and these form the basis of retardation measurement using compensation techniques.

A compensator is an instrument whose birefringence is known and can be varied. If the optical retardation through the compensator can be varied, we are able to compensate for and hence measure the birefringence in the specimen. The optical effect of superimposition of the two sources of birefringence, namely of the specimen and compensator, is shown in Figure 6.4. At a general point the state of the stress can be expressed by σ_1 and σ_2, and the optical effect is proportional to $\sigma_1 - \sigma_2$. However, when a compensator of Babinet type is in place with its axis parallel to either the σ_1 or the σ_2 direction [Kuske et al. 1974], the optical response of the combined system can be varied by altering the effective birefringence of the compensator using a micrometer screw to change the overall thickness of the compensator. If, in particular, the birefringence of the compensator is set equal to that of the model by letting $\sigma^* = \sigma_1 - \sigma_2$, then the combined fringe order goes to zero.

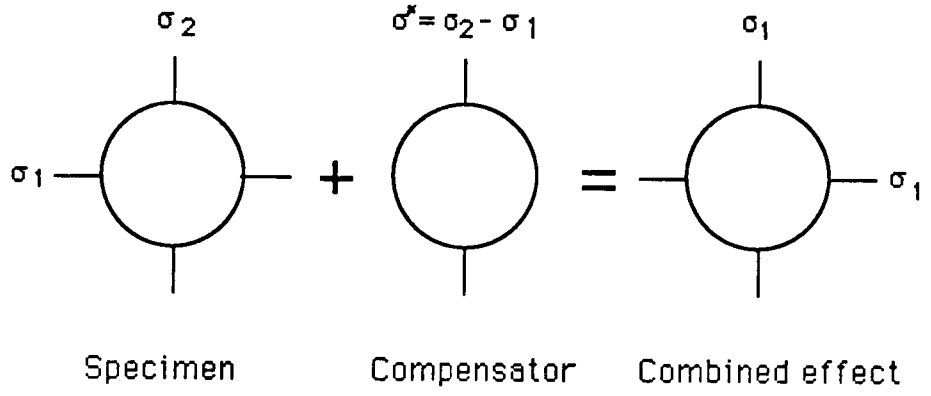


Figure 6.4 Superposition of retardation exhibited by specimen and compensator.

When using a compensator of the Brace-Köehler type, the effective birefringence of the compensator can be altered by rotating it.

Upon rotating the specimen, extinction at the point under study can be achieved. When this occurs,

$$\alpha = 0 \text{ or } \frac{\pi}{2}, \quad I = 0$$

i.e., principal direction of either σ_1 or σ_2 coincides with the axis of either the analyzer or the polarizer. The fringe pattern produced by the sin 2α term in Eq.(6-9) is known as the isoclinic fringe pattern. If the specimen is rotated through 45°, i.e.,

$$2\alpha = \frac{\pi}{2}, \quad I = k \sin \frac{\Delta}{2}.$$

In this case, it is possible to add to or subtract from the retardation introduced by the compensator, that caused by the specimen simply by rotating the compensator to achieve extinction again,

$$\frac{\Delta}{2} = n\pi, \quad I = 0$$

The fringe pattern produced by the sin $\frac{\Delta}{2}$ term in Eq. (6-9) is known as the isochromatic fringe pattern.

Using the isoclinic and isochromatic fringe patterns, photoelastic techniques can be employed to analyze the stress state in the specimen. In the case of three dimensional stress field, photoelasticity studies are more complicated [Kuske et al. 1974].

6.2 Poincaré sphere analysis

Determination of the state of stress, generated in a carbon fiber/epoxy resin composite during water immersion, from optical retardation measurements, is simplified by means of the Poincaré sphere construction [Poincaré 1892]. A single point on the surface of the sphere represents the polarization of electromagnetic oscillation at any point in the system. Any change in this polarization is represented by displacement of the point across the surface of the sphere in accordance with the following simple rules. For a polarized light wave, the end point of the electric vector, **E**, describes an elliptical helix and this helix projects onto a plane parallel to the wavefront as an ellipse where **a** and **b** are the lengths of the semi-major and semi-minor axes. The orientation of the ellipse with respect to some arbitrary Cartesian basis (**I**, **J**) normal to the optic axes, is specified by the angle α (Figure 6.5). The point, **P**, representing the state of polarization defined by the angle α and β is plotted on the surface of the unit sphere at a latitude of 2β relative to the equator and a longitude of 2α relative to some arbitrary meridian (Figure 6.6). By convention, points in the upper hemisphere are used to represent electromagnetic radiation in which the **E** vector rotates counter-

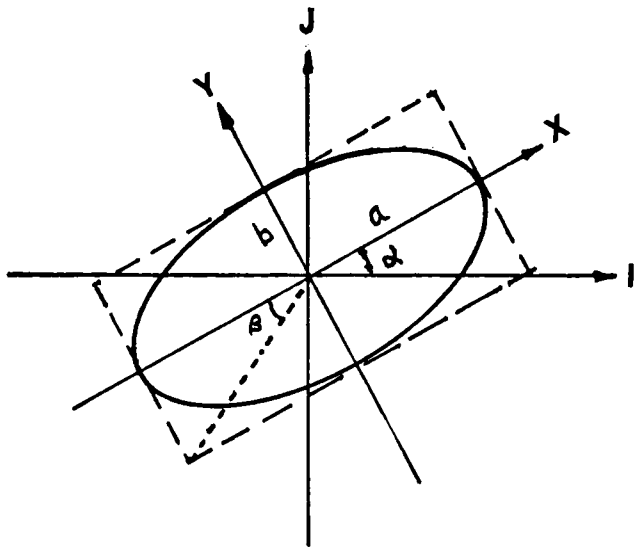


Figure 6.5 Projection of the **E** vector helix.

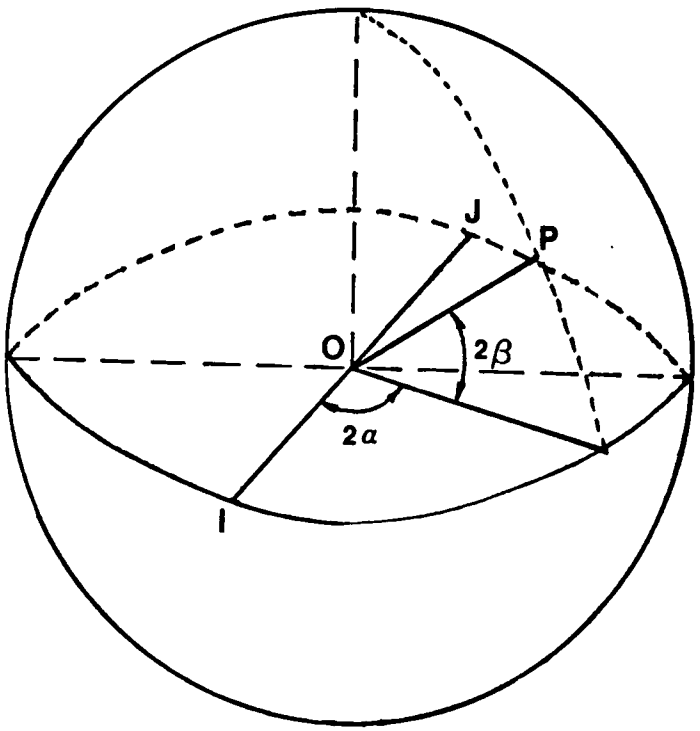


Figure 6.6 Poincaré sphere construction.

clockwise, and those in the lower hemisphere are used to represent electromagnetic radiation in which **E** rotates clockwise.

From this mode of representation a number of very simple propositions result. All the points on the same latitude (β=constant) correspond to ellipses of the same form but variable orientation. In particular, the points on the equator (β=0) represent linearly polarized vibrations of all orientations. All points on the same meridian (α=constant) represent ellipses of all shapes but with their axes in the same directions. The poles ($2\beta = 90^{o}$, $\tan\beta = \frac{b}{a} = 1$) represent circular vibrations. Two linearly polarized vibrations oriented at right angles to each other, such as the principal vibrations in a birefringent plate, have their representative points situated at the two ends of any diameter representing elliptical vibrations described in opposite senses; the ratio of the axes is the same for the two ellipses, but the major axis of one coincides with minor axis of the other.

The Poincaré sphere can be used to determine the phase and amplitude relationship between two waves. The vector **E** of an elliptically polarized electromagnetic wave as a function of time is

$$\mathbf{E}(t) = \begin{bmatrix} a\cos\omega t \\ b\sin\omega t \end{bmatrix} \begin{bmatrix} \mathbf{X} \\ \mathbf{Y} \end{bmatrix}$$

The intensity of the light is a^2+b^2, which is a constant, see later, and only the phase difference will be considered during the following analysis. For the sake of simplicity, we take $a^2+b^2=1$, then,

$$\mathbf{E}(t) = \begin{bmatrix} \cos\beta\cos\omega t \\ \sin\beta\sin\omega t \end{bmatrix} \begin{bmatrix} \mathbf{X} \\ \mathbf{Y} \end{bmatrix} \tag{6-10}$$

where **X** and **Y** are unit vectors parallel to the major and minor axes whose lengths are a and b respectively and $\beta=\tan\frac{a}{b}$ (Figure 6.5). Using axes **I** and **J** inclined at α to **X** and **Y**, **E** can be expressed as

$$\mathbf{E}(t) = \begin{bmatrix} \mathbf{A}\cos(\omega t-\theta_1) \\ \mathbf{B}\sin(\omega t-\theta_2) \end{bmatrix} \begin{bmatrix} \mathbf{I} \\ \mathbf{J} \end{bmatrix} \tag{6-11}$$

where:

θ_1, θ_2 = the phase angles of the two waves of the elliptically polarized vibration, **E**, and the phase difference between θ_1 and θ_2 will be determined using the Poincaré sphere, and

A, **B** = the amplitudes of the two waves.

Since

$$\begin{bmatrix} \mathbf{X} \\ \mathbf{Y} \end{bmatrix} = \begin{bmatrix} \cos\alpha & \sin\alpha \\ -\sin\alpha & \cos\alpha \end{bmatrix} \begin{bmatrix} \mathbf{I} \\ \mathbf{J} \end{bmatrix} \tag{6-12}$$

substituting Eq. (6-12) into Eq. (6-10), we obtain

$$\mathbf{E}(t) = \begin{bmatrix} \cos\beta\cos\omega t \\ \sin\beta\sin\omega t \end{bmatrix} \begin{bmatrix} \cos\alpha & \sin\alpha \\ -\sin\alpha & \cos\alpha \end{bmatrix} \begin{bmatrix} \mathbf{I} \\ \mathbf{J} \end{bmatrix} \tag{6-13}$$

Expanding Eq. (6-11) and comparing terms with Eq. (6-13) yields

$$\begin{aligned} \mathbf{A}\cos\theta_1 &= \cos\alpha\cos\beta \\ \mathbf{A}\sin\theta_1 &= -\sin\alpha\sin\beta \\ \mathbf{B}\cos\theta_2 &= \cos\alpha\sin\beta \\ \mathbf{B}\sin\theta_2 &= -\sin\alpha\cos\beta \end{aligned} \qquad (6\text{-}14)$$

That is

$$\begin{aligned} \mathbf{A}^2 &= \cos^2\alpha\cos^2\beta + \sin^2\alpha\sin^2\beta \\ \mathbf{B}^2 &= \cos^2\alpha\sin^2\beta + \sin^2\alpha\cos^2\beta \\ \tan\theta_1 &= -\tan\alpha\tan\beta \\ \tan\theta_2 &= -\frac{\tan\alpha}{\tan\beta} \end{aligned} \qquad (6\text{-}15)$$

which, on rearranging, become

$$\begin{aligned} \mathbf{A}^2 + \mathbf{B}^2 &= 1 \\ \mathbf{A}^2 - \mathbf{B}^2 &= \cos2\alpha\cos2\beta = \text{constant} \\ \tan(\theta_1-\theta_2) &= \frac{\tan\theta_1 - \tan\theta_2}{1 + \tan\theta_1\tan\theta_2} \\ &= \frac{\sin2\alpha\cos2\beta}{\sin2\beta} \end{aligned} \qquad (6\text{-}16)$$

On entering a birefringent material, plane polarized light can be considered as resolved into two components, which are elliptically polarized [Kuske et al. 1974], parallel to the fast and slow axes of the material in the plane normal to the optic axis. The two waves pass through the specimen with different velocities, and their relative

amplitudes remain the same, shown in Eq. (6-15), but the phase difference between them changes by an angle, shown in Eq. (6-16), $d\theta=\theta_1-\theta_2$, proportional to the thickness, t, of material traversed and to the difference in magnitude of the refractive index in the fast and slow directions, dn [Maxwell 1853].

From Figure 6.7, It can be seen that

$$Pm = \sin 2\beta$$

$$mH = \cos 2\beta \sin 2\alpha$$

and from Eq.(6-16), the angle $\angle$ PHu ($=\angle$ PHm) is $d\theta$, i.e.,

$$\tan(\angle \text{ PHu}) = \frac{\sin 2\alpha \cos 2\beta}{\sin 2\beta} \qquad (6\text{-}17)$$

It is the angle that measures the phase difference, whick is shown in Eq. (6-11), between two components of a elliptically polarized wave, it being produced by a birefringent material when a plane polarized light passes through the material.

On the other hand, using the Poincaré sphere representation, the phase difference generated by a birefringent specimen can be easily obtained by rotating a angle about a certain axis. For example, by assuming **I** and **J** to be fast and slow directions respectively (Figure 6.7), point **P**, representing a elliptically polarized light, is the incident wave, where the phase difference is $\angle$ PHu (see Eq.(6-17)); point **P'** is the emerging wave from the specimen, where the phase difference is

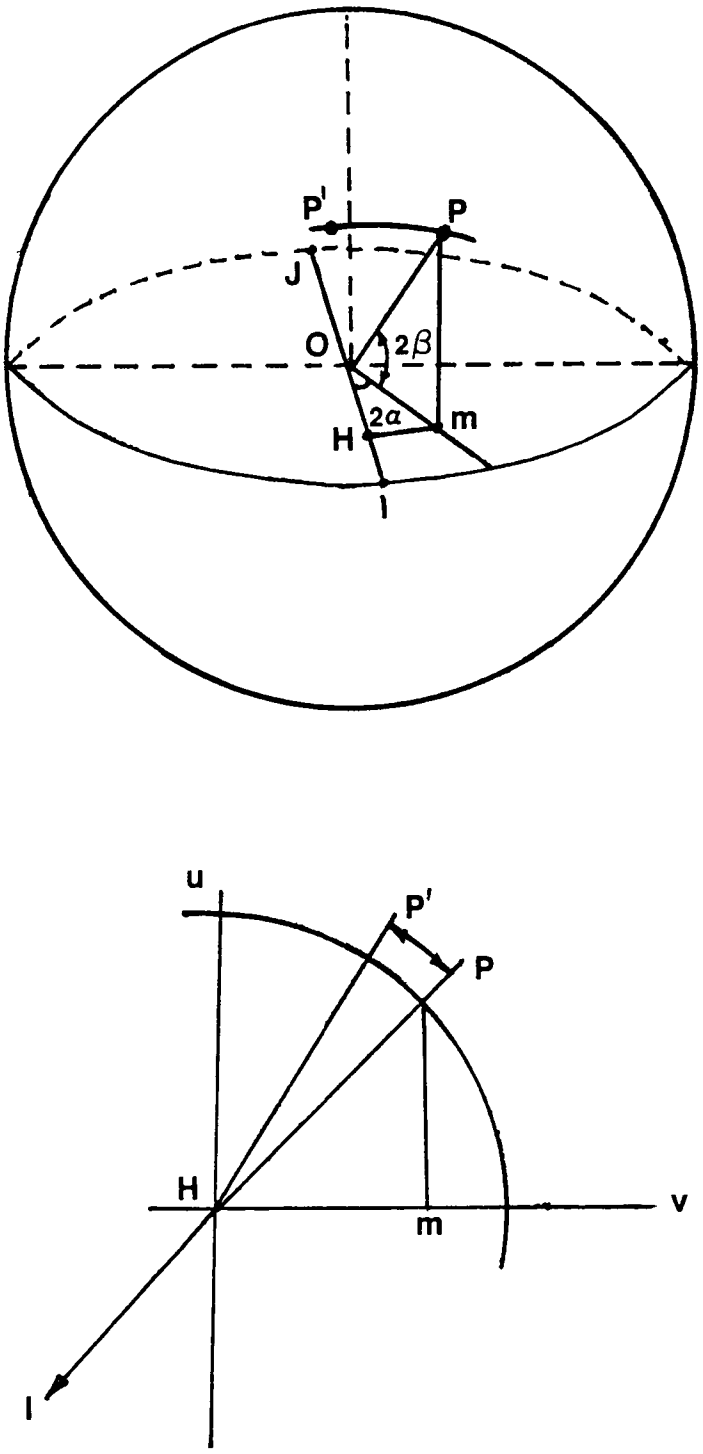


Figure 6.7 Effects of retardation on elliptically polarized light can be seen by rotating through angle $\delta\theta=\psi$ about the axis **IJ**.

$\angle$P'Hu, the phase difference, ψ, due to the birefringent material, can be obtained by rotating $\angle$P'HP, which is equal to the phase difference, ψ, counter clockwise about the axis **IJ** as indicated.

The magnitude of the birefringence in an around embedded fibers is in the grey region of the Michel-Lèvy chart, and is conveniently measured with a Brace-Köhler compensator, while larger retardations (larger retardation than that retardation a Brace-Köhler compensator can measure, but samller than that a Sénarmont compensator can measure), can be measured with a Sénarmont compensator. The Poincaré sphere analysis of retardations measured by the Brace-köhler compensator has been discussed by Vaudin and Ashbee [1982], that is,

$$R = R_0 \sin 2\phi \qquad (6\text{-}18)$$

where:

R = measured retardation,

R_0 = the retardation for the Brace-Köhler compensator,

ϕ = the angle rotated during measurement.

In the Sénarmont method, only the analyzer quarter-wave plate is used. This is set with axes parallel to those of the crossed polaroids and at 45° to the principal axes of stress at the particular point in the specimen. The analyzer is then rotated through an angle, ψ, until the intensity of light passing through the whole system is a minimum. The Poincaré sphere analysis of the experimental system is shown in Figure 6.8. **P** and **A** respectively represent the polarization directions

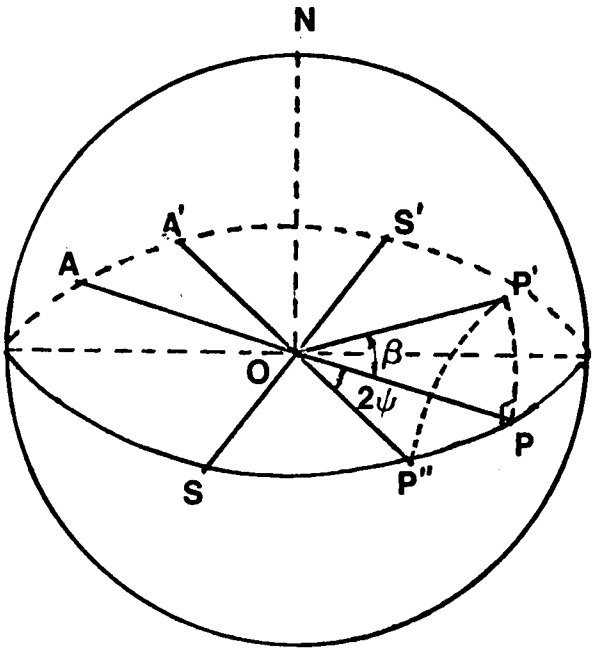


Figure 6.8 Poincare sphere analysis of retardation measured by Sénarmont method.

of the polarizer and analyzer, as well as the fast and slow directions of the quarter-wave plate. The point **P** denoting light emerging from the polarizer is displaced by the specimen through an angle β equal to $\frac{2\pi R}{\lambda}$ (λ = wavelength)about the axis **SS'** (perpendicular to **AP**); hence **P** moves to **P'**. The quarter-wave plate rotates the point **P'** through an angle $\frac{\pi}{2}$ equal to $\frac{2\pi R_o}{\lambda}$, where $R_o = \frac{\lambda}{4}$, about axis **PA**, since it's axes are parallel to those of the cross polaroids, to a point **P"**. The condition for minimum light intensity transmitted through the analyzer is that obtained by rotating the analyzer through an angle ψ about the axis **NO** since it is linearly polarized light. It is easily shown that

$$\tan (\angle \mathbf{P'OP}) = \tan (\angle \mathbf{POP''}) \qquad (6\text{-}19)$$

i.e., the phase difference is identical for the two retardations produced by the specimen and the quarter-wave plate respectively. To correspond with Eq.(6-19), the angles are identical,

$$\frac{2\pi R}{\lambda} = \frac{2\psi 2\pi}{360} \quad \text{i.e.,} \quad R = \frac{\psi}{180}\,\lambda \qquad (6\text{-}20)$$

That is, using Sénarmont compensator, the retardation, R, associated with the birefringent specimen, is given by Eq. (6-20),

6.3 A new method to measure stresses in a specimen

In this section the photoelastic formulas used in the determination of internal stresses in a specimen of cylindrical symmetry have been developed along the lines of Poritsky [1934].

The relative optical retardation, dR, of the two components of the light vector polarized along x and z directions is given by

$$dR = \beta (\sigma_{zz} - \sigma_{xx})\, dy$$

If the directions of principal stresses, σ_{zz} and σ_{xx}, in the plane of the wavefront do not vary very much along the path of light, the total birefringence is generated by the thickness from a_1 to a_2 and is given by

$$R = \beta \int_{a_1}^{a_2} (\sigma_{zz} - \sigma_{xx})\, dy \qquad (6\text{-}21)$$

where:

β = the stress-optical coefficient and assumed to be constant. Assuming there is a cylinder with a great length, then there will be no shear components (such as $\sigma_{\theta r}$, $\sigma_{\theta z}$ and σ_{rz}), and σ_{rr}, $\sigma_{\theta\theta}$ and σ_{zz} will depend on r only. The principal stresses σ_{zz} and σ_{xx} can be replaced in terms of stress components (σ_{rr}, $\sigma_{\theta\theta}$ and σ_{zz}) in cylindrical polar coordinates (r, θ, z) [Poritsky 1934]. Under these conditions, the axial direction is a principal direction. The other principal stress σ_{xx} is given by,

$$\sigma_{xx} = \sigma_{rr} \cos^2\theta + \sigma_{\theta\theta} \sin^2\theta \qquad (6\text{-}22)$$

Substituting for σ_2 in Eq.(6-21),

$$R = \beta \int_{-\sqrt{b^2-c^2}}^{\sqrt{b^2-c^2}} (\sigma_{zz} - \sigma_{rr} \cos^2\theta - \sigma_{\theta\theta} \sin^2\theta)\, dy \qquad (6\text{-}23)$$

where:

c = the normal distance of the path of light from the specimen axis (Figure 6.9).

It can be seen from Figure 6.9 that, $\sin\theta = \frac{y}{r}$, $\cos\theta = \frac{c}{r}$, $y = \sqrt{r^2-c^2}$ and therefore $dy = \frac{r}{y}\, dr$. Thus,

$$R = 2\beta \int_c^b \sigma_{zz} \frac{r}{y}\, dr - 2\beta \int_c^b \left(\frac{c^2}{ry} \sigma_{rr} + \frac{y}{r} \sigma_{\theta\theta} \right) dr \qquad (6\text{-}24)$$

Since the condition for equilibrium in cylindrical polar coordinates is

$$\frac{d\sigma_{rr}}{dr} + \frac{\sigma_{rr} - \sigma_{\theta\theta}}{r} = 0 \quad \text{i.e., } \sigma_{\theta\theta} = \left[\frac{d\sigma_{rr}}{dr} + \frac{\sigma_{rr}}{r} \right] r$$

the second term of Eq.(6-24) becomes,

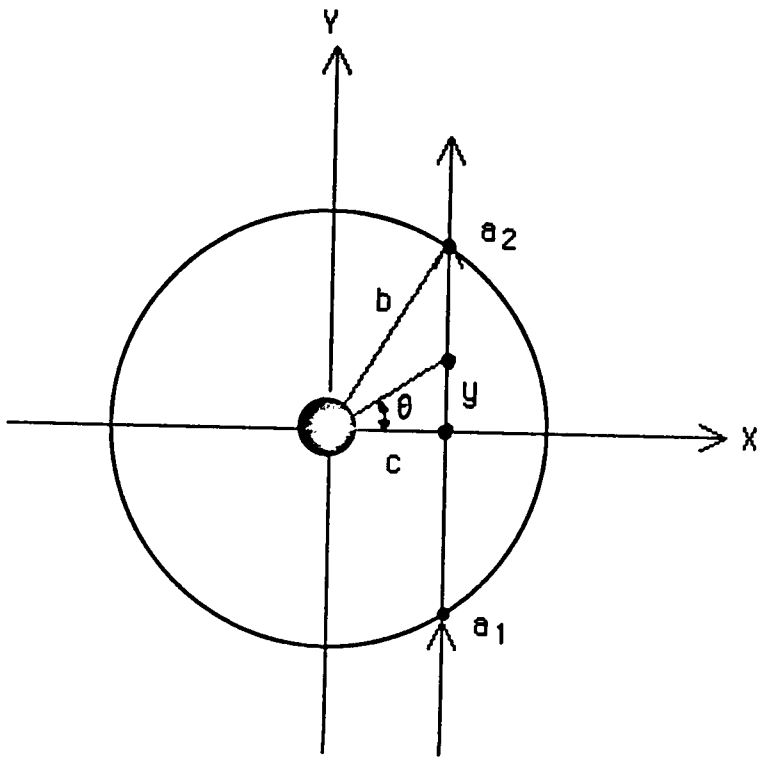


Figure 6.9 Total birefringence are generated by the polarized light through a cylinder from a_1 to a_2.

$$\int_c^b \left(\frac{c^2}{ry} \sigma_{rr} + \frac{y}{r} \sigma_{\theta\theta} \right) dr = \int_c^b \frac{d}{dr} \left(\sigma_{rr} \sqrt{r^2 - c^2} \right) dr$$

$$= \sigma_{rr} \sqrt{b^2 - c^2} = 0$$

where $\sigma_{rr} = 0$ at $r = b$. This result indicates that the retardation for such a ray depends merely upon σ_{zz} and is given by

$$R = 2\beta \int_{a_1}^{a_2} \sigma_{zz} \, dy \tag{6-25}$$

In accordance with the definition of integrals, the integration can be obtained by adding a large number of units. Consider that the specimen consists of a large number of concentric rings and the total birefringence along a path of light is the sum of contributions of individual rings, illustrated in Figure 6.10, then,

$$R = 2\beta \left[\sigma_{zz_1} \Delta y_1 + \sigma_{zz_2} \Delta y_2 + \ldots + \sigma_{zz_n} \Delta y_n \right]$$

i.e.,

$$R = 2\beta \sum_{i=1}^{n} \sigma_{zz_i} \Delta y_i \tag{6-26}$$

where:

n = the number of rings traversed by a path of light,

σ_{zz_i} = the stress σ_{zz} in the i^{th} ring, and

Δy_i = the path length through the i^{th} ring.

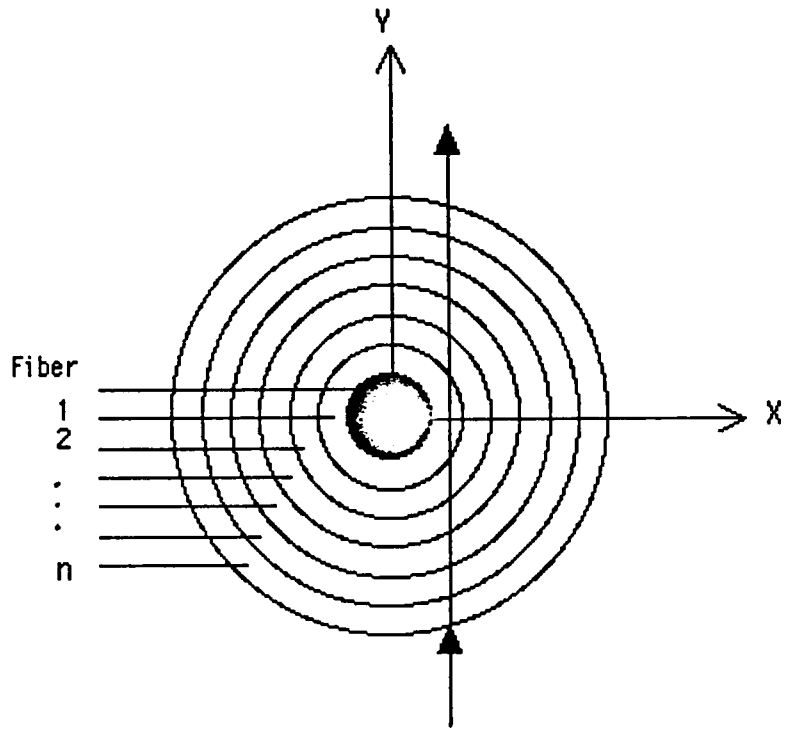


Figure 6.10 A cylinder consists of a large number of concentric rings such that the total birefringence along a path of light is the sum of contributions of individual rings.

If the number of rings is large enough, the stress in each ring can be regarded as constant. This calculation procedure can be carried out by computer programming.

The interfacial shear stress, τ, can be computed from the isochromatic (retardation) and isoclinic measurements, as follows,

$$\tau = \frac{\sigma_1 - \sigma_2}{2} \sin 2\zeta \qquad (6\text{-}27)$$

where ζ is the isoclinic angle on inclination of σ_1 with respect to the fiber direction.

Therefore, using the assumption that elliptical symmetry, transferred from a system of conic symmetry, with its semi axis ratio near to 1, can be treated as cylindrical symmetry, this technique can be employed to investigate the shear stress distribution at the interface, and hence can be used to monitor the interfacial debonding.

CHAPTER VII

MEASUREMENT OF SMALL DEFORMATION

7.1 Introduction

For the whole field of materials science and engineering, measurement techniques are of significance. The measurements of small deformation is especially important because the responses of materials to the environments in which they are used are mostly associated with small displacements, for instance, thermal expansion, moisture swelling, crack propagation, elastic and plastic deformation, and so on. Any investigation of moisture induced degradation, e.g., of swelling stress due to volumetric swelling associated with water uptake by composites and by electronic packages, requires the measurement of small deformation.

Many techniques to measure small deformation have been developed, some of which are summarized in Table 7.1. The most widely used technique involves some kind of strain gage, the displacement sensitivity for which is typically about 1 to 0.1 μm. The use of optical interferometry to measure small displacements is also well developed, for which displacement sensitivities are a fraction of the wavelength used. This sensitivity can be improved, for example, 0.004 nm is claimed for a so-called phase shift holographic interferometry optical-digital technique. Electron tunelling microscopy is the most sensitive method known to date and can meassure displacements as small as 0.0001 μm.

Table 7.1

Methods of Small Deformation Measurement

Method	Displacement Sensitivity (μm)
1. Strain Gauge	0.1 - 1.0
2. Stereophotogrammetry	10-20
3. SEM Stereoimaging Analysis	Submicron
4. Speckle Photography	1
5. Diffractographic Method	0.3 - 0.4(along a line)
6. Speckle Interferometry	0.001 (vibration)
7. Holographic Interferometry	0.16 (out-of-plane)
8. Phase Shift Holographic Interferometry	0.004 (out-of plane) 0.02 (in-plane)
9. Moire Interferometry	0.06* (out-of-plane)
10. Optical Caustic foci	0.01* (out-of-plane)
11. Scanning Tunnelling Electronic Microscopy	0.0001

* Our measurements.

7.2 Optical interferometry

7.2.1 Theory of interferometry [Hecht 1987]

The wave theory of the electromagnetic nature of light provides a natural basis from which the phenomenon of interference proceeds. The expression describing optical disturbance is given by Maxwell's equations governing the behavior of electric and magnetic fields. The vector expressions are

$$\nabla^2 \mathbf{E} = \varepsilon_o \mu_o \frac{\partial^2 \mathbf{E}}{\partial t^2}$$
$$\nabla^2 \mathbf{B} = \varepsilon_o \mu_o \frac{\partial^2 \mathbf{B}}{\partial t^2} \qquad (7\text{-}1)$$

where:

$\mathbf{E}$ = the electric field,

$\mathbf{B}$ = the magnetic induction field of light,

ε_o = the permittivity, and

μ_o = the permeability of the free space.

Since the expression describing optical disturbance is a second-order, homogeneous, linear, partial, differential equation, it obeys the important principle of superposition. Accordingly, the resultant electric field intensity $\mathbf{E}$, at a point in space where two or more lightwaves overlap, is equal to the vector sum of the individual constituent disturbances. Therefore optical interference may be defined as an interaction of two or more lightwaves yielding a resultant radiation that deviates from the sum of the component radiations.

7.2.2 Two-Beam Interference

Interference bands of this kind are analogous to the constant-height contour lines of a topographical map. Each fringe is the locus of all points in the specimen for which the optical thickness is a constant. Consider parallel rays, A_1 and A meeting the surface B_1 and B of a plane parallel sheet of material of thickness t and refractive index μ_2, as shown in Figure 7.1. The ray A_1B_1 refracts to C_1, where it reflects to B. At B, it meets the ray AB and both travel towards C. The two rays are in a condition to interfere. It can be seen from Figure 7.1 that the optical path difference, Δ, is given by

$$\Delta = 2\,\mu_2 t\,\cos\theta \qquad (7\text{-}2)$$

where:

θ = the incident angle.

Since $\mu_1 > \mu_2$, the reflection at B will introduce a phase change of π [Hecht 1987], which is equivalent to altering the optical path length by $\frac{\lambda}{2}$. As the beams would have reinforced when the retardation is an integral number of waves, and considering the phase change due to reflection, it follows that when $n\lambda = 2\mu_2\, t\, \cos\theta$, the interference produces a bright fringe, and when $(2n+1)\lambda = 2\mu_2\, t\, \cos\theta$, the interference produces a dark fringe.

For normal incidence of rays, in which $\theta = 0$, the conditions for interference fringes generation become

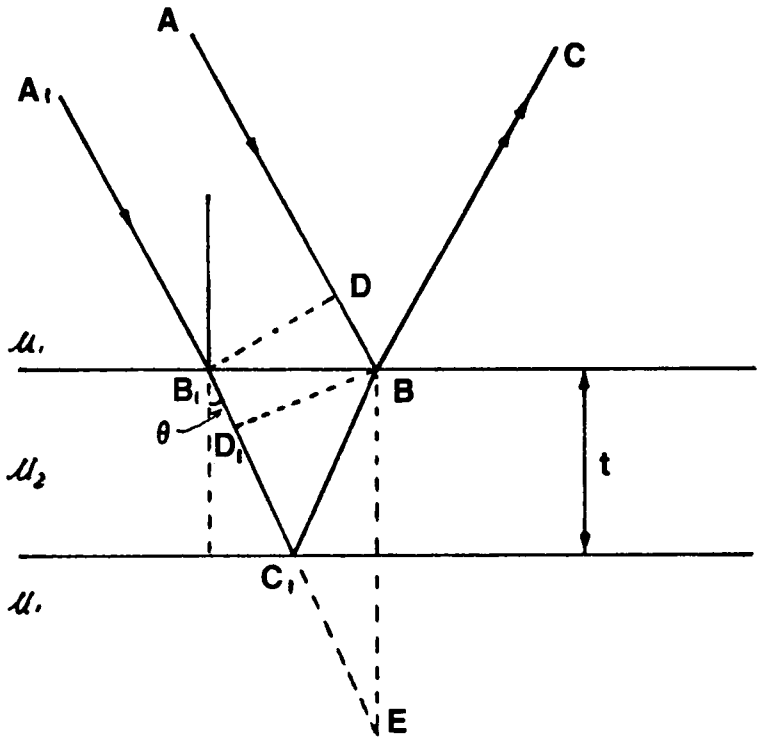


Figure 7.1 Schematic of two-beam interference.

$$(n + \frac{1}{2})\lambda = 2\mu_2 t \quad \text{for dark fringe} \qquad (7\text{-}3)$$

$$n\lambda = 2\mu_2 t \quad \text{for bright fringe.}$$

Thus, the number of fringes N to have passed a given point is simply related to the normal thickness change, W, as

$$W = \frac{N\lambda}{2\mu} \qquad (7\text{-}4)$$

7.2.3 Multiple-beam Interference

The phenomenon whereby two coherent beams are combined to produce interference patterns is described above. There are, however, other circumstances under which a much larger number of mutually coherent waves are made to interfere. In fact, whenever the amplitude-reflection coefficients are not small, the higher-order reflected waves become quite significant.

Consider the set of parallel reflected rays in Figure 7.2. Each ray bears a fixed phase relationship to all the other reflected rays. The difference, δ, in optical path length between adjacent rays is given by Eq.(7-2). The phase differences arise from a combination of optical path-length differences and phase shifts occurring at the various reflections. Nonetheless, the waves are mutually coherent, and if they are collected and brought to a point focus by a lens, they will all interfere. The resultant amplitude expression has a particularly simple

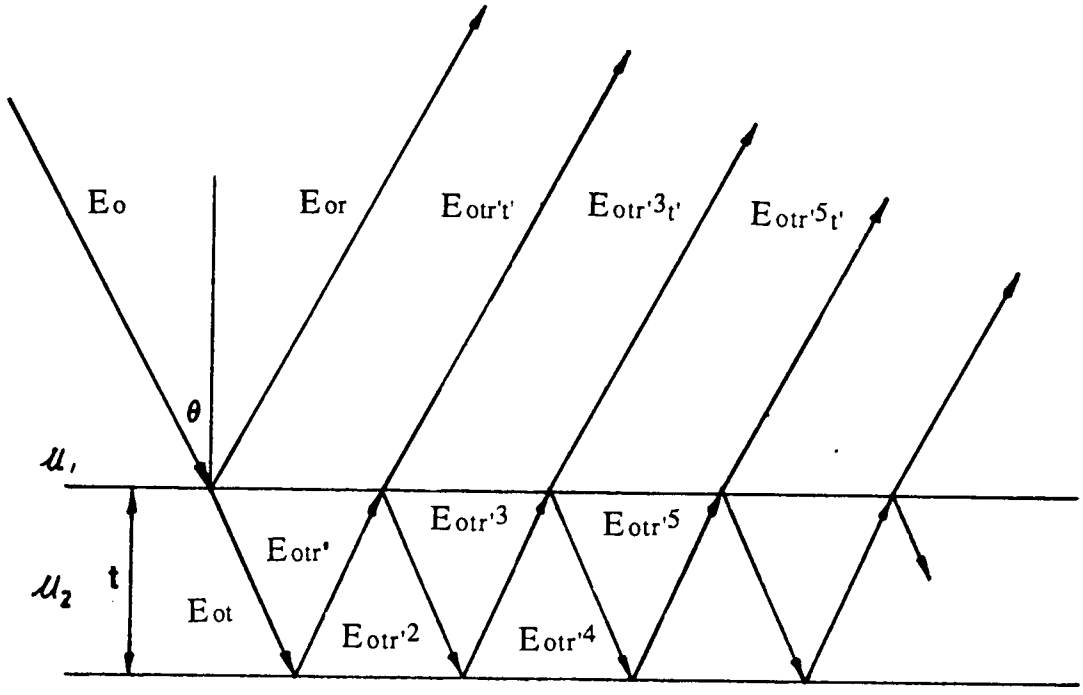


Figure 7.2 Schematic of multiple-beam interference.

form for a case where $\mu_1=\mu_2$. The reflected flux density at the focus point I_r is given (Appendix A) by

$$\frac{I_r}{I_i} = \frac{F \sin^2(\frac{\delta}{2})}{1 + F \sin^2(\frac{\delta}{2})} \qquad (7\text{-}5)$$

where:

I_i = the incident flux density,

δ = the difference in optical path length between adjacent rays, see Eq. (7-2),

F = the coefficient of finesse.

The term $[\ 1+ F \sin^2(\frac{\delta}{2})]^{-1} = \mathbf{A}(\theta)$ is known as the **Airy function**. The complementary function $[\ 1 - \mathbf{A}(\theta)]$ is Eq.(7-5). Thus the fringe intensity distribution in reflection is obtained by the complementary function, as shown in Figure 7.3. The fringes are now narrow dark fringes on a bright background. Thus, multiple-beam interference has resulted in a redistribution of the energy density in comparison to the sinusoidal two-beam pattern. The advantage of the multiple-beam interference is that the very fine dark fringes can be obtained, as shown in Figure 7.3.

7.2.4 Moire optical interference technique

In the previous section, the techniques of optical interference have been introduced. For the present research work, two-beam interference has been used for composite specimens and multiple-

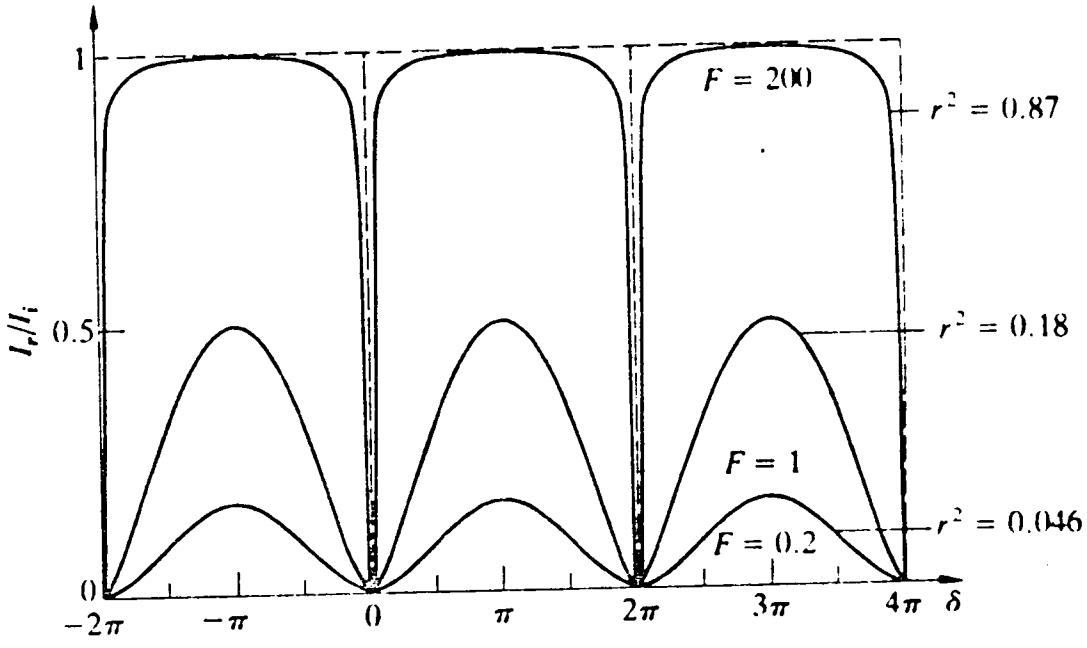


Figure 7.3 The complementary function [1-**A**(θ)].

beam interference for protective coatings, the set-up for both of which are shown schematically in Figure 7.4. One further technique has been used in the research. Although optical interference can be used to view the topography of the surface, the following moire fringes method is more convenient in practice.

The basic idea is firstly the generation of interference fringes (Newton's rings) between a polished surface and optical flat. Secondly the formation of moire fringes when two nearly identical periodic patterns are superimposed one on the other. The spatial distribution of moire fringes faithfully follows changes in shape of the specimen surface which reveals the dimensional changes of the underlying specimen.

The interference fringes precisely reflect the surface topography of the cover slip and therefore of the underlying specimen; they are contours of the glass cover slip, the contour level with respect to the reference flat differing by $\frac{1}{2}\lambda$ from one dark or bright fringe to the next. If the shape of the cover slip changes, as happens when the resin part of the specimen swells due to the water that has diffused in, the pattern of interference fringes changes. It is evident that direct observation and recording of these changes can be used to measure increments of the deformation. However, it is more convenient to collect this information by superimposing, on the interference pattern photographed before water immersion, successive photographs of the pattern as the immersion proceeds. The superimposition generates

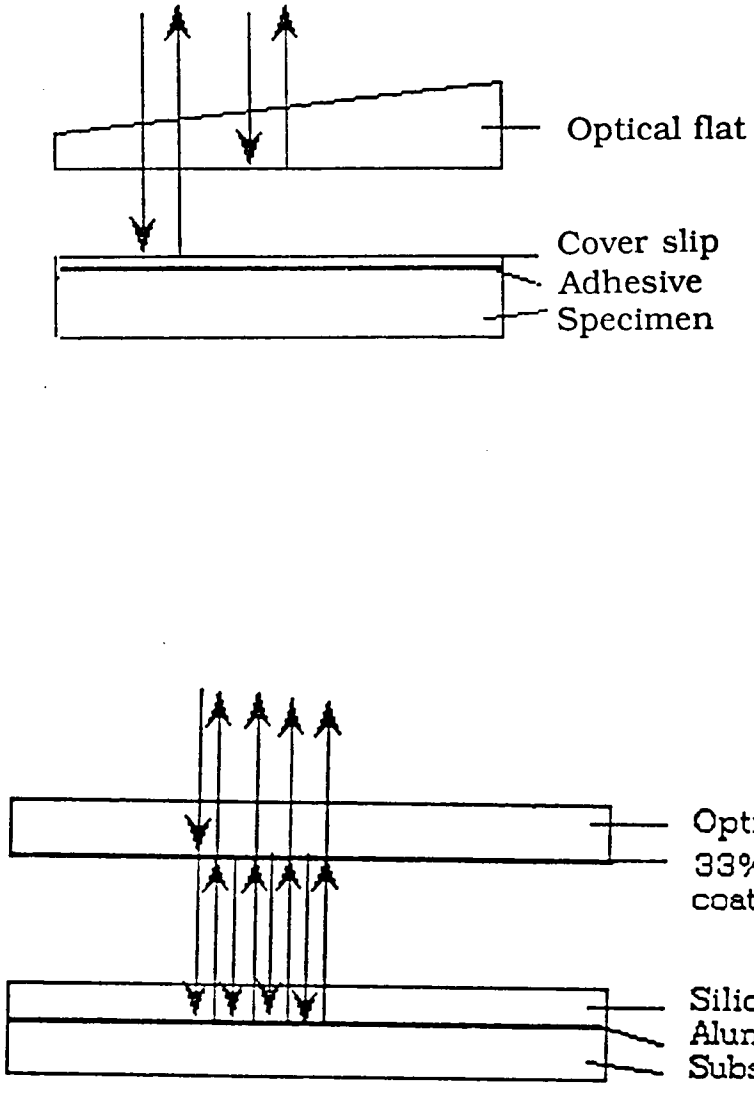


Figure 7.4 (a) Two-beam interference generated between a cover slip adhering to a specimen and an optical flat. (b) Multiple-beam interference generated between a light reflective surface coated with transparent polymer and an optical flat.

moire fringes, the spatial distribution of which faithfully follows changes in shape of the cover slip.

Moire fringes are generated when patterns with nearly identical periodic structures are made to overlap. Here, it is the photographic images of the interference pattern that constitute the nearly identical periodic structures and it is the small differences in the pattern, seen on comparing the image photographed before the water immersion with an image taken during water immersion, that give rise to the moire effect. As water diffuses into the specimen, new interference fringes are generated at the edge and migrate towards the center, each fringe representing the locus of points of identical displacement normal to the specimen. Similarly, in the moire pattern, a new moire fringe is generated and migrates in from the edge of the specimen whenever a new interference fringe is generated. Thus successive moire fringes map out the loci of position which differ in displacement normal to the specimen by half a wavelength. Hence the number of moire fringes N to have passed a given point is simply related to the normal displacement of the specimen **w** by

$$\mathbf{w} = \frac{N\lambda}{2\mu} \qquad (7\text{-}6)$$

where:

λ= wavelength of light,

μ= refractive index of the immersion liquid.

7.2.5 Interferometric "strain gauge"

An optical system have been developed to generate and record the various sets of optical interference fringes, formed between a plate of composite specimen containing a single glass fiber, the surface of the glass fiber and an optical flat. These sets of interference fringes allow us to measure fiber radial displacement resulting from the deformation during water uptake of the self-stressed epoxy resin. These fringes can be used as an interferometric "strain gauge" of considerable precision, say $\lambda/10$.

Figure 7.5 shows a schematic of the system developed to record the interference fringes. Where these interference fringes are generated is shown in Figure 7.6. There are three sets of fringes. Set #1 is due to interference between incident light and light reflected from the near surface of the plate. Set #2 is due to interference between incident light and light reflected from the fiber/matrix interface. Set #3 is used to eliminate the contribution of the support to the measured displacement so as to obtain the net displacement of the specimen. The measured displacement, after correcting for the specimen deformation, permits calculation of the fiber radial displacement resulting from resin swelling during water uptake.

7.3 Caustic Foci

Caustics are the most general way of describing the focusing of a wavefield. They are surfaces of high wave intensity as opposed to the point focus of paraxial optics. Figure 7.7 shows the point focus of paraxial optics, where image errors, known as aberrations, are

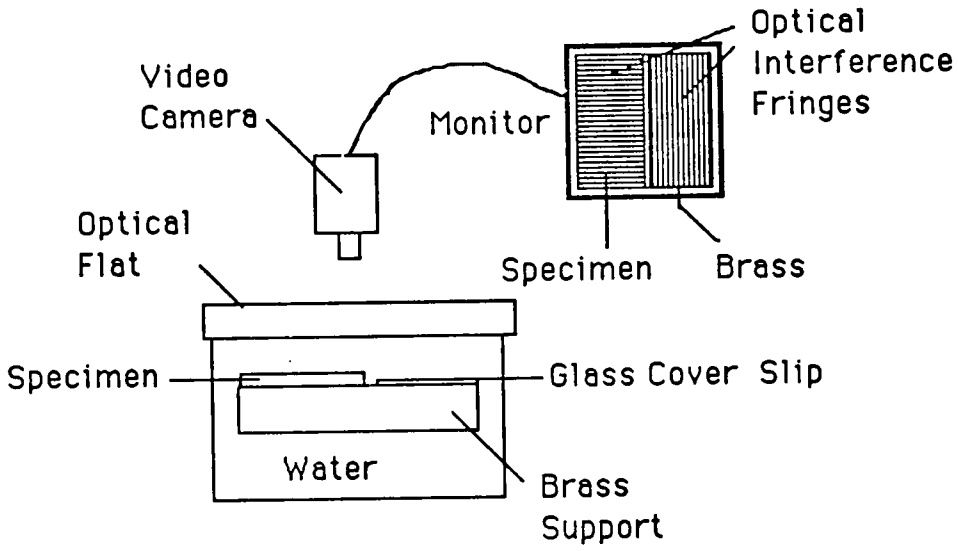


Figure 7.5 Schematic of optical system developed to measure radial deformation of fiber in specimen immersed in distilled water. The light source is the same as in Figure 5.8.

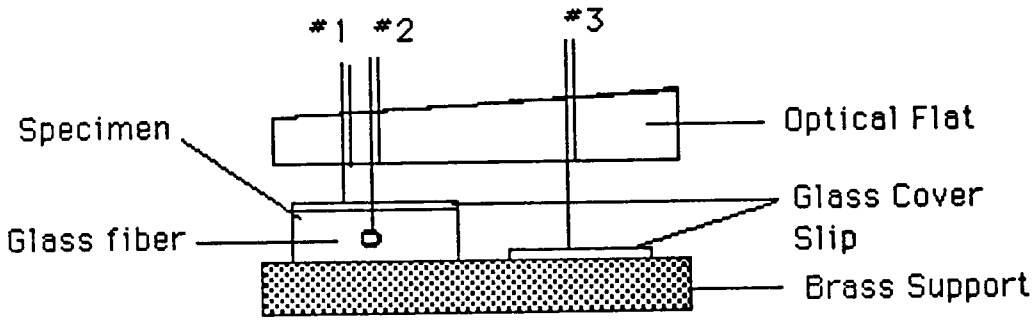


Figure 7.6 Schematic of the generation of the three sets of the interference fringes.

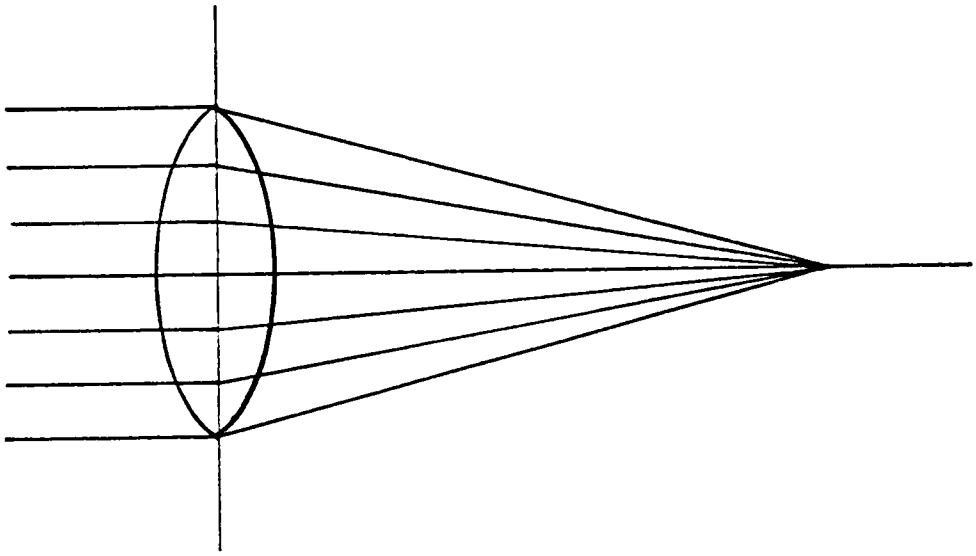


Figure 7.7 The point focus of paraxial optics.

effectively absent. The defect known as spherical aberration arises for nonparaxial rays from the dependence of focal length on aperture size; marginal rays undergo more refraction than do paraxial rays and are focused in front of the paraxial rays. The resulting envelope of the refracted rays, illustrated in Figure 7.8, is called a caustic [Hecht 1987].

One of the easiest caustics to observe is that which forms in a cup of coffee when light shining into the cup is reflected off the cylindrical insides surface, yielding a caustic of a form, called "caustic rosette". Figure 7.9(a) shows the caustic rosette formed in a cup of coffee. Figure 7.9(b) is the ray diagram showing how the sharp, bright curves to which the light rays are tangential, are generated.

7.3.1 The fundamentals of caustic theory

Consider the simple case shown in Figure 7.10, where a parallel beam of light along the Z-axis is incident on a curved surface S

$$Z = S(x,y) \tag{7-7}$$

The light reflected from the surface obeys the well-known laws of reflection. Using Snell's law, the correspondence between points on the same ray of light in the surface, S(x,y), and on the screen is given by

$$\begin{aligned} u &= x + [z_0 - S(x,y)] \tan 2\alpha \\ v &= y + [z_0 - S(x,y)] \tan 2\beta \end{aligned} \tag{7-8}$$

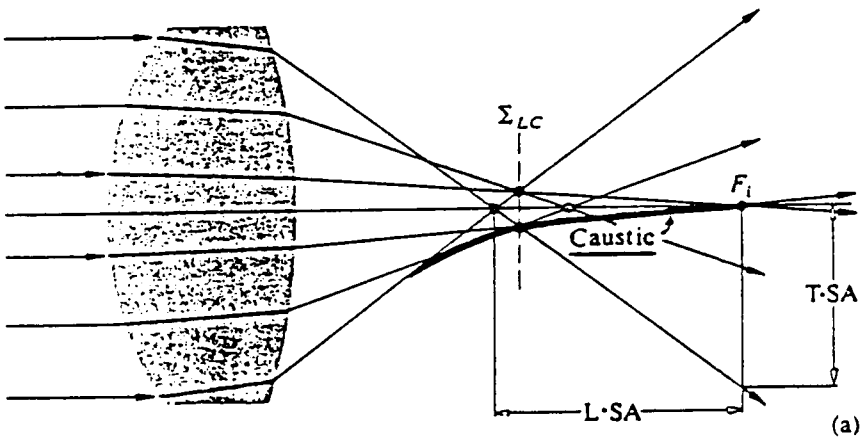


Figure 7.8 Spherical aberration for a lens. The envelope of the refracted rays is called a caustic. (Source: Hecht 1987).

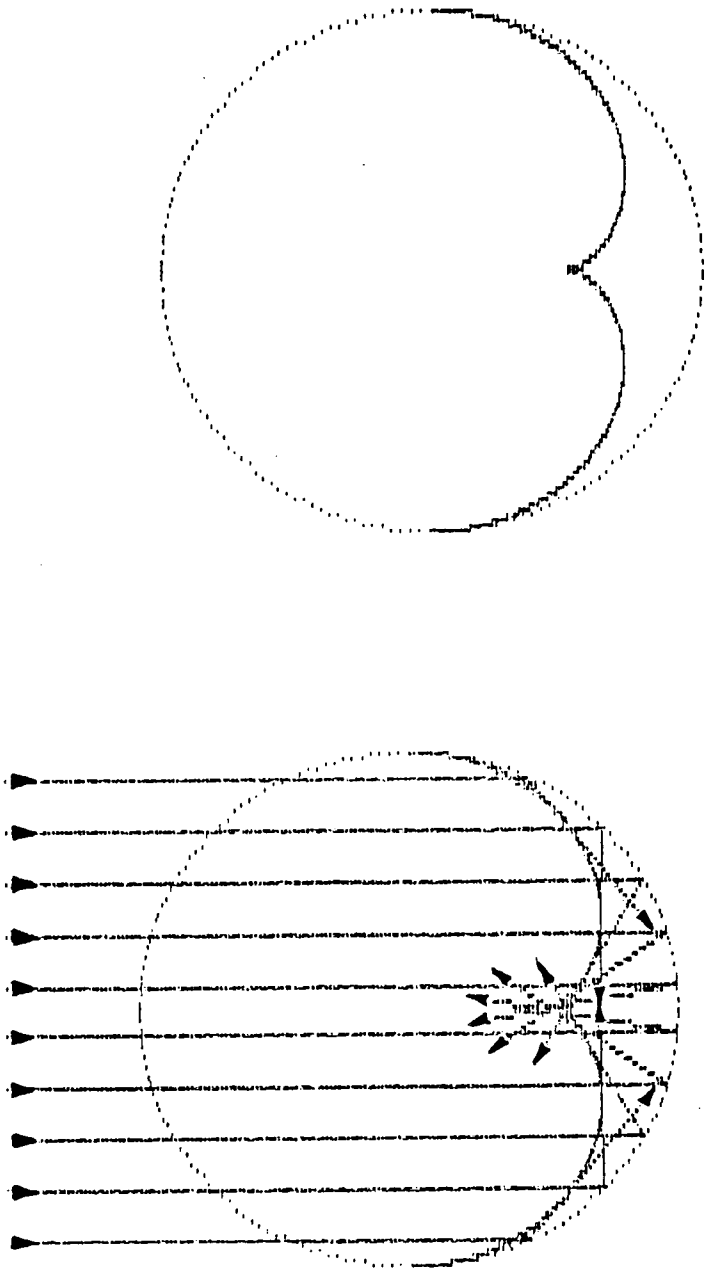


Figure 7.9 Formation of caustics in a cup of coffee. (a) the caustic rosette formed in a cup of coffee; (b) a ray diagram showing how the sharp, bright curves are generated.

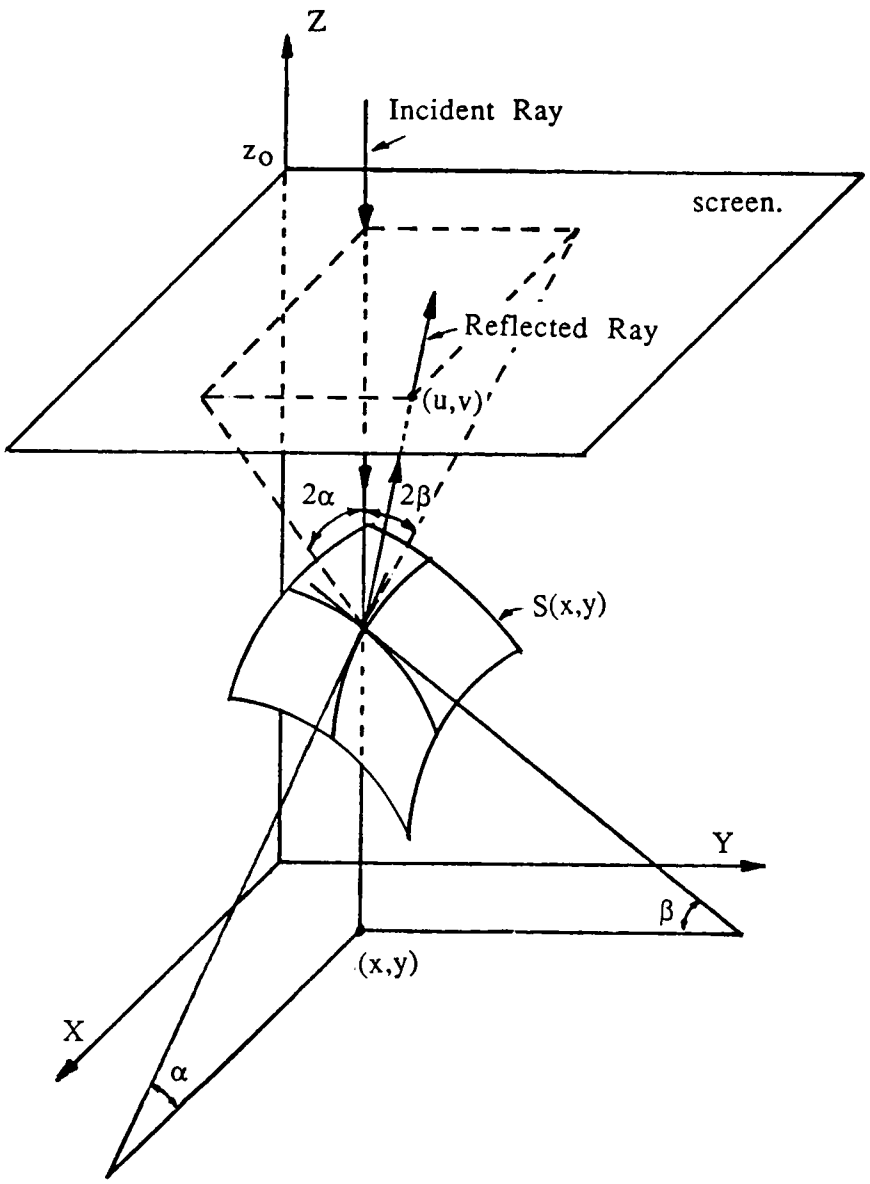


Figure 7.10 Geometrical relationship between incident ray and reflected ray in 3-dimensions.

where:

x, y = co-ordinates in the surface S(x,y), and

u, v = co-ordinates on the screen.

α, β, the angles of incidence on S(x,y) for a given ray, measured in the xoz- and yoz-planes respectively, are given by

$$\tan\alpha = \frac{\partial S(x,y)}{\partial x}$$
$$\tan\beta = \frac{\partial S(x,y)}{\partial y} \qquad (7\text{-}9)$$

Using

$$\tan 2\alpha = \frac{2\tan\alpha}{1-\tan^2\alpha} \qquad (7\text{-}10)$$

and substituting Eq.(7-9) in to Eq.(7-10), the image on the screen of any point of the surface is given by

$$u = x + [\, z_o - S(x,y)] \frac{\frac{2\partial S(x,y)}{\partial x}}{1 - [\frac{\partial S(x,y)}{\partial x}]^2}$$
$$v = y + [\, z_o - S(x,y)] \frac{\frac{2\partial S(x,y)}{\partial y}}{1 - [\frac{\partial S(x,y)}{\partial y}]^2} \qquad (7\text{-}11)$$

Eq. (7-11) is the optical transform that relates the reference surface S(u,v) to the specimen surface S(x,y).

Several incident and reflected rays are shown in Figure 7.11. The reflected rays are intercepted by the screen at points having x-coordinates smaller than x_0. In order to form a caustic on the screen it is necessary that u takes a maximum or minimum value for v = constant, see Figure 7.11, or, conversely, that v reaches a maximum or minimum value for u = constant. These conditions can be expressed mathematically as follows. The transformation described by Eq.(7-11) is singular at the points where its Jacobian determinant, **J**, equals zero, i.e.,

$$J = \frac{\partial(u,v)}{\partial(x,y)} = \begin{bmatrix} \frac{\partial u}{\partial x} & \frac{\partial u}{\partial y} \\ \frac{\partial v}{\partial x} & \frac{\partial v}{\partial y} \end{bmatrix} = 0 \qquad (7\text{-}12)$$

Ray diagrams are formulated such that the intensity of radiation is proportional to the density of rays. Hence, it is evident that the energy is highly concentrated in the vicinity of the caustic. In fact, from the viewpoint of energy conservation, the intensity is infinite exactly on the caustic because of the singularity in the optical transformation. It can also be seen from Figures 7.8 and 7.9, that the caustic forms a well defined boundary within a set of rays; on crossing a caustic, one moves from a region of shadow into one of illumination.

7.3.2 The application of caustics

The use of caustics as experimental probes is relatively new. It was originally introduced by Manogg [1964] for investigating crack tip

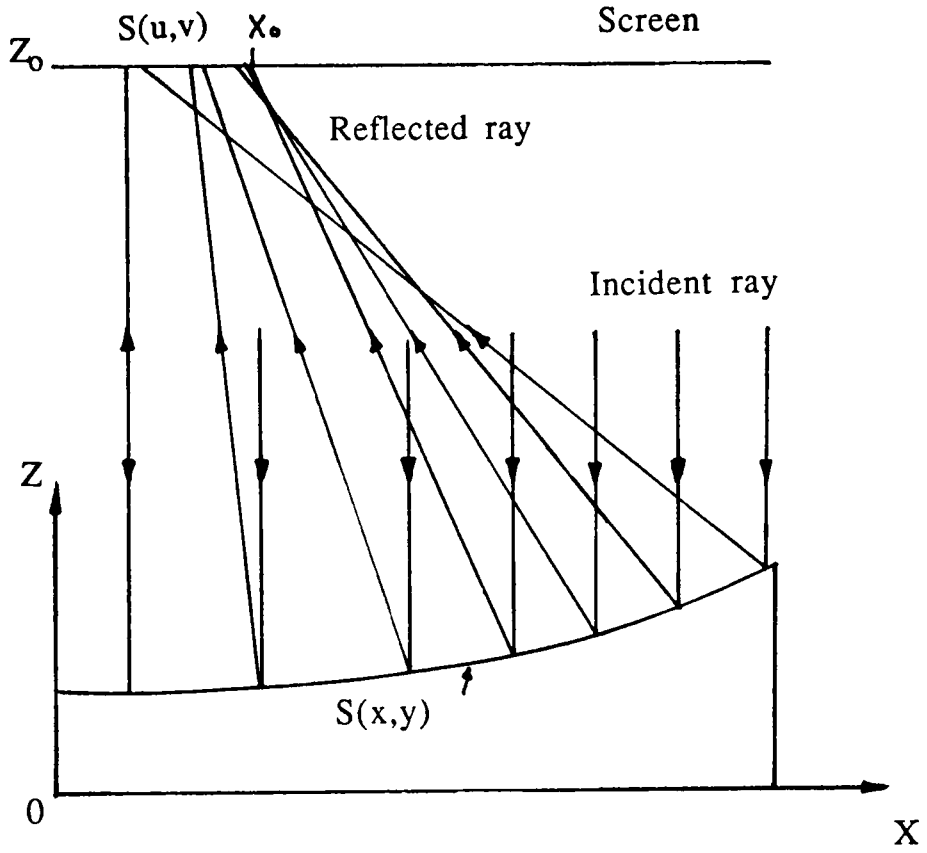


Figure 7.11 Geometric interpretation of the formation of a caustic, cf. Figure 7.10.

stress intensifications. The method is sensitive to gradients of elastic displacement and is therefore an appropriate tool for investigating stress concentration problems. The technique was later extended for the same purpose by Theocaris [1970], and by Kalthoff [1977] to explore material behavior under various static and dynamic loading conditions. Recently, Brewster [1989] has further developed the technique for ultrasonic non-destructive evaluation purposes.

7.3.3 A New Method to Measure Small Deformation

In the previous section, we have showed how the phenomenon known as an optical caustic is related to the geometric optics of light rays reflected by a curved surface. The physical principles and the mathematical description of caustics will be now described in order to develop a new method to measure small changes in curvature of such a surface.

In Figure 7.12, consider the geometry of a caustic associated with a surface, initially flat, that has been deformed to a surface of cylindrical symmetry. The angle of incidence equals to the angle of reflection, that is,

$$\theta_i = \theta_r$$

$$a = 90^o - (\theta_i + \theta_r) \qquad (7\text{-}13)$$

Since

$$\theta_i = \tan^{-1}\left(\frac{ds}{dx}\right) \qquad (7\text{-}14)$$

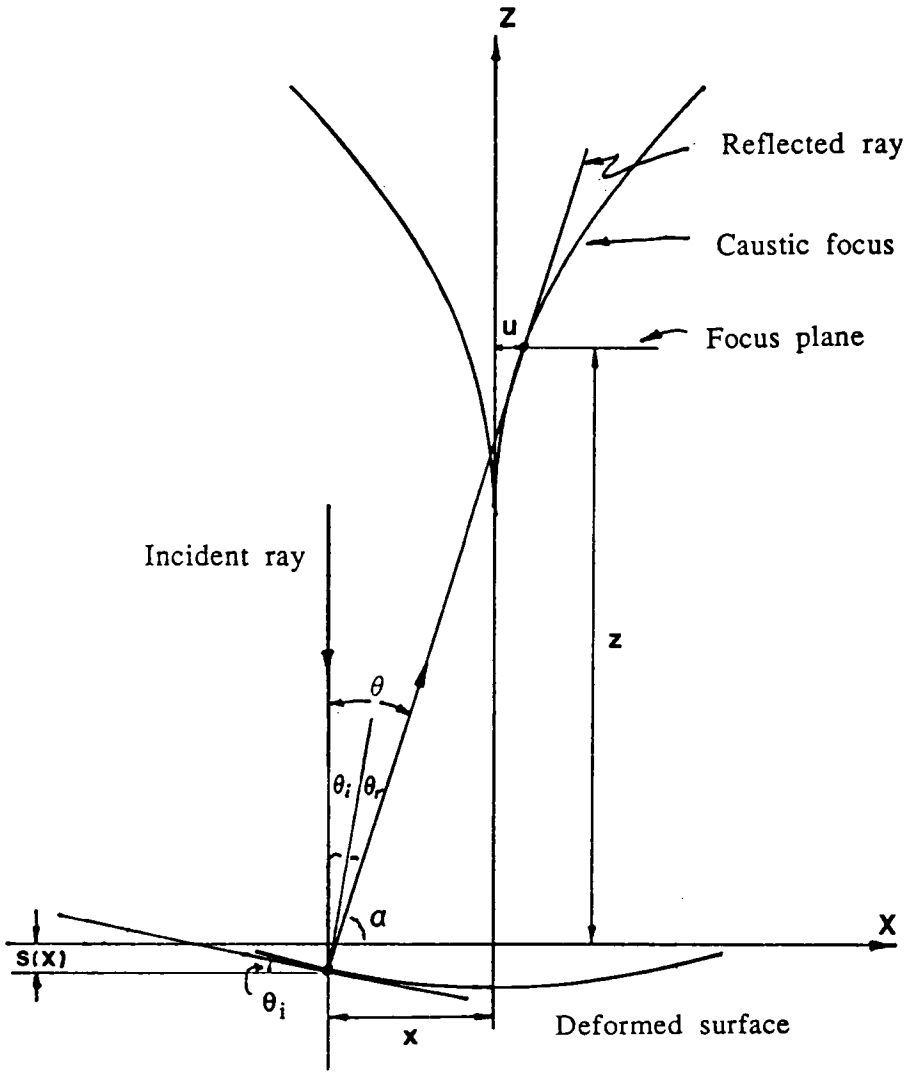


Figure 7.12 The caustic geometry associated with a surface deformed from flat to cylindrical shape.

$$\alpha = 90^{o} - 2 \tan^{-1} \left(\frac{ds}{dx}\right) \qquad (7\text{-}15)$$

Thus the orientation of the reflected ray is such that the geometry of the caustic is a function of a gradient of the displacement field, $\frac{ds}{dx}$.

Consider a parallel beam of light incident along the Z-axis in Figure 7.12. Let it illuminate a curved surface, S, of cylindrical symmetry,

$$Z = S(x)$$

Referring to Figure 7.12, correspondence between points in the surface, S, and in the focus plane, S_f, for a given light ray, is expressed by,

$$u - x = [\, z - S(x)] \tan\theta \qquad (7\text{-}16)$$

where, for a given ray, x is its co-ordinate in the surface S and u is its co-ordinate in the focus plane S_f.

Using Eq.(7-12),

$$J = \frac{du}{dx} = \frac{d}{dx} (x + (\, z - S) \tan\theta)$$

$$= 1 + ((z - S) \frac{1}{\cos^2\theta} \frac{d\theta}{dx} - \tan\theta \frac{dS}{dx}\ ) = 0$$

Hence,

$$z = S + (\tan\theta \frac{dS}{dx} - 1) \cos^2\theta \frac{dx}{d\theta} \qquad (7\text{-}17)$$

where $\frac{dx}{d\theta}$ can be derived as follows. Using Eq.(7-10) and

$$\tan(\frac{1}{2}\theta) = \pm \frac{dS}{dx} = \pm Sx$$

In the following derivation, $Sx = \frac{dS}{dx}$, $Sxx = \frac{d^2S}{dx^2}$.

Taking the positive solution,

$$\tan\theta = \tan(2(\frac{1}{2}\theta)) = \frac{2\frac{dS}{dx}}{1 - (\frac{dS}{dx})^2} = \frac{2Sx}{1 - S^2x}$$

i.e.,

$$\theta = \tan^{-1}(\frac{2Sx}{1 - S^2x}) \qquad (7\text{-}18)$$

Using

$$\frac{d}{dx}(\tan^{-1}\upsilon) = \frac{1}{1 + \upsilon^2}\frac{d\upsilon}{dx}$$

and Eq.(7-18), we obtain

$$\frac{d\theta}{dx} = \frac{d}{dx}(\tan^{-1}(\frac{2Sx}{1 - S^2x}))$$

$$= \frac{1}{1 + (\frac{2Sx}{1 - S^2x})^2} \frac{(1-S^2x)Sxx - 2Sx(-2SxSxx)}{(1-S^2x)^2}$$

$$= \frac{(1 - S^2x)^2}{(1 - S^2x)^2 + 4S^4x} \frac{2Sxx\,(1 + S^2x)}{(1 - S^2x)^2}$$

$$= \frac{2S_{xx}}{1 + S^2_x}$$

Hence,

$$\frac{dx}{d\theta} = \frac{1 + S^2_x}{2S_{xx}} \qquad (7\text{-}19)$$

Substituting Eq.(7-17) into Eq.(7-16),

$$u = x + \left(\tan\theta \frac{dS}{dx} - 1 \right) \cos^2\theta \tan\theta \frac{dx}{d\theta} \qquad (7\text{-}20)$$

This is the required relationship between the deformation $(\frac{dS}{dx})$ of the reflecting surface and the co-ordinate of the caustic focus (u). Measurement of the latter can evidently be used to determine the deformation of the reflecting surface.

If Figure 7.12 represents a surface of small slope,

$$\tan\theta_i \approx \theta_i$$

Eq.(7-14) becomes

$$\theta_i = \frac{dS}{dx}$$

i.e.,

$$\theta = 2 \frac{dS}{dx}$$

Since S << z, Eq.(7-21) can be written as

$$u = x - 2zS_x \tag{7-21}$$

where negative sign is due to sign of S_x, and since

$$\frac{du}{dx} = 1 - 2zS_{xx} = 0$$

$$z = \frac{1}{2S_{xx}} \tag{7-22}$$

Substituting into Eq.(2-21),

$$u = x - \frac{S_x}{S_{xx}} \tag{7-23}$$

Note that,

$$\frac{d^3S}{dx^3} = \frac{1}{\text{curvature of caustic}}$$

and,

$$\frac{d^3S}{dx^3} = 0 \text{ at the cusp point in a caustic focus.}$$

Note that values for $\frac{d^2S}{dx^2}$, the second differential of the surface displacement can be obtained directly from the caustic focus. Referring to Figure 7.13, the turning points a, b and b' on the second differential, corresponding to A, B and B' on the caustic focus can be

located by inspection of the geometry of the caustic focus and, by sketching in the intermediate points, the overall shape of the second differential of reflecting surface can be deduced immediately. Note that the second differential of the displacement field of a thin plate is a measure of the bending moment. Furthermore, by differentiating two more times to get the 4th differential, the distribution of stress normal to the plate can be obtained. On the other hand, by integrating twice, the deformation field itself can be obtained.

For the purposes of measuring dimensional changes associated with water uptake by a model composite or by coatings on the chip on board, we first have to map out the caustic focus and then invert it in order to obtain the surface profile, which is expected to change with increase of immersion time.

In order to measure the caustic foci, the focus plane of the camera needs to be moved from infinity to some finite distance from the specimen surface during the measurement procedure, since the caustic focus at different distance is of different size, as is evident from Figure 7.14. Figure 7.14 is a computer simulation showing how the geometry of the caustic focus changes when the curvature of the reflecting surface changes. Using camera or video tape, the in-line displacement can be measured by this procedure.

There are two ways by which caustic foci can be inverted into surface profiles, namely, integration and iteration. If the geometry of the caustic focus is amenable to standard curve fitting procedures

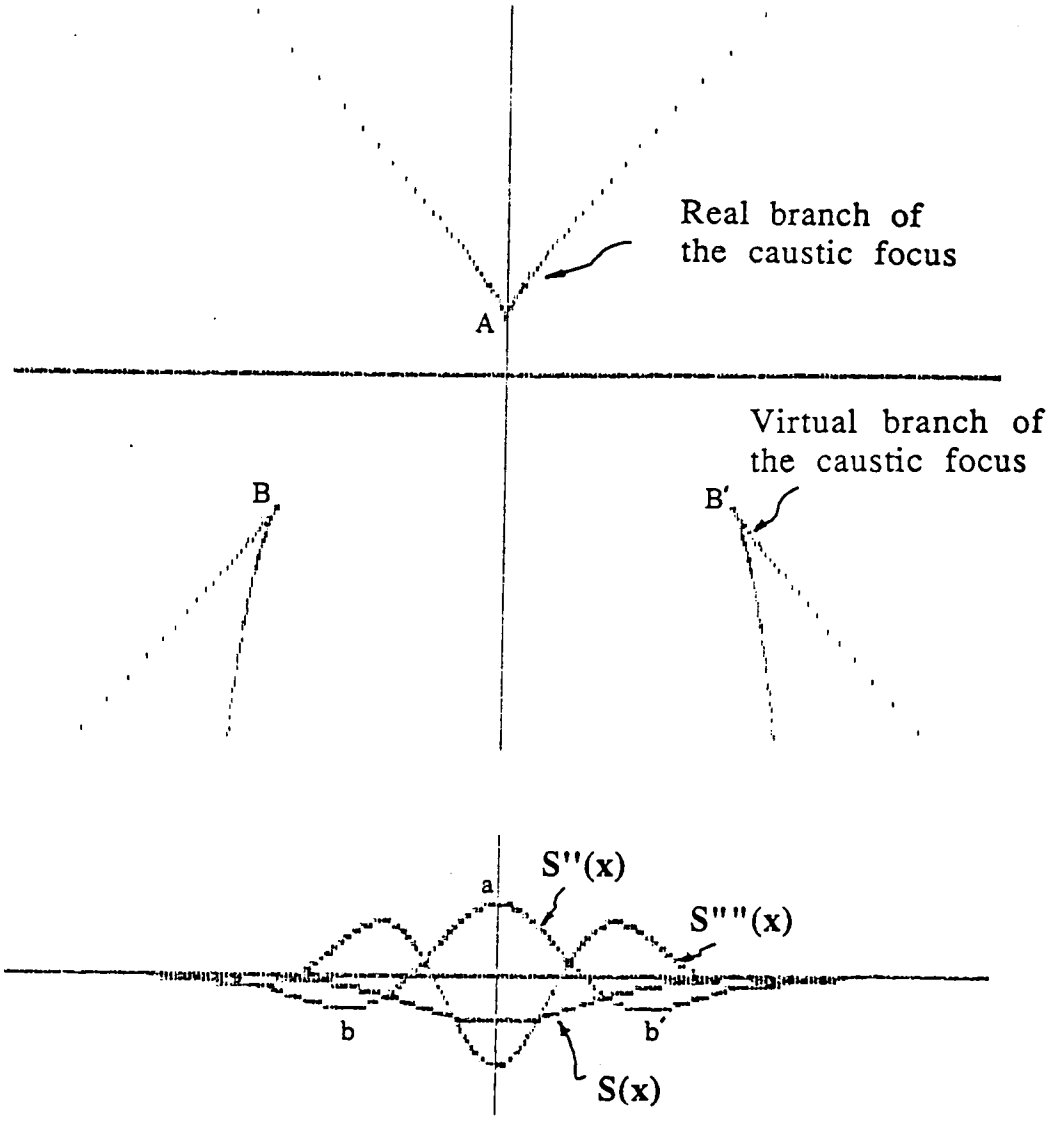


Figure 7.13 Showing how, in this case, the sinusoidal shape of the second differential of the reflecting surface in (b) may be deduced from the relative positions of the cusps in the caustic focus (a).

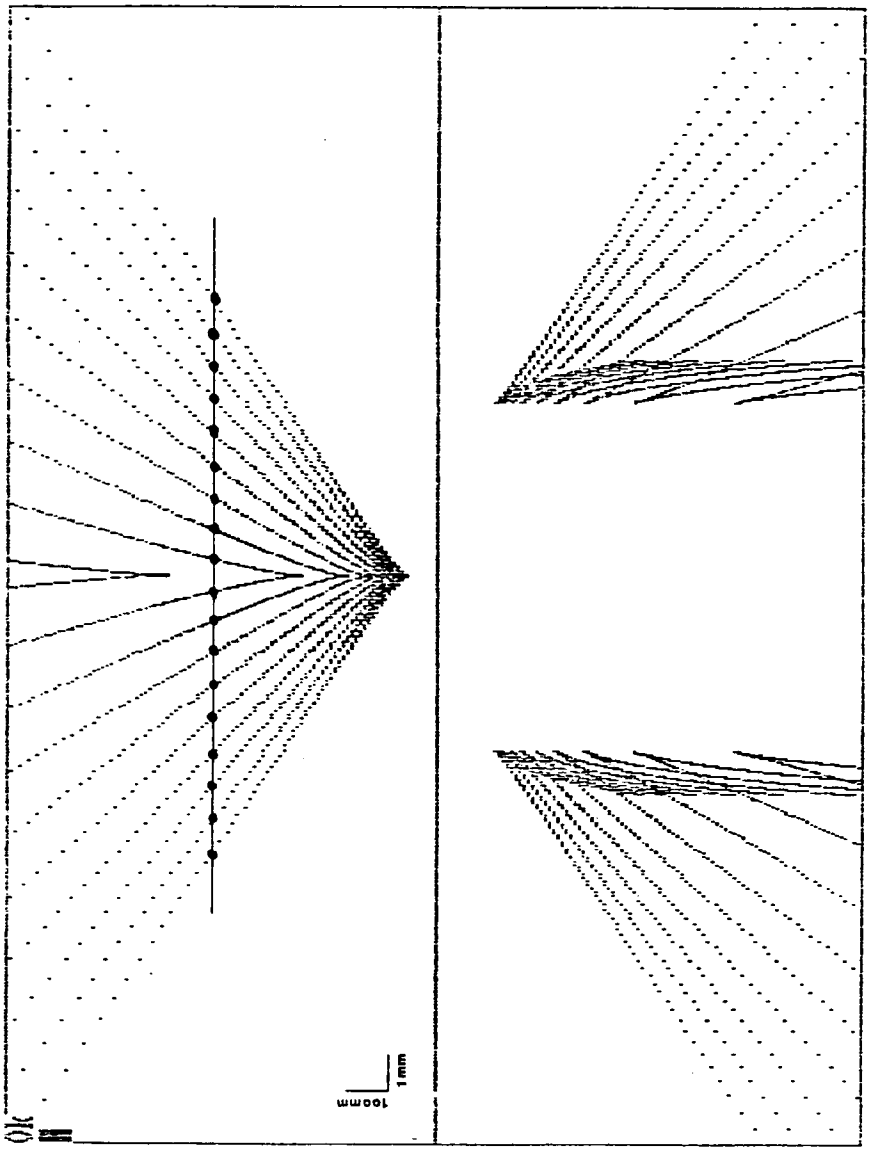


Figure 7.14 The different geometries of the caustic foci corresponding to the increment of center displacement of the reflecting surface. The position of cusp point migrates towards the specimen surface with increasing center displacement.

then, by twice integrating the second differential obtained directly from measured co-ordinates of the caustic focus, we can generate the surface profile. Since it is more generally useful, however, we will now describe the iteration method for obtaining surface profiles from caustic foci.

In Figure 7.15, consider a small number of rays reflected by a surface. Ray R_i, after reflection from point P_i on the surface, subtends an angle α_i to the X-axis. Rays, R_{i+1}, ..., R_n, similarly subtend angles α_{i+1}, ..., α_n respectively. Each point on the reflecting surface, corresponding to a single ray, has its own unique inclination to the X-axis. The relationship between the local slope, θ_{i-1}, of the reflecting surface and the angle subtended by individual rays can be derived as follows.

Referring to Figures 7.12 and 7.15, it can be seen

$$\tan 2\theta_{i-1} = \tan(90^\circ - \alpha_i) = \frac{1}{\tan\alpha_i}$$

$$= \frac{2\tan\theta_{i-1}}{1-\tan^2\theta_{i-1}}$$

Hence

$$\tan^2\theta_{i-1} + 2\tan\alpha_i \tan\theta_{i-1} - 1 = 0$$

solutions to which are given by

$$\tan\theta_{i-1} = -\tan\alpha_i \pm \sqrt{\tan^2\alpha_i + 1} \qquad (7\text{-}24)$$

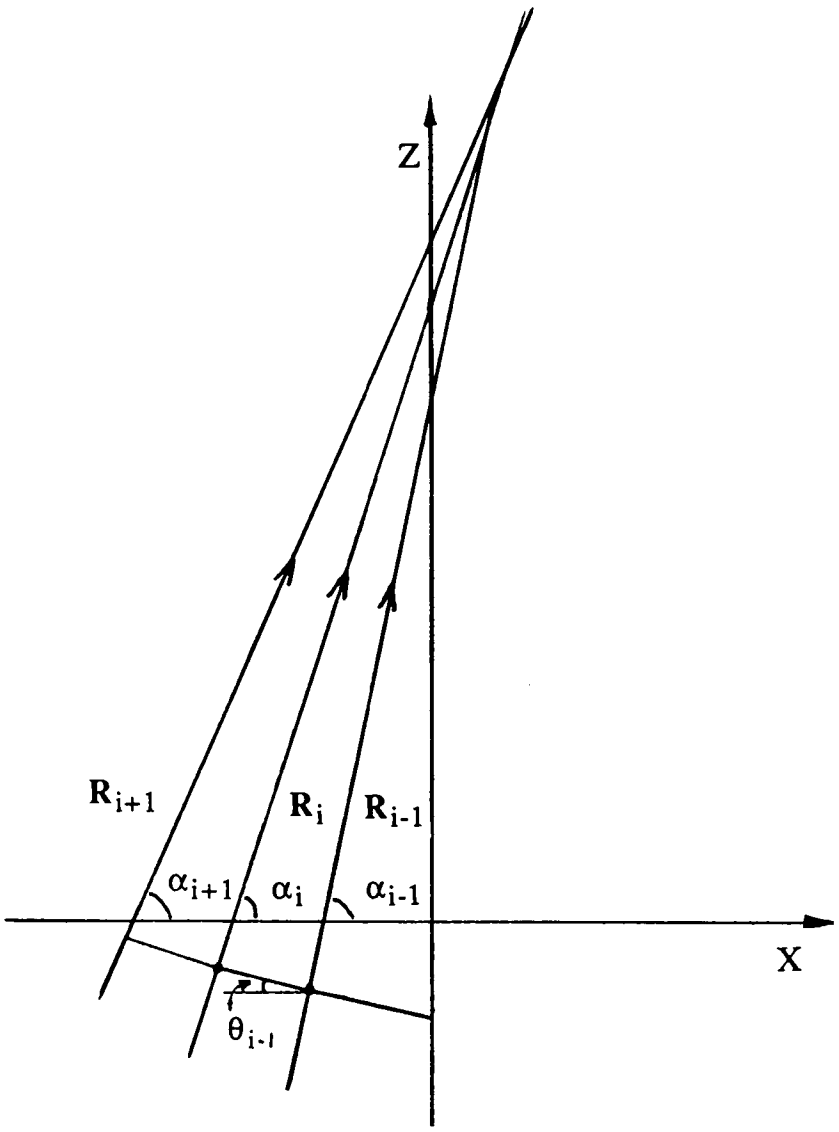


Figure 7.15 Generation of surface profile from a caustic focus by iteration.

The sign of the square root is chosen to yield physically meaningful solutions. The equation to the line representing ray R_i is

$$Z_i = X_i \tan\alpha_i + C_i \qquad (7\text{-}25)$$

where $C_i = z_i - u_i \tan\alpha_i$, z_i and u_i locate the caustic focus.
The equation to the tangent to the surface at point, P_i, is

$$Z_i = Z_{i-1} + \tan\theta_{i-1} (X_i - X_{i-1}) \qquad (7\text{-}26)$$

where Z_{i-1} and X_{i-1} are the co-ordinates of a point, P_{i-1}.
Point, P_i, lies at the intersection of these two lines. Hence its co-ordinates can be obtained by solving equations (7-25) and (7-26) as simultaneous equations, viz

$$X_i \tan\alpha_i + C_i = Z_{i-1} + \tan\theta_{i-1} (X_i - X_{i-1})$$

thus,

$$X_i = \frac{Z_{i-1} - X_{i-1}\tan\theta_{i-1} - C_i}{\tan\alpha_i - \tan\theta_{i-1}} \qquad (7\text{-}27)$$

Substituting Eq.(7-24) into Eq.(7-27),

$$X_i = \frac{Z_{i-1} - (-\tan\alpha_i \pm \sqrt{\tan^2\alpha_i + 1})\, X_{i-1} - C_i}{\tan^2\alpha_i + \sqrt{\tan^2\alpha_i + 1}}$$

$$Z_i = Z_{i-1} - (\tan\alpha_i \pm \sqrt{\tan^2\alpha_i + 1}) \left(\frac{Z_{i-1} - (\tan\alpha_i \pm \sqrt{\tan^2\alpha_i + 1})\, X_{i-1} - C_i}{\tan^2\alpha_i + \sqrt{\tan^2\alpha_i + 1}} - X_{i-1} \right) \tag{7-28}$$

where $\tan\alpha_i$, X_{i-1}, Z_{i-1}, and C_i, can be obtained by $(i-1)^{th}$ iteration. For $i = 0$, $X_i = 0$, Z_i can be adjusted until the asymptotic curve of the surface profile closes to zero after the n^{th} iteration.

It is evident that very high accuracy, for inversion of the caustic focus into the reflecting surface that gives rise to it, can be achieved if $(X_i - X_{i-1})$ is very small. By way of illustration of the accuracy offered by this method, Figure 7.16 shows two surface profiles, one being the original that gives rise to the caustic, and the other being the experimentally determined surface obtained by inverting the caustic focus.

To estimate the precision offered by this new method for measuring surface profiles, error analyses have been carried out by considering a small random error made in the co-ordinate measurements for a caustic focus. For example, consider a random error of ± 20μm in the X-direction co-ordinate. Using the cubic spline method to smooth the experimental curve, we get the two caustic foci curves shown either side of the correct curve in Figure 7.17. Using the iteration procedure, we derive the two surface profiles shown in

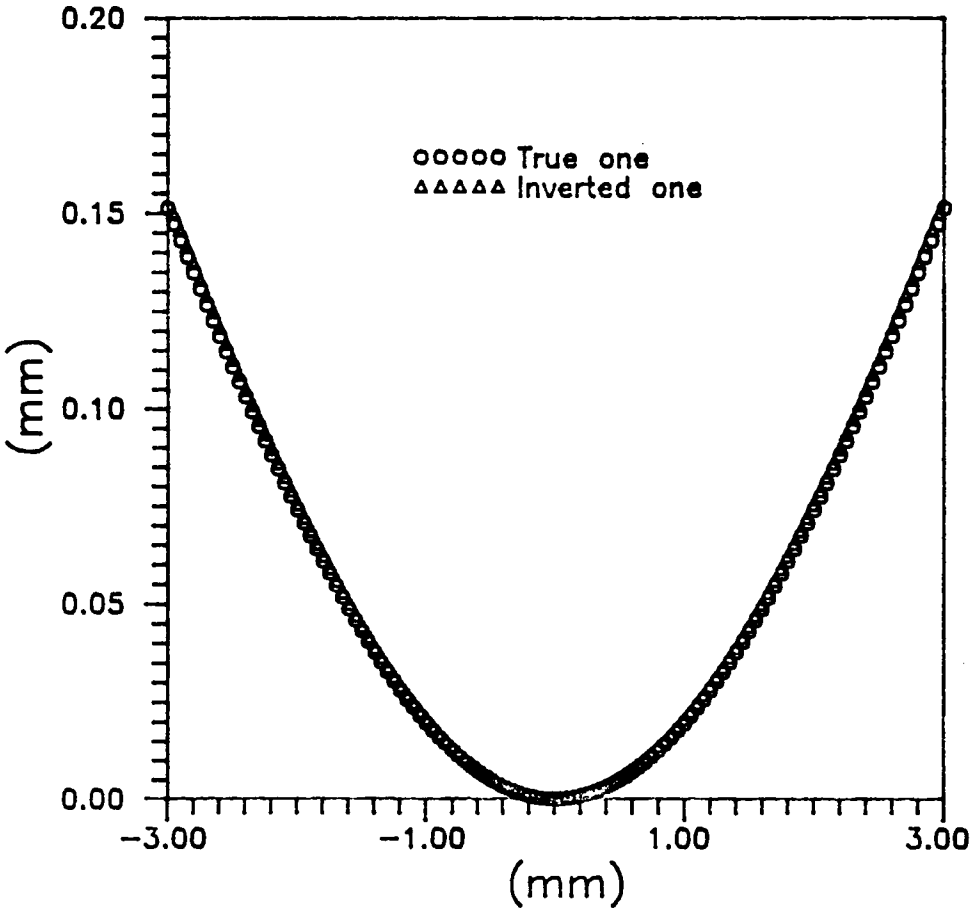


Figure 7.16 Comparison of the inverted surface profile obtained from caustic foci measurement and its true surface profile.

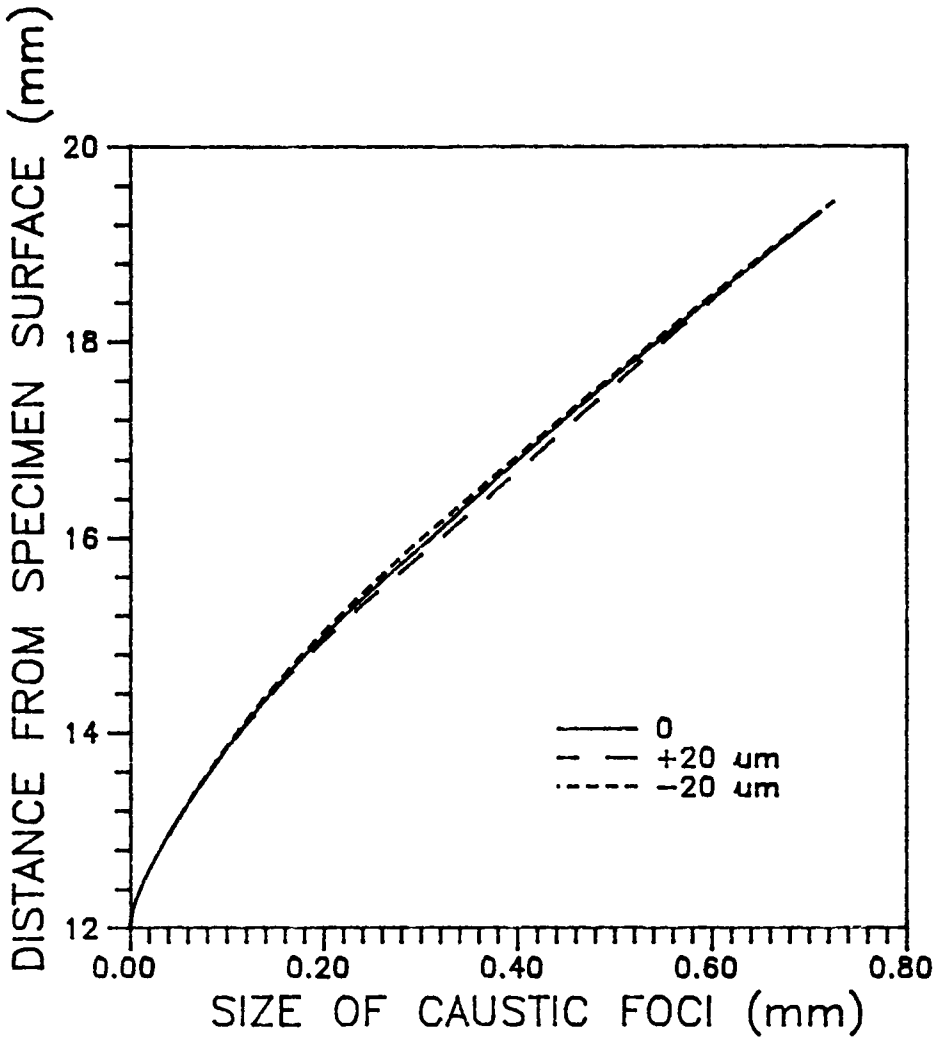


Figure 7.17 The effect on surface profile determination of an error, $\Delta x = \pm 20\mu m$, made in measurement of the position of a caustic focus.

Figure 7.18. The deviation, (Z'-Z), at a number of points has been calculated and is presented in Figure 7.19. These results indicate that a measurement error of ± 20 μm generates an error, in the Z-direction in the derived surface profile, of only 0.50 μm.

Now consider how small a deformation of the reflecting surface might be detectable by our method. Consider a specimen with a deformed surface described by $Z = - H \exp(- x/w)$, where H=0.1 mm, w=5 mm. Figure 7.20 shows that for, say, 1m from the specimen surface in a typical experiment, a displacement of 10 nm at the specimen surface can be detected if the corresponding displacement of caustic focus, 10 μm, can be recorded. Moreover, the longer the distance from the reflecting surface at which the caustic co-ordinates are measured, the greater the accuracy.

If it contains one, the cusp in a caustic focus provides a unique method for measurement of small deformations. Referring to Figure 7.21, the cusp is at infinity when the specimen surface is flat. When deformation of the specimen begins, the cusp moves rapidly towards the specimen surface.

The advantages and disadvantages of optical caustic focus measurement, as a method for measuring small displacement measurement, are summarized in Table 7.2.

7.3.4 Application to the Measurement of Dimensional Changes

Using optical caustic focus measurement, we have investigated the effect of water uptake on specimens consisting of a single fiber in a cylindrical block epoxy of resin, to opposite ends of which are

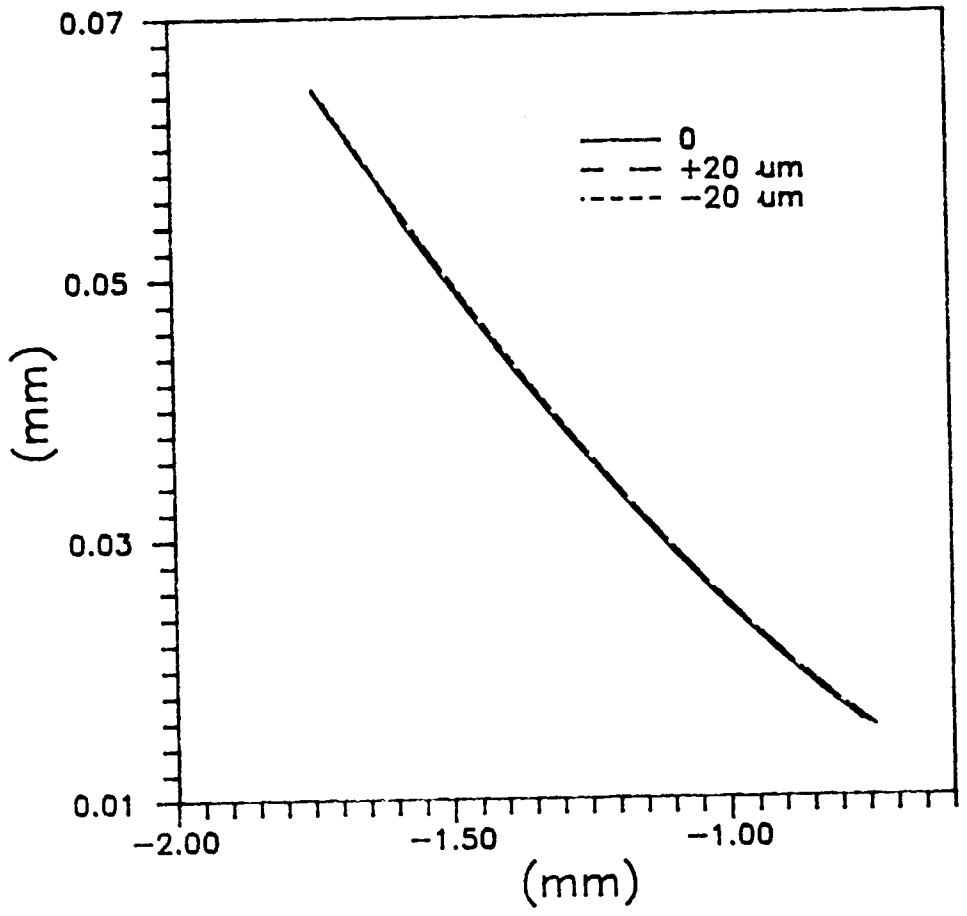


Figure 7.18 Surface profiles obtained by inverting the caustic focus shown in Figure 7.17.

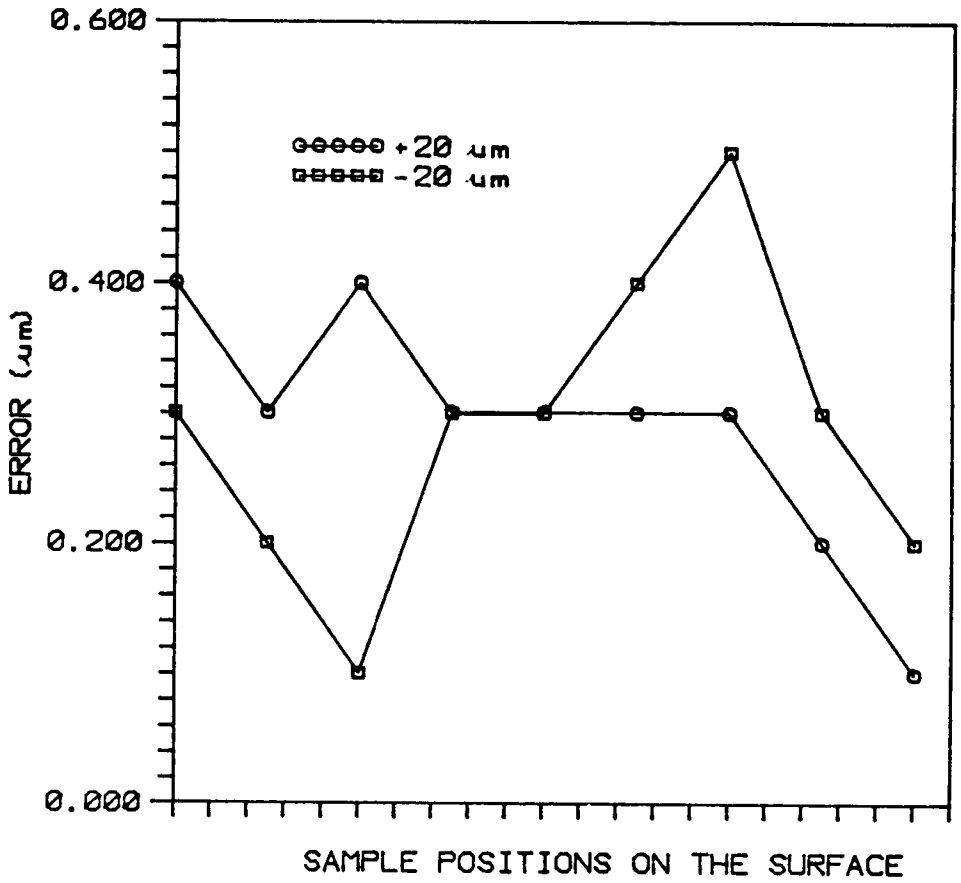


Figure 7.19 The deviation of experimentally determined surface profile at various sites, that is caused by the measurement error shown in Figure 7.16.

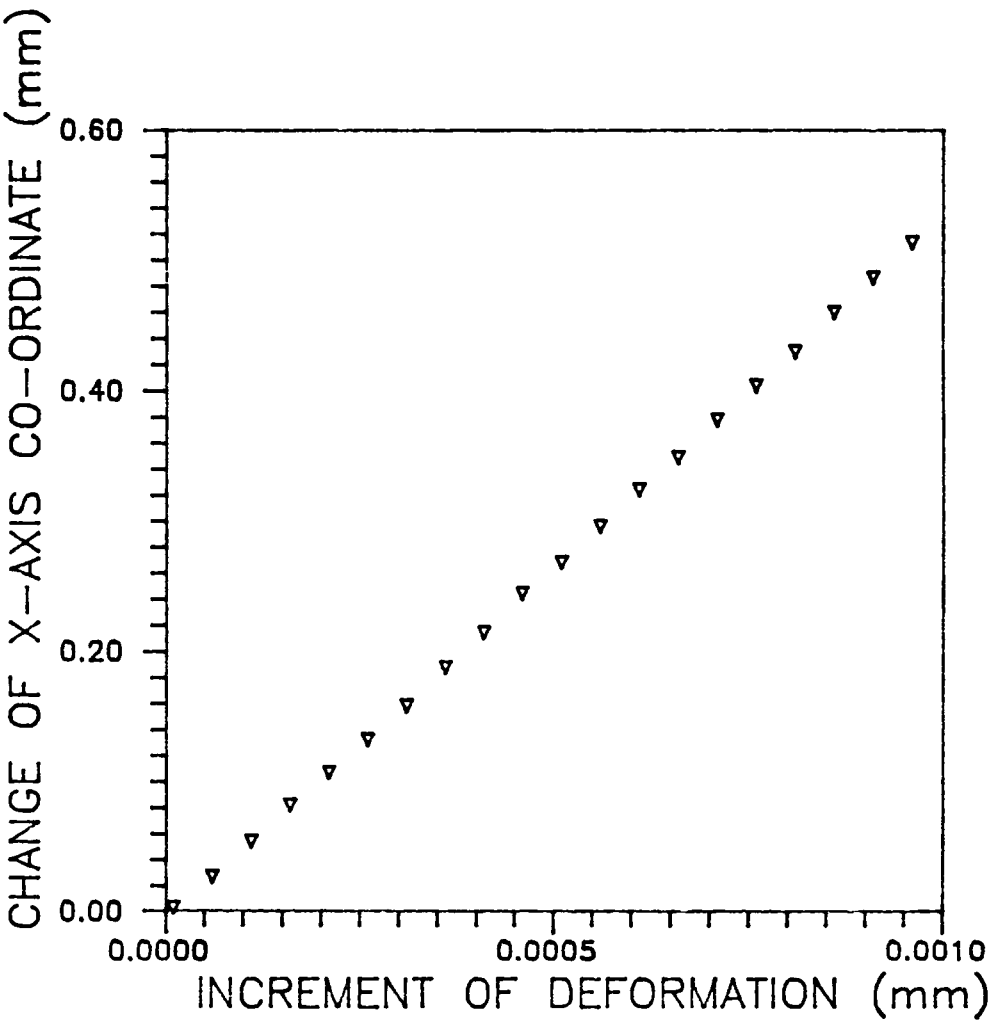


Figure 7.20 The change, with increments of reflecting surface deformation, of x-axis co-ordinate of the caustic focus.

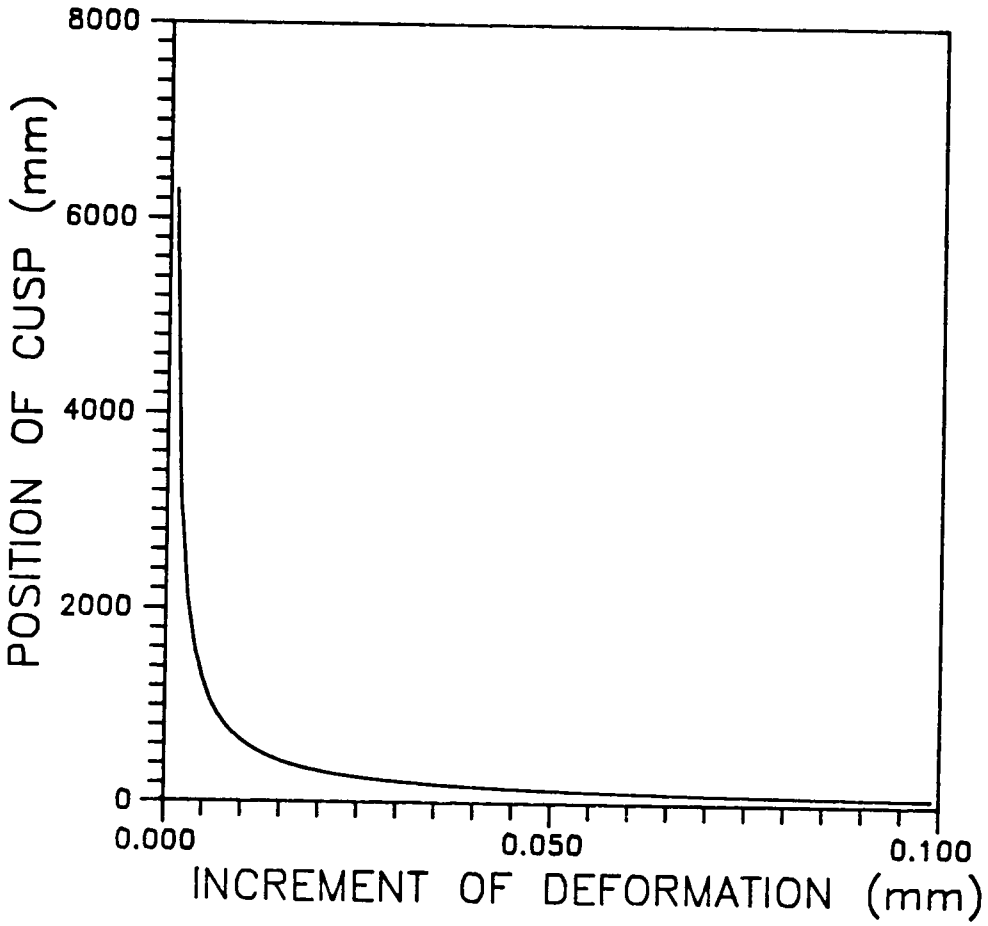


Figure 7.21 Displacement of a cusp in a caustic focus as a function of deformation of the reflecting surface.

Table 7.2

The advantages and limitations of optical caustic focus measurement as a method for measuring small displacement

Advantage	Limitation
1. Simplicity in instrumentation	1. Requires a smoothly curved surface
2. In-time measurement	2. Requires a reflecting surface
3. For small or large displacement	3. Requires an axisymmetric surface
4. Giving S'' directly	
5. High accuracy and sensitivity	

bonded a flexible glass cover slip and a rigid substrate. The interfacial bond between resin and fiber locally inhibits swelling of the resin that accompanies water uptake. As a consequence, the cover slip deforms to a "saucer" shape. Figure 7.22 shows schematically the geometry of a caustic generated by reflection from the deformed cover slip. Figures 7.23 and 7.24 show examples of sections through caustics that have been photographed at different distances from the specimen surface. The respective cover slip deformations were induced by immersion of the composite in distilled water for 250 hours at 50°C (Figure 7.23) and for 264 hours at 25°C (Figure 7.24). The corresponding caustic foci, and the cover slip displacements derived from the foci, are presented in Figures 7.25 and 7.26, and 7.27 and 7.28, respectively. It is evident that displacement of the cover slip end of the composite, arising from the effects of water uptake by the matrix, can be studied by photographing and measuring the caustic foci produced by reflection from the cover slip. As pointed out in Section 7.3.3, the raw data obtained from the caustic focus is the second differential of the normal displacement. By differentiating two more times, we have obtained the distribution of normal stress that gives rise to the observable cover slip displacement. Figure 7.29 shows the caustic focus measured after different immersion times at 25°C. The normal stress at the specimen center, i.e., the axial stress in the fiber, calculated by twice differentiating the data presented in Figure 7.29, is shown in Figure 7.30.

The caustic focus photographed in Figure 7.23 and shown in vertical section in Figure 7.25 is a real image. That photographed in

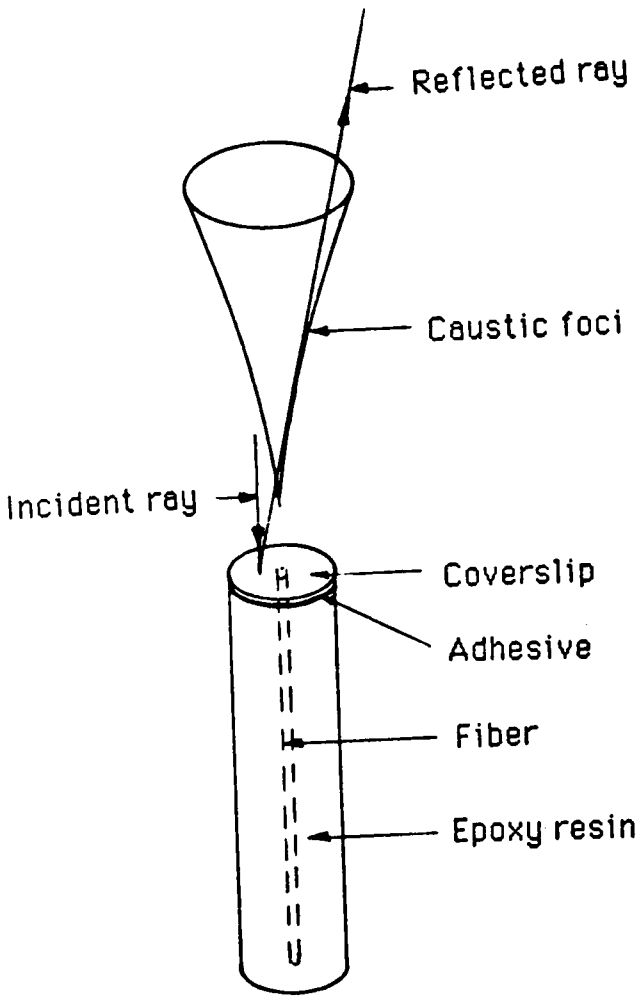


Figure 7.22 Schematic of a caustic focus in the form of a conical surface of high light intensity that is everywhere tangential to the rays reflected by a deformed cover slip bonded to the end of a self-stressed uniaxial composite.

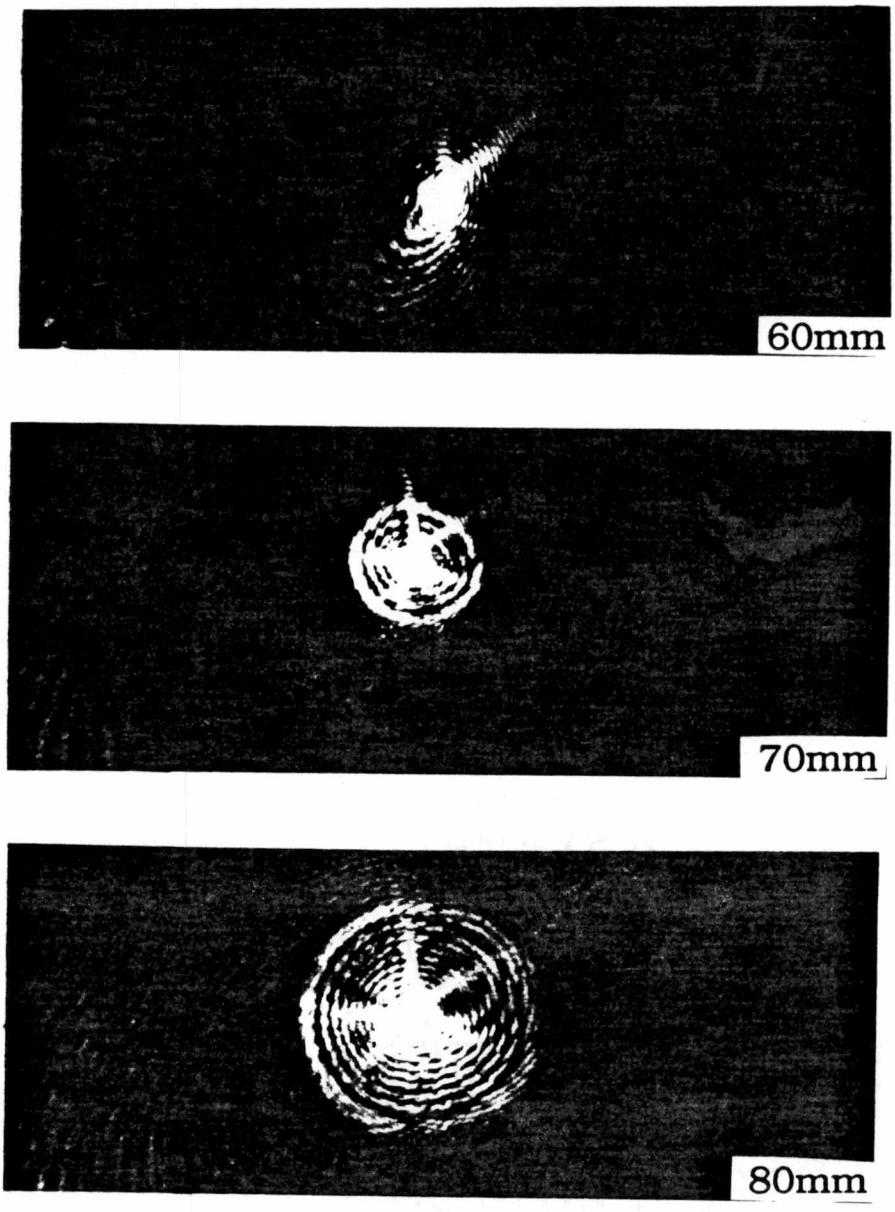


Figure 7.23 Three sections through a caustic focus (bright star-shaped contrast and associated rings at the center of the field of view) formed by light reflected from the deformed cover slip bonded to one end of a uniaxial composite that has been self-stressed by immersing in distilled water for 250 hours at 50°C. The less bright family of concentric fringes extending over the whole of the field of view are Newton's rings resulting from interference in the water gap between the cover slip and the optical flat.

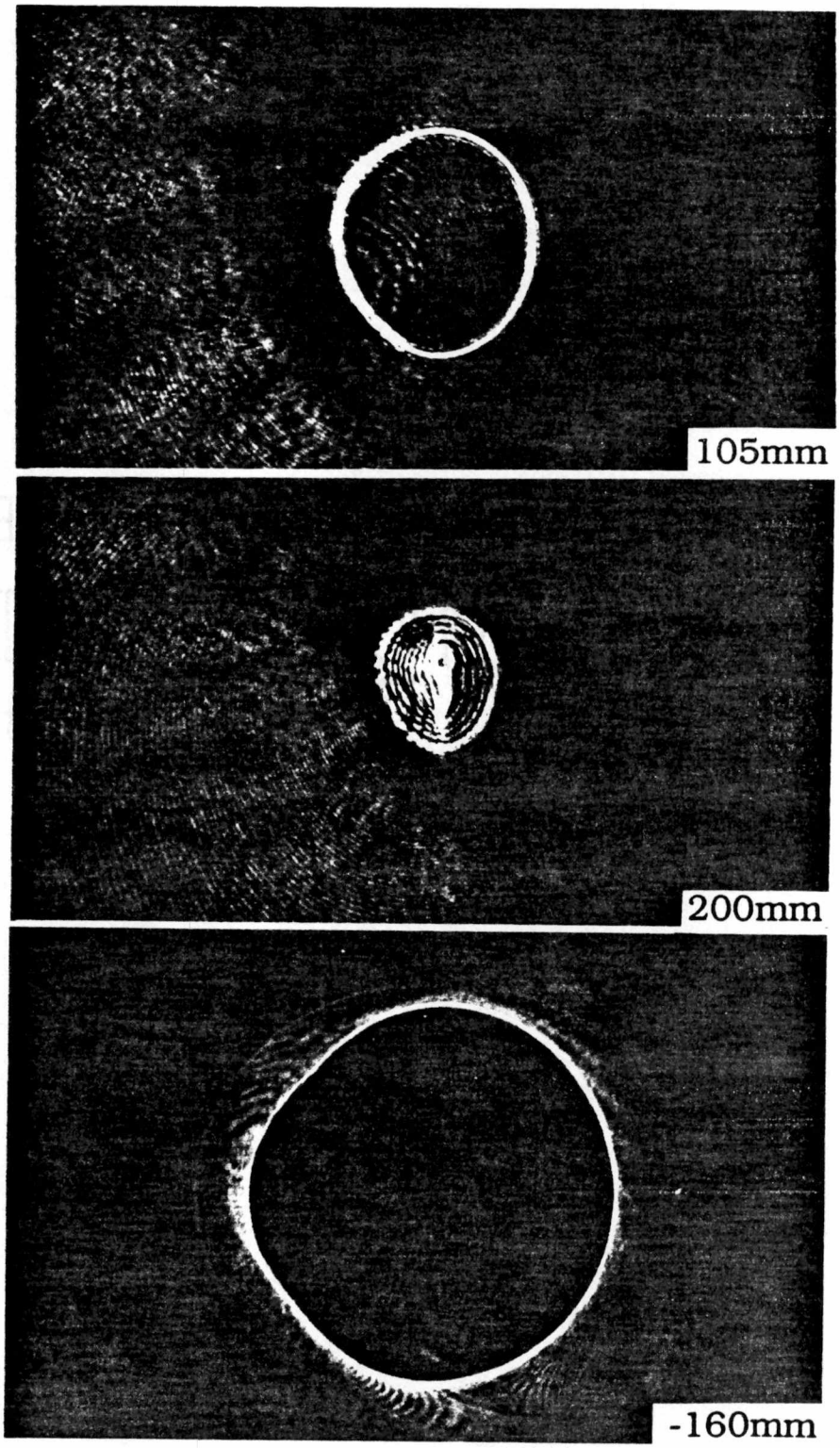


Figure 7.24 Same as Figure 7.23 but for immersion in distilled water for 264 hours at 25°C.

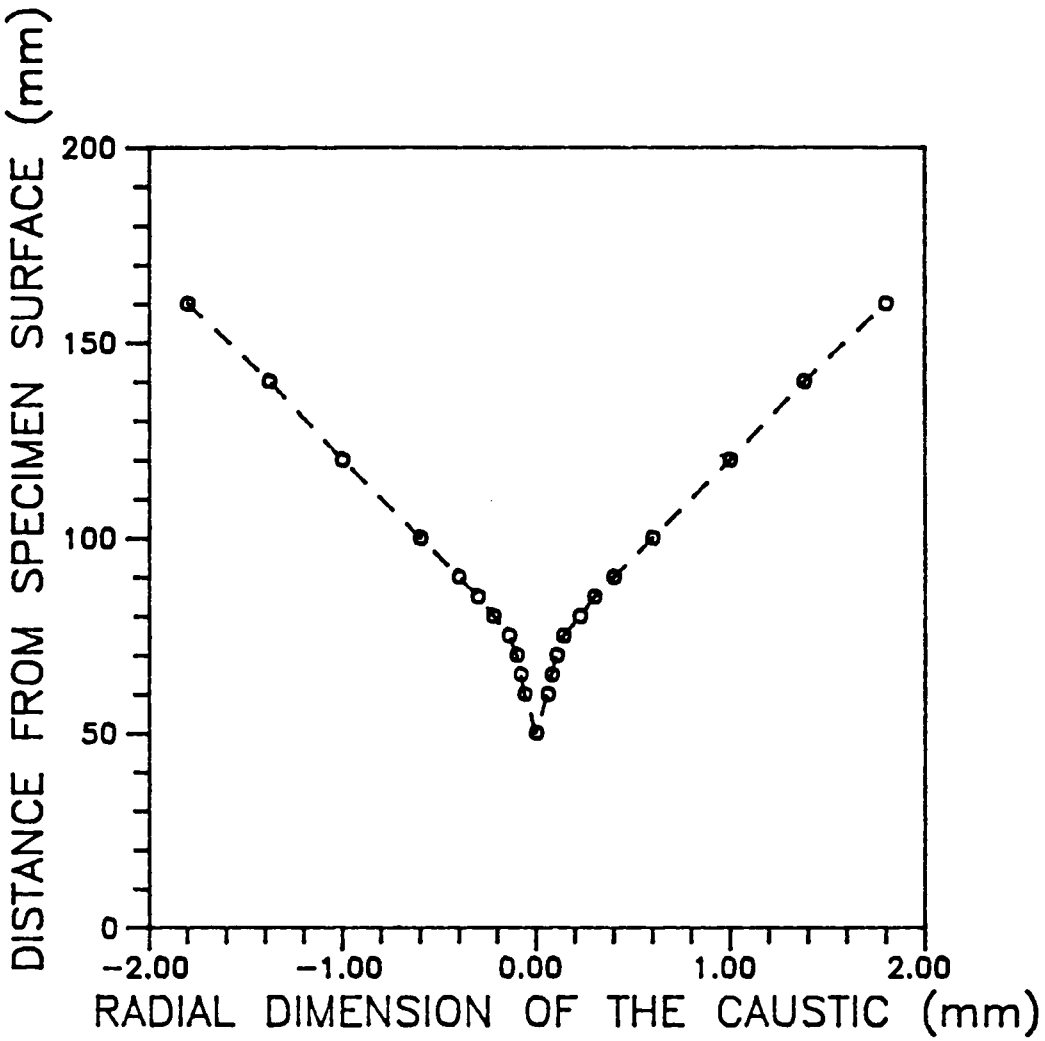


Figure 7.25 Vertical section through the caustic focus recorded in Figure 7.23.

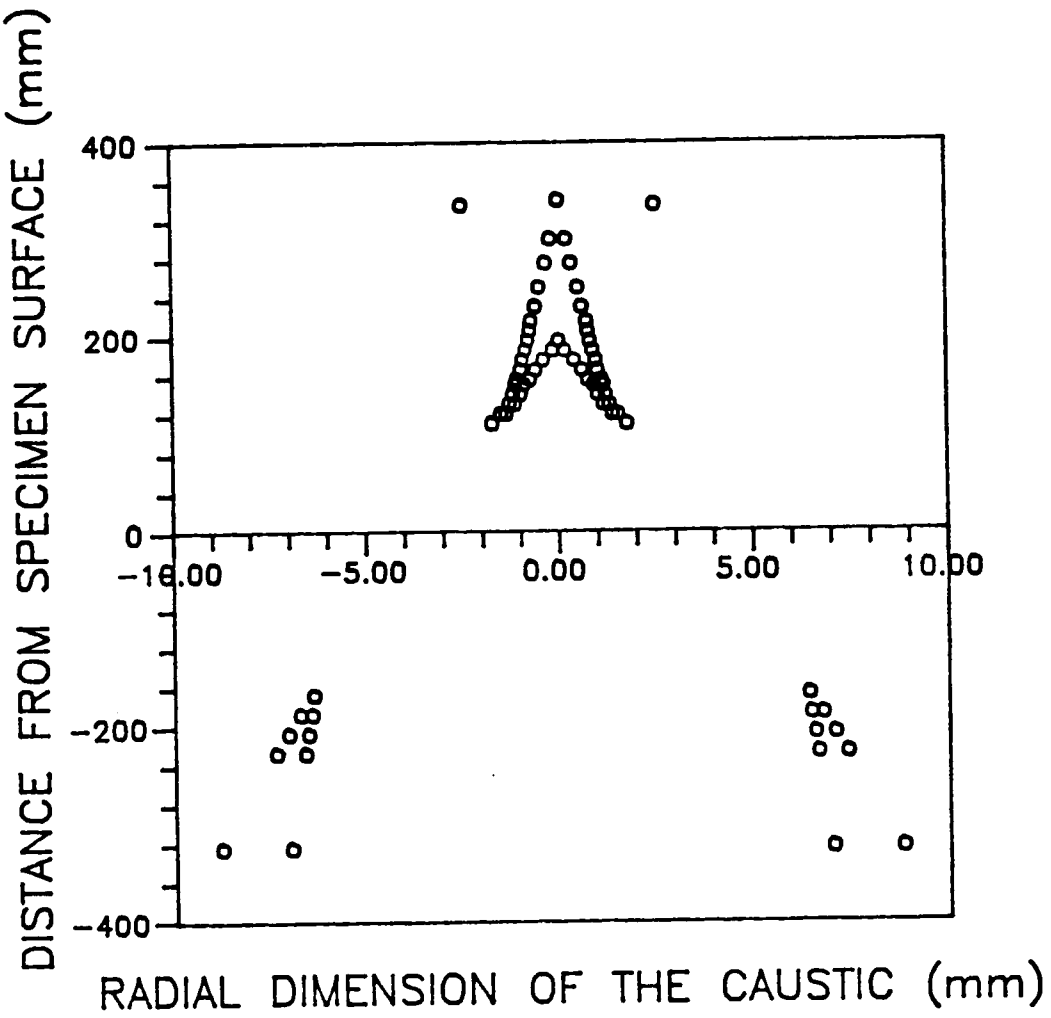


Figure 7.26 Vertical section through the caustic focus recorded in Figure 7.24. Note that the virtual part of the caustic has has been measured.

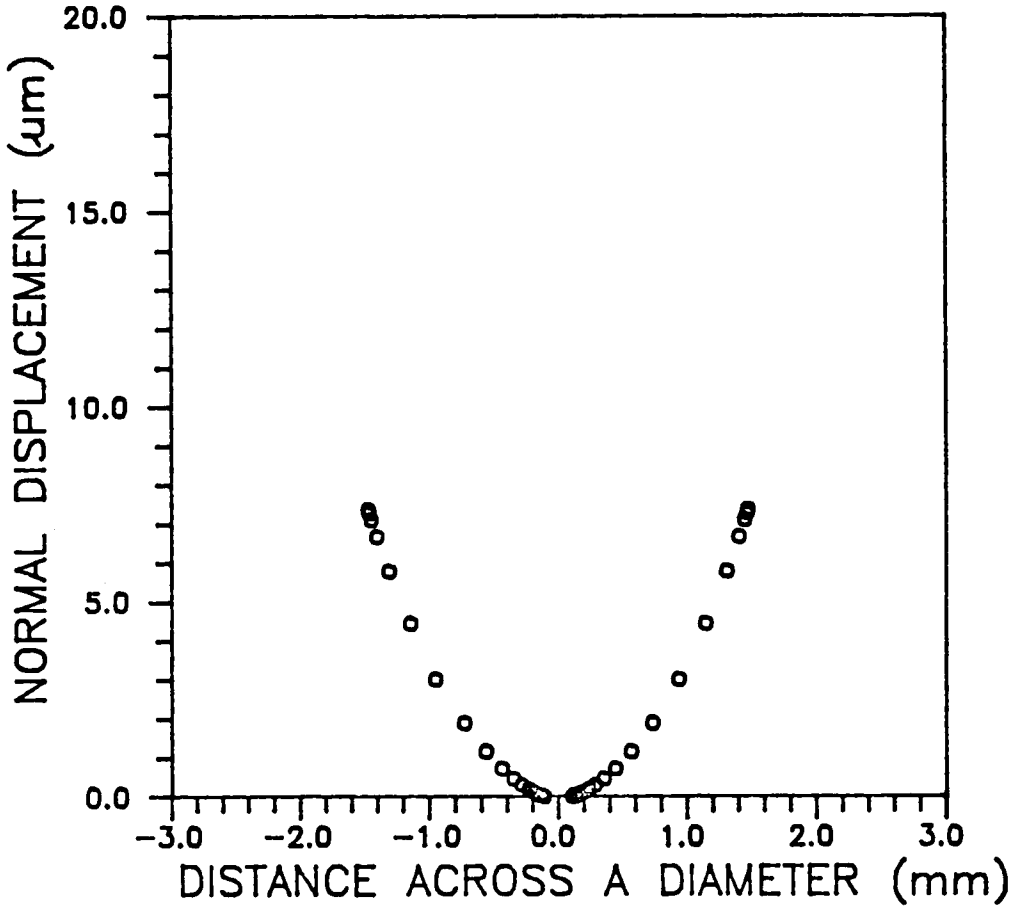


Figure 7.27 Cover slip displacement deduced from the measured caustic geometry presented in Figure 7.24.

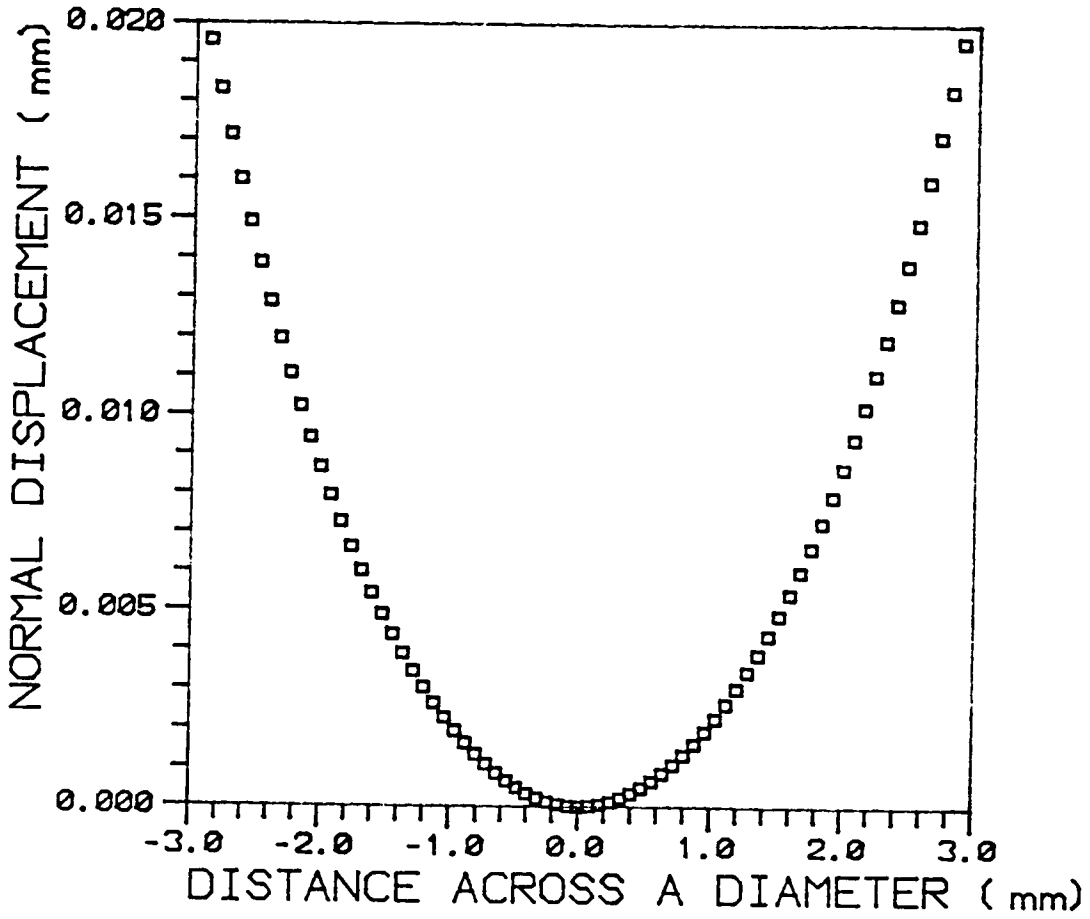


Figure 7.28 Cover slip displacement deduced from the measured caustic geometry presented in Figure 7.25.

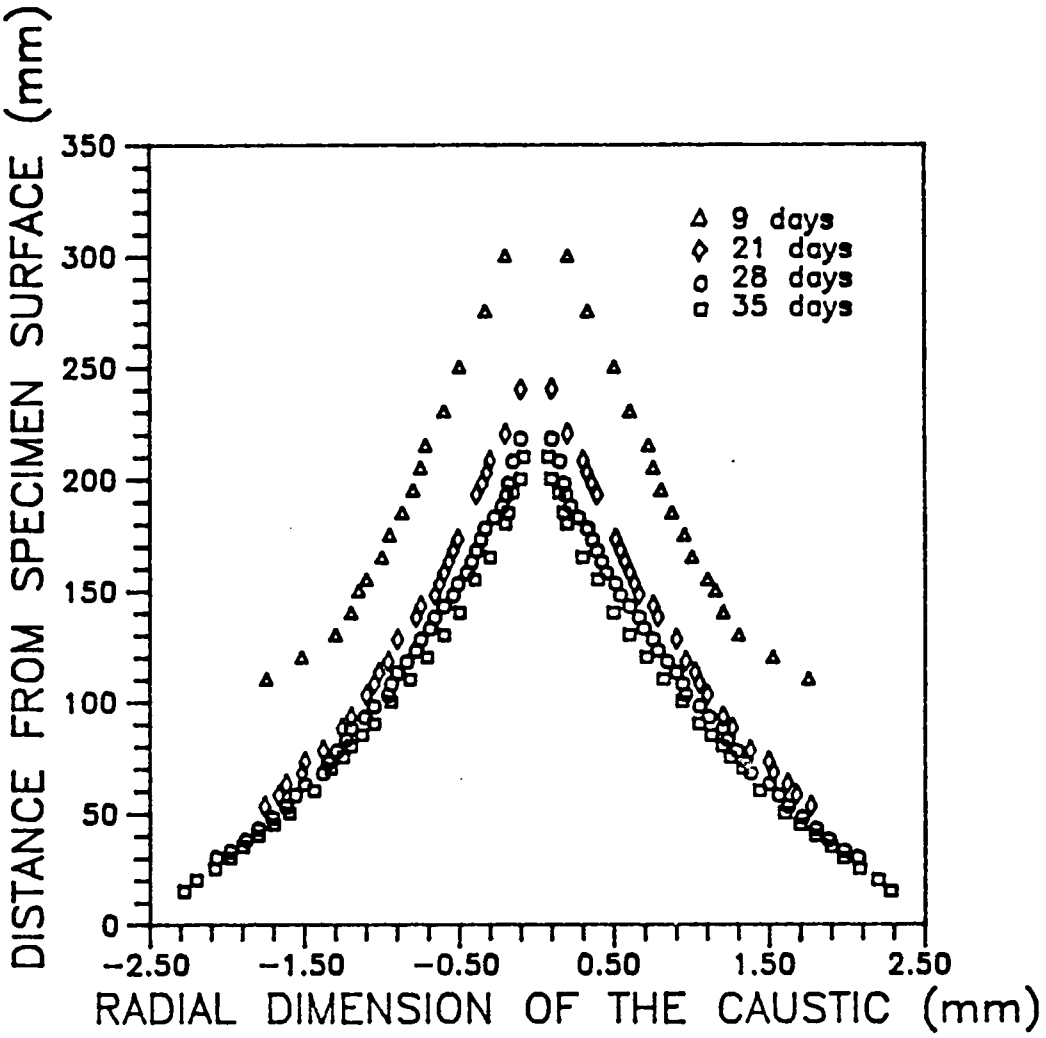


Figure 7.29 Showing how the size of the caustic changes with increasing time of immersion in water at 25°C.

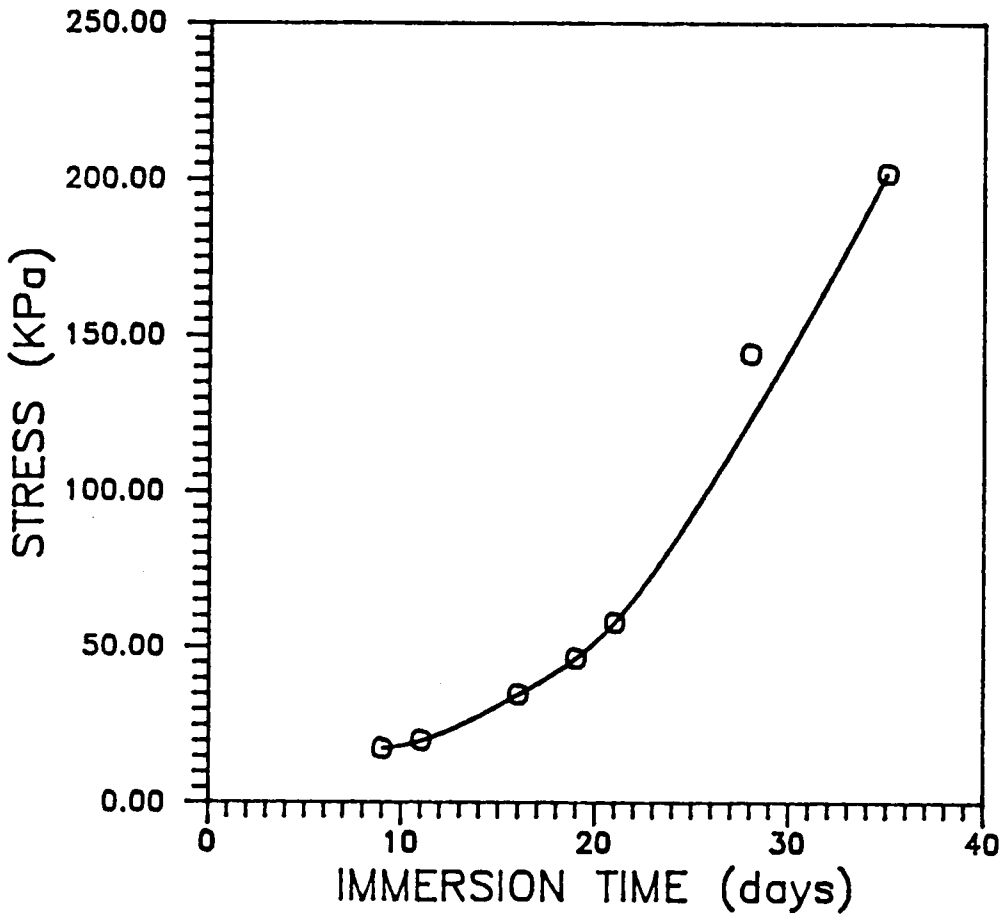


Figure 7.30 The build-up of stress at the center of the cover slip during immersion in water at 25°C.

Figure 7.24 and shown in vertical section in Figure 7.26 contains a real part and two virtual parts. Ray diagrams for each case have been computed and are reproduced in Figures 7.31 and 7.32. Figure 7.32 also shows the respective second differentials of the displacement field, and the respective surface profiles. Note that the two profiles differ only slightly, demonstrating the great sensitivity of caustic foci to the shape of the reflecting surface; small differences in surface curvature cause substantial differences in caustic geometry. This suggests that details of the deformation field very close to a fiber can be investigated using this technique.

Now let us turn to the application of this new technique to measure dimensional changes of polymer coatings on chip on board (COB) components. The technique can be used because of the smoothly curved edges of the coating, in all probability a geometry fortuitously dictated by the wettability of the substrate. It is reflection, by the curved edge to form a caustic focus, that we have successfully exploited in order to measure the surface distortion associated with small water uptake by the coating.

Figure 7.33 shows a computer simulation of a transparent coating illuminated by parallel light that is reflected at the substrate. Consider the effects of all the interfaces between water, coating, an optical flat and air. Correspondence between the points on the coating and in the focus plane S_f, shown in Figure 7.34, is given by

$$U - X = (Z_1 - S)\tan\alpha + Z_2 \tan\beta + Z_3 \tan\gamma \qquad (7\text{-}29)$$

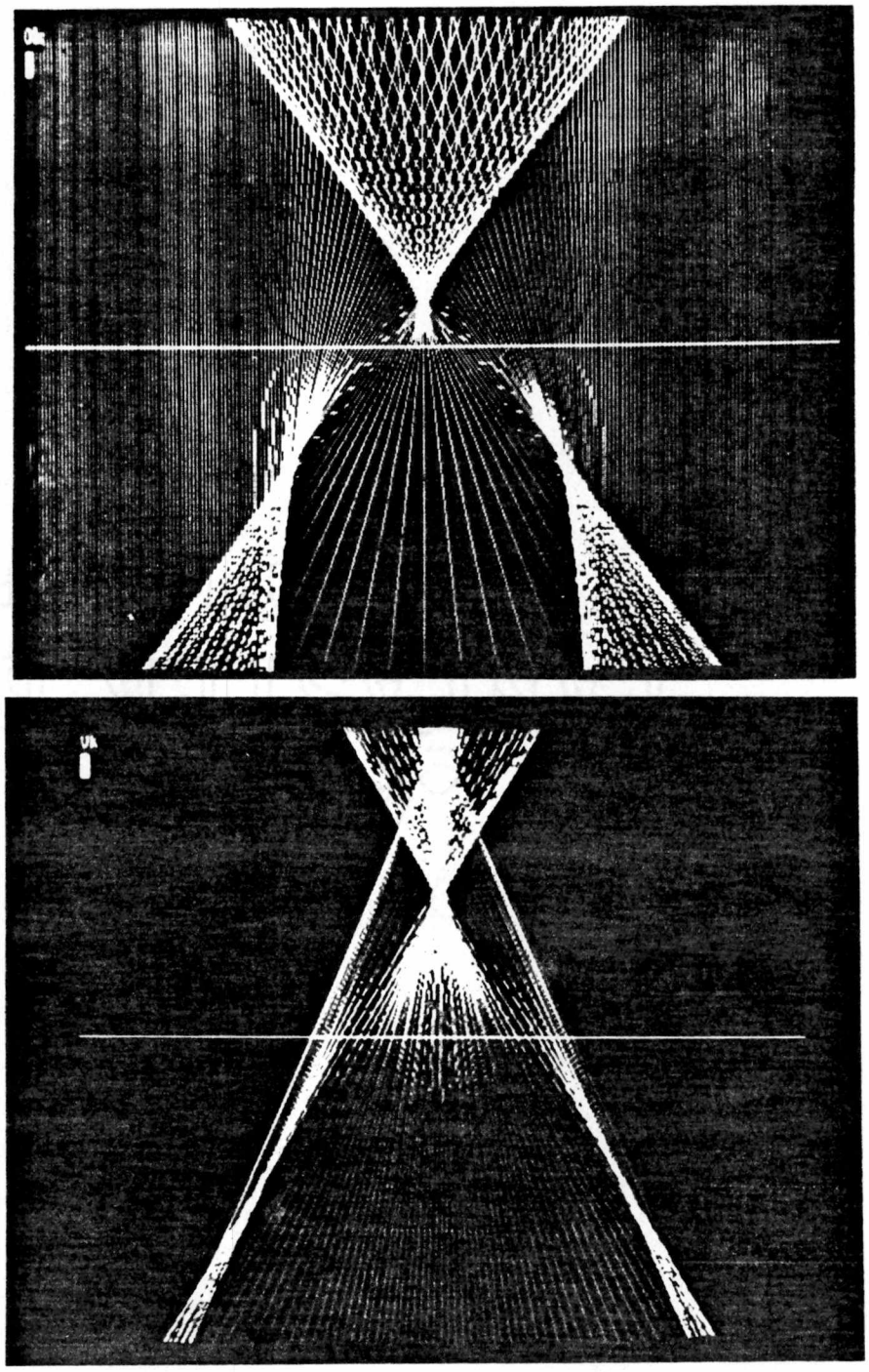


Figure 7.31 The reflected ray diagrams that form caustic foci. The two examples shown here are associated with the different surface geometries, cf. Figure 7.32.

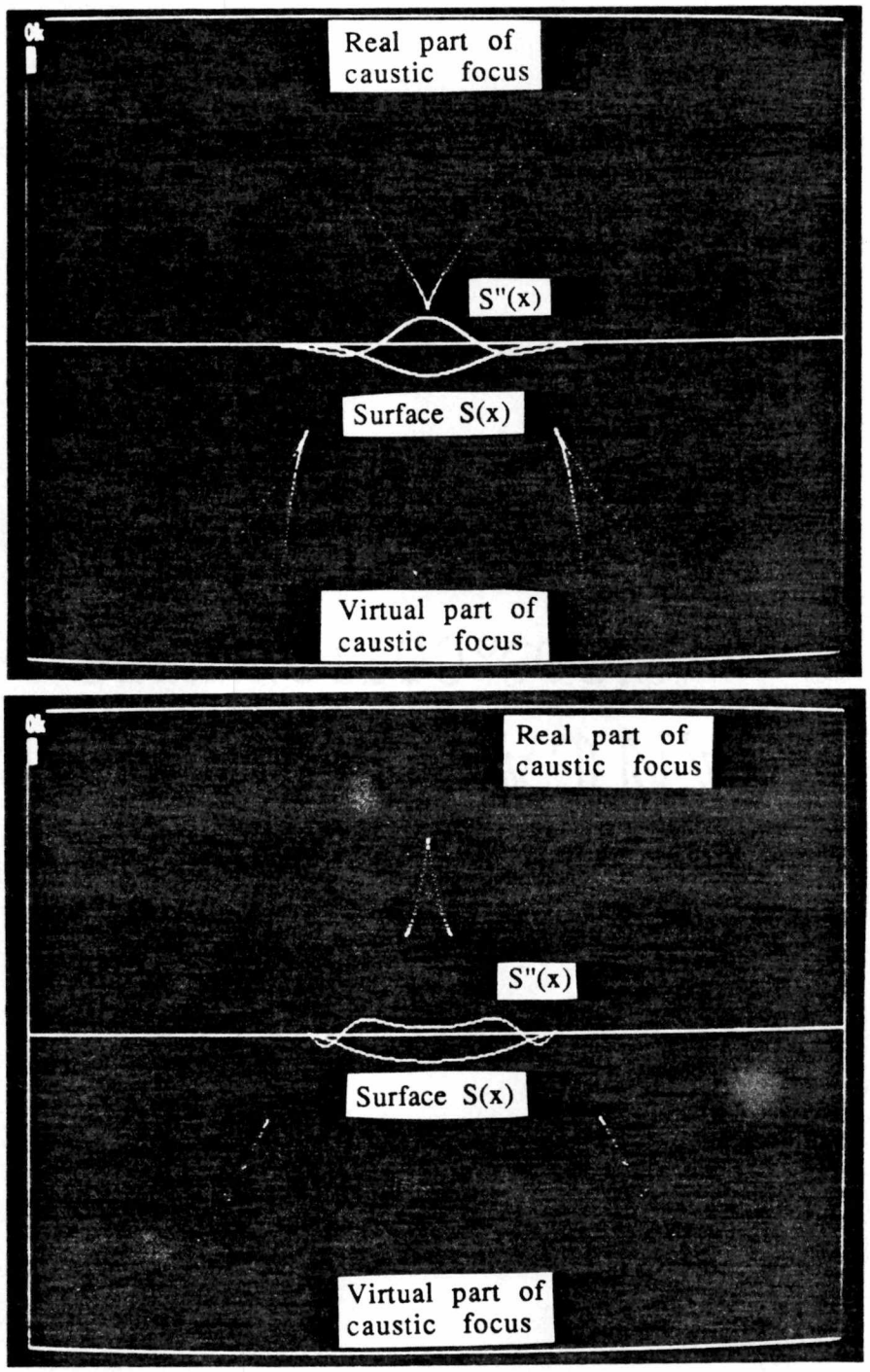


Figure 7.32 Showing the vastly different shape of caustic focus that results from very small differences in profile of the reflecting surface. Note that the 2nd differential is also markedly changed.

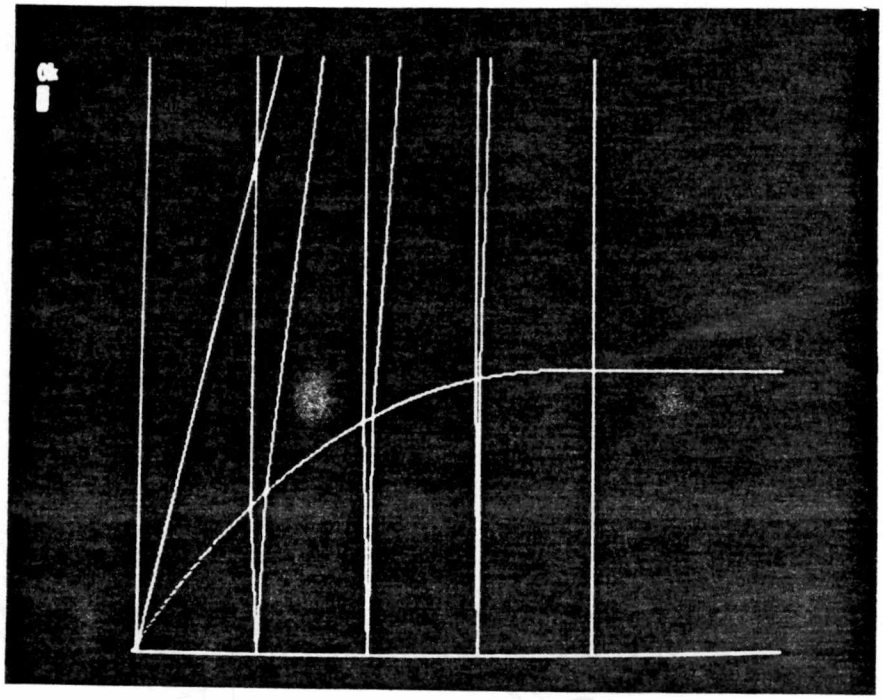


Figure 7.33 Computer simulation showing the propagation of rays through a transparent coating that has a smoothly curved edge.

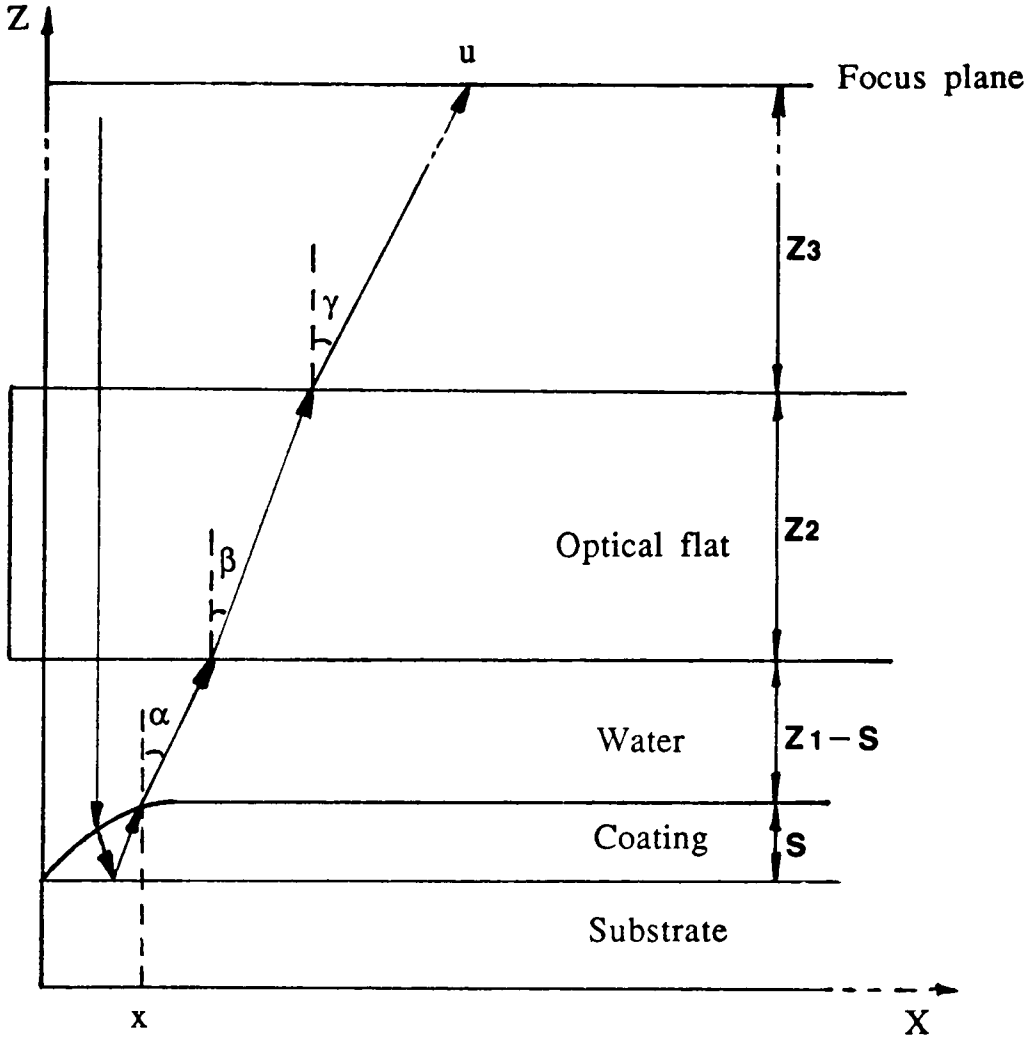


Figure 7.34 Propagation of a ray striking the specimen at normal incidence.

where:

S = the thickness of the coating,

$Z_1 - S$ = the depth of immersion water,

Z_2 = the thickness of the optical plate,

Z_3 = the distance from the optical flat to the caustic focus,

α, β, γ = the refracted angles of the reflected ray at the interfaces.

Using exactly the same approach as before, the equation to the caustic focus can be obtained. The relationship [Appendix B] is given by

$$Z_3 = (-1 - (Z_1 - S)\frac{1}{\cos^2\gamma}\frac{d\gamma}{dx} + \frac{dS}{dx}\tan\gamma + Z_2 R_1 \frac{\sqrt{M}\frac{d\gamma}{dx}\cos\gamma + \frac{R_1 \sin^2\gamma \cos\gamma \frac{d\gamma}{dx}}{\sqrt{M}}}{M})/T \qquad (7\text{-}30)$$

where:

$$T = R_1 R_2 \frac{\sqrt{N}\frac{d\gamma}{dx}\cos\gamma + \frac{R_1 R_2 \sin^2\gamma \cos\gamma \frac{d\gamma}{dx}}{\sqrt{N}}}{N}$$

$$M = 1 - (R_1 \sin\gamma)^2$$

$$N = 1 - (R_1 R_2 \sin\gamma)^2$$

$$R_1 = \frac{n_0}{n_1}$$

$$R_2 = \frac{n_1}{n_2}$$

n_0 = 1.00, n_1 = 1.52, and n_2 = 1.30 are the refractive indices for air, optical flat and water, respectively.

The computer-generated ray diagram and the corresponding caustic focus formed by the protective coating are shown in Figure 7.35. The computed changes of caustic focus associated with uniform swelling due to water absorption are shown in Figure 7.36. For a change in coating thickness from 40 μm, the original thickness, to 44 μm causes the caustic focus to be displaced vertically by 10 mm, an easily detected change. The accuracy of measurement is the same order as discussed previously.

Figure 7.37 shows the geometric relationship between the incident ray, the reflecting surface and the ray emerging from the coating surface. To invert the caustic focus into a surface profile, an assumption has to be made. The relationship between the orientation of the emergent ray and surface profile can be derived as follows. Referring to Figure 7.37,

$$\alpha_1 = \frac{\pi}{2} - \alpha = \frac{\pi}{2} - (\phi_2 - \tan^{-1}(S_{2x})) \qquad (7.31)$$

$$\psi_2 = \theta + \tan^{-1}(S_{2x})$$

$$\theta = \phi_1 - \psi_1$$

$$\phi_1 = \tan^{-1}(S_{1x})$$

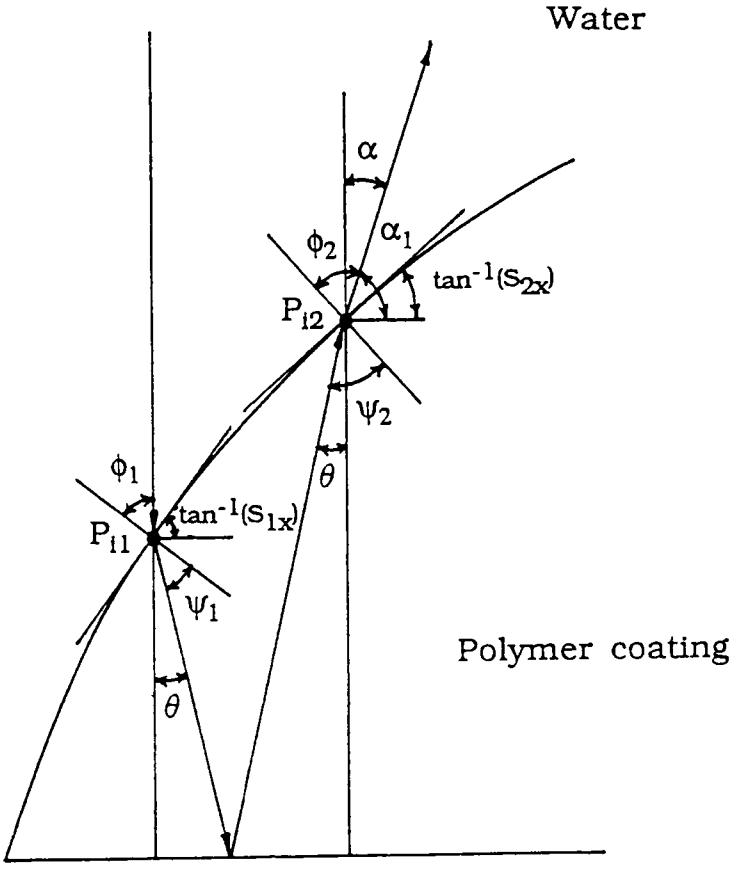


Figure 7.35 The geometry used to deduce Equation (7-35).

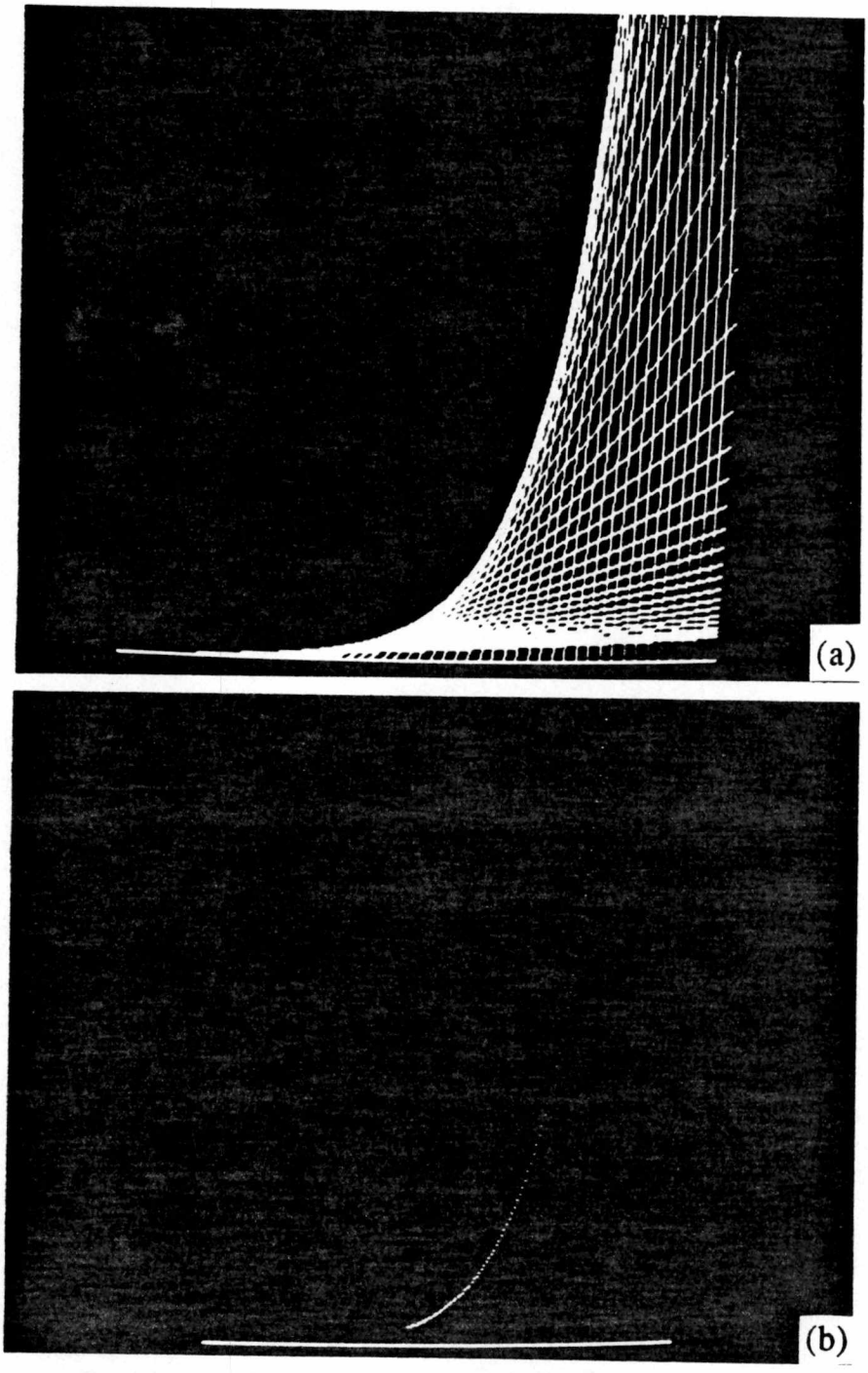


Figure 7.36 The computer generated ray diagram (a) and corresponding caustic focus (b) formed by the protective coating.

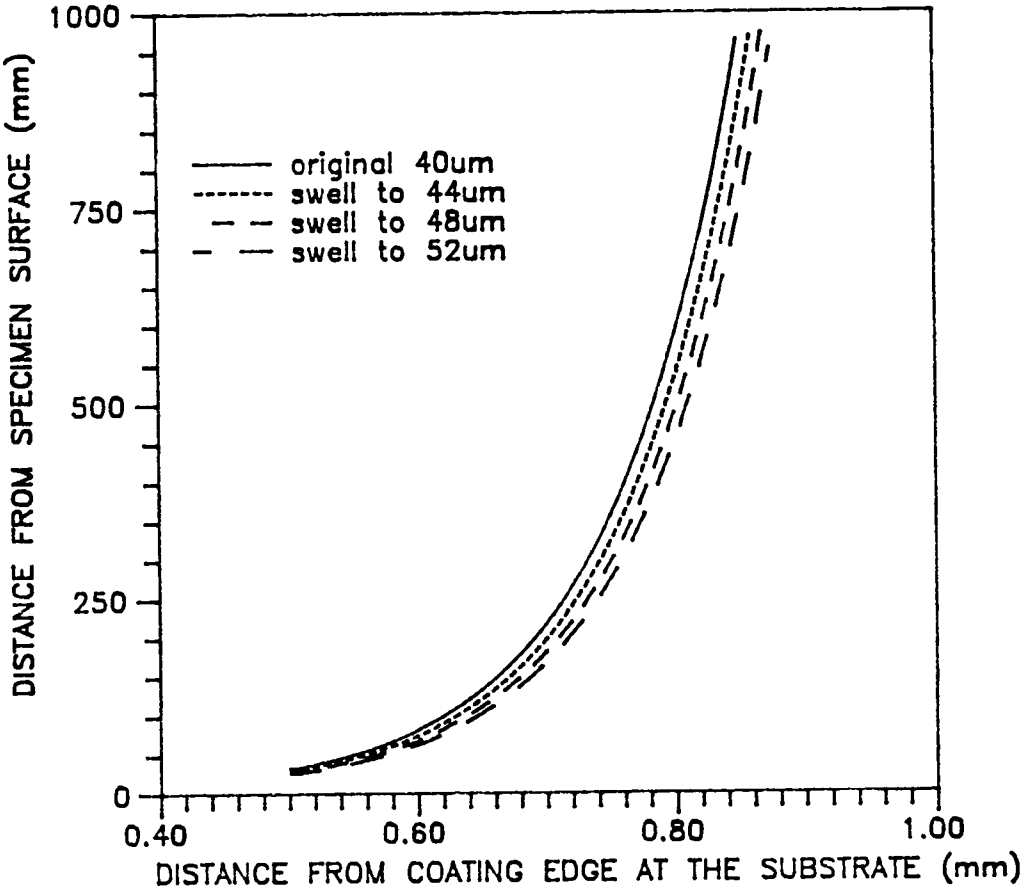


Figure 7.37 Change of caustic associated with uniform swelling of coating during water uptake.

where:

S_{1x}, S_{2x} = the slopes at the points P_{i1} and P_{i2},

thus,

$$\psi_2 = \tan^{-1}(S_{1x}) - \psi_1 + \tan^{-1}(S_{2x}) \tag{7-32}$$

Using Snell's Law,

$$\frac{\sin\psi_2}{\sin\phi_2} = \frac{n_2}{n_3}, \quad \frac{\sin\phi_1}{\sin\psi_1} = \frac{n_3}{n_2}$$

where n_3 is the refractive index for polymer coating,

one obtains

$$\psi_1 = \sin^{-1}\left(\frac{n_2}{n_3} \sin(\tan^{-1}(S_{1x})) \right) \tag{7-33}$$

$$\phi_2 = \sin^{-1}\left(\frac{n_2}{n_3} \sin \psi_2 \right) \tag{7-34}$$

Substituting Eqs. (7-32), (7-33) and (7-34) into Eq. (7-31),

$$\gamma = \frac{\pi}{2} - \left(\sin^{-1}\left(\sin(\tan^{-1}(S_{1x}) - \sin^{-1}\left(\frac{n_2}{n_3} \sin(\tan^{-1}(S_{1x})) \right) \right. \right.$$
$$\left. \left. + \tan^{-1}(S_{2x}) \right) \frac{n_3}{n_2} \right) + \tan^{-1}(S_{2x}) \tag{7-35}$$

Since the coating thickness is very small, about 30-40μm, the points, P_{i1} and P_{i2}, defined by the incidence and emergence of ray i (refer to

Figure 7.35), are sufficiently close together for their slopes to be regarded as approximately equal. With this approximation, the slope at P_{i2} can be calculated from the caustic focus.

As pointed out, this method can be used to measure very small displacements at the center of the reflecting surface, as small as 10nm. Also, since the caustic focus is directly related to the second differential of displacement of the reflecting surface, this method offers significant advantages when the stresses (for a thin plate, they are given by the fouth differential of its displacement, see Eq. (5-1)) normal to the specimen surface is to be studied.

CHAPTER VIII

RESULTS AND DISCUSSION

8.1 Water uptake

8.1.1 Dimensional changes of epoxy resin during fabrication and during water uptake

In order to interpret effects arising from water immersion, it is important to know the dimensional changes undergone by resin during water immersion. Measurements of linear dimensional changes were made on epoxy films containing no fibers. Any dimensional changes of the mold during specimen fabrication, were found to be too small to be detected. Hence the net dimensional changes of the epoxy resin after curing can be measured in situ, as shown in Figure 8.1. It turns out that the resin linear shrinkage generated during fabrication is about 0.43% ((20.000 - 19.914)/20.000 = 0.43%).

Experimental measurements of changes in linear dimensions during water immersion for specimens containing no fibers, see Figure 8.2, demonstrate that the resin swelling is much greater than the resin shrinkage generated during fabrication. Since fiber can be assumed to be dimensionally stable relative to resins, it is evident that swelling of the epoxy matrix must be restrained by the fibers embedded in a composite. The overall result is that the volumetric swelling of the matrix produces tensile stress in fiber and axial compressive stress in matrix around fiber, both of which are along the fiber direction as discussed late.

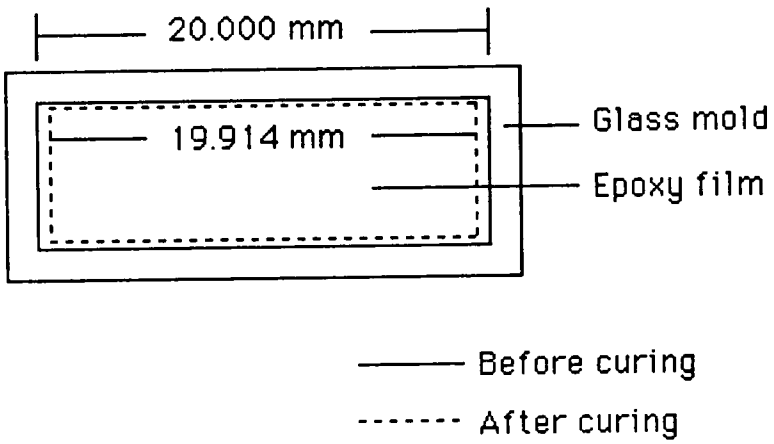


Figure 8.1 Schematic of the shrinkage of epoxy after curing and the measurement of linear dimensional change.

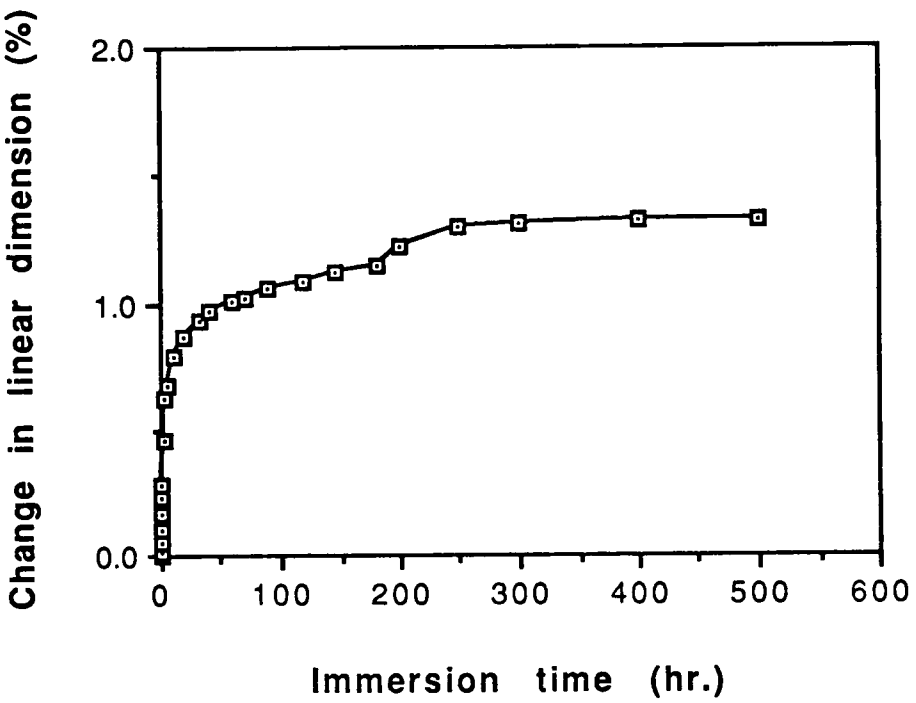


Figure 8.2 Linear dimensional changes of the neat epoxy resin during immersion in distilled water at boiling temperature. Measurements were made at room temperature.

8.1.2 The change in state of stress of epoxy resin due to volumetric swelling associated with water uptake

The volumetric swelling of epoxy resin caused by water uptake will lower the density of epoxy resin. The change of its density will change the speed of the light, i.e., the index of refraction of that medium, since the frequency of the absorption and emissions of light by atoms changes [Hecht 1987]. These physical phenomenon were employed to identify the densification in deformation of glass [Ernsberger 1968, Mackenzie 1965]. Since epoxy resin is a birefringent material, the volumetric swelling results in changes in the indices of refraction in two perpendicular directions for the two dimensional case (thin epoxy resin film). This effect has been used here to study the effects of surface treatments of carbon fiber on water uptake by the matrix resin.

As mentioned above, the change from shrinkage resulting from curing, to expansion resulting from water uptake, can be detected by observing the changes in the directions of the optical axes of epoxy resin samples. Thus, the water uptake phenomenon causing volumetric swelling can, by way of the changes in the directions of the optical axes, be qualitatively studied.

Measurement for the five specimens, see Figure 8.3, indicate that the times needed for specimens to change from a state of shrinkage to expansion at the position near the fiber ends are almost same. Thus the effects of surface treatment of the fibers on the water uptake by the matrix resin can be neglected.

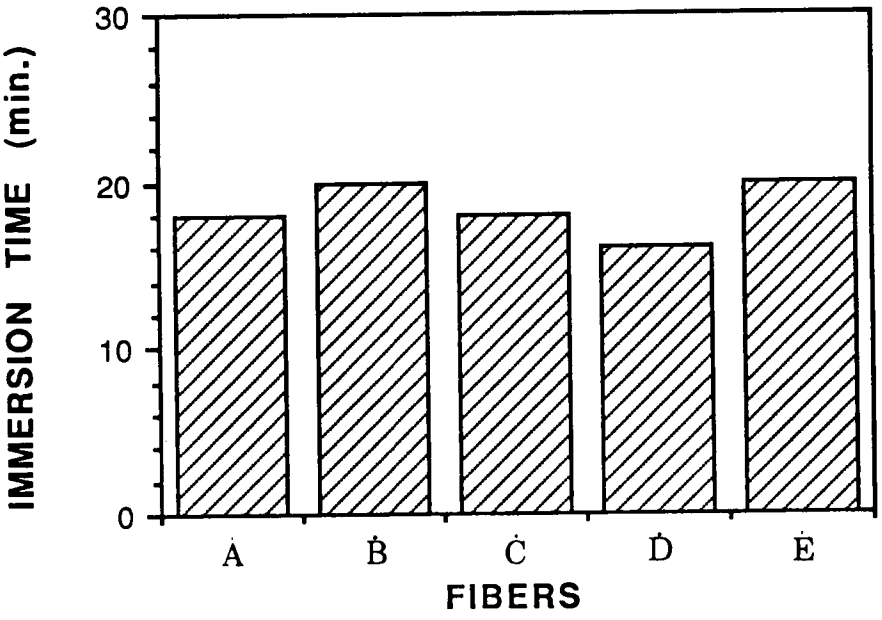


Figure 8.3 The time needed for specimens to change from a state of compression to tension at point near the fiber end.

8.1.3 Moisture expansion and water uptake by a model composite

Figure 8.4 shows the development of a sequence of moire fringe loops during water immersion of a cylindrical specimen with axial fiber with cover slip bonded to one end. The moire fringes (circular loops originally seen only in the outer regions of the specimen) migrate towards the center of the cylinder. The number of moire fringes increases with increasing time of immersion. The displacement along the z-axis of the specimen, measured across a diameter in Figure 8.4, is plotted in Figure 8.5.

Consider the dimensional changes measured by our method. We assume that swelling in the radial direction is negligible compared with that in the axial direction; this assumption is justified by the fact that the specimens have large (>6) length/radius ratio. Then the overall volumetric swelling can be obtained by integrating the area of the transverse section, thus,

$$\int_0^{2\pi} \int_0^{a} f(r)\, r\, dr\, df \qquad (8\text{-}1)$$

where:

a = the radius of the specimen,

f(r) = displacement field.

The integrations are made using Simpson's method.

Typically data for volumetric swelling swelling volume, so obtained from the displacement data in Figure 8.5, are shown as a function of immersion time, t, in Figure 8.6. In Figure 8.7, the

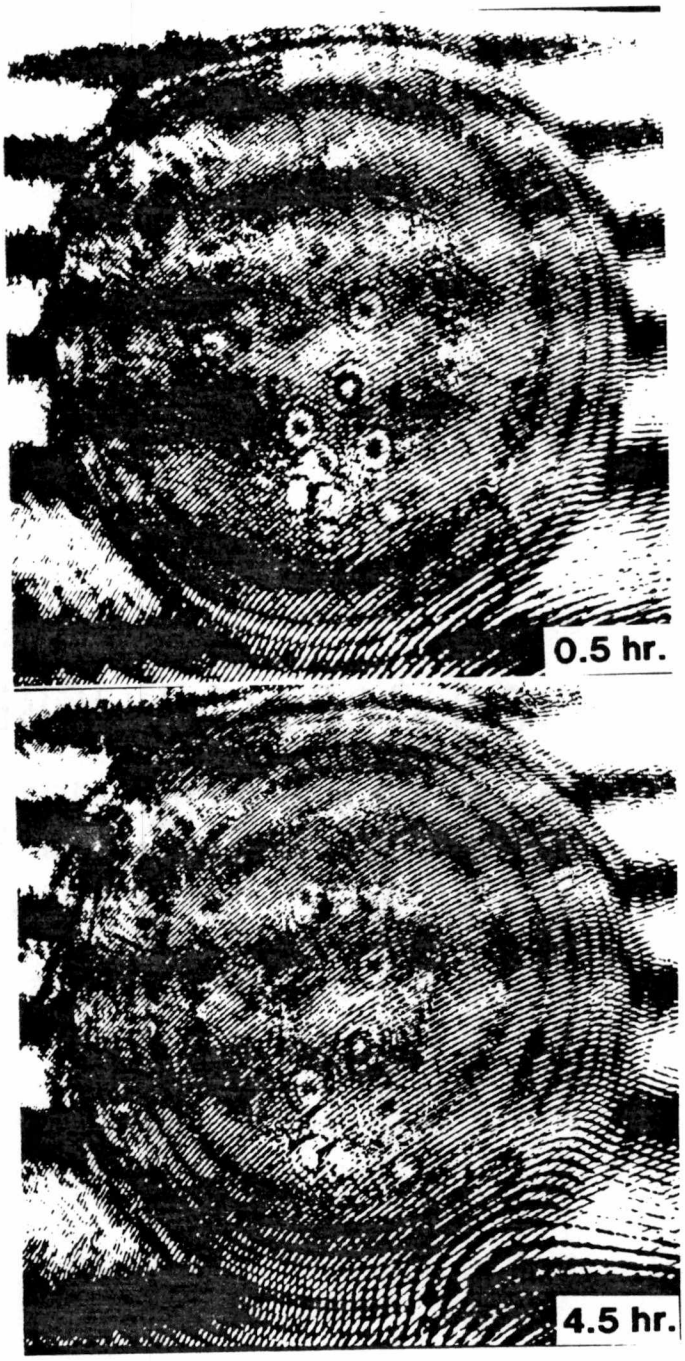


Figure 8.4 Moire fringe loops created by superimposing on the initial interference pattern, the same pattern photographed at subsequent intervals during water immersion at 24.6°C.

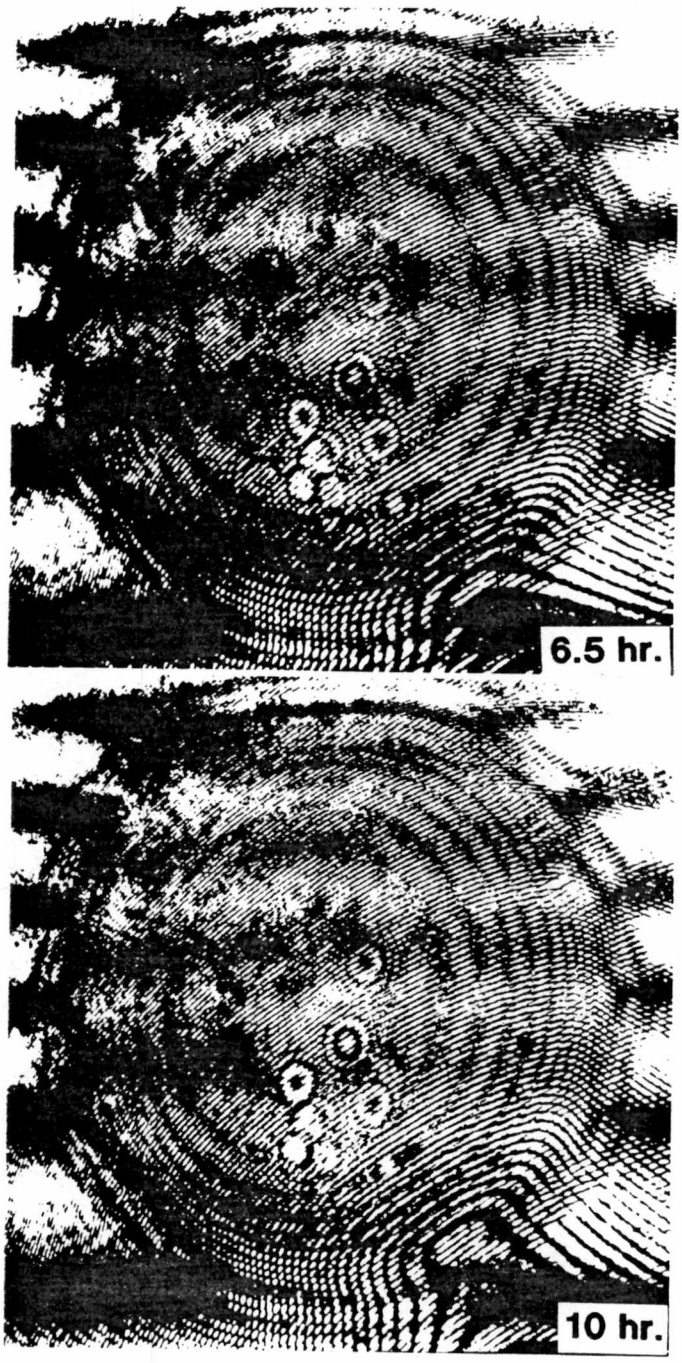


Figure 8.4 Continued.

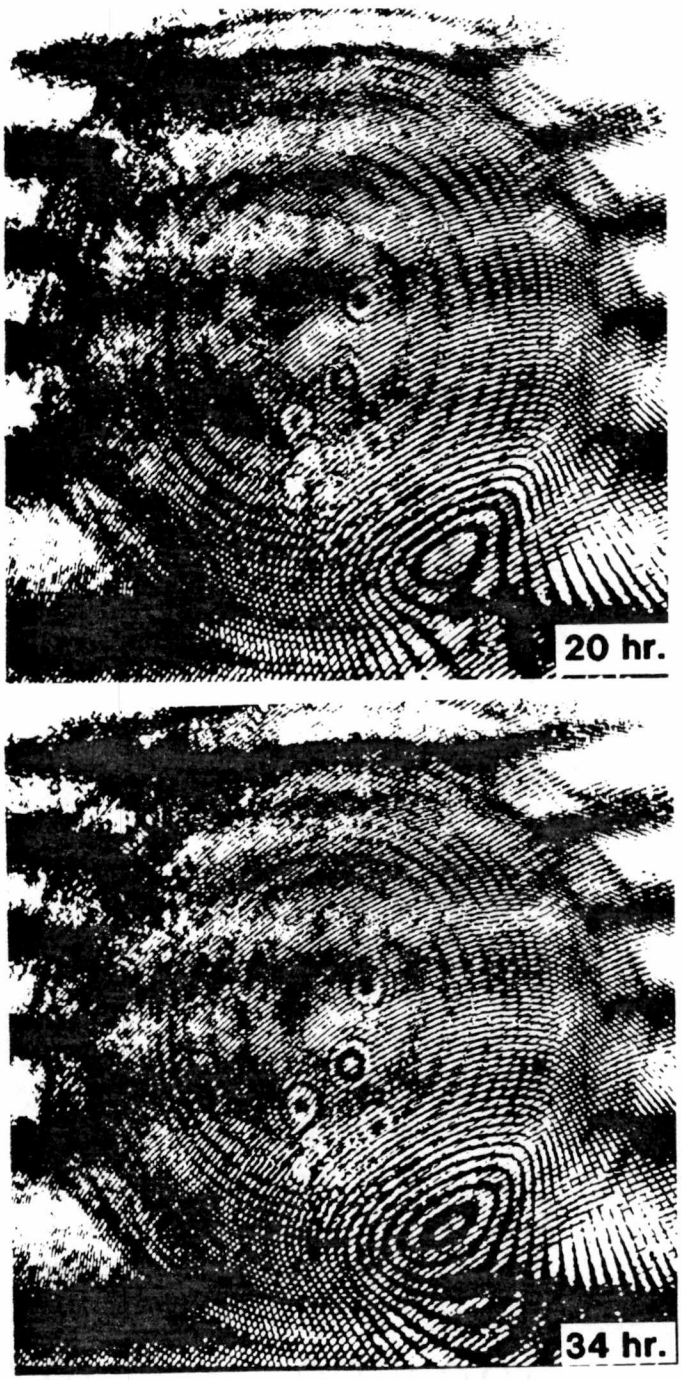


Figure 8.4 Continued.

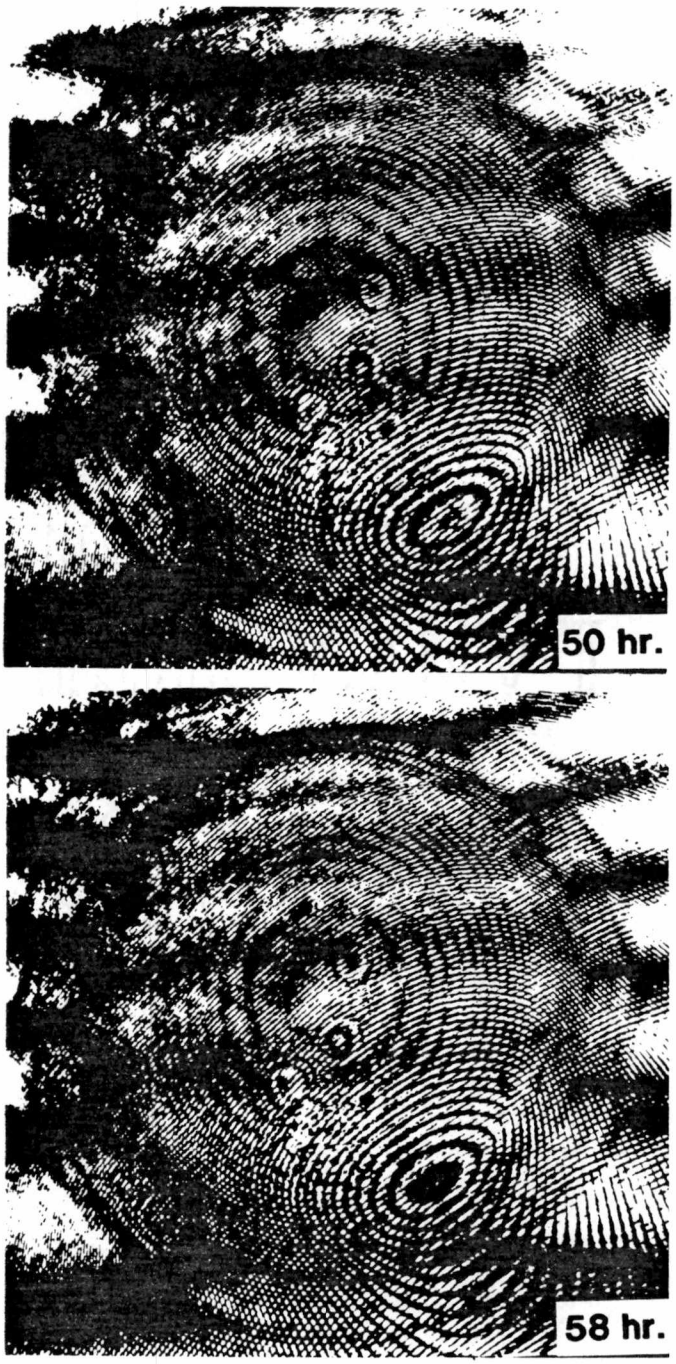


Figure 8.4 Continued.

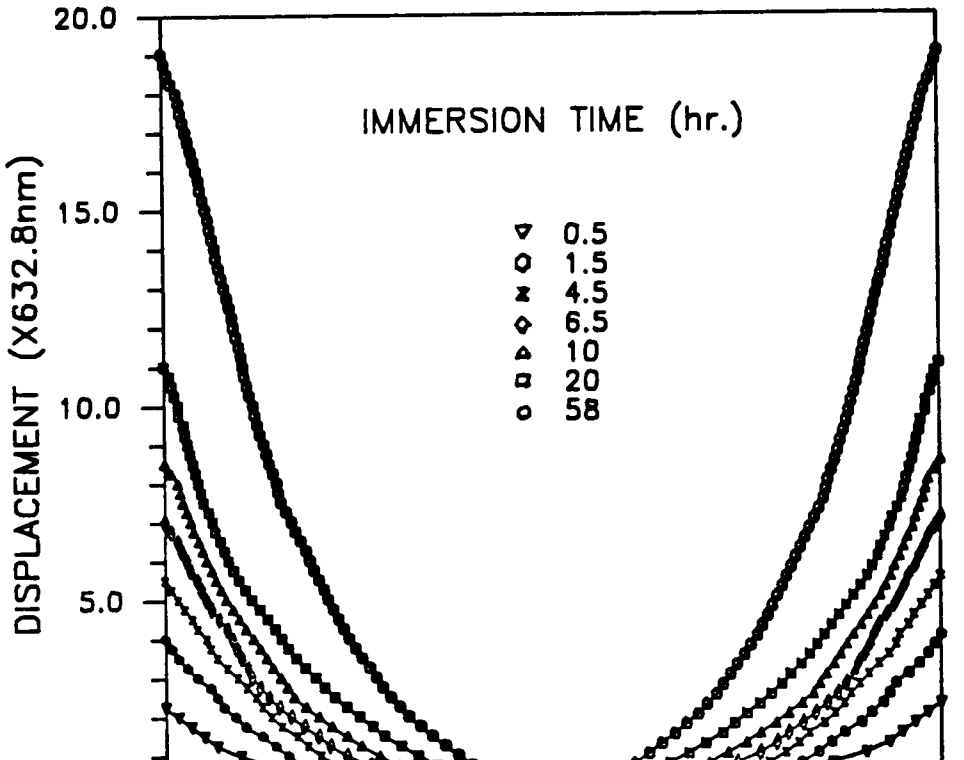


Figure 8.5 Normal displacement measured across a diameter in Figure 8.4.

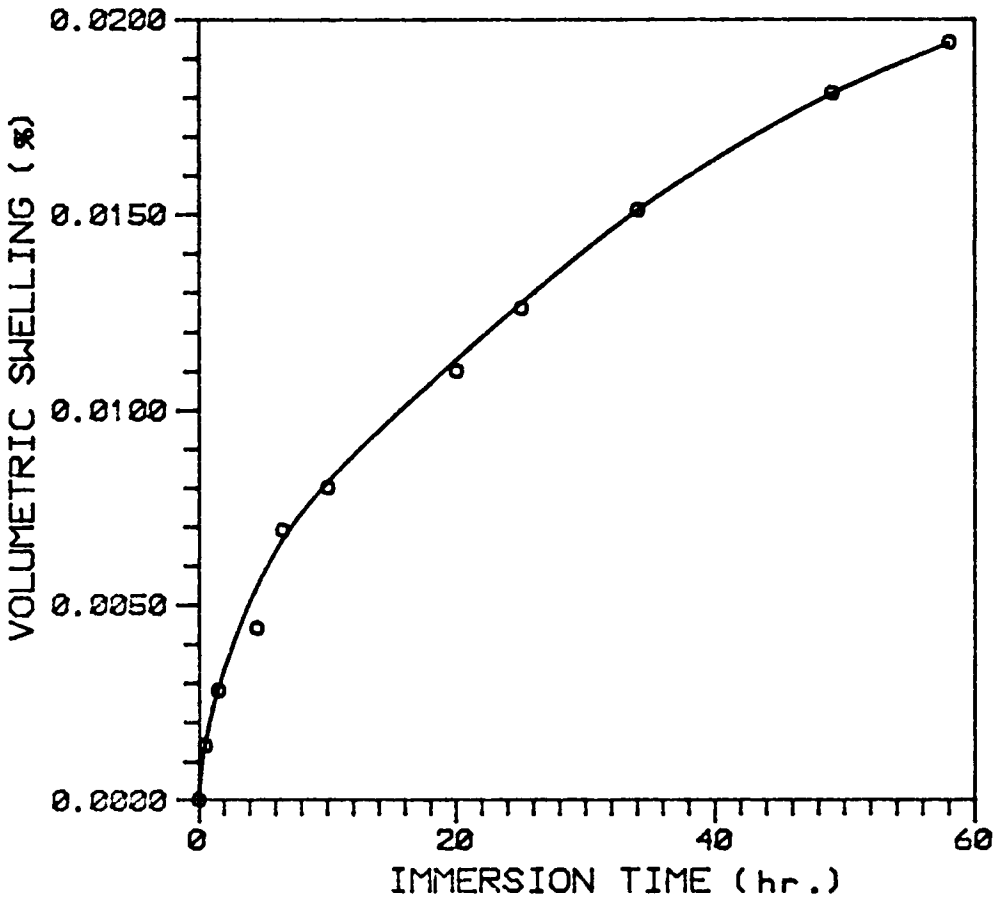


Figure 8.6 Volumetric swelling versus immersion time.

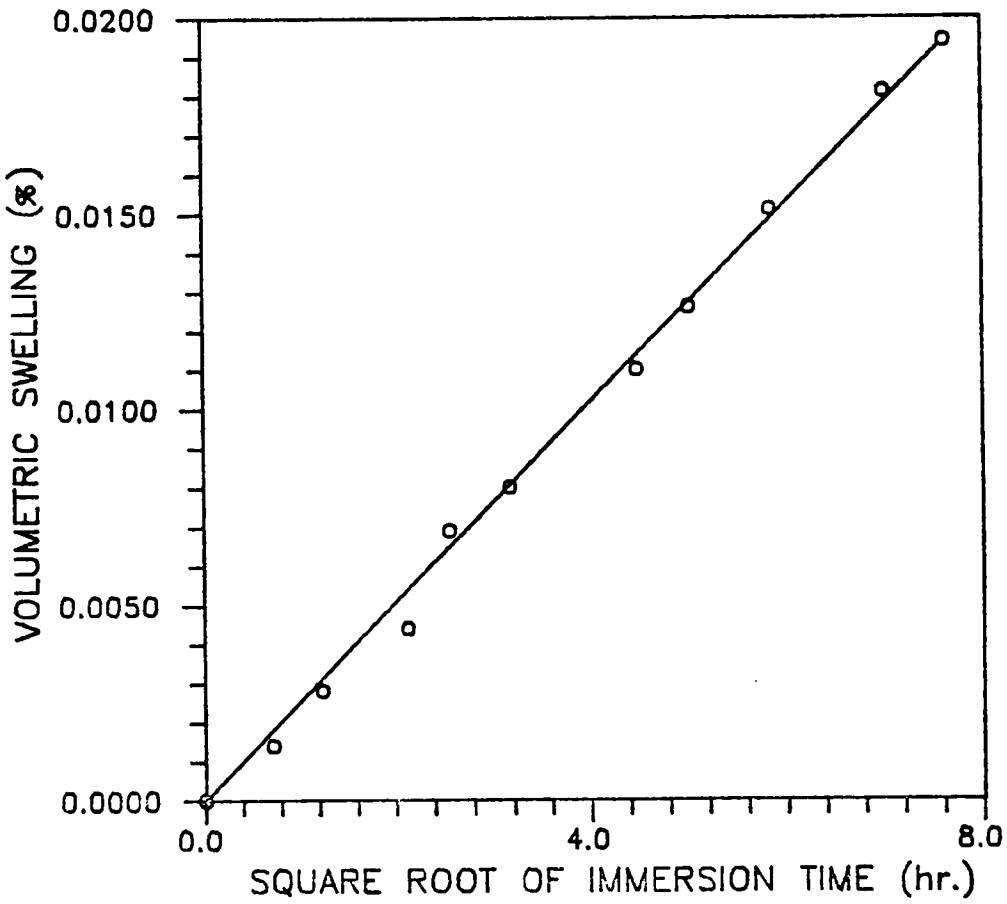


Figure 8.7 Volumetric swelling versus square root of immersion time.

volumetric swelling is replotted, versus the square root of immersion time. A linear relationship between the swelling volume and $\sqrt{t}$ is expected if swelling is governed by Fickian Diffusion (second law) of water, i.e., if the volume is linearly proportioned to water concentration,

$$V\% = A\sqrt{t} \tag{8-2}$$

Referring to Eq. (5-4), the total amount of water absorbed, M_t, at immersion time, t, by the specimen can be obtained by integration

$$M = \int_0^{2\pi} \int_0^{a} C(r, t)\, r\, dr\, df \tag{8-3}$$

where:

C(r,t) = a function of the moisture concentration.

In a cylindrical specimen of large length to radius ratio, swelling in the axial direction is expected to be a linear function of swelling strain, ε, in that direction, e.g. $V \propto \varepsilon$. So

$$\begin{aligned} V &= 0 && M_t \le M_0 \\ V &= B'(M_t - M_0) && M_t > M_0 \end{aligned} \tag{8-4}$$

Where:

V = swelling volume,

B' = coefficient of moisture swelling,

M_0 = a threshold water absorption.

For some composites and neat resins, M_0 may vanish in which case the swelling is linear with water uptake, up to full saturation.

Figure 8.8 is a plot of volumetric swelling versus the water content for our specimen; the relationship is evidently of the form of Eq.(8-4) where $M_0 = 0$. Here, the amount of water uptake was obtained from measurement of weight gain.

In the case of a cylindrical specimen with axial dimension large compared with the radius, diffusion of water molecules is essentially one dimensional radial in nature and the diffusion equation becomes

$$\frac{dc}{dt} = \frac{1}{r}\frac{d}{dr}\left(r D \frac{dc}{dr}\right) \tag{8-5}$$

In a cylinder of radius a, the boundary conditions are

$$\begin{aligned} C &= C_0, \qquad r = a,\ t \geq 0 \\ C &= C_i, \qquad 0 < r < a,\ t = 0 \end{aligned} \tag{8-6}$$

and if M_t denotes the mass of water that has entered the resin in time t and M_∞ the corresponding quantity after time ∞, then one corresponding solution to Equation (8-5) is

$$\frac{M_t}{M_\infty} = 1 - \sum_{n=1}^{n} \frac{4}{a^2 \alpha_n^2} \exp\left(-D \alpha_n^2 t\right) \tag{8-7}$$

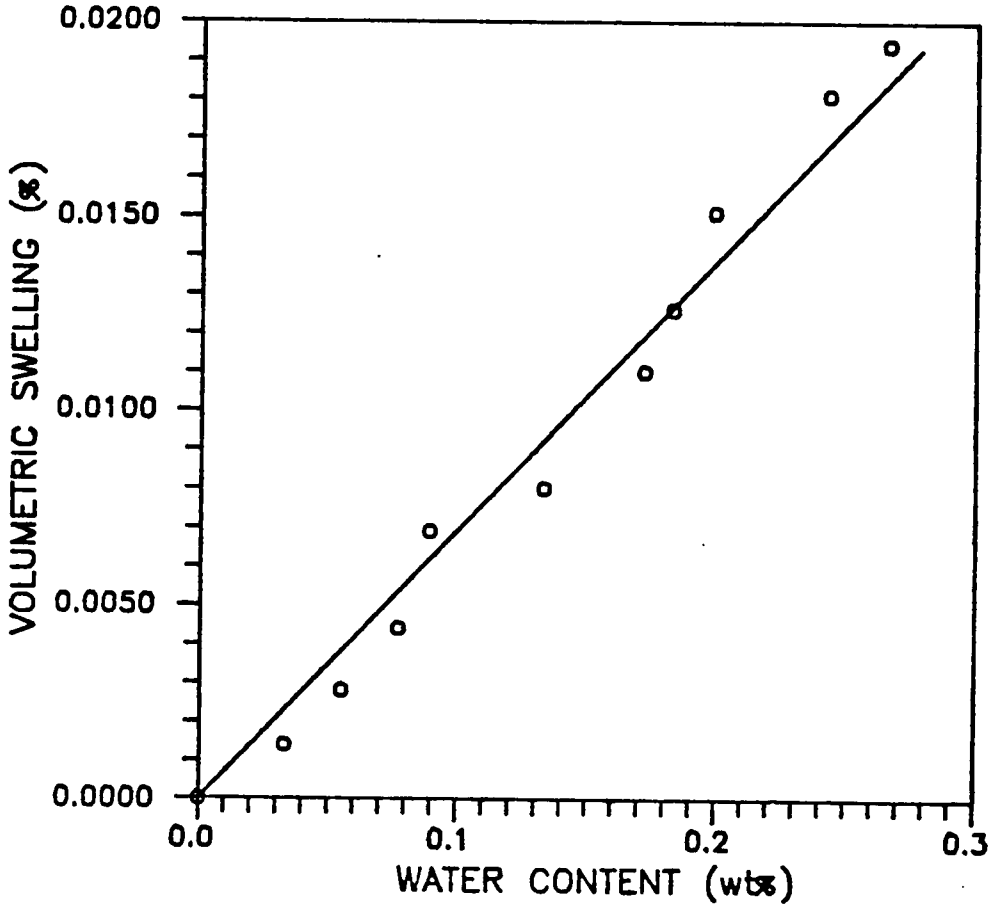


Figure 8.8 The linear relationship between volumetric swelling and water content.

where:

α_ns = the positive roots of the Bessel's function $J_0(a\ \alpha_n) = 0$.

Another solution to Eq.(8-5) for the boundary conditions defined in Equation (8-6), is

$$\frac{Mt}{M_\infty} = \frac{4}{\sqrt{\pi}}\sqrt{(\frac{Dt}{a^2})} - \frac{Dt}{a^2} - \frac{1}{3\sqrt{\pi}}\sqrt[3]{\frac{Dt}{a^2}} \qquad (8\text{-}8)$$

This equation best describes the process at small times, while Eq. (8-7) is better for moderate and large times. The value of D can be deduced from the initial gradient of a graph of $\frac{Mt}{M_\infty}$, that is,

$$\frac{Mt}{M_\infty} = \frac{4}{\sqrt{\pi}}\sqrt{(\frac{Dt}{a^2})} \qquad (8\text{-}9)$$

As discussed previously and shown in Eqs. (8-2) and (8-4), Eq. (8-9) can be rewritten as

$$V = B'\ M_\infty \frac{4}{r}\sqrt{\frac{D}{\pi}}\sqrt{t} \qquad (8\text{-}10)$$

where the diffusion coefficient

$$D = (\frac{Ar}{4B'M_\infty})^2\pi \qquad (8\text{-}11)$$

B' and M_∞ are constants for a given material under constant

conditions.

Using a linear regression method to find A and B' in Eqs. (8-2) and (8-4) respectively at the initial stage, and measuring M_∞, and then substituting into Eqs. (8-6) and (8-10), the apparent diffusion coefficient can be evaluated. For the data reported here, it is

$$D = 2.5 \times 10^{-8} \ (cm^2/s)$$

It can be shown from the Boltzman Solution of Fick's laws [Lefebvre et al. 1989] that this method for determining D can be used when D is dependent upon concentration for the diffusing species.

Eq. (8-7) is plotted in Figure 8.9 using as diffusion coefficient the value calculated above. Evidently, there is good correlation between calculated and measured moisture content at small time.

In deriving Eqs. (8-7) and (8-8) it was assumed that the radius of the cylinder remains constant as diffusion proceeds. In practice this is demonstrably not the case; the cylinder swells.

8.2 Effects of water uptake on stress-optical coefficient of epoxy resin

As discussed in the Chapter VI, when using photoelastic analysis, it is necessary to know the stress-optical coefficient of the materials studied. In order to investigate the moisture induced degradation of composites by means of photoelasticity analysis, the effects of water uptake on the stress-optical coefficient of matrix materials must be known. Measurements for two epoxy resins used in the present

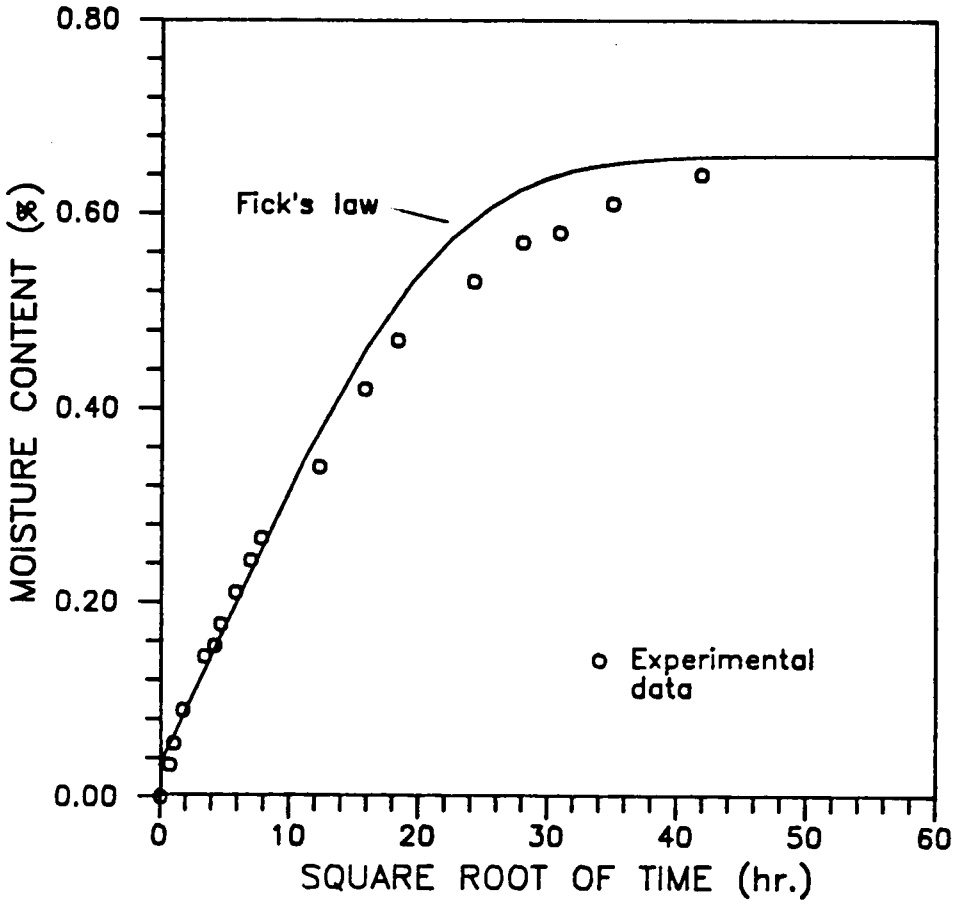


Figure 8.9 Experimental data fitted to Fick's law using the diffusion coefficient evaluated from the measurement of volumetric swelling.

research have been made. Figures 8.10 and 8.11 show measurements of optical retardation vs. tensile stress applied uniaxially on specimens of neat epoxy resin. The linear relationships between retardation and stress did not change during water immersion up to 300 hours. That the straight lines for each specimen of different epoxy resin, Figures 8.10 and 8.11, have almost same slopes, which indicates that the stress-optical coefficient for each specimen is constant, i.e., water uptake does not affect the stress-optical coefficients of these epoxy resins. This can be explained as follows.

The theory which relates the changes in index of refraction to the state of stress is due to Maxwell. Maxwell [1853] noted that the changes in indices of refraction were linearly proportional to the stresses induced in the material and followed the relationships

$$n_1-n_0 = \begin{vmatrix} c_1 & -c_2 \\ \sigma_2 & \sigma_1 \end{vmatrix}$$

$$n_2-n_0 = \begin{vmatrix} c_1 & -c_2 \\ \sigma_1 & \sigma_2 \end{vmatrix} \qquad (8\text{-}12)$$

Where:

n_0 = index of refraction of the stress-free specimen,

n_1, n_2 = indices of refraction along the two principal axes associated with σ_1 and σ_2, respectively,

c_1, c_2 = stress-optical coefficients,

σ_3 = assumed to be zero in this instance.

A stressed photoelastic material behaves like a temporary wave

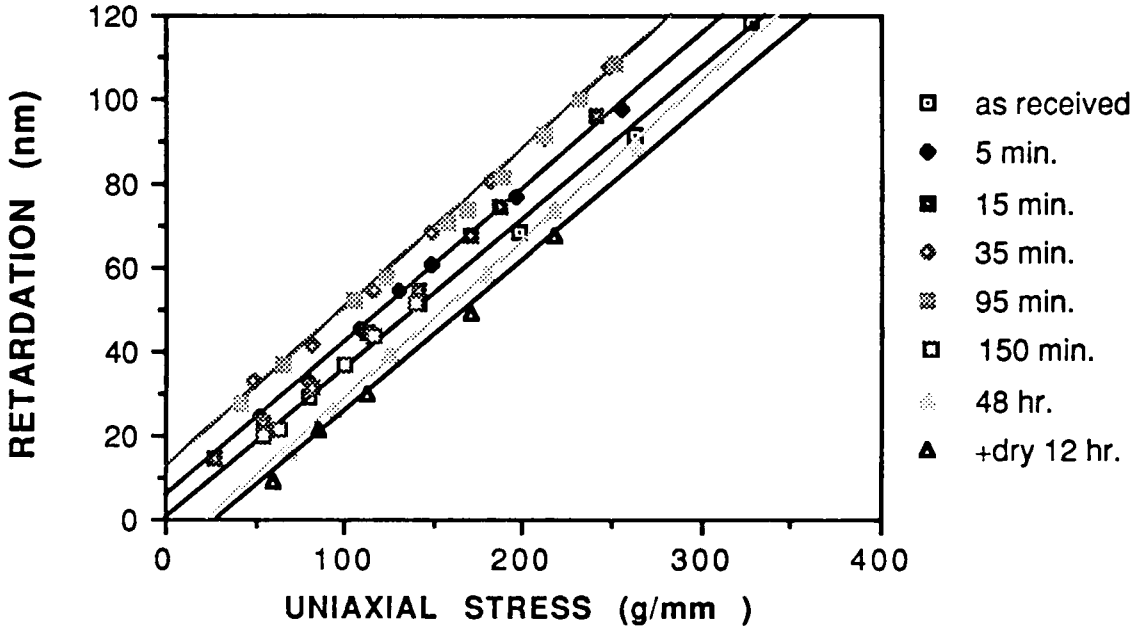


Figure 8.10 Retardation measured versus tensile stress applied uniaxially on a specimen of neat epoxy resin.

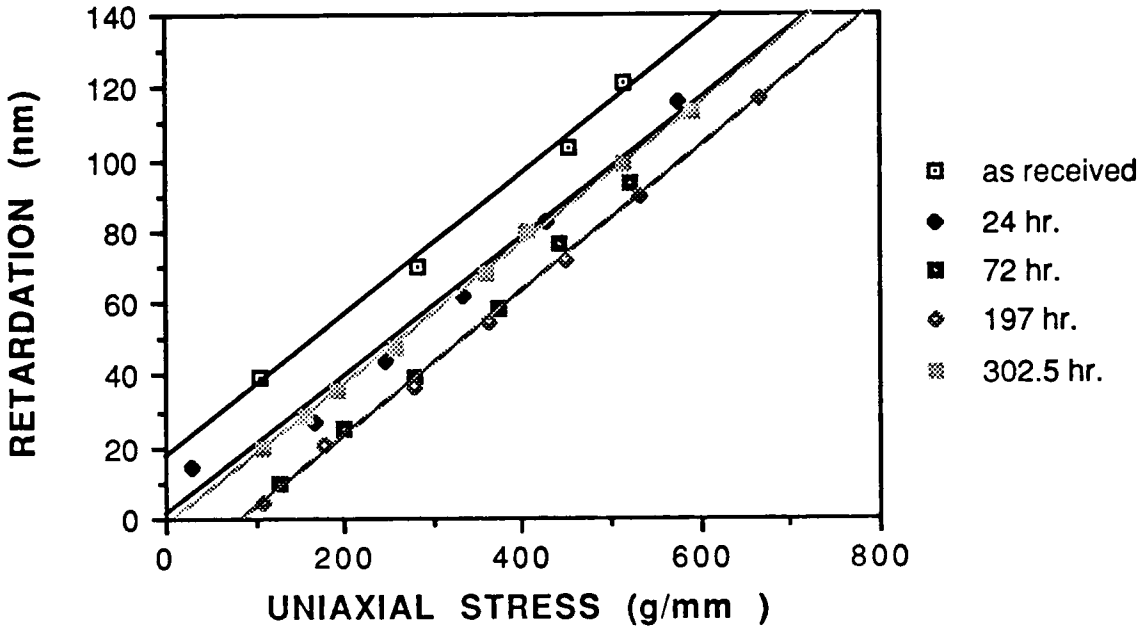


Figure 8.11 Retardation measurement of another specimen.

plate with optical properties that are described by the refractive index difference $n_1 - n_2$,

$$n_1 - n_2 = \frac{\lambda \Delta}{2\pi h} \tag{8-13}$$

where:

λ = wavelength,

Δ = the relative retardation,

h = the specimen thickness.

By substituting Eq. (8-12) into (8-13), it is clear that

$$\Delta = \frac{2\pi h}{\lambda} (c_1 - c_2) (\sigma_1 - \sigma_2) \tag{8-14}$$

If $c_1 - c_2$ is set equal to C, the relative stress optical coefficient, the relative retardation, Δ, is given by

$$\Delta = \frac{2\pi hC}{\lambda} (\sigma_1 - \sigma_2) = \beta (\sigma_1 - \sigma_2) h \tag{8-15}$$

where:

β = a constant known as the stress-optical coefficient.

The relative retardation Δ is linearly proportional to the difference in the principal stress $(\sigma_1 - \sigma_2)$ since β and h are constants.

Density changes result in the changes of the refractive index. Since water uptake causes epoxy resin to swell, changing the spacings

between molecules, it is expected that water uptake may change the refractive index. However, according to the present experimental results, the effects of water uptake on stress-optical coefficient are not significant. To understand this, consider Eq. (8-12). If the two equations presented in Eq. (8-12) are subtracted to eliminate n_0,

$$n_1-n_2 = (c_1-c_2)(\sigma_1-\sigma_2) = C(\sigma_1-\sigma_2) \qquad (8\text{-}16)$$

C is associated with c_1-c_2. Although water uptake may affect the indices of refraction individually, n_0, n_1 and n_2, the net effects have been eliminated. Thus there is no a priori reason why C, or β, or both, should not be constant during water immersion.

By plotting the retardation (nm) against the applied stress (g/mm^2), the stress-optical coefficient can be found using Eq.(5-1). For the data shown in Figure 8.10, the stress-optical coefficient is,

$$\beta = 6.80\text{x}10^{-8}\ (mm^2/g)$$

with standard deviation S,

$$S = \sqrt{\frac{\sum\beta^2-\sum\bar{\beta}^2}{n-1}} = 2.34\text{x}10^{-9}\ (mm^2/g)$$

For the data in Figure 8.11,

$$\beta = 7.01\text{x}10^{-8}\ (mm^2/g)$$

$S = 2.60 \times 10^{-9}$ (mm^2/g)

The y-axis intercepts of the straight lines in Figures 8.10 and 8.11 is attributed to residual retardation associated with volumetric swelling.

8.3 Durability of interfacial bonding

8.3.1 Stress-induced birefringence patterns

As pointed out previously, epoxy resin undergoes shrinkages during curing and during cooling from curing temperature to the room temperature. Because of the axial thermal expansion coefficient for most fibers is less than the thermal expansion coefficient of most matrix resins, a state of compression is generated in the resin adjacent to fiber ends. During water uptake, volumetric swelling occurs and this may be large enough to compensate for the compression, and eventually to leave the resin adjacent to fiber ends in a state of tension. Stress-induced birefringence measurements show the change of resin stress state from compression to tension as a reversal in the directions of fast and slow axes. Using the measurement procedure presented in Chapter VI, experimental results show that the direction of the optical fast axis of the epoxy resin, used in the present research, is parallel to the direction of tension generated as mentioned above, while the direction of the optical slow axis is parallel to the direction of compression. The local distribution of stress-induced birefringence is also changed. Figure 8.12 shows the patterns of birefringence near fiber ends observed in a

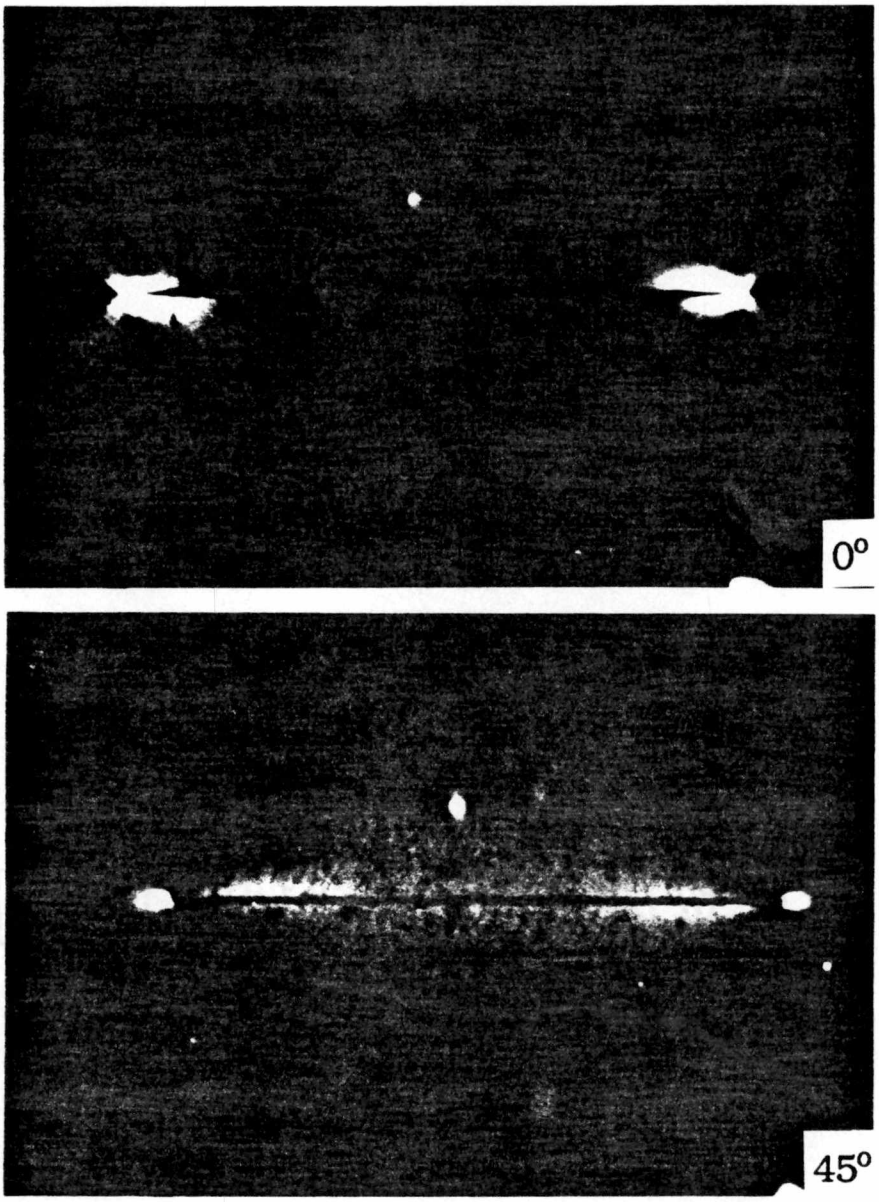


Figure 8.12 The patterns of stress-induced birefringence around a single fiber totally embedded in a film of epoxy resin. (a). viewed at 0° to the polarizer axes, and (b). at 45° to the axes.

specimen before water immersion. Extinction along the fiber direction when viewed at 0° to the polarizer axes, follows from the condition for isoclinic fringe formation, where the principal axis of either σ_1 or σ_2 coincides with the axis of polarization of either the analyzer or the polarizer. Comparing with the original patterns, Figure 8.13 shows that the patterns of birefringence change in the extent as well in nature. In order to interpret these changes, retardation measurements have been made, Figure 8.14. The retardation increases as the amount of swelling increases.

8.3.2 Shear stress distribution and occurrence of debonding

Figure 8.15 shows retardation measurements made near fiber end at points along a radial direction from a fiber totally embedded in epoxy resin and immersed in boiling water. Using the procedure described in Chapter VI, the magnitude of the stress in the epoxy resin acting parallel to the fiber axis can be obtained, and is shown in Figure 8.16. It is seen that the axial stress is concentrated at the fiber/matrix interface. Referring Figures 6.9 and 6.10, the retardation measured using that model is the sum of contributions from individual rings. Since most of the stress is concentrated near the interface, it is here that the stress-induced birefringence makes most important contribution to the measured retardation, i.e. retardation measurements made close to the interface are more important than made further away.

So, to investigate interfacial bond behavior during water uptake, the distribution of interfacial shear stress distribution close to the

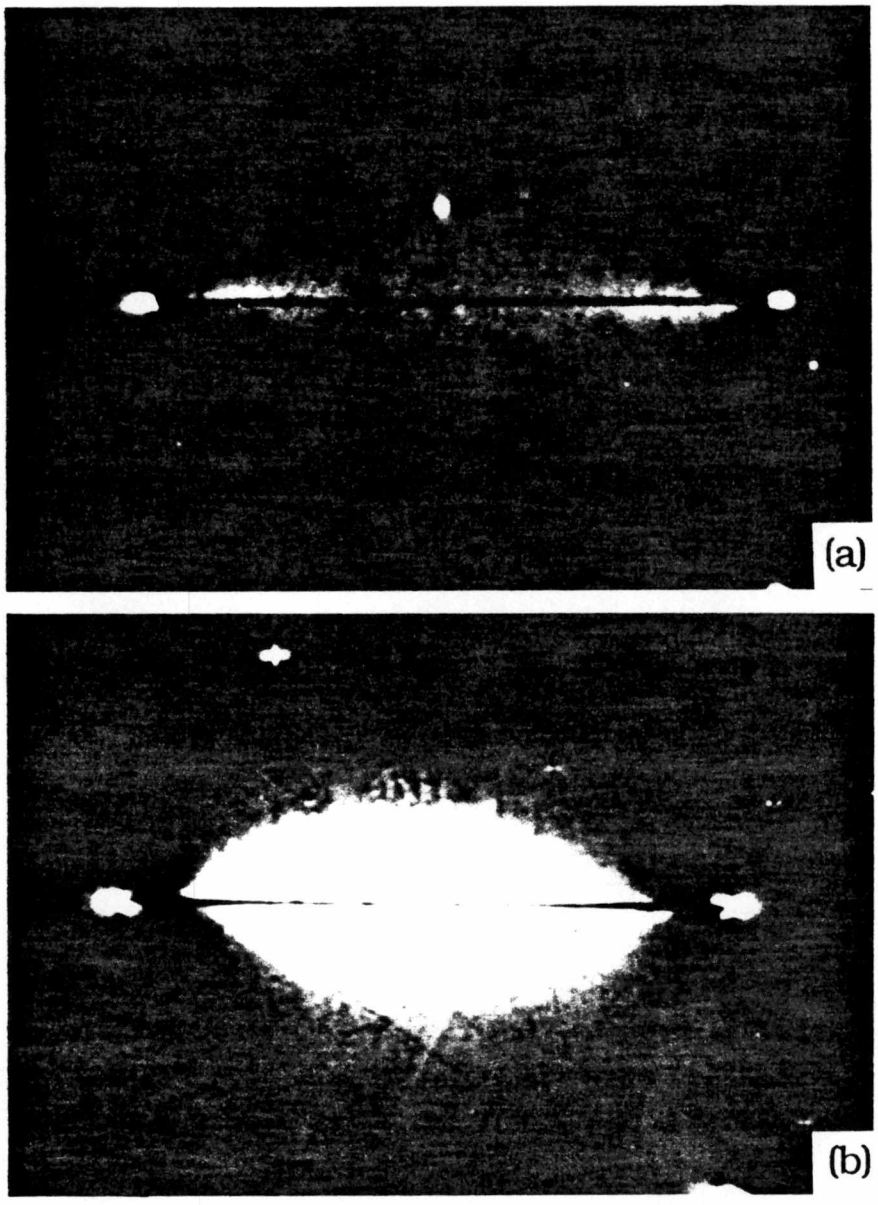


Figure 8.13 The patterns of stress-induced birefringence change after immersion in boiling water. (a) before and (b) after water immersion.

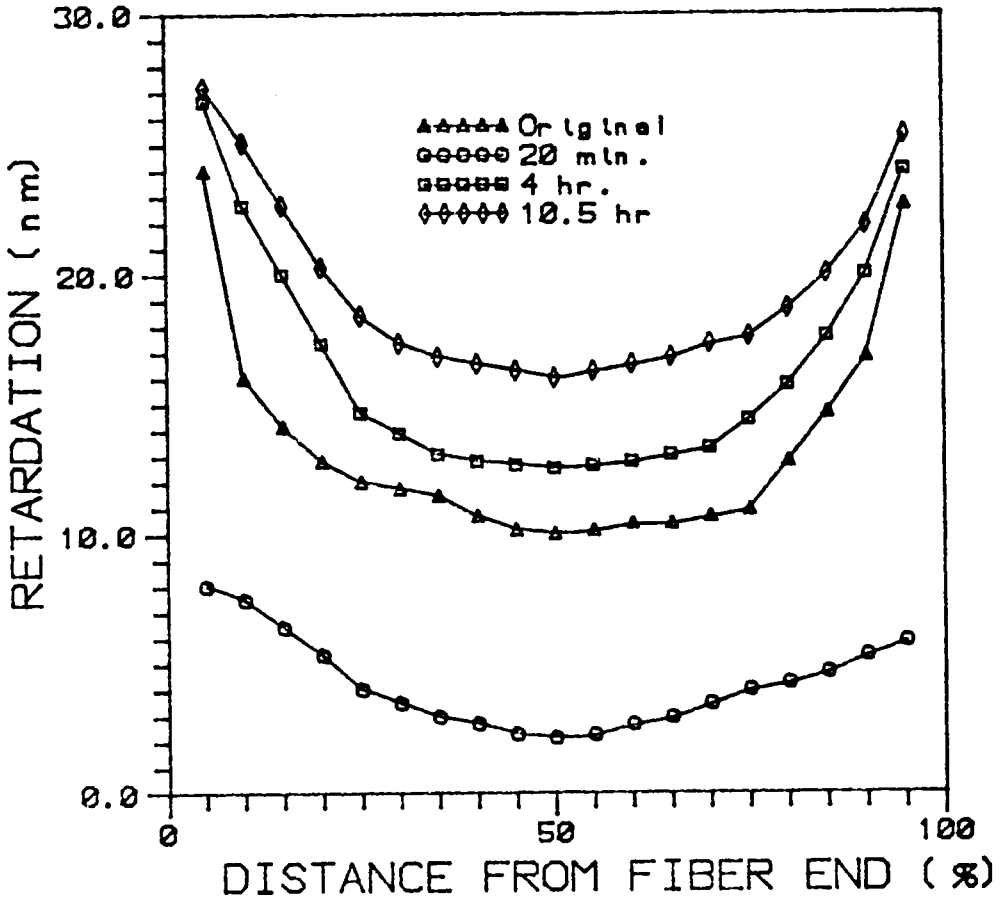


Figure 8.14 The retardation increases as immersion time increases.

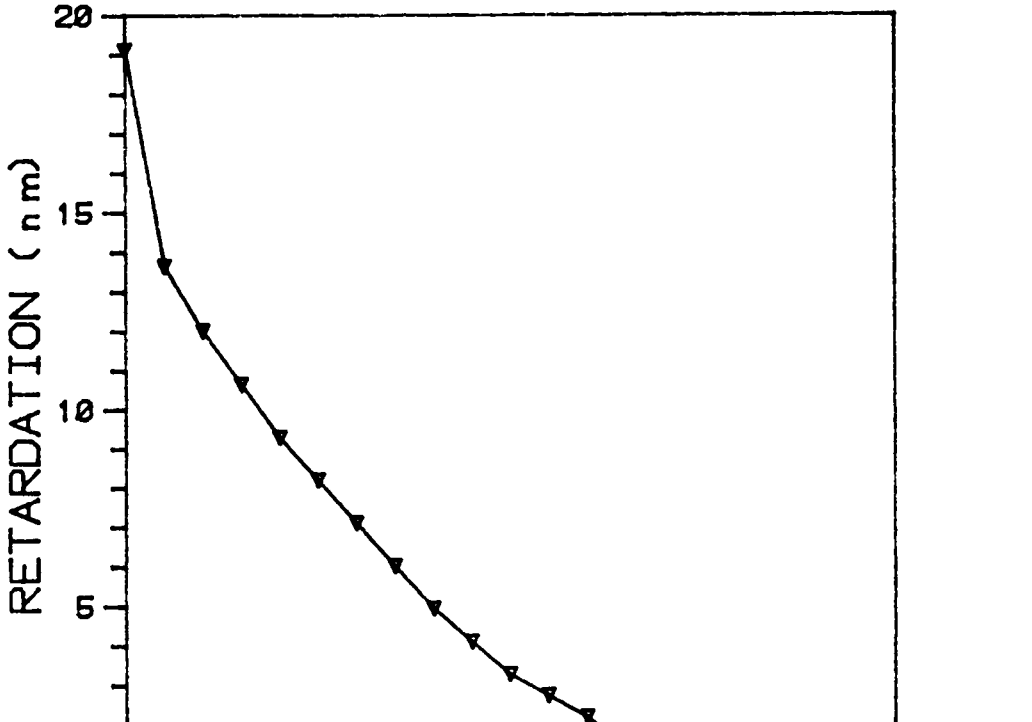


Figure 8.15 Typical retardation measurements made near fiber ends at points along a radial direction from a fiber totally embedded in epoxy resin and immersed in boiling water.

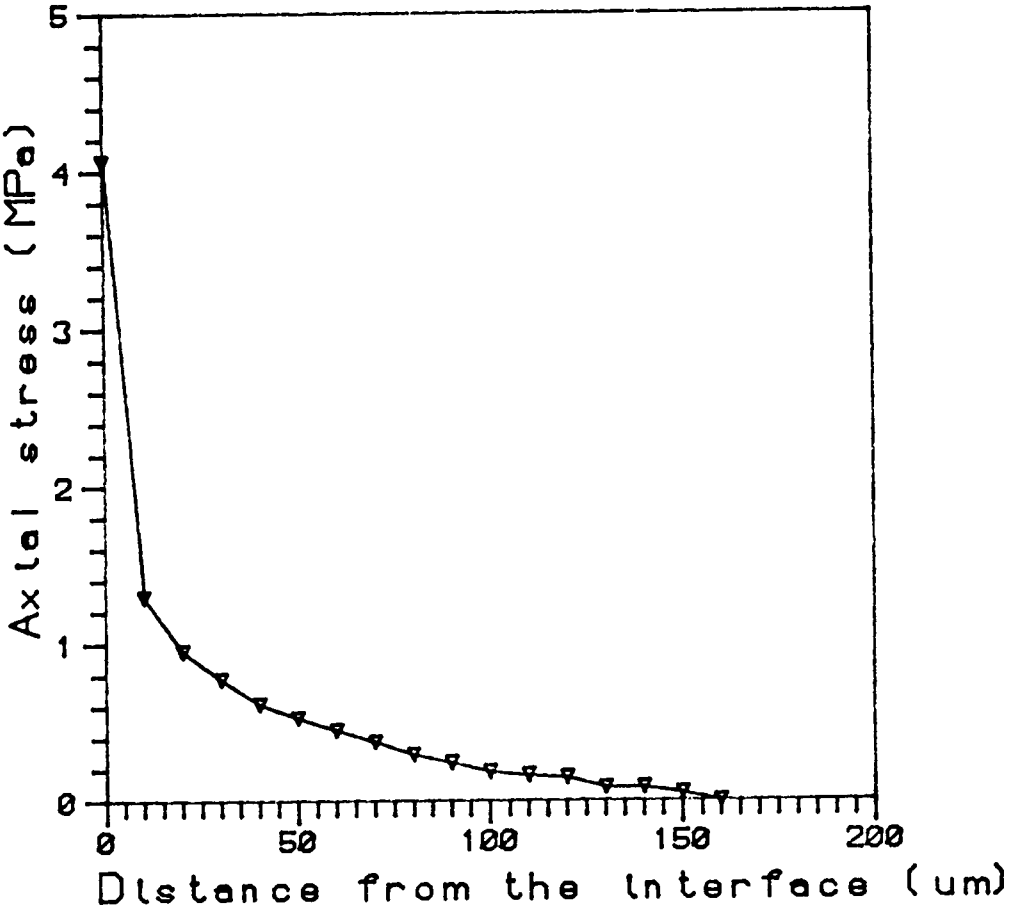


Figure 8.16 The magnitude of the stress in the epoxy resin acting parallel to the fiber axis.

interface between fiber and matrix is of most significance. Since the overall retardation measured is the sum of contributions from elastic and plastic deformation (here the plastic portion has been neglected), and since the assumption made in the Chapter VI for a cylindrical model is assumed, the shear stresses listed are at best only semi-quantitative. Figure 8.17 shows the shear stress distribution close to the interface for fiber **B**. Initially, the stress in the resin adjacent to the fiber is in a compressive state, giving rise to the direction of shear stress towards the fiber end identified as negative. After water uptake, the direction of the shear stress changes and the directions of optical fast and slow axes reverse. With increasing time of water uptake, the position of maximum shear stress migrates towards the fiber center, as revealed in Figure 8.17. This can be interpreted by considering the mechanism of load transfer. With a perfect interfacial bonding, the maximum shear stress occurs at the end of the fiber (a more sophisticated model [Whitney et al. 1987] shows that the position of maximum shear stress is very close to but not at the end of the fiber.), and may be large enough to exceed the strength of interfacial bonding. If so, debonding occurs. The position of highest shear stress is then no longer at the fiber end, but has moved towards the center of the fiber.

8.3.3 Effects of different surface treatment of fibers on the durability of interfacial bonding

If the time for the position carrying maximum shear stress to migrate, say, by a distance of one fiber diameter towards the center of the fiber is taken as criterion for the onset of debonding, the

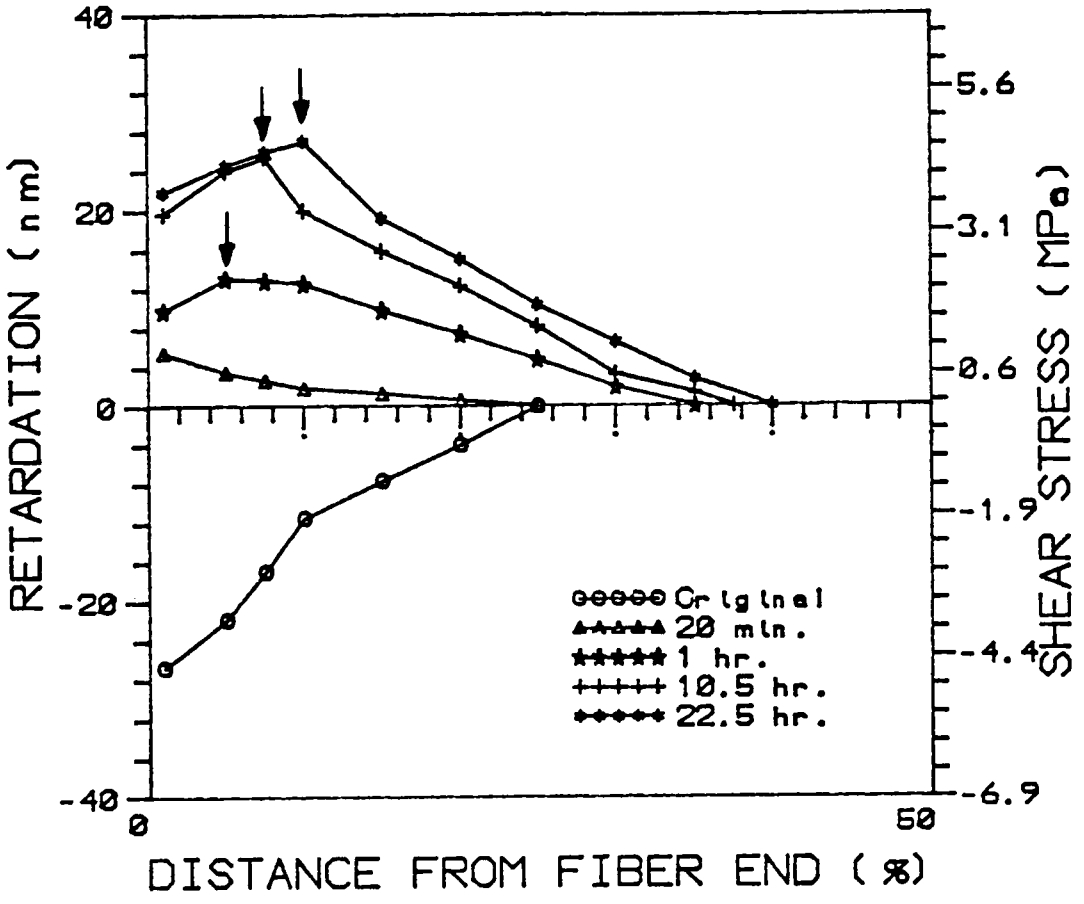


Figure 8.17 Fiber **B** Optical retardation changes close to the interface during boiling water uptake.

debonding times for different fiber surface treatments can be compared. Figure 8.18 shows shear stress distributions for a specimen containing a length of Fiber **C**. The interfacial debonding, as defined here, is established after 20 minutes of water uptake. Figure 8.19 shows the time needed for specimens containing each of fibers **A**, **B**, **C**, **D** and **E** to debond. This bar chart was constructed using data from 3 specimens for each fiber and the times shown are the average values. It is seen that Fiber **B** offers the longest durability and Fiber **C** offers the least durability against uptake of water at 100°C. In passing, it is interesting that Figure 8.19 is not the order of merit anticipated by the manufacturer of the fiber samples.

8.4 Effects of different surface treatment of fibers on surface energy of interfacial debonding cracks

Figures 8.17 and 8.18 show displacements of the position of maximum interfacial shear stress. The distance from the fiber end of the position of maximum shear stress can be considered as a length over which the interface has effectively failed. Hence relationships between the length of interfacial failure and water uptake time for different fibers can be obtained, see Figure 8.20. As expected, Fiber **B** is characterized by having the shortest debonded length at any time, and Fiber **C** the longest.

Since all five composites have the same epoxy resin, and have been subjected to the same fabrication procedure and the same water immersion treatment, the internal energy due to the volumetric swelling associated with water uptake can be taken to be same for

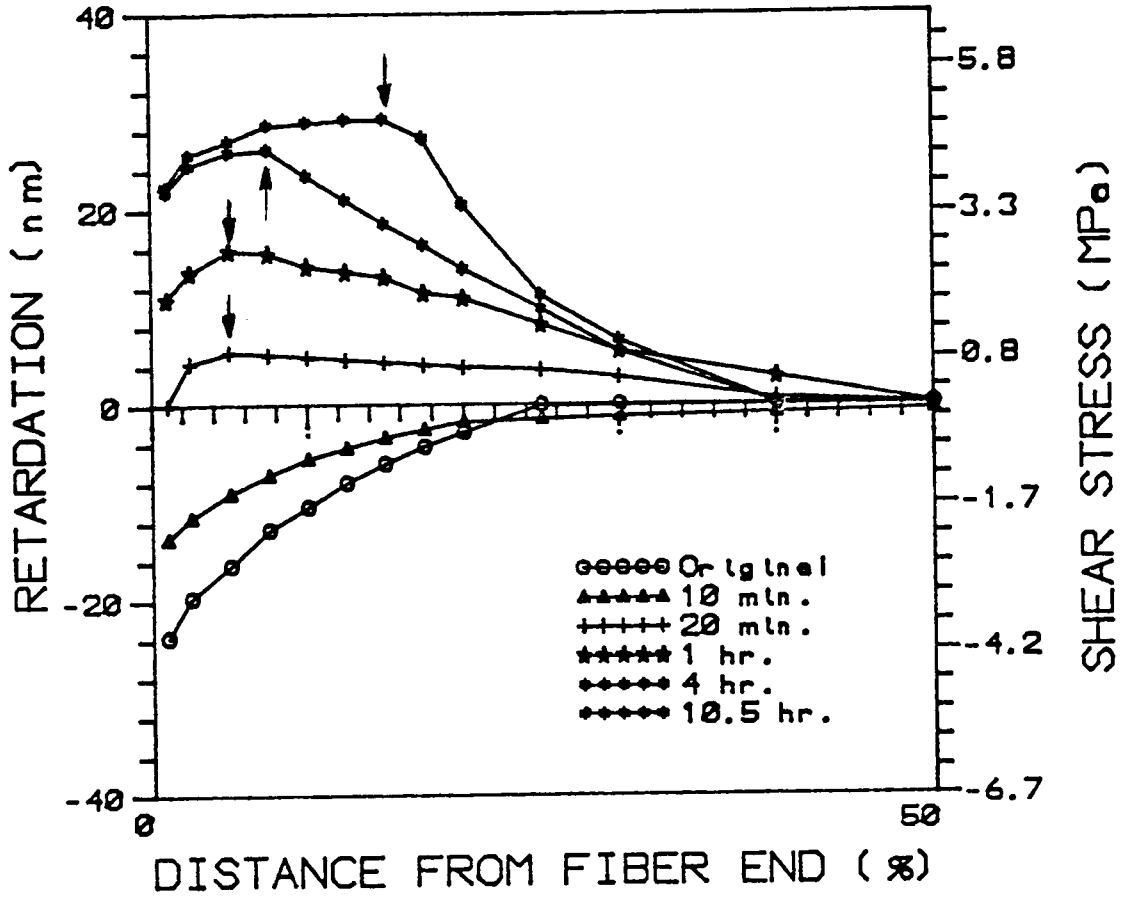


Figure 8.18 Fiber **C** Optical retardation changes close to the interface during boiling water uptake.

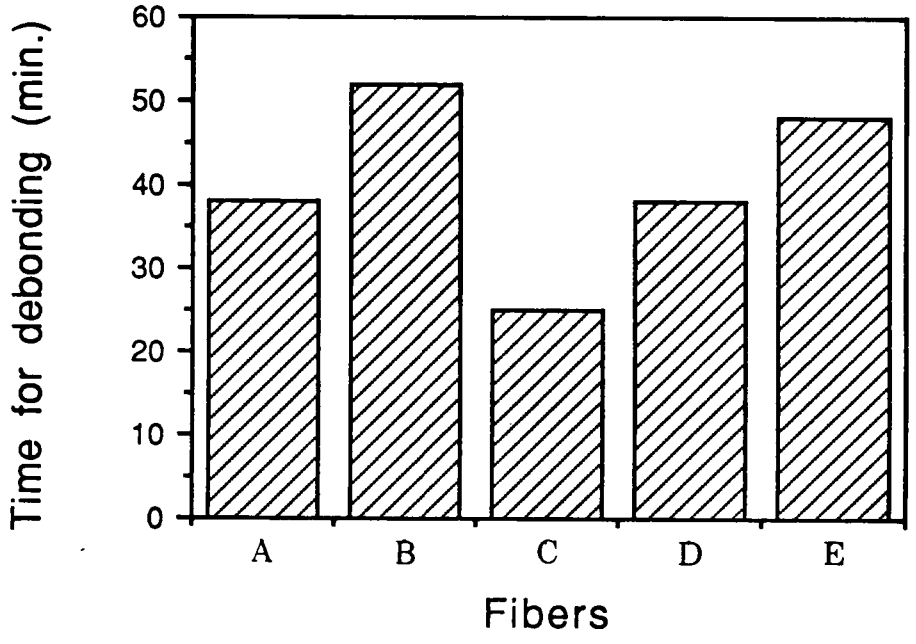


Figure 8.19 The immersion time needed for specimens containing each of fibers **A**, **B**, **C**, **D** and **E** to debond.

each and, by assuming that the elastic properties of the fibers will not be affected by the different surface treatments, the differences in debonding length can be attributed to different fracture surface energies.

Consider the elastic energies of the specimens after 60 minutes of boiling water uptake. The respective interfacial crack lengths can be obtained from Figure 8.20. Internal elastic energy is released to create the new surface that constitutes an interfacial crack. This energy is given by

$$W = 8 \pi R \gamma L_d \qquad (8\text{-}17)$$

where:

R = radius of fiber,

γ = fracture surface energy, and

L_d = debonded length.

The interfacial fracture surface energies normalized to that for fiber **C** are shown in Figure 8.21. It is concluded that the interfacial fracture surface energy can be increased by appropriate fiber surface treatment, and by as much as 30% (fiber **B**).

From the results of durability for durability of interfacial bonding, Figure 8.18, and for fracture surface energies, Figure 8.21, it is concluded that the adhesion of fiber **C** to the epoxy resin was relatively low and that for fiber **B**, it was relatively high.

8.5 Microcracking of matrix resin

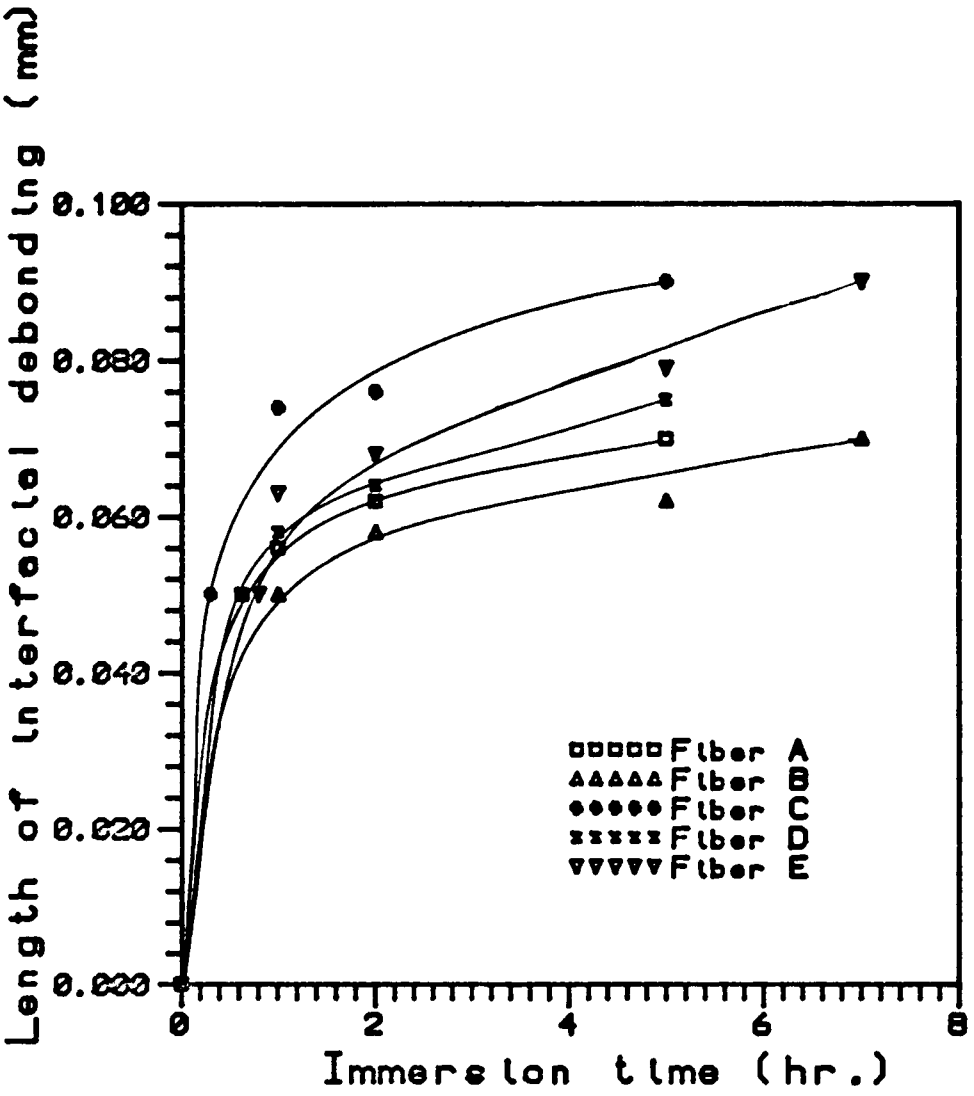


Figure 8.20 The relationships between the length of interfacial failure and water uptake time for different fibers.

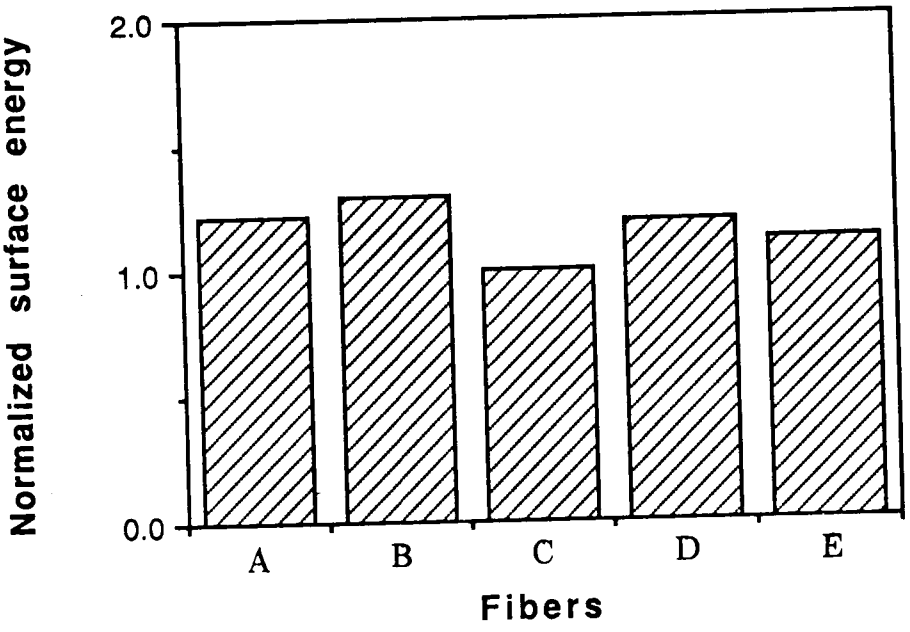


Figure 8.21 The interfacial fracture surface energies, normalized to that for fiber **C**, for specimens with fibers of different surface treatments.

Microcracking of matrix resin resulting from hot water uptake, has been observed during the course of this research. Figure 8.22 shows a disk- or penny-shaped crack inside epoxy resin after water immersion. This is attributed to osmosis; the osmotic pressure for solutions of many inorganic salts is the same order of magnitudes as the pressure required for stabilization of penny-shaped cracks. The micrograph in Figure 8.22(b) reveals large stress-induced birefringence concentrated around the crack edge.

Another kind of crack in the resin matrix has been observed, and is shown in Figure 8.23. This crack may result from the inclusions in the epoxy resin. The different physical properties between the inclusions and epoxy generate a mismatch between them in the deformation associated with water uptake. The tension stress generated due to volumetric swelling and concentrated at the interface between the inclusions and matrix, may exceed the adhesion between them, resulting in microcracking at the interface.

8.6 Fracture of fibers

8.6.1 Deformation of fiber due to matrix swelling associated with water uptake

When the matrix in a composite material deforms in response to the environment with which it is in contact, mechanical forces will be generated in the fibers. If the fiber becomes tensioned in the fiber direction, it undergoes a radial Poisson contraction. Using our interferometric "Strain Gage" technique, described in Chapter VI, the radial fiber displacement can be measured.

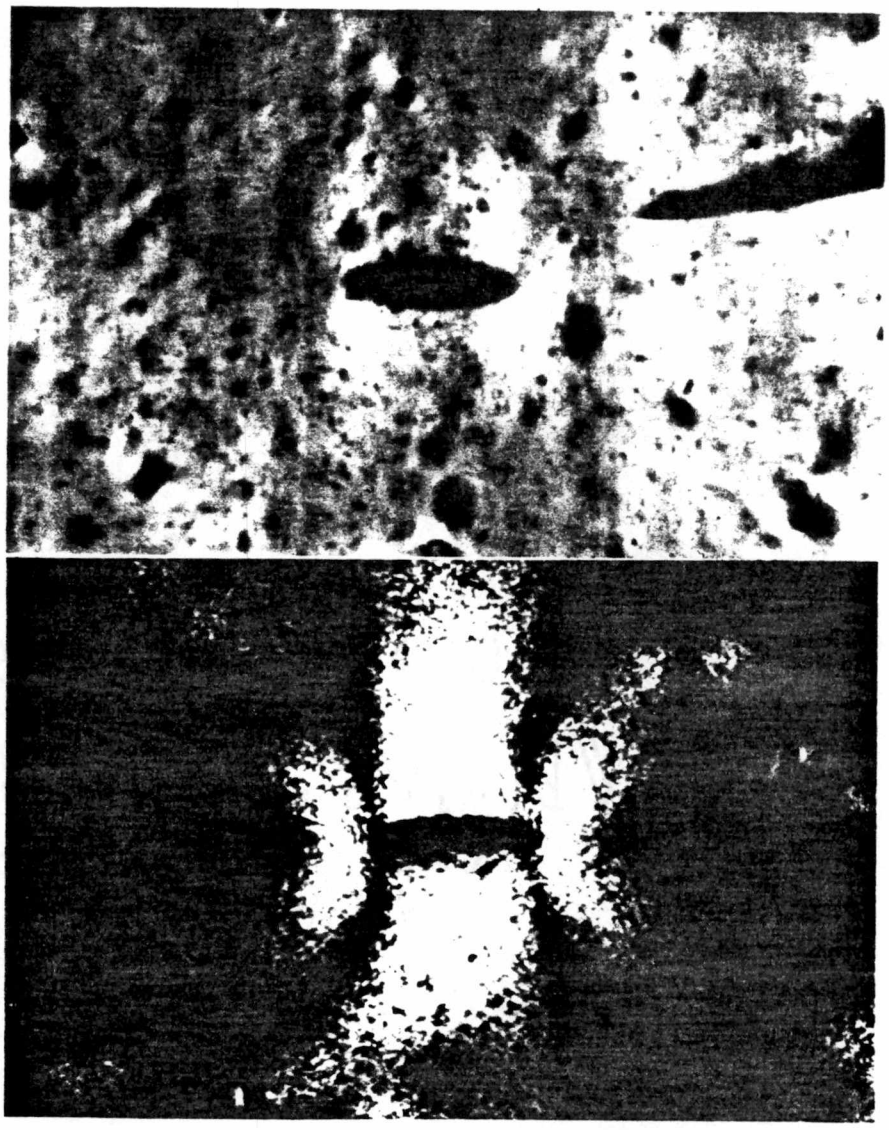


Figure 8.22 Penny-shaped crack in epoxy resin due to osmotic pressure generated by the diffused water.

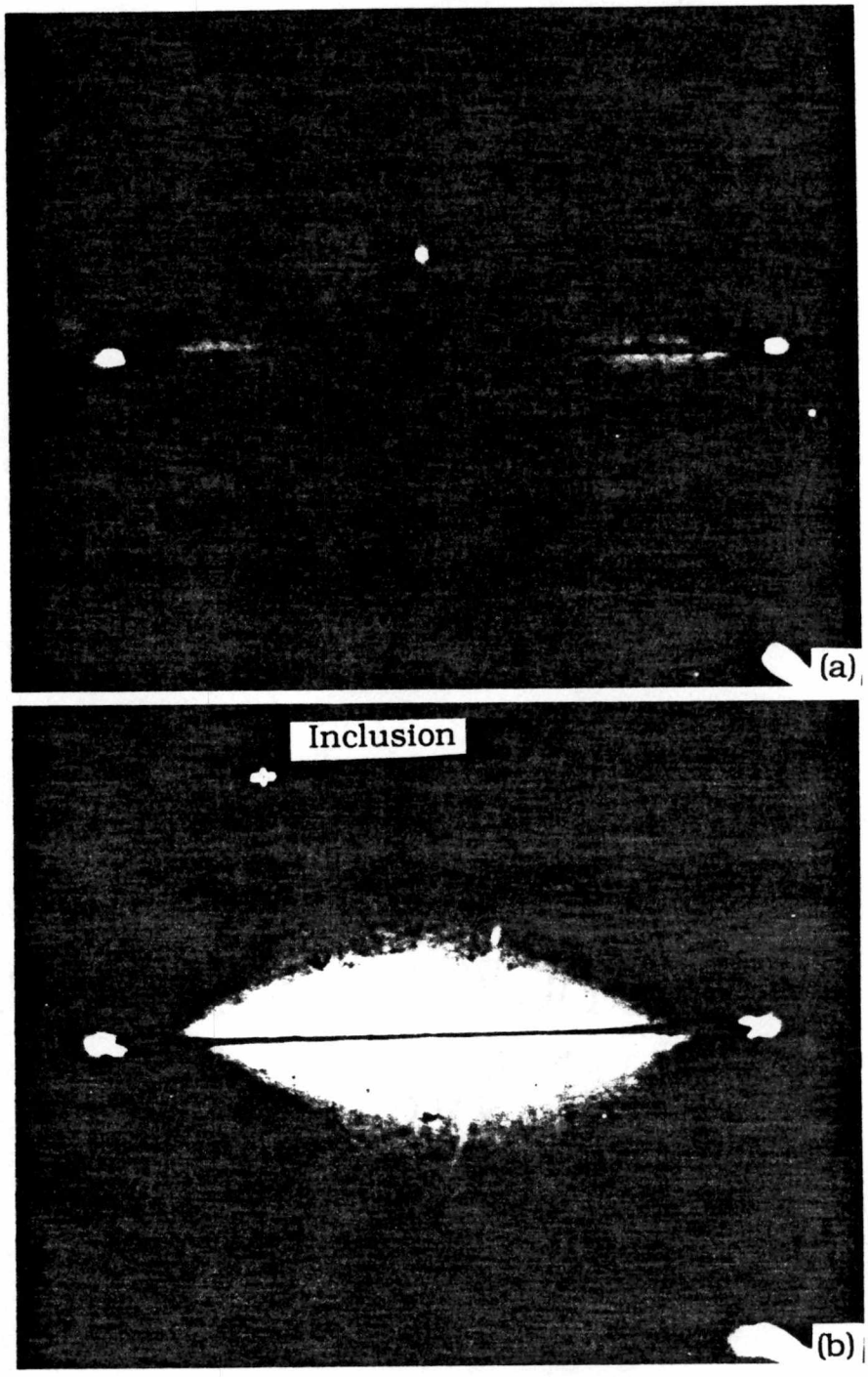
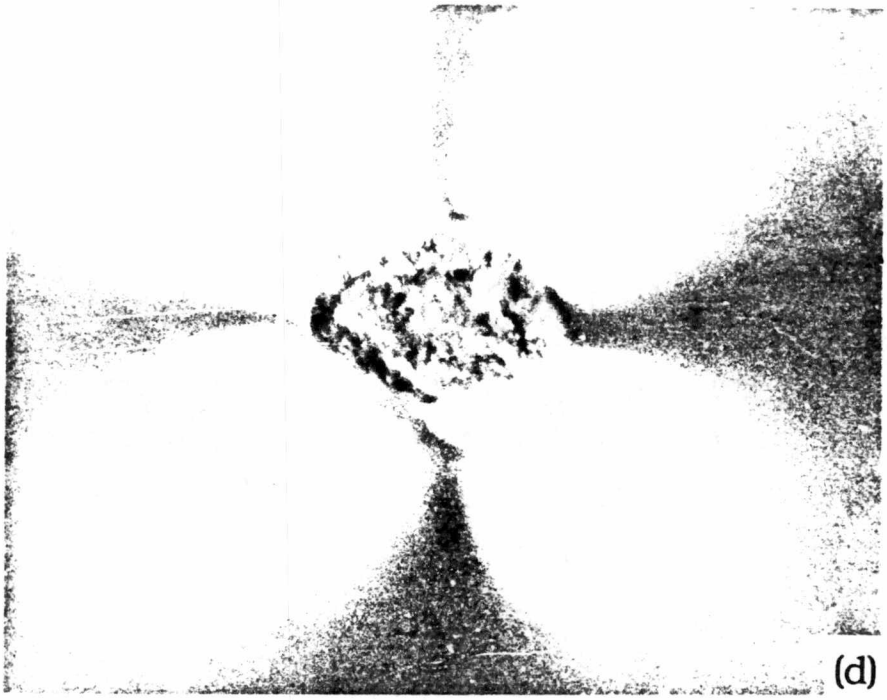


Figure 8.23 Crack in epoxy resin around a inclusion due to the mismatch of moisture swelling between them. (a) initial; (b) after 10.5 hours immersion in boiling water; (c) an inclusion embedded in epoxy shown in (b); (d) an inclusion viewed at a polarizing microscope.



(c)



(d)

Figure 8.23 Continued.

Figure 8.24 shows an example. The sample is a 1mm thick plate of epoxy resin containing a single glass fiber of diameter nominally 300μm and oriented more or less parallel to the plate. There are two sets of fringes. The family of curved fringes covering the whole field of view is due to interference between incident light and light reflected from the near surface of the flat, identified as set #1 in Figure 7.6. A much finer set of fringes of elliptical shape, can be seen confined to a zone across the middle of the field of view. These latter fringes are due to interference between incident light and light reflected at the fiber/resin interface, identified as set #2 in Figure 7.6. Both patterns of fringes change during exposure of the specimen to an aqueous environment. Figure 8.25 shows the changes recorded during immersion of the specimen in water at 25°C. Note, for example, the change in contrast from black to white at the center of the family of ellipses.

Figure 8.26 shows the measured radial displacement (curve #4). The radial displacement was estimated as follows. The geometry of the specimen is shown schematically in Figure 8.27. The overall displacement comprises three segment displacements:

$$\Delta H = \frac{\Delta h_1}{h_1} h_2 + \Delta h_1 + \Delta D \qquad (8\text{-}18)$$

where H, h_1, h_2 and D are identified in Figure 8.27.

By assuming the resin swelling is homogeneously through the specimen, ΔH was obtained from interference fringe set #1, and set

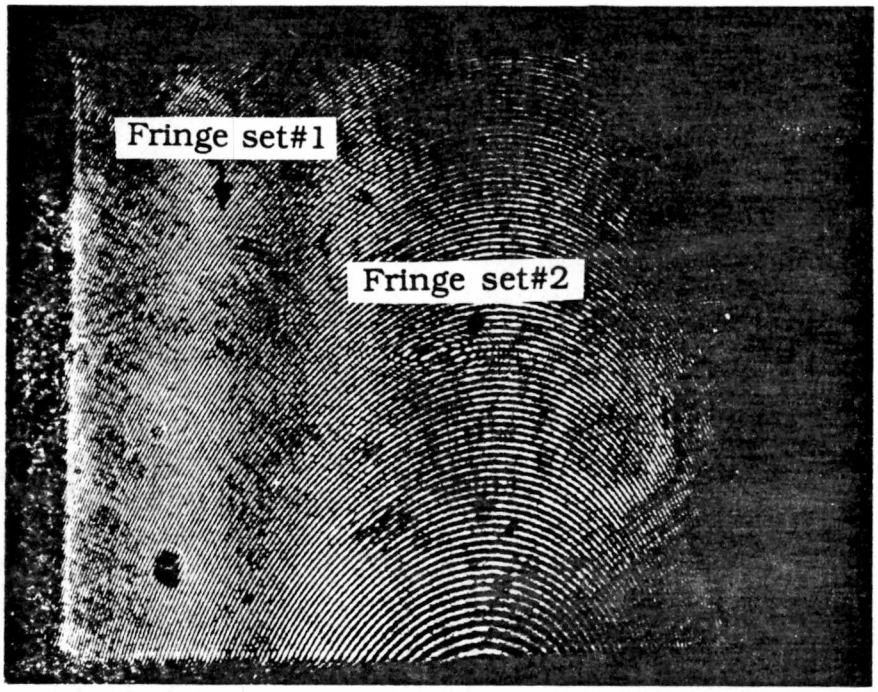


Figure 8.24 Optic interferometry from a single fiber in a thin film.

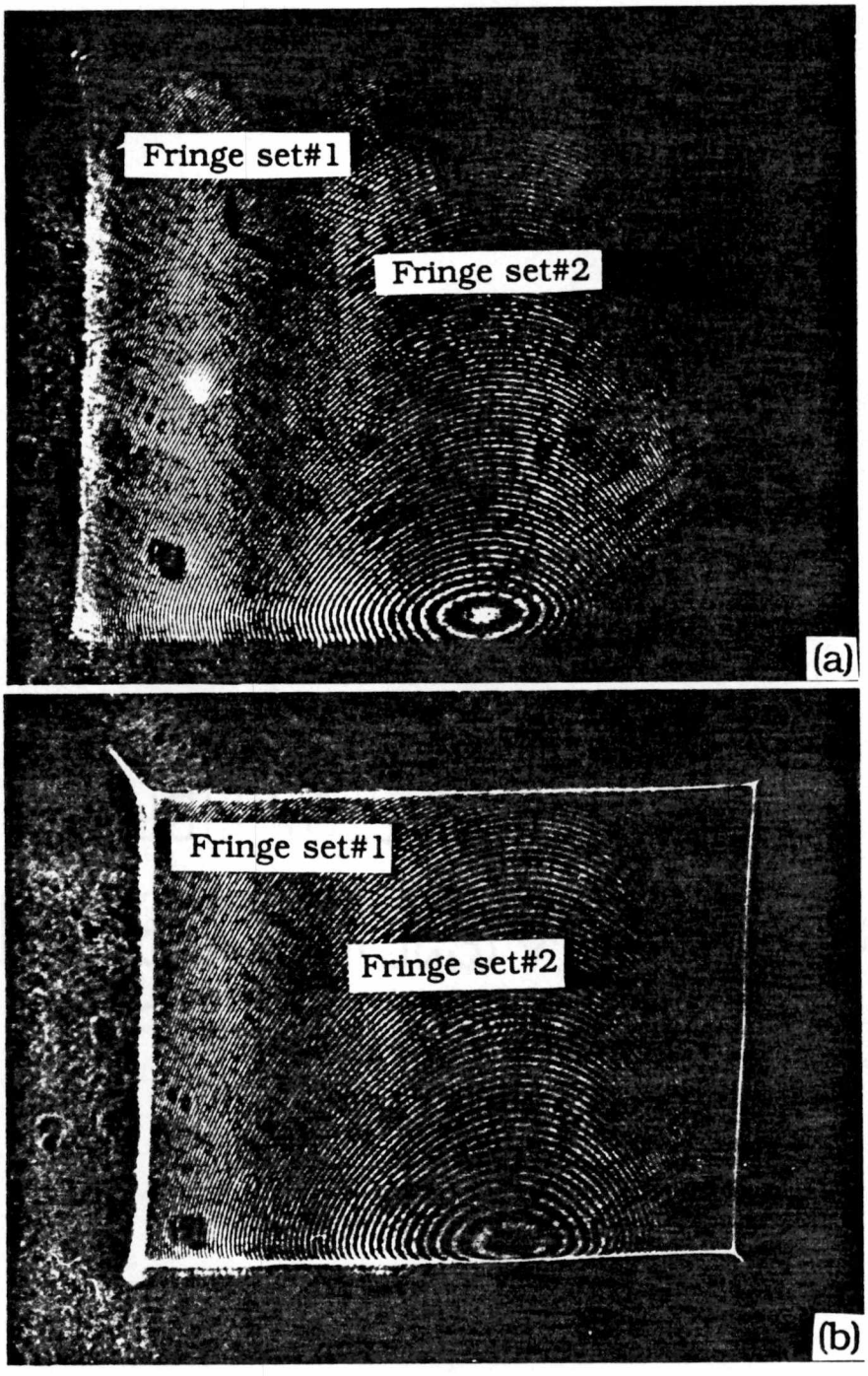


Figure 8.25 Changes in the patterns of interference fringes during water uptake. The same specimen as Figure 8.24 but after (a) 150 h. and (b) 500 h. of water immersion at 25°C.

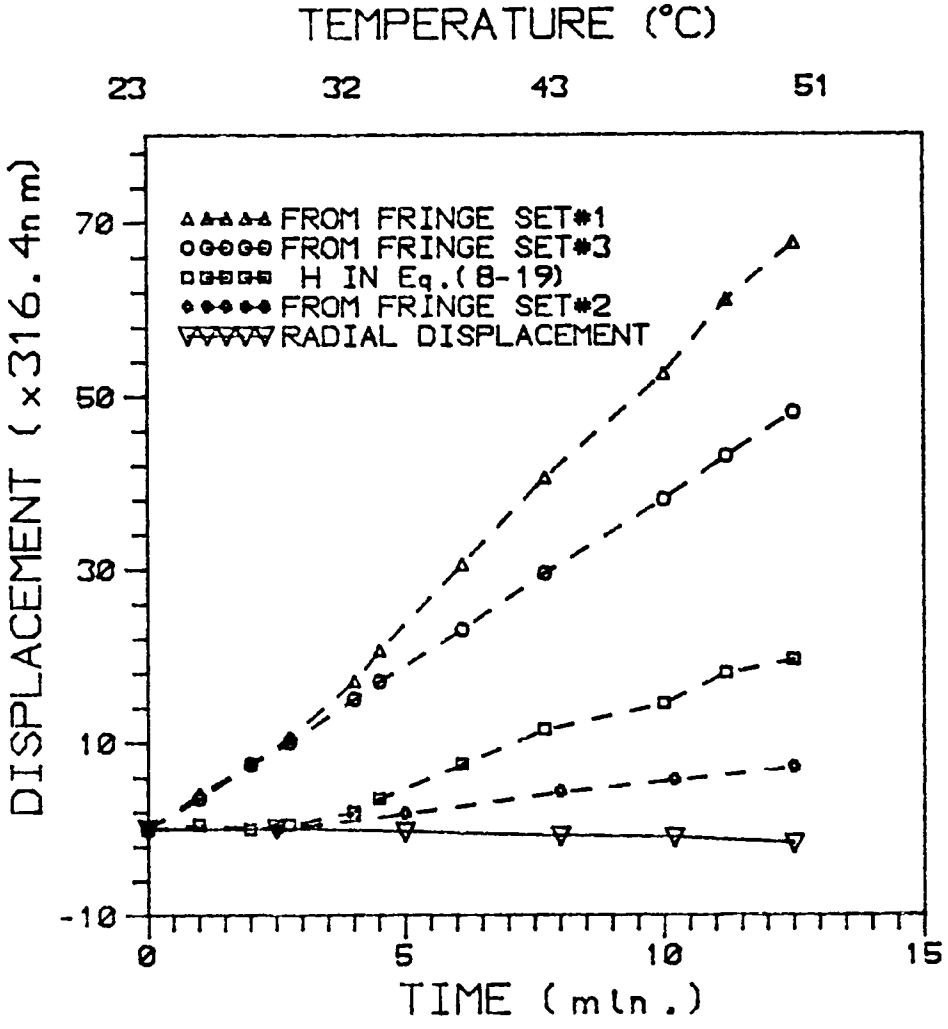


Figure 8.26 The measured displacements permitting calculation of the fiber radial displacement resulting from deformation of the epoxy resin during water uptake.

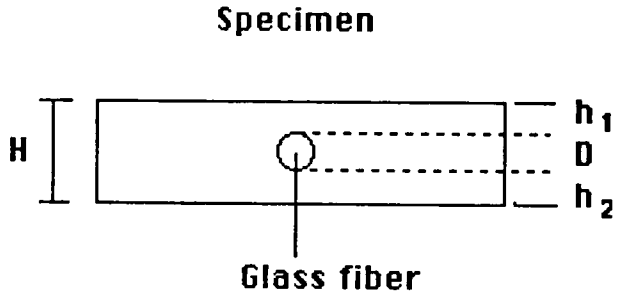


Figure 8.27 The geometry of a specimen.

#3, and Δh_1 from set #2.

Rewriting Eq. (8-18)

$$\Delta D = \Delta H - \Delta h_1 \left(\frac{h_2}{h_1} + 1 \right) \qquad (8\text{-}19)$$

The radial displacement of fiber is shown in Figure 8.26. The displacement is linear to begin with. In a prolonged test, Figure 8.28, the radial displacement of the fiber can be as large as 4μm. These results confirm that the fiber is under tension.

8.6.2 Stress distribution around a single fiber

Fiber displacement in the radial direction, caused by matrix swelling associated with water uptake, has been observed as discussed in the previous section. Further studies of the matrix swelling-induced stresses around a single fiber in epoxy resin undergoing water uptake have been carried out and will be discussed in this section.

By making the assumptions (i) that water which has diffused into resin matrix composites is uniformly distributed, and (ii) that the resin swelling accompanying water uptake is linearly related to the amount of water absorbed, several researchers have defined a hydrothermal expansion coefficient in order to draw an analogy with linear thermal expansion when attempting to calculate the self-stress field of composites during exposure to aqueous environments. In all cases known to the present author, such calculations have concentrated on the distribution of normal stress and tangential stress

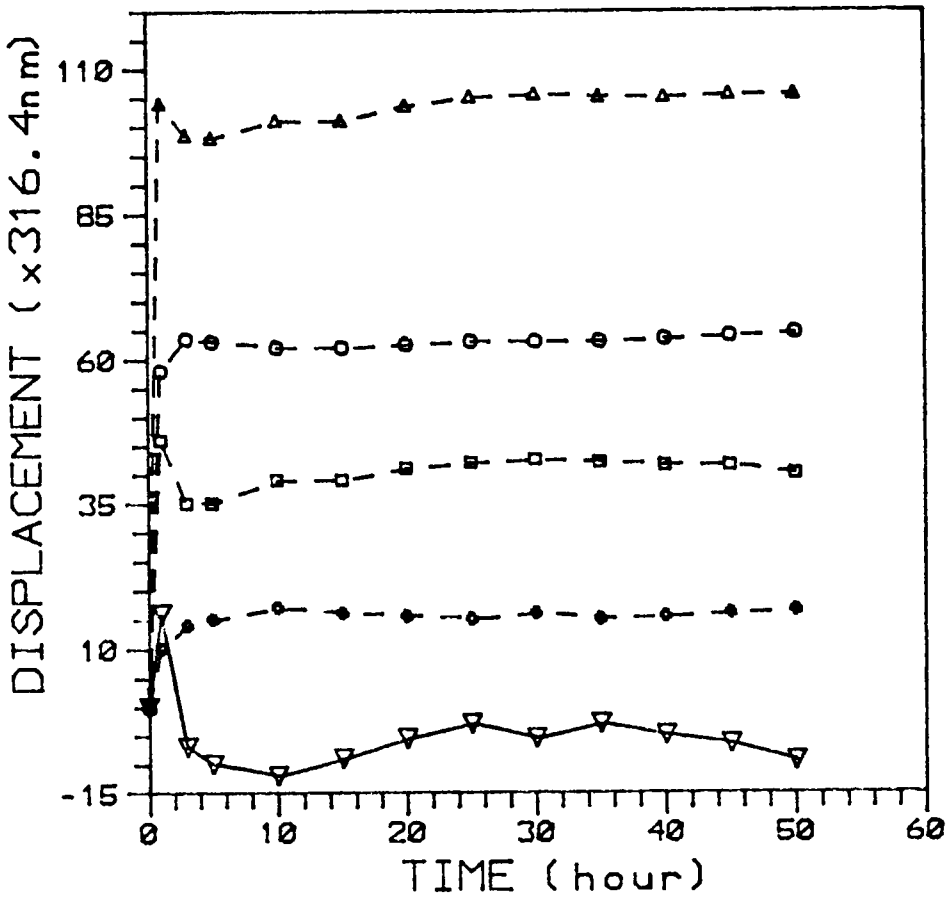


Figure 8.28 Measured displacements for another specimen. The legends are used in the same way as in Figure 8.26.

in the plane perpendicular to the direction of fiber reinforcement. Our attention has been drawn to the fact that, from a practical standpoint, the distribution of normal stress in the fiber direction can be more important leading, in extreme cases, to fiber fracture. The axial stress in the fiber direction is increased since more constraint, offered by the fiber, is generated in order to balance between the further swelling of the epoxy resin and the fiber of stable dimension. These suggest that the axial stress in the fiber direction may be dominant in causing the fracture of the fiber.

Composite specimens, comprising a single axial fiber in a cylindrical block of epoxy resin, to opposite ends of which are bonded a flexible glass cover slip and a rigid substrate, have been self-stressed by immersion in water. The cover slip constitutes a "marker", the flexing of which can be analyzed to give the distribution of axial stress in the underlying resin and fiber. Our measurements of the axial displacement field have permitted us to explore its inhomogeneous nature and its dependence on water uptake.

Referring back to Figure 8.9, it reveals that the rate of approach to equilibrium is slower than predicted by Fick's law with constant diffusion coefficient. This may reflect a concentration-dependent diffusion process. Alternatively, it may be attributed to a stress dependence of the diffusion process in terms of the constraint offered by fiber.

When water permeates into the specimen, refer to Figure 8.4, a sharp advancing boundary separates the inner unswollen region from the outer swollen material. We measured, from the photographs in

Figure 8.4, the thickness of the swollen region at different times, and present these data in Figure 8.29. The thickness of the swollen region increases rapidly during the first few hours. In Figure 8.30, it can be seen that the rate of advance of the swollen resin decreases with increasing immersion time. Possible reasons for this include the constraint offered by fiber, since the swollen resin usually advances at constant velocity for diffusion of small molecules into a neat glassy polymer [Alfrey et al. 1966].

As shown in Figure 8.4, the displacement field indicates that the specimen consists of an unswollen core surrounded by a swollen shell. Once water invades the specimen, a sharp advancing boundary separates the inner undeformed core from the outer swollen material. Because of constraints exerted by unswollen core, i.e., the fiber of stable dimension, the outer shell is self-stressed.

Stress analysis done for circular deformation are shown in Eqs.(5-2) and (5-3). Radial pressure distribution can be derived from a synthesis of all 4 differential.

To get these estimates first measure the displacement across a diameter of a moire picture. This displacement is then differentiated four times. Unfortunately this has to be done by hand as there are not sufficiently sophisticated software program available. Simply differentiating the displacement numerically leads to wild oscillations in the differentials since the data is decrete and has some inherent scatter. Thus each differentiation must be done by hand and the curve smoothed between each step in order to avoid this problem.

Figure 8.31 shows the first four differentials of W(r) for the

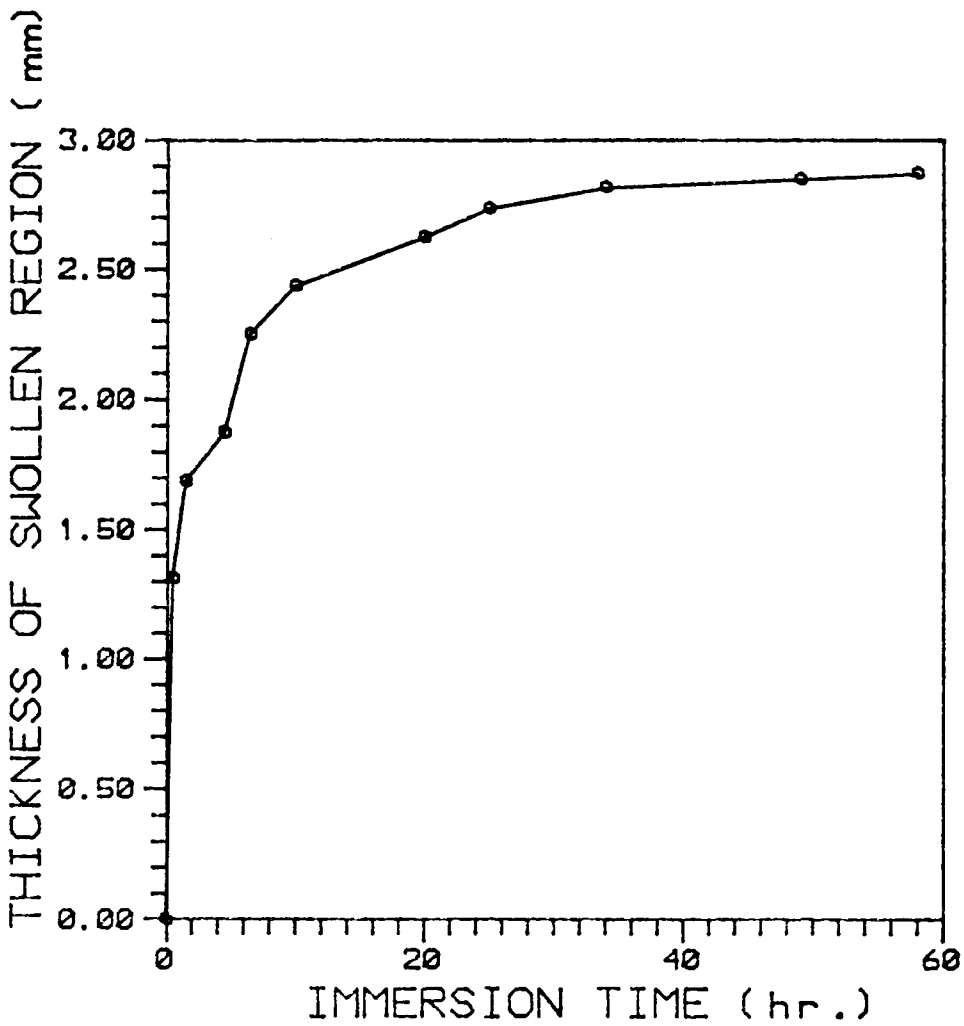


Figure 8.29 Thickness of the swollen region versus immersion time.

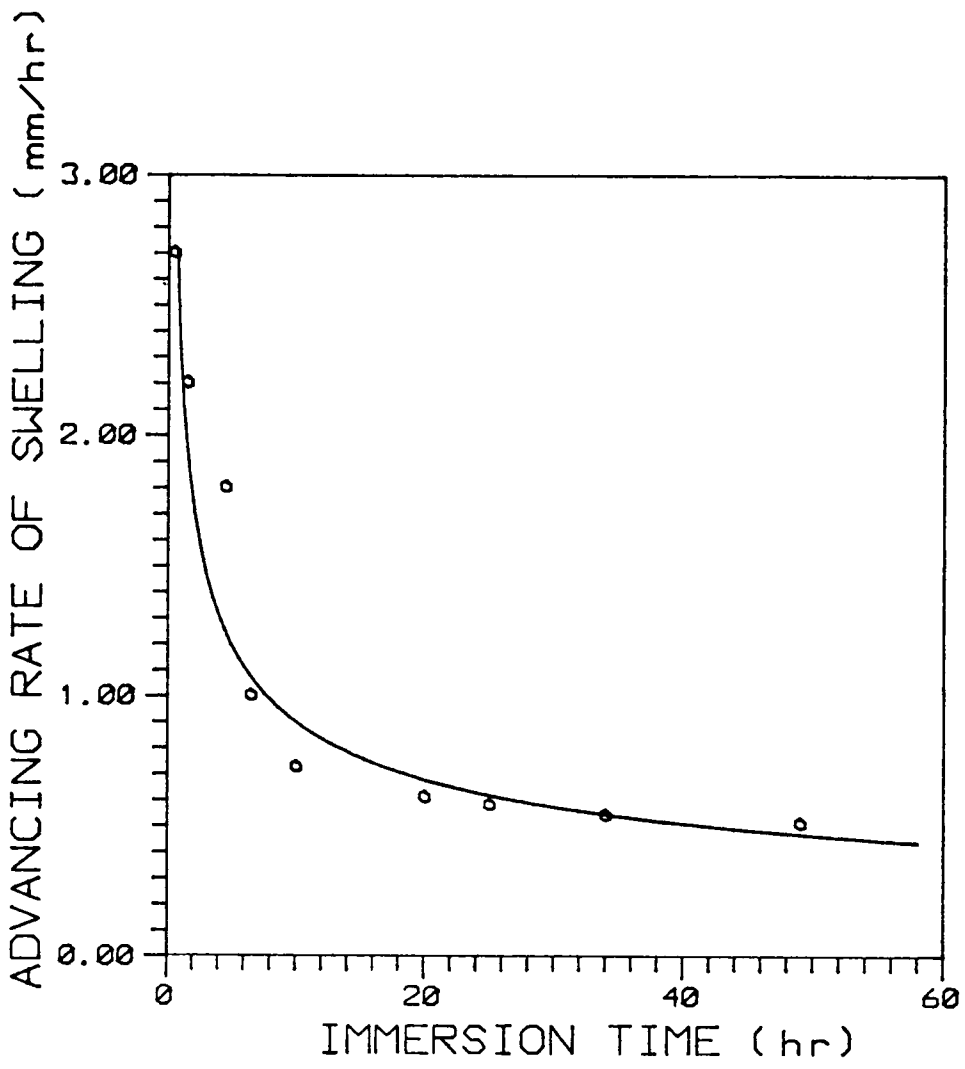


Figure 8.30 Rate of advance of the swollen resin versus the immersion time.

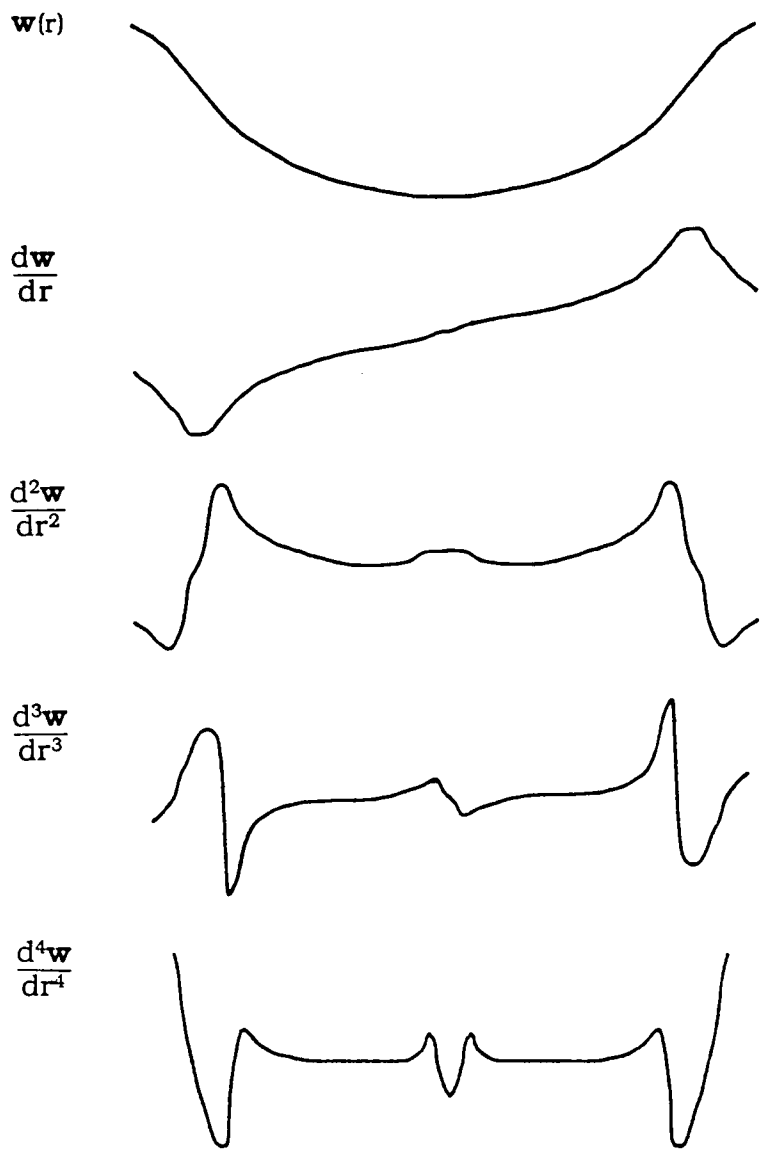


Figure 8.31 Graphically differentiation of the displacement W(r) for 58 hours immersion see Figure 8.5.

displacement after 58 hours immersion in Figure 8.5. The differentials shown in Figure 8.31 were generated graphically by hand. The reason for this procedure lies on the difficulty of differentiating four times a discrete set of data points where a small amount of scatter in the initial displacement data leads to wild oscillation in the differentials. The minimum and maximum deviations of W by using this method has been reported [Ashbee et al. 1988]; a ±30% peak height (maximum stress) error and a ±0.03 mm radius positional error are predicated.

To qualify this method, a regression method to fit the displacement data has been used so that differentiation can be performed using a regression equation and the different methods can be compared. Using a set of data discribed by Gaussian function,

$$y = -H\, e^{-(x/w)^2} \tag{8-21}$$

where H, and w are different constant associated with the individual shapes of the displacement curves. It is possible to fit Eq. (8-21) to the displacement by summing different values for y_i,

$$y = \sum_{i=1}^{n} y_i = \sum_{i=1}^{n} -H_i\, e^{-(x/w_i)^2} \tag{8-22}$$

Since

$$e^x = 1 + \frac{x}{1!} + \frac{x^2}{2!} + \ldots + \frac{x^n}{n!} \qquad x < \infty$$

then

$$-H_i\, e^{-(x/w_i)^2} = -H_i \left(1 - \frac{(x/w_i)^2}{1!} + \frac{(x/w_i)^4}{2!} + \ldots \right. \tag{8-23}$$

$$+ (-1)^m \frac{(x/w_i)^{2m}}{m!})$$

$$y = \sum_{i=1}^{n} -H_i e^{-(x/w_i)^2}$$

$$= \sum_{i=1}^{n} (H_i + H_i \sum_{j=1}^{n} (-1)^j \frac{((x/w_i)^2)^j}{j!}) \qquad (8\text{-}24)$$

So the regression equation of Y = f(x) can be found. The results of 4th differentiation of those data by graphical, regressional and analytical methods are shown in Figure 8.32. Ignoring the boundary effect, the deviants of derived from the regression function give 30% peak height error and 10% radial position error, and the deviants from graphical method 20% and 5%, when compared with the 4th differentiation of the original data of Eq.(8.21) by analytical method.

Figure 8.33 plots the normal stress distribution across a diameter, derived from the displacement curves shown in Figure 8.5. The sign "+" of stress denotes a compressive stress here and "-" a tensile stress according to Eq.(5-1).

At the start, although the water concentration was zero, the specimen was self-stressed because of the resin curing procedure. The residual normal stress is compressive in the fiber and tensile in resin near the fiber. Tensile stress is believed to increase the diffusivity of water in polymers [Leffbvre et al. 1989]. As soon as the specimen is immersed in water, water enters the surface layers but the deeper

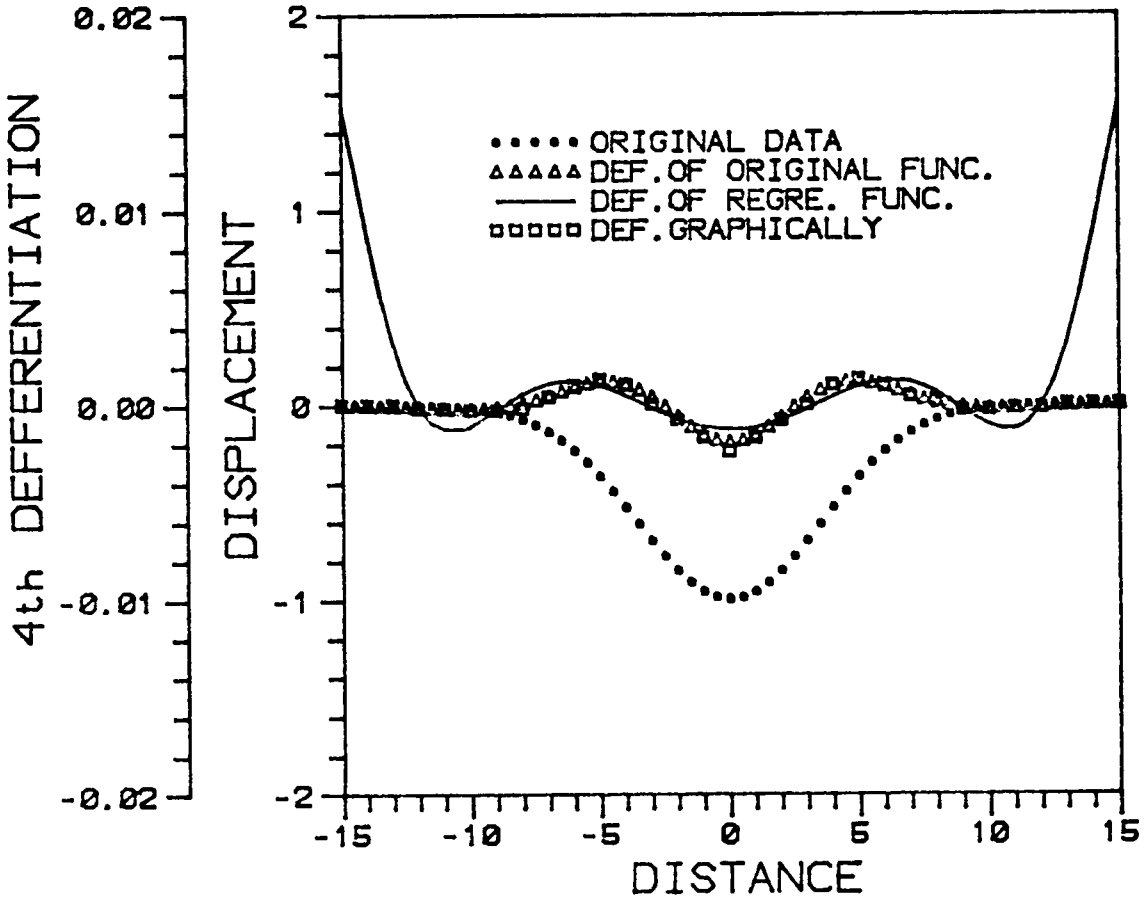
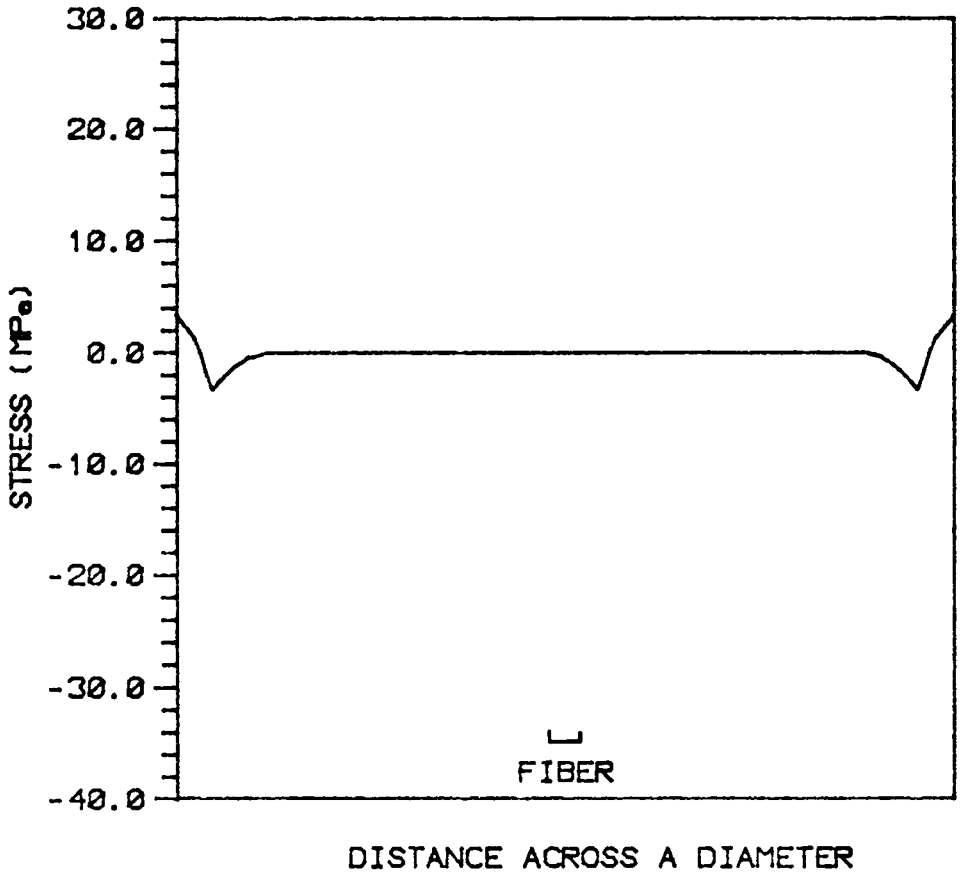
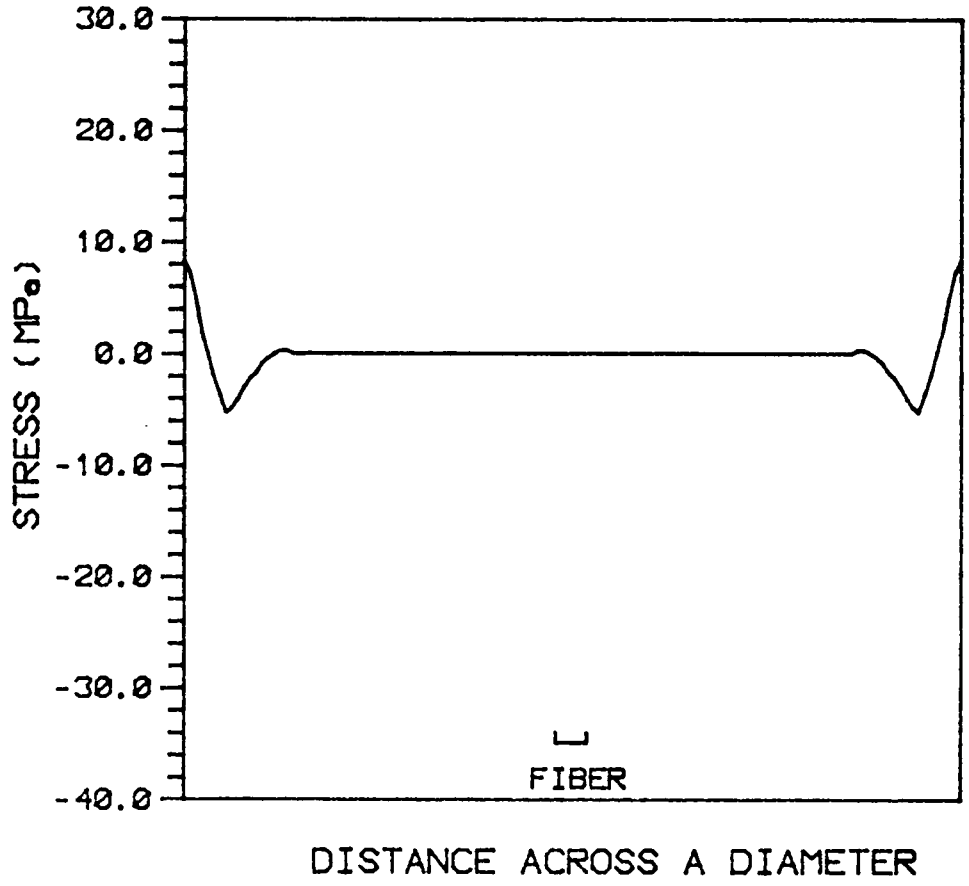


Figure 8.32 Maximum and minimum deviants obtained by regression method and compared with graphical and analytical methods.



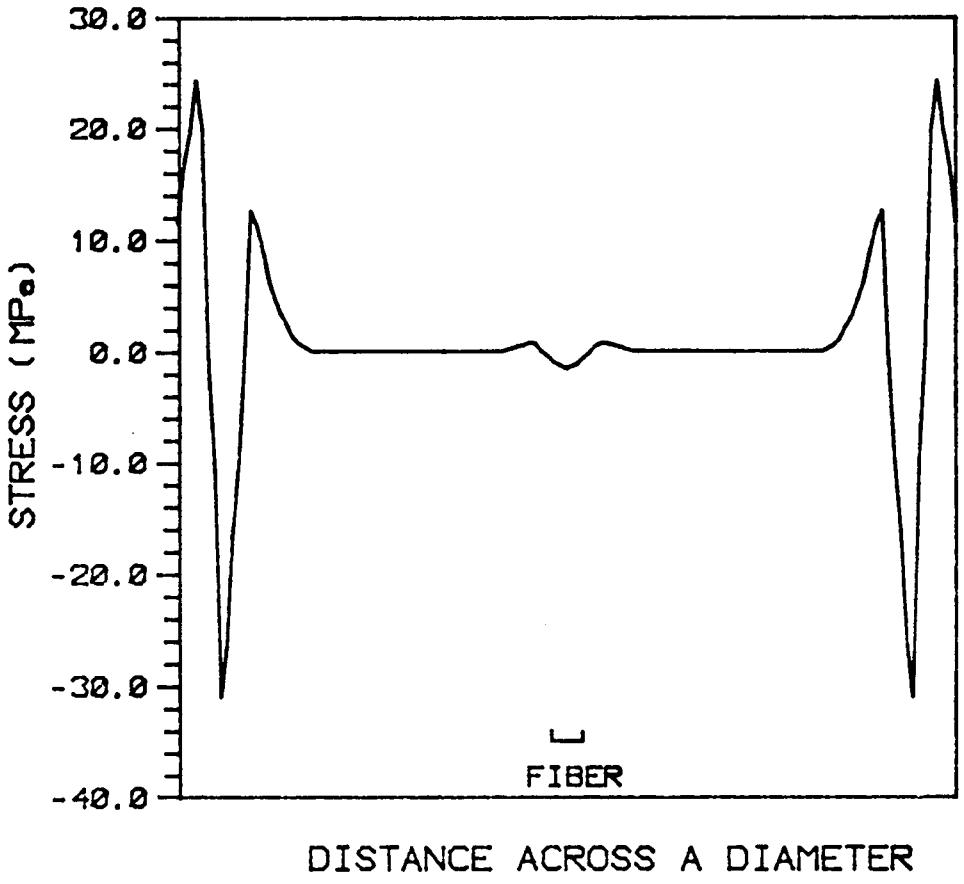
(a)

Figure 8.33 Radial stress distribution generated by graphical differentiation from displacement curves in Figures 8.5. (a). 0.5, (b). 4.5, (c). 20 and (d). 58 hours.



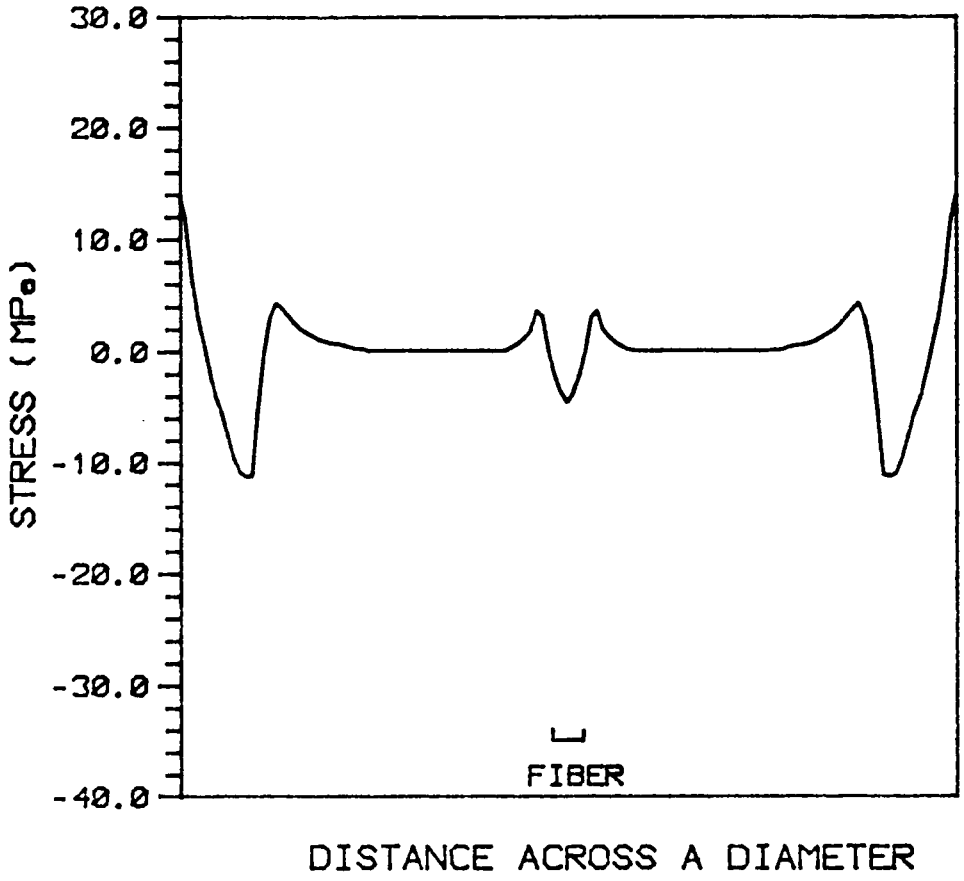
(b)

Figure 8.33 Continued.



(c)

Figure 8.33 Continued.



(d)

Figure 8.33 Continued.

layers remain dry. The surface swelling associated with the diffused water generates compression and this requires that tension be simultaneously generated in the deeper layers, as revealed in Figure 8.33(a) and (b). As water uptake proceeds, the stress is redistributed. When the boundary between no water and some water reaches close enough to the already self-stressed layers, the stress becomes compressive in the resin near the fiber and there is axial tension in fiber, as shown in Figure 8.33 (c) and (d).

There exist annular rings of axial stress in the specimen, see Figure 8.33. As water uptake continues, the axial stress at the outer layer of the specimen is decreased since further swelling releases the initial constraint offered by the unswollen core at initial stage of water immersion; however, the axial stress at the center of the specimen is increased since more constraint is generated, offered by fiber, to balance between the further swelling of the epoxy resin and the fiber of stable dimension. As a consequence, larger axial tension is generated inside the fiber and it may be sufficiently large to fracture fiber.

As discussed previously and shown in Figures 8.4 and 8.33, the advancing front of the swelling layer experiences compressive stress in the axial direction, as a result of which the diffusion coefficient is decreased in the radial direction. The tensile residual stress near the fiber should increase the diffusion coefficient, but as swelling releases the residual stress the diffusion coefficient is observed to decrease; then the axial residual stress becomes compressive and a further decrease in the diffusivity is expected to accompany further swelling.

It should be point out that water uptake by the resin could also introduce a time-dependent relaxation process. This would render D not only concentration-dependent but also time-dependent. No attempt was made to investigate any time-dependence of diffusion coefficient.

8.6.3 Birefringence observation of fiber fracture and identification of the failure modes

Figure 8.34 shows the changing pattern of stress-induced resin birefringence for fiber **B** during a water immersion test. After immersion for 10.5 hours, the birefringence, Figure 8.34(b), is very different from the initial pattern, Figure 8.34(a). Not only has compensation occurred for the "compressive" birefringence; a net "tensile" birefringence has taken its place. As water uptake continues, more volumetric swelling of the matrix occurs, the axial tensile stress in the fiber increases as discussed previously, see Figure 8.33, and eventually becomes large enough to fracture the fiber, Figure 8.34(c). A further increase in immersion time causes the region of birefringence at the fiber break to enlarge(Figure 8.34(d)).

A very different sequence of birefringence patterns was observed for fiber **C**, see Figure 8.35. After 151 hours immersion, the fiber began to fracture, evidence for which is the change of birefringence pattern in figure 8.35(c). The difference in the birefringence pattern associated with fiber fracture in Figures 8.34(c) and 8.35(c), suggests a failure mode different from that for the specimen **B**. From a careful examination of these patterns, one common and two main differences

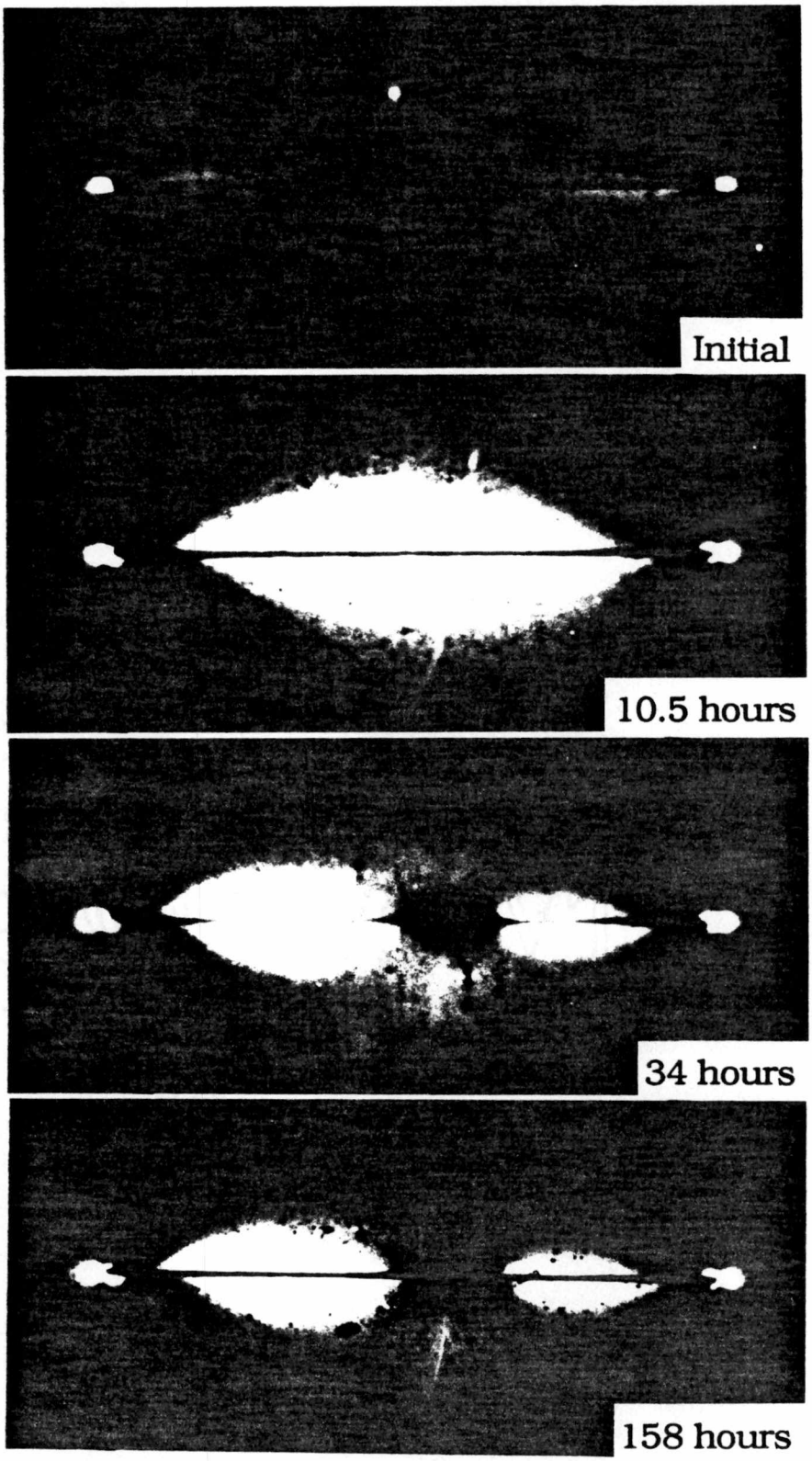


Figure 8.34 The sequence pattern of stress-induced birefringence of fiber **B** during water immersion, viewed at 45° to the polarizer axes.

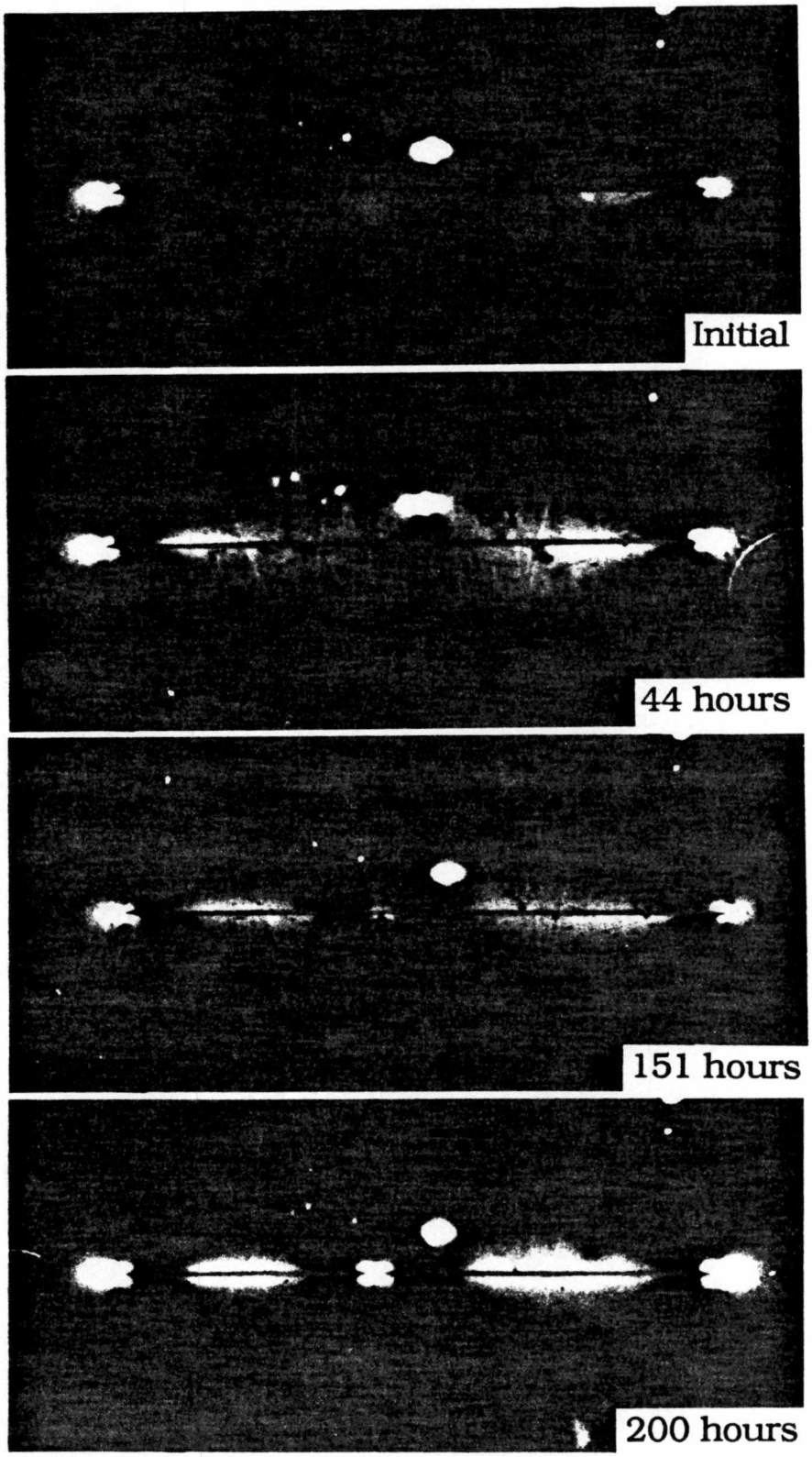


Figure 8.35 The sequence pattern of stress-induced birefringence of fiber **C** during water immersion, viewed at 45° to the polarizer axes.

between the two patterns can be seen. Common in these two fiber failure modes is the fact that the fibers have fractured into two approximately equal lengths, that is, fracture occurs at the fiber center where the axial tensile stress is a maximum[Cox 1952]. The axial tension generated along the fiber during water uptake. by load transfer via interfacial shear stress, can be large enough to fracture the fiber. Of the differences, one is the time required for fiber fracture. Fracture occurred after 10.5 hours immersion for fiber **B** and after 151 hours immersion for fibber **C**.

The second difference concerns the patterns of stress-induced birefringence. When viewed at 45° to the polarizer axes, the pattern of birefringence near a fiber fracture is one of extinction (black contrast) for fiber **B** and one of non-extinction (white contrast) for fiber **C**. This difference reveals a characteristic difference in fracture mode. In order to to explain the difference, the respective optical retardations have been carefully measured. Figure 8.36 shows optical retardation data measured adjacent to the interface and the associated shear stress, plotted as a function of fiber length and immersion time. After fiber **B** fractures, the shear stress near the fracture is still very large. For fiber **C**, the retardation measurements, shown in Figure 8.37, show that the shear stress near the fiber fracture is relieved by the fracture process, that is, debonding has occurred in association with the fiber fracture. Figure 8.38(a) shows a schematic for the fracture mode observed in fiber **B**, which is a disk-shaped or penny-shaped crack oriented perpendicular to the fiber and extending into matrix material. The stress state at fracture is also sketched in Figure 8.38(a).

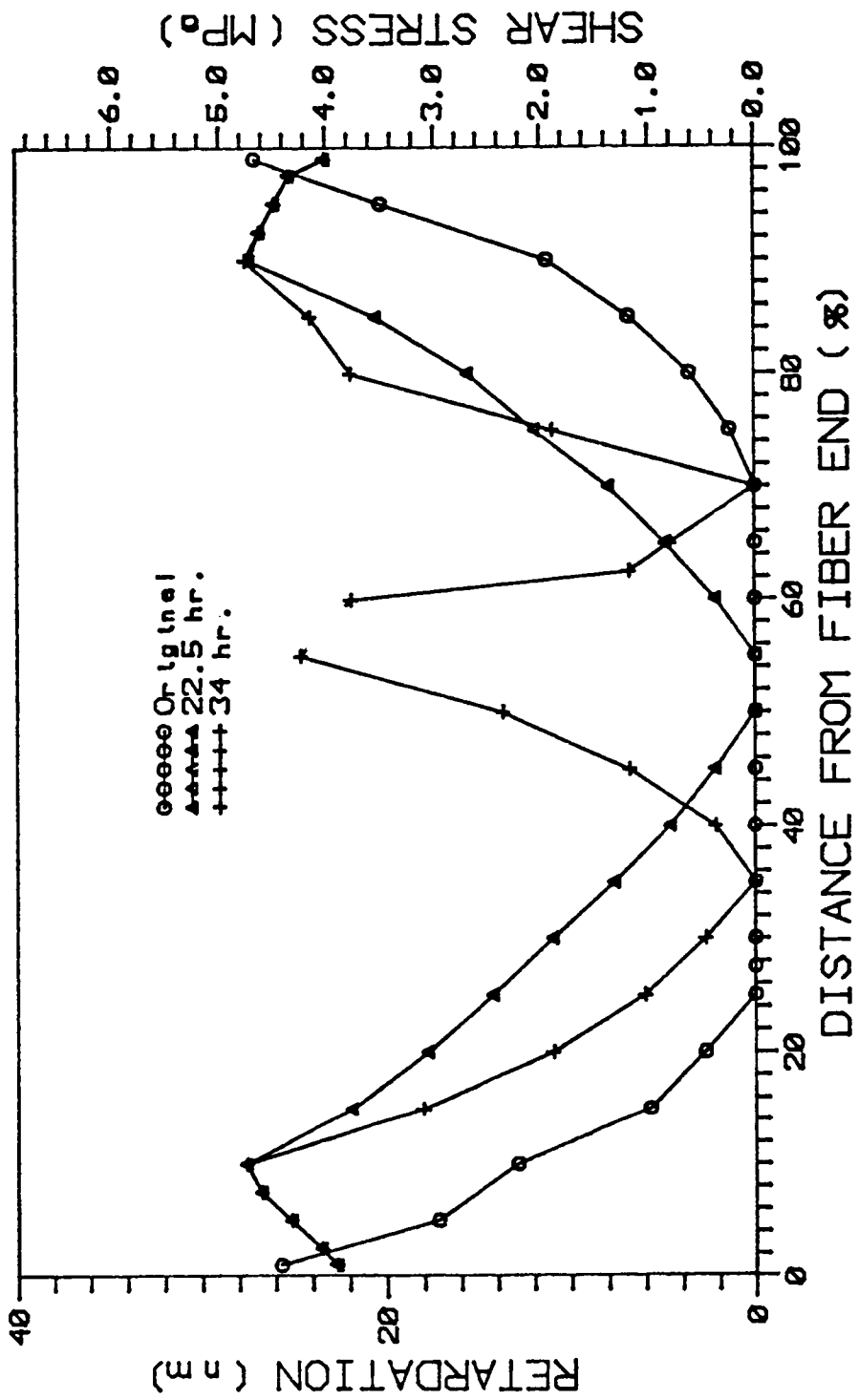


Figure 8.36 Fiber **B** Optical retardation measured through the resin adjacent to the interface and the corresponding interfacial shear stress, plotted as a function of both fiber length and immersion time.

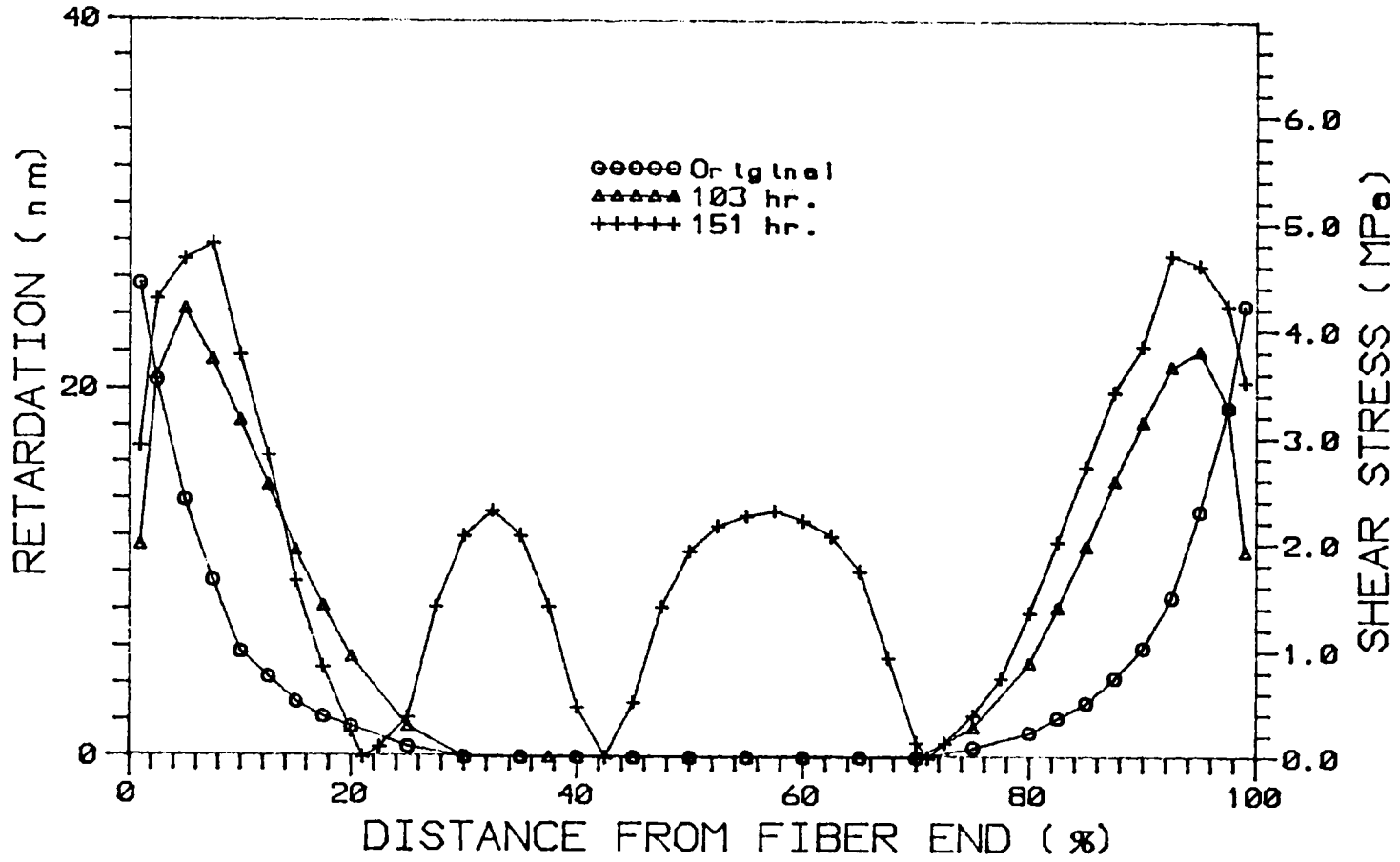
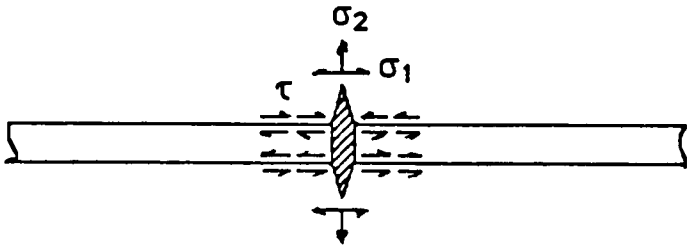
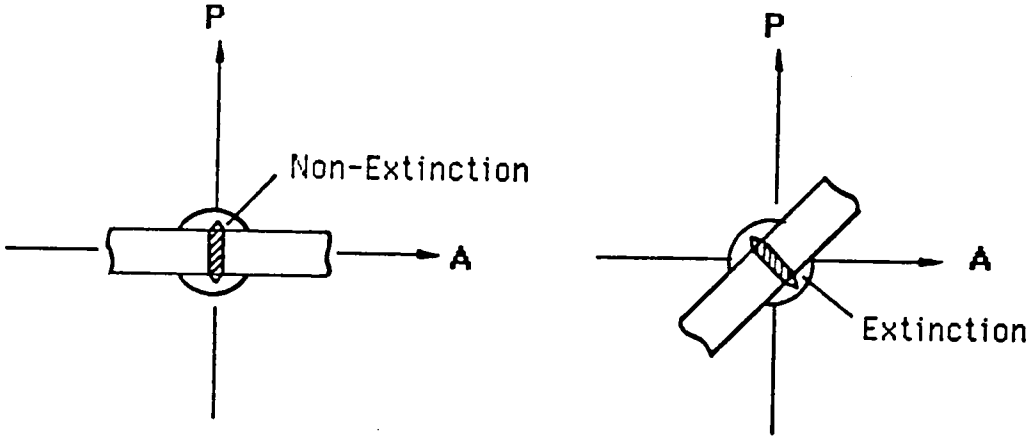


Figure 8.37 Fiber **C** Optical retardation measured through the resin adjacent to the interface and the corresponding interfacial shear stress, plotted as a function of both fiber length and immersion time.



(a)



(b)

Figure 8.38 (a) Schematic of failure mode observed in fiber **B**. (b) The tress birefringence observed with fiber axis at 0° and 45° to the polarizer, **P** and analyzer, **A** axes.

When the directions of principal stress are coincident with the polarization direction of the polarizer and analyzer, extinction occurs. For the stress state in Figure 8.38(a), there are some principal stresses, having 45° direction related to the fiber axis (note that stresses σ_1 and σ_2 in Figure 8.38(a) are not principal stresses), near the fiber fracture since there are large shear stresses. When the fiber axis is at 45° to the axes of the polarizer and analyzer, extinction is observed. When the fiber axis is at 0° to the axes of the polarizers, extinction is not observed, see Figures 8.38(b) and 8.39.

Using the same procedure, the stress state near the fiber fracture for fiber **C** can be identified and is sketched in Figure 8.40(a). Since there is no shear stress near the fiber fracture, the directions of principal stress must be parallel to and perpendicular to the direction of the fiber axis. When the fiber axis is coincident with the polarization direction of either the polarizer or the analyzer, the condition for extinction is satisfied. Figure 8.40(b) shows the conditions for extinction and non-extinction. This analysis is consistent with experimental observation. Figure 8.41 shows what have been seen for Fiber **C**. When viewed at 0° to the axes of the polarizer and analyzer, the pattern appears dark, whereas when viewed at 45° to the axes, the pattern appears bright.

As the water immersion test continues, and more stress is generated, the crack propagates, see Figures 8.42 and 8.43.

Figure 8.44 shows SEM confirmation of the fracture of fiber **B**; a "penny-shaped" crack has propagated from the fiber into the epoxy matrix.

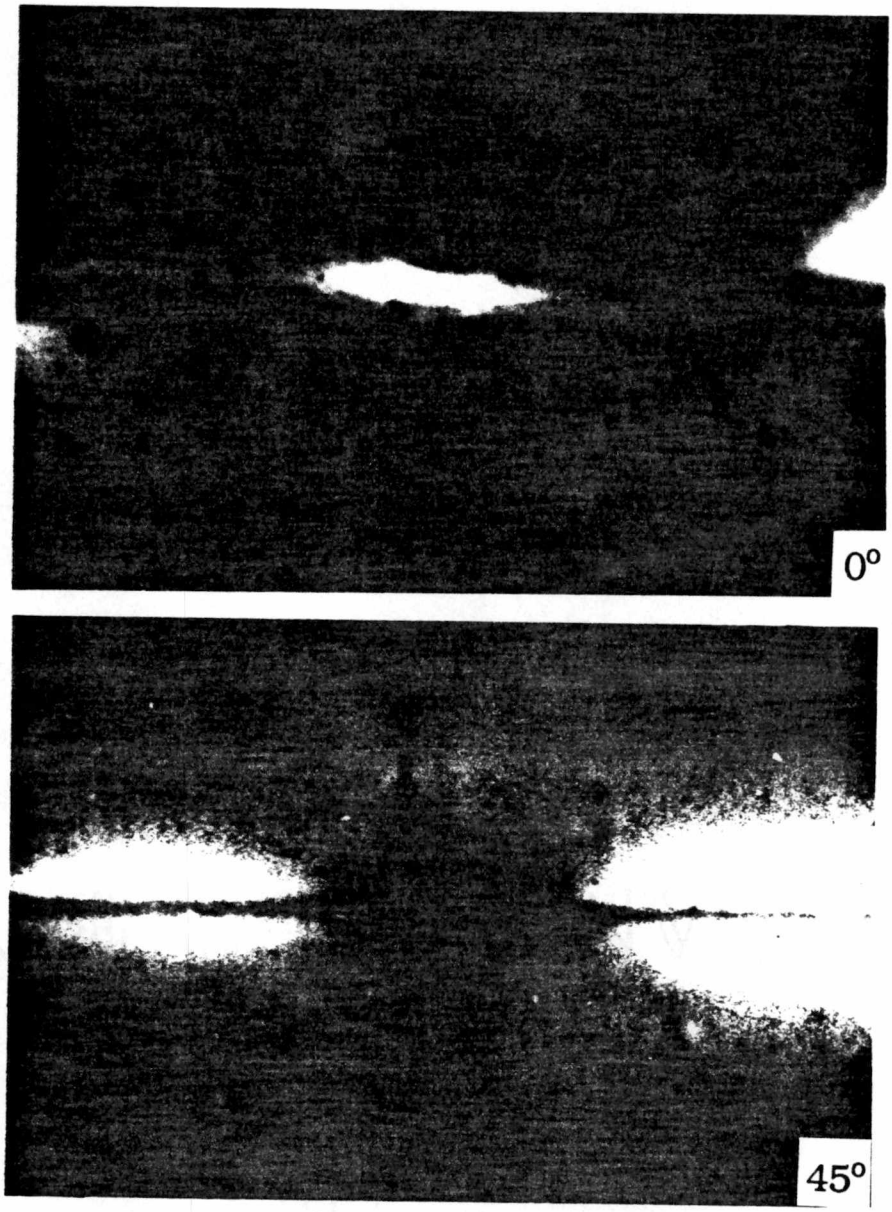
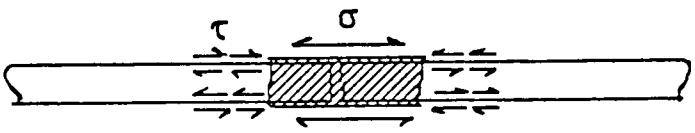
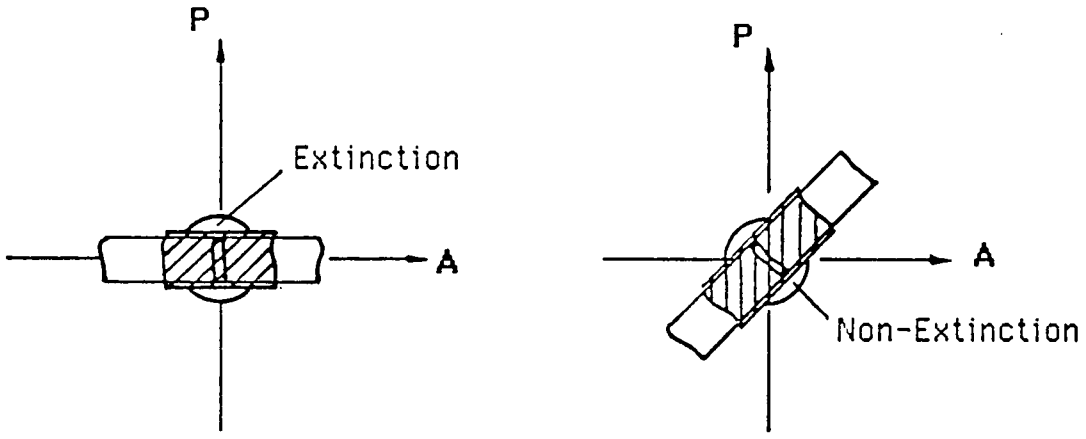


Figure 8.39 The patterns of stress-induced birefringence near the fracture of fiber **B**, viewed at 0° and to 45° to the polarizer axes respectively.



(a)



(b)

Figure 8.40 (a) Schematic of failure mode observed in fiber **C**. (b) the stress birefringence observed with fiber axis at 0° and 45° to the polarizer, **P**, and analyzer, **A**, axes.

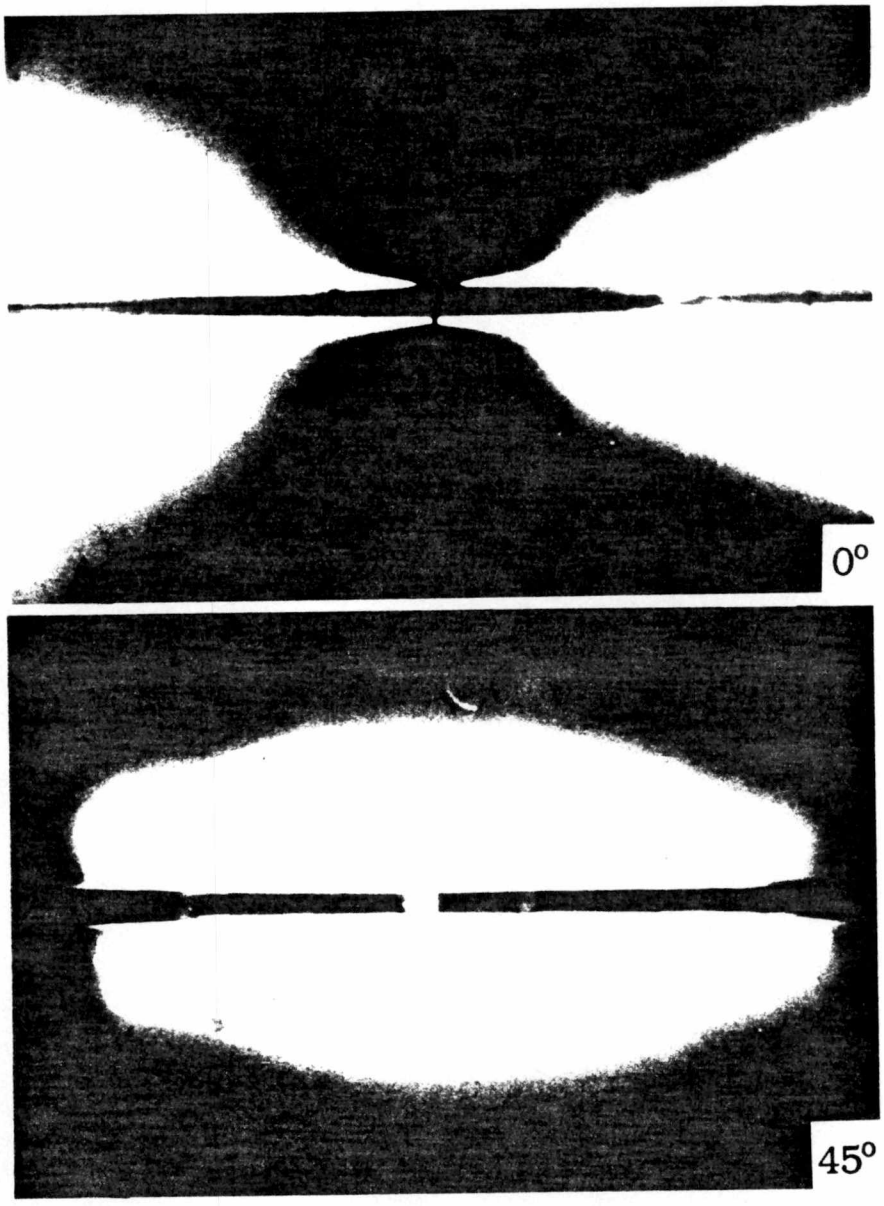


Figure 8.41 The patterns of stress-induced birefringence near the fracture of fiber **C**, viewed at 0° and to 45° to the polarizer axes respectively.

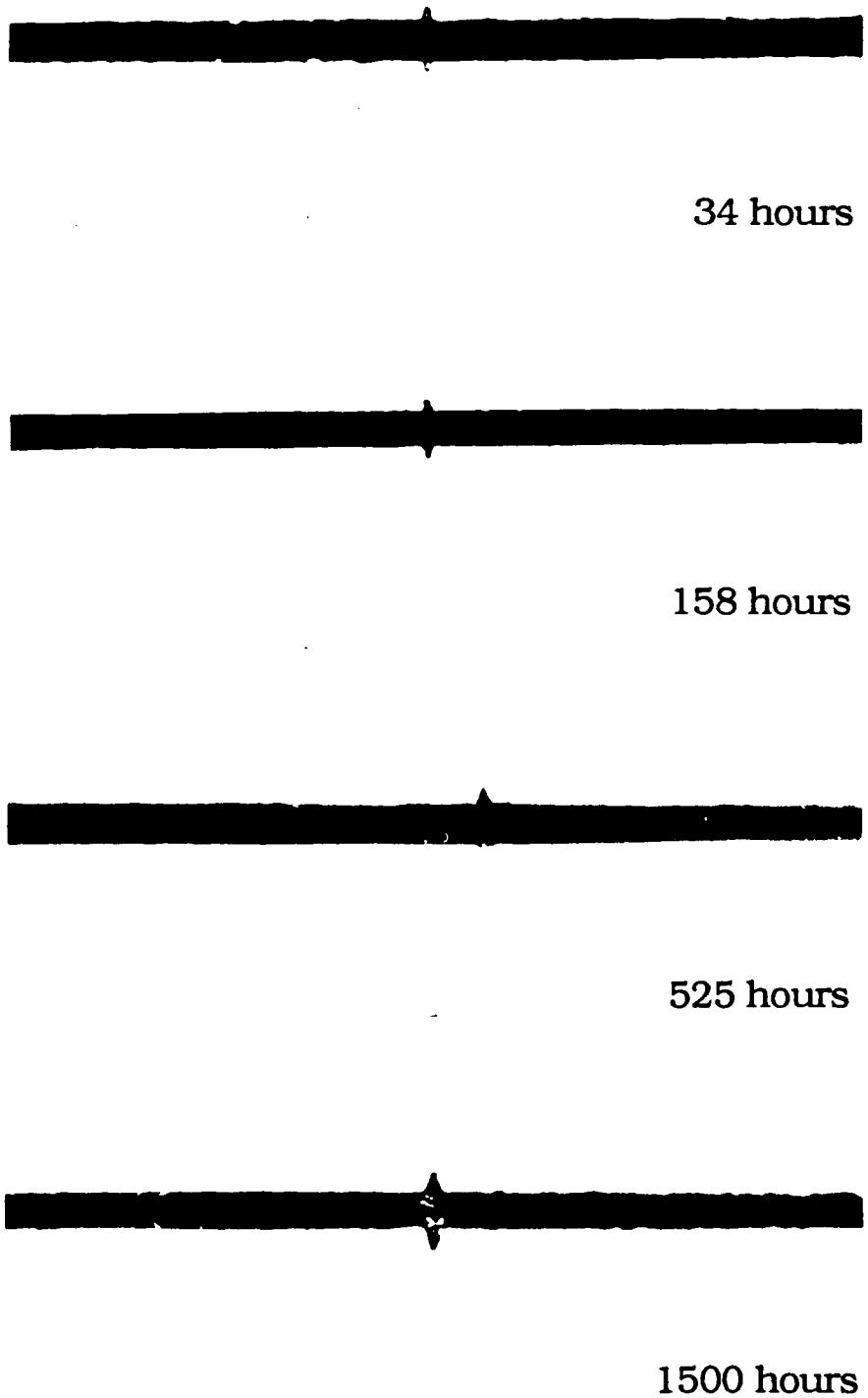


Figure 8.42 The sequence of the fracture of single carbon fiber **B** in epoxy resin after immersion in water at boiling temperature.

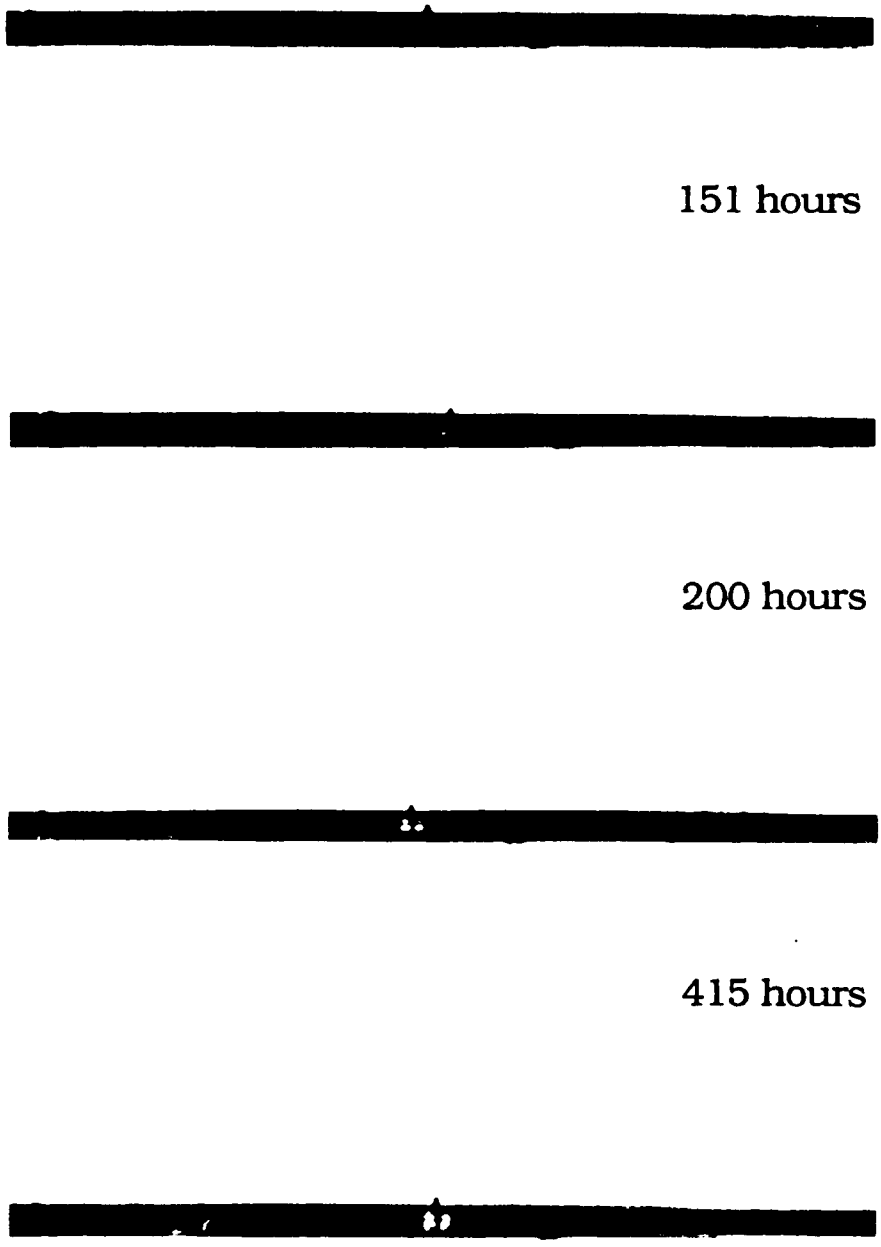


Figure 8.43 The sequence of the fracture of single carbon fiber **C** in epoxy resin after immersion in water at boiling temperature.

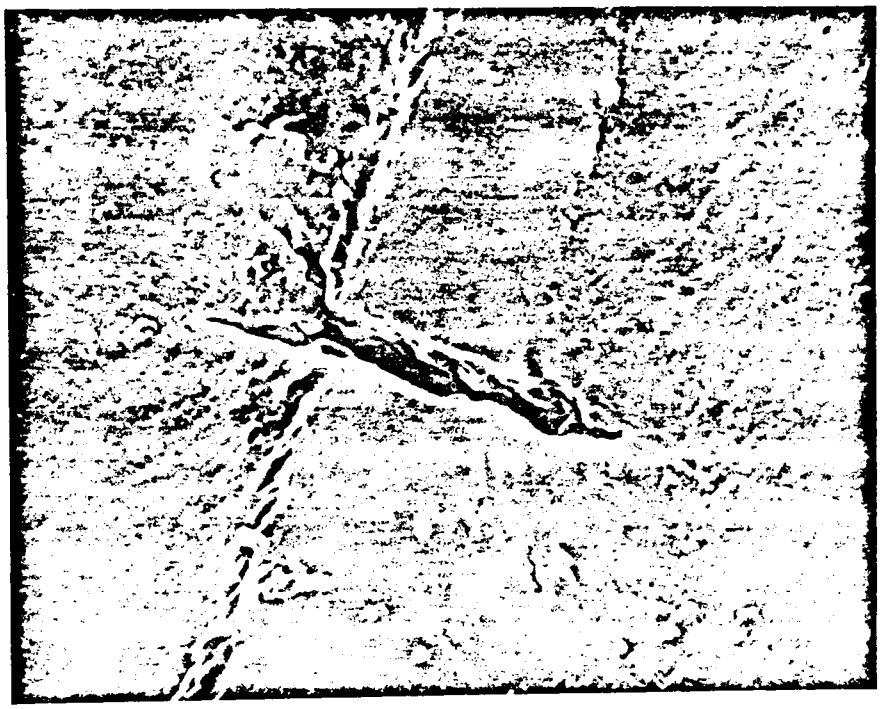


Figure 8.44 The SEM observation of a fiber fracture (fiber **B**) in the matrix self-stressed by water uptake.

Similar crack propagation from single fibers have been observed for fibers **A**, **D** and **E**, see Figure 8.45.

8.6.4 Fiber pull-out length

Figure 8.46 shows two typical fracture surfaces of composite specimens pulled in tension parallel to the fiber direction after 14 days immersion in boiling distilled water. Figure 8.47 shows the distributions of fiber pull-out lengths seen in Figure 8.46. The differences in pull-out lengths of fibers reflect differences in strength and differences in longevity of interfacial bonding. As discussed in Chapter II, Eq. (2-1), the stronger the interfacial bonding, the shorter the pull-out length; the more resistant the interfacial bonding is to attack by the aqueous environment, the shorter the pull-out length. This is controlled by the different responses of the surface treatments to the aqueous environment.

8.6.5 Discussion

The advent of improved fiber surface preparations for carbon fiber is well illustrated by this experiment. The durability of load transfer between matrix resin and fiber has been enhanced to such an extent that swelling deformations large enough to fracture the fiber can be realized. Any reduction in the ability of a fiber/matrix interface to support shear stress will diminish the rate of increase of fiber axial stress with distance from the fiber end. For the extreme case of an interface incapable of supporting any shear stress, there can be no build-up of axial fiber stress. The patterns of resin stress



Fiber **A**

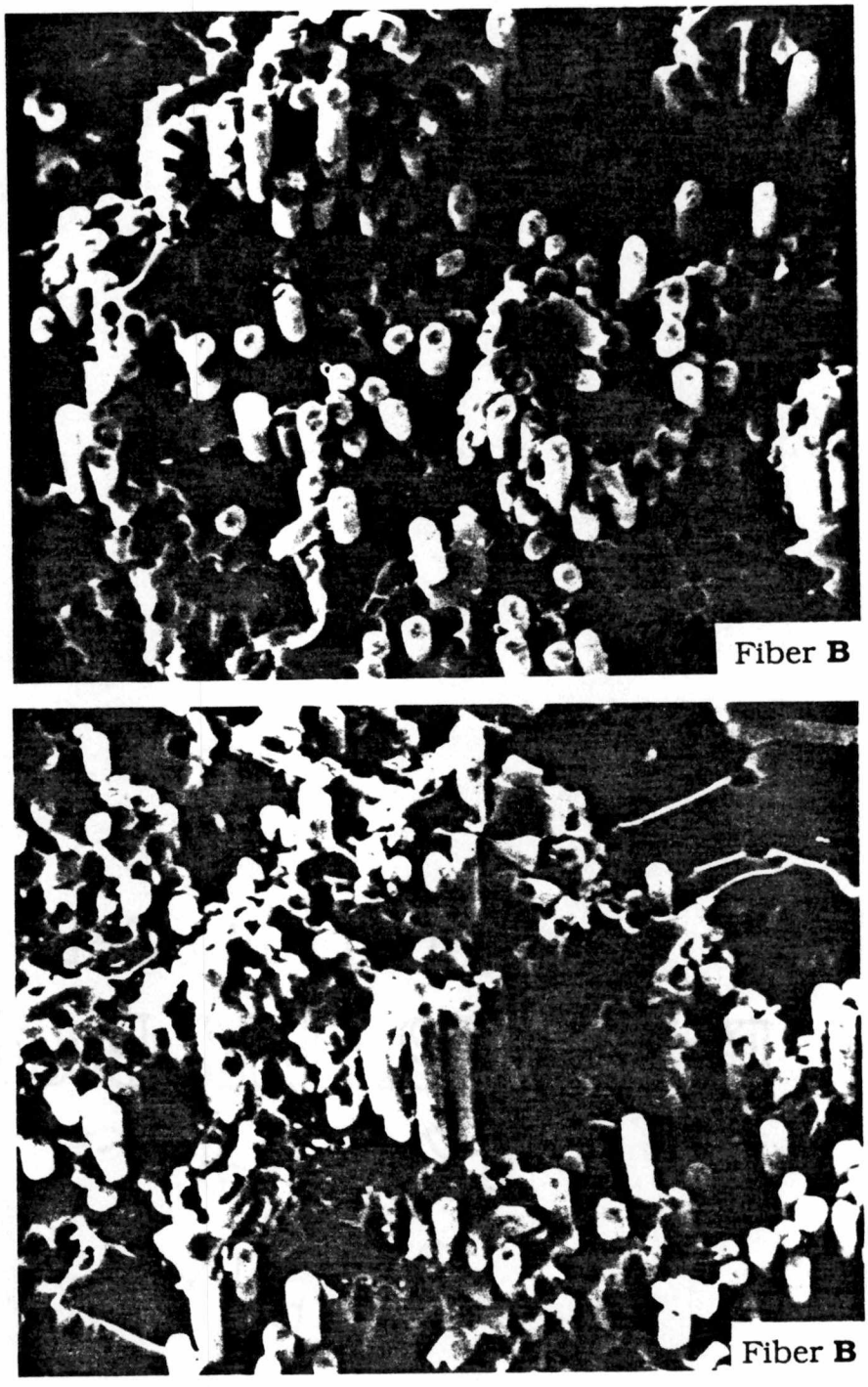


Fiber **D**



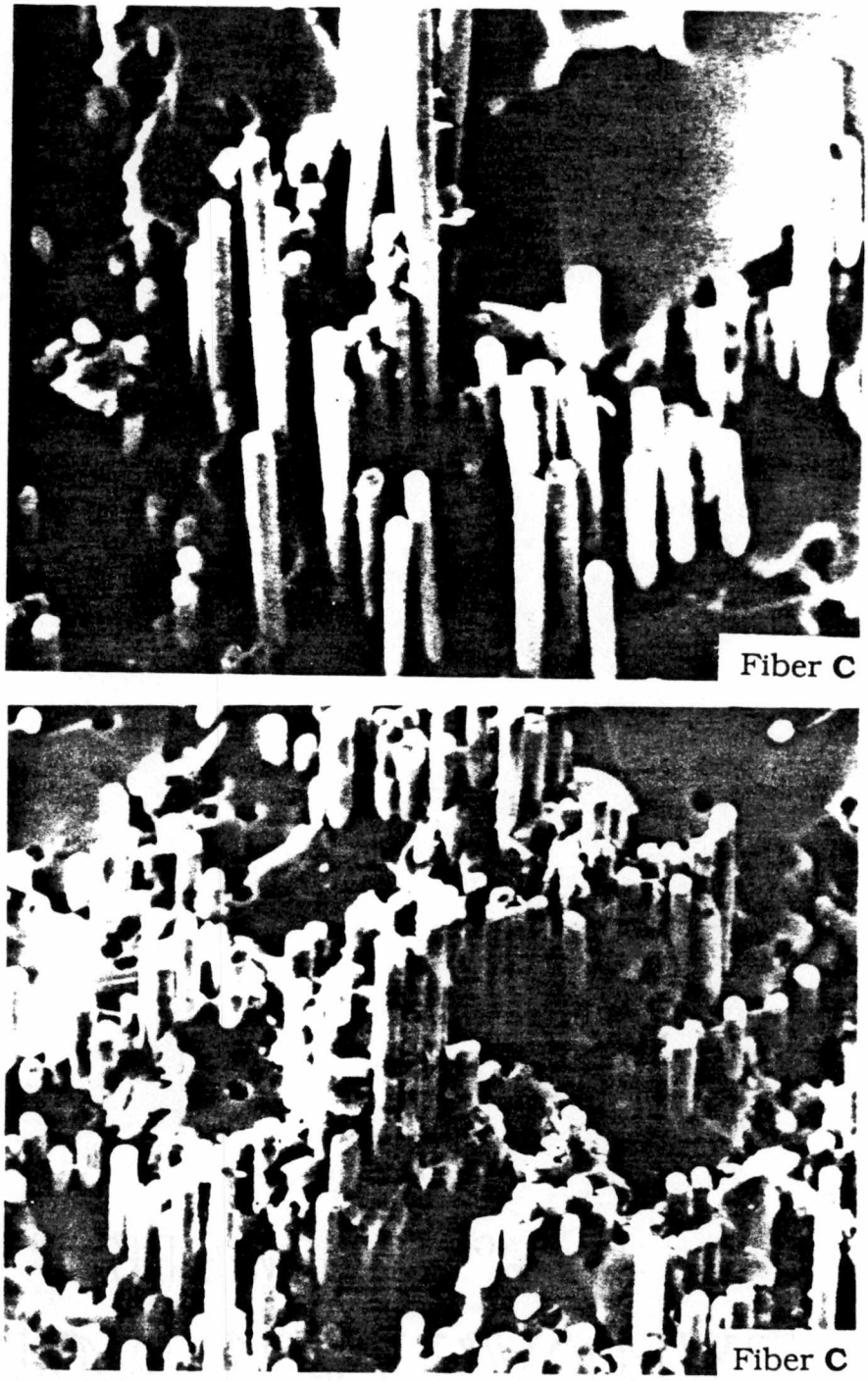
Fiber **E**

Figure 8.45 Similar crack propagation from single fibers for fibers **A**, **D** and **E**.



(a)

Figure 8.46 The SEM observation of the typical fracture surface of specimens after 14 days immersion in distilled water at boiling temperature. (a) a specimen containing a bundle of fiber **B**, (b) a specimen containing a bundle of fiber **C**.



(b)

Figure 8.46 Continued.

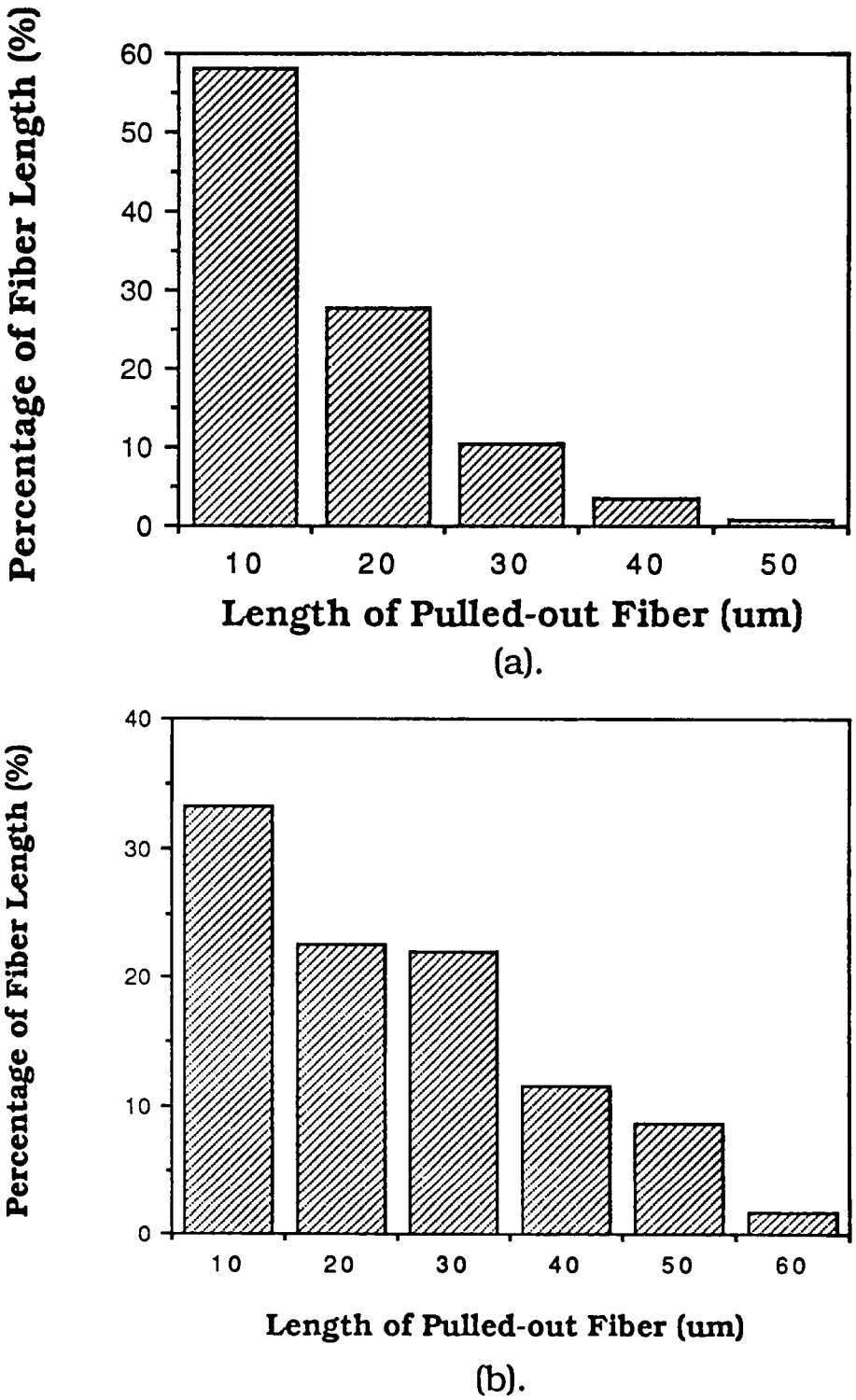


Figure 8.47 The distribution of the pulled-out lengths of fiber under same conditions as Figure 4.46. (a) specimens containing a bundle of fiber **B**, (b) specimens containing a bundle of fiber **C**.

birefringence, shown in Figures 8.34 and 8.35, indicate that the fiber has fractured into two approximately equal lengths, that is, fracture of fiber occurs at the fiber center where the axial tensile stress in a maximum. The longer the interfacial bonds survive during water immersion, the higher the build up the axial fiber stress and hence, the sooner the occurrence of fiber fracture. From this point of view, for interfacial bonds fiber **B** (fracture occurred after 10.5 hours immersion) may have survived longer than for fiber **C** (fracture occurred after 151 hours immersion). These conclusions are consistent with the experimental results further immersion time required for different fibers to debond interfacially. Figure 8.48 shows the times required for the occurrences of debonding and fracture for all five fibers. The longer the interfacial bonds survive during water immersion, the shorter the time before fiber fracture occurs. The same conclusion was also reached from the SEM observations in Figures 8.46 and 8.47 of the fracture surfaces of tensile test specimens.

As discussed above, the effectiveness of reinforcement depends in a very fundamental way upon the stress transfer between fiber and matrix. Stress transfer, however, is limited by the strength of the "interfacial region," i.e., the material within the matrix and adjacent to the surface of the fiber. This material is very much effected by the different surface treatments. The mechanical behavior of the "interfacial region" also controls the stress distribution that leads to fiber fracture. In the wholly elastic case, the maximum interfacial shear stress occurs at the fiber ends, and here we include including at

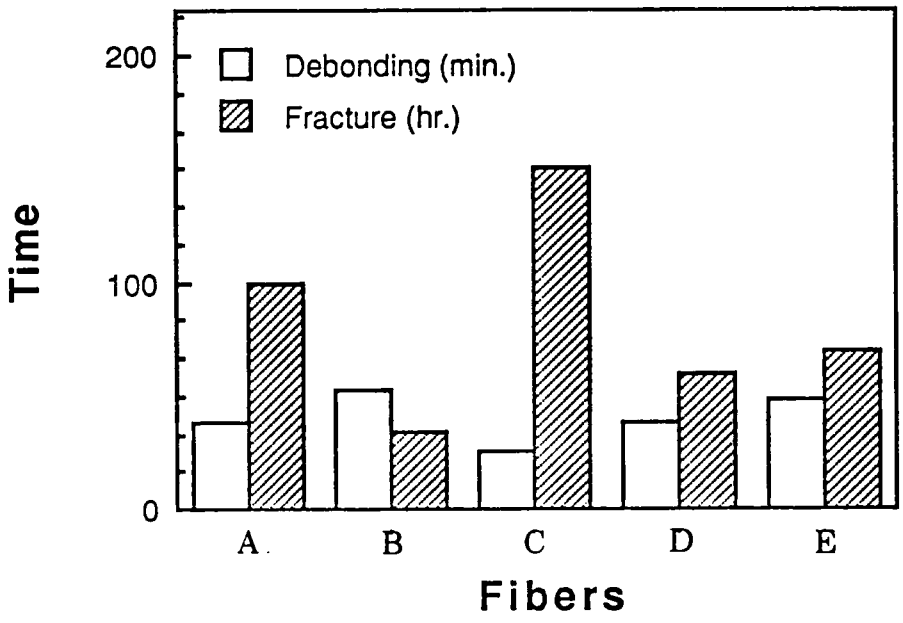


Figure 8.48 The times required for the occurrence of debonding and fracture for all five fibers.

the fiber breaks. If the high shear stress concentration exceeds the "interfacial region" strength, there is local debonding of matrix from the fiber for some distance from the fiber break. This debonding displaces the shear stress concentration towards the centers of the remaining fiber lengths. The matrix adjacent to the fiber at the fracture location is suddenly stressed so as to carry the tension previously carried by the fiber. If the tensile strength of the matrix is exceeded, the fiber breakup propagates into the matrix to form a disk-shaped crack normal to the fiber axis.

Two distinct types of fiber failure behavior have been observed. The energy released during fracture of these specimens, accounts for the fracture surface energies of the fiber and matrix materials, and of interfacial crack. If there exists sufficient bonding between matrix and fiber, the extent to which a disk-shaped or a penny-shaped crack propagates into the resin depends upon the ability of the matrix to absorb energy at the ever increasing circumference of the crack. On the other hand, debonding at the interface between fiber and matrix can relieve the stress concentration induced by fiber fracture and can prevent propagation into the matrix. The energy released and the energy absorbed, and the conditions for these two cases occurring have been discussed by Mullin and Mazzio [1971].

8.7 Protective coating

The caustic foci generated by the smoothly curved edges of polymer coatings on the COB during water immersion have been recorded both periodically by photographing and continuously by video

recording.

Five specimens, identified in Table 5.1, have been investigated.

Most, if not all, organic coatings are permeable to moisture. Apart from swelling in order to accommodate the presence of water, the coating slowly permits access of water to, and probably corrosion of, the underlying substrate. Depending on the Pelling-Bedworth ratio, the products of corrosion are likely to bolster the swelling. In such cases, the overall swelling, and hence the measured change in caustic geometry, is attributable partly to the coating and partly to the substrate, see Figure 8.49.

8.7.1 Volumetric swelling of substrate associated with water uptake

The volumetric swelling associated with substrate corrosion has been investigated using the multiple-beam interferometry technique. The experimental set-up is similar to that illustrated in Figure 5.9 with a coated optical flat, in place of the uncoated optical flat.

Figure 7.4 schematically shows multiple-beam interference generated in the space between an optical flat and a highly reflective surface coated with transparent polymer. Each of a set of parallel reflected rays bears a fixed phase relationship to all the other rays. The phase differences arise from optical path length differences after the various reflections. The waves are coherent and, if collected and brought to a point focus by a lens, an interference pattern is obtained. When two nearly identical periodic patterns are superimposed one on the other, moire fringes are formed. The spatial distribution of moire fringes, which are contours of the specimen with contour level with

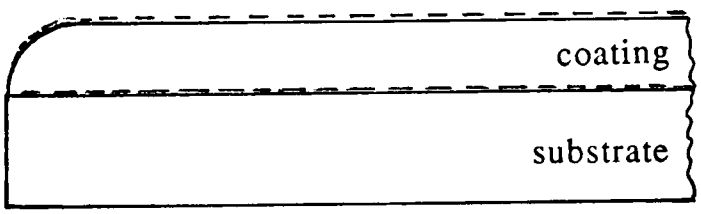


Figure 8.49 Schematic, showing the overall thickness change of coating and substrate. Solid lines indicate dimensions of an as-received specimen; dashed lines represent dimensions after water uptake.

respect to a reference flat differing by $\frac{\lambda}{2}$ from a dark or bright fringe to the next, faithfully follows normal displacement of the specimen surface.

Experimental results for specimens #2, #3 and #5, obtained by using multiple beam interference to generate moire fringes, are shown in Figures 8.50-52. The moire fringes from these photographs are sketched in Figure 8.53 and, for each specimen, they indicate that the normal displacement at the the substrate/coating interface is very small, less 1/4 wavelength (λ=632.8nm). The average displacement in the direction normal to the specimen plane, obtained by dividing the swelling volume obtained by integrating the displacement revealed in Figure 8.53 by the area exposed to water, see Figure 8.54, suggests that the effects of post-curing treatments of specimens #2 and #3, on the absorption of water by the substrate materials are not significant.

8.7.2 Volumetric swelling of coatings

Figure 8.55 shows schematically the formation of the caustic focus generated by the curved edges of the coating on the COB. Figure 8.56 is typical of the observed caustic focus so generated. The geometry of the caustic focus can be obtained by measuring its size at different distances from the specimen using either conventional photography or a video camera. Figures 8.57-60 are data from the caustic focus for the different samples after different water immersion times. The coating surface profiles obtained by inverting the caustic focus using interative method outlined in the Chapter IV, are

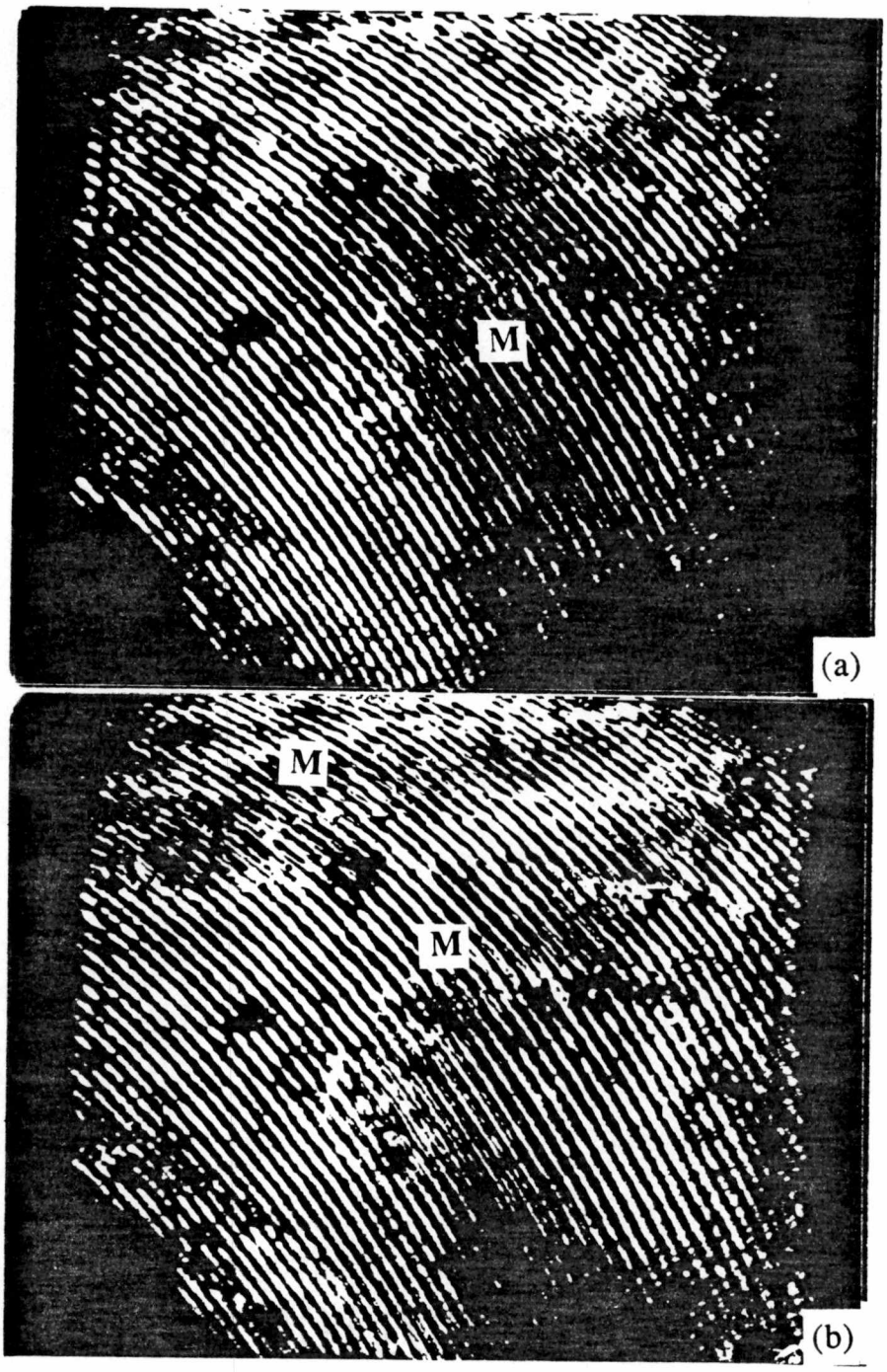


Figure 8.50 Moire fringes, **M**, for sample #2 after immersion in distilled water at 25°C for (a) 10 days and (b) 20 days.

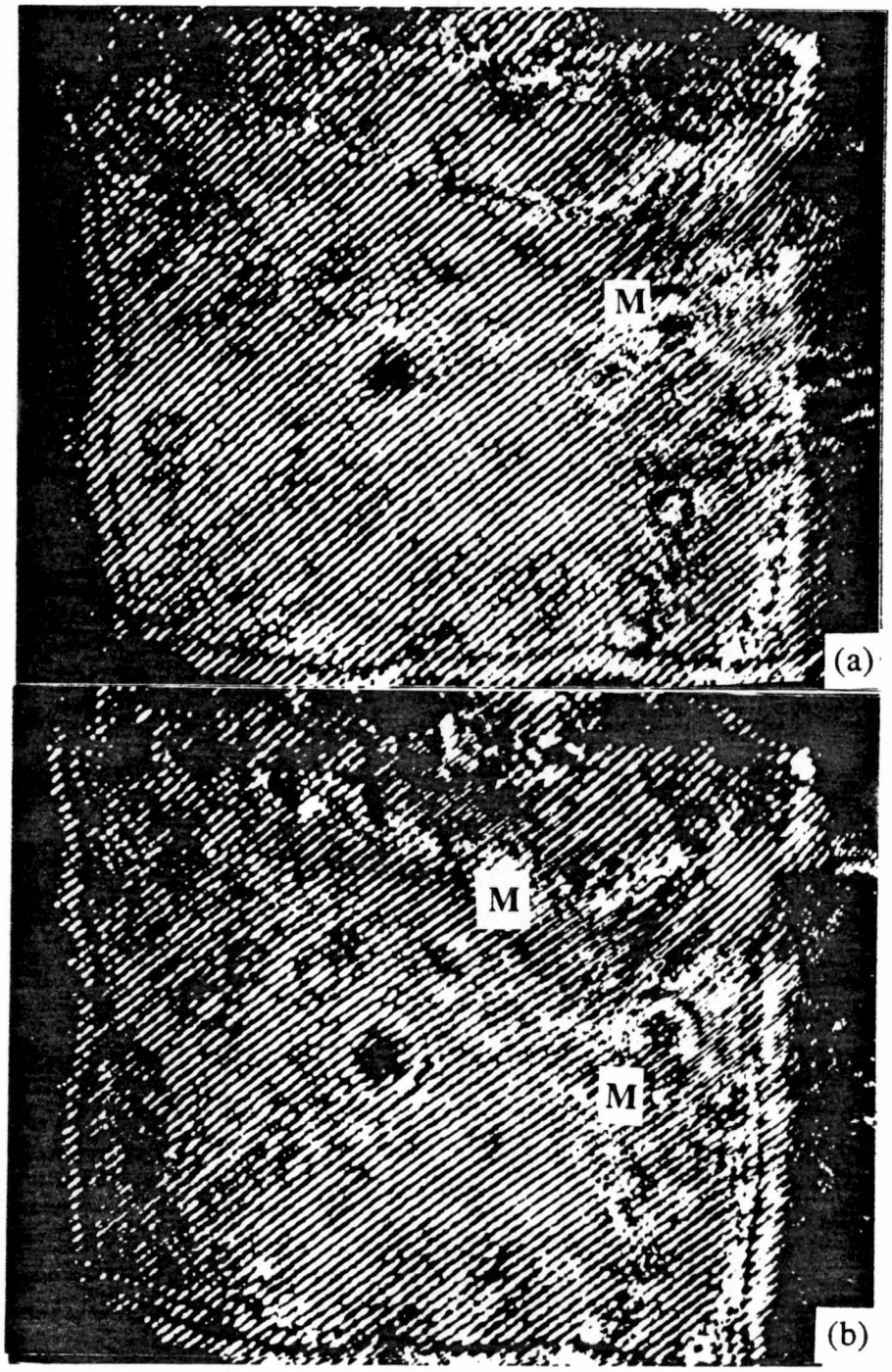


Figure 8.51 Moire fringes, **M**, for sample #3 after immersion in distilled water at 25°C for (a) 13 days and (b) 33 days.

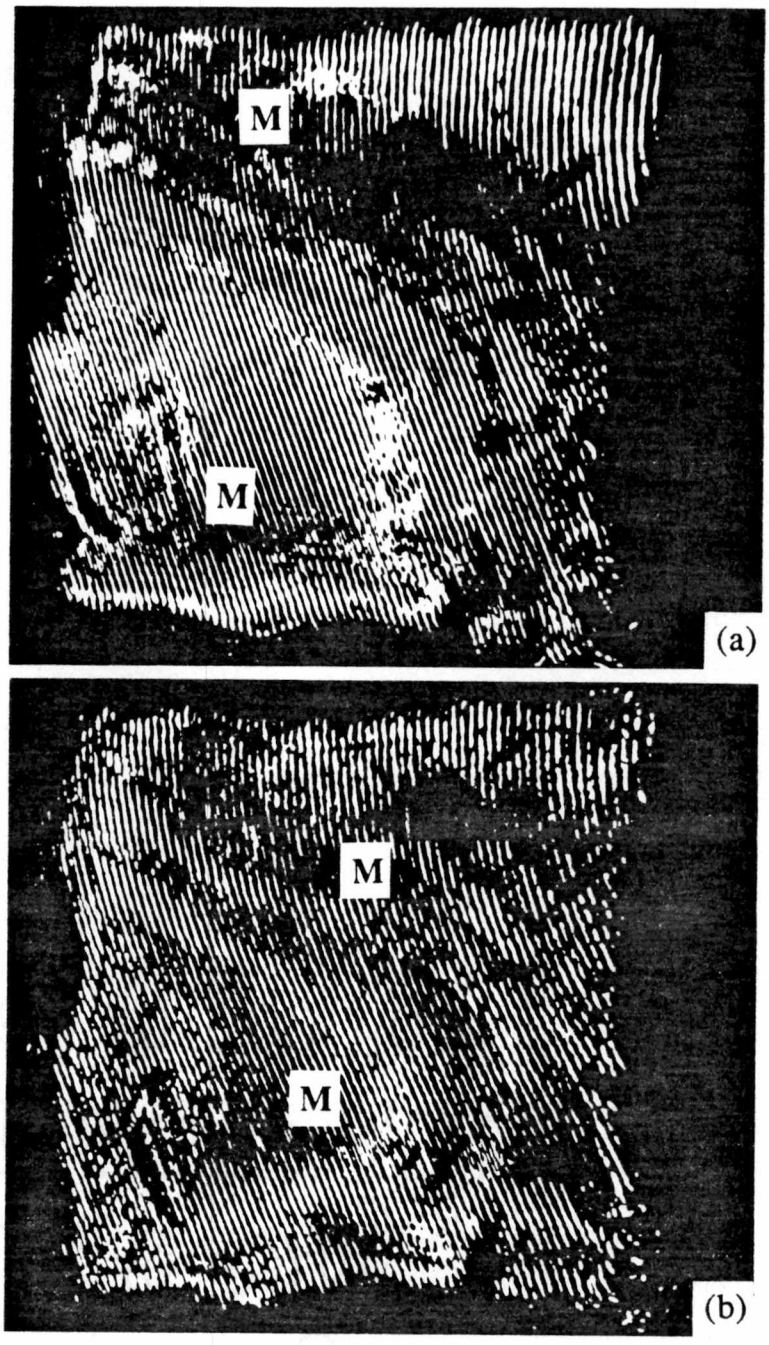


Figure 8.52 Moire fringes, **M**, for sample #5 after immersion in distilled water at 25°C for (a) 12.5 days and (b) 28.5 days.

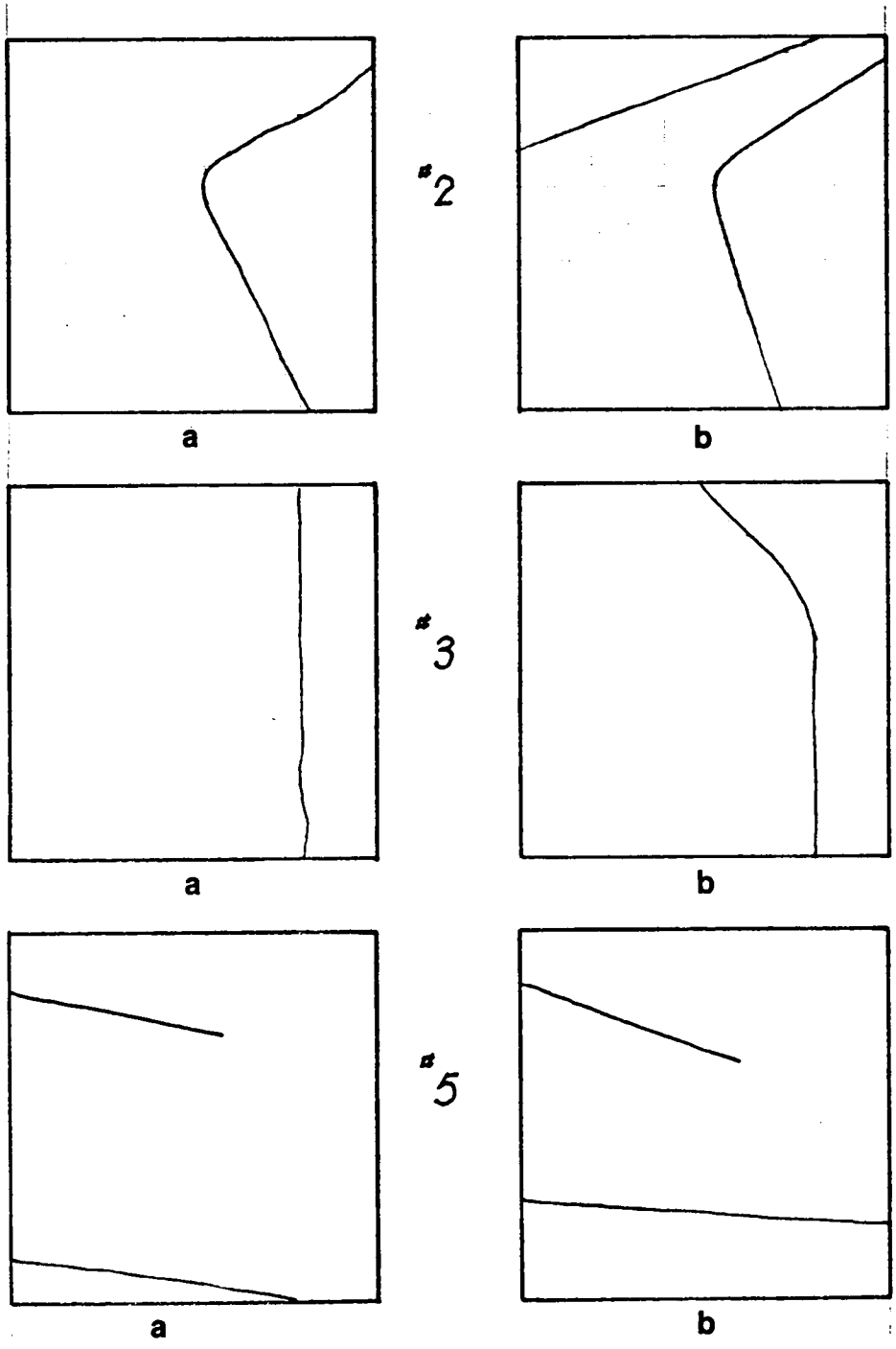


figure 8.53 Sketches of the Moire fringe patterns for the samples #2, #3 and #5, photographed in Figures 8.51, 8.51 and 8.52.

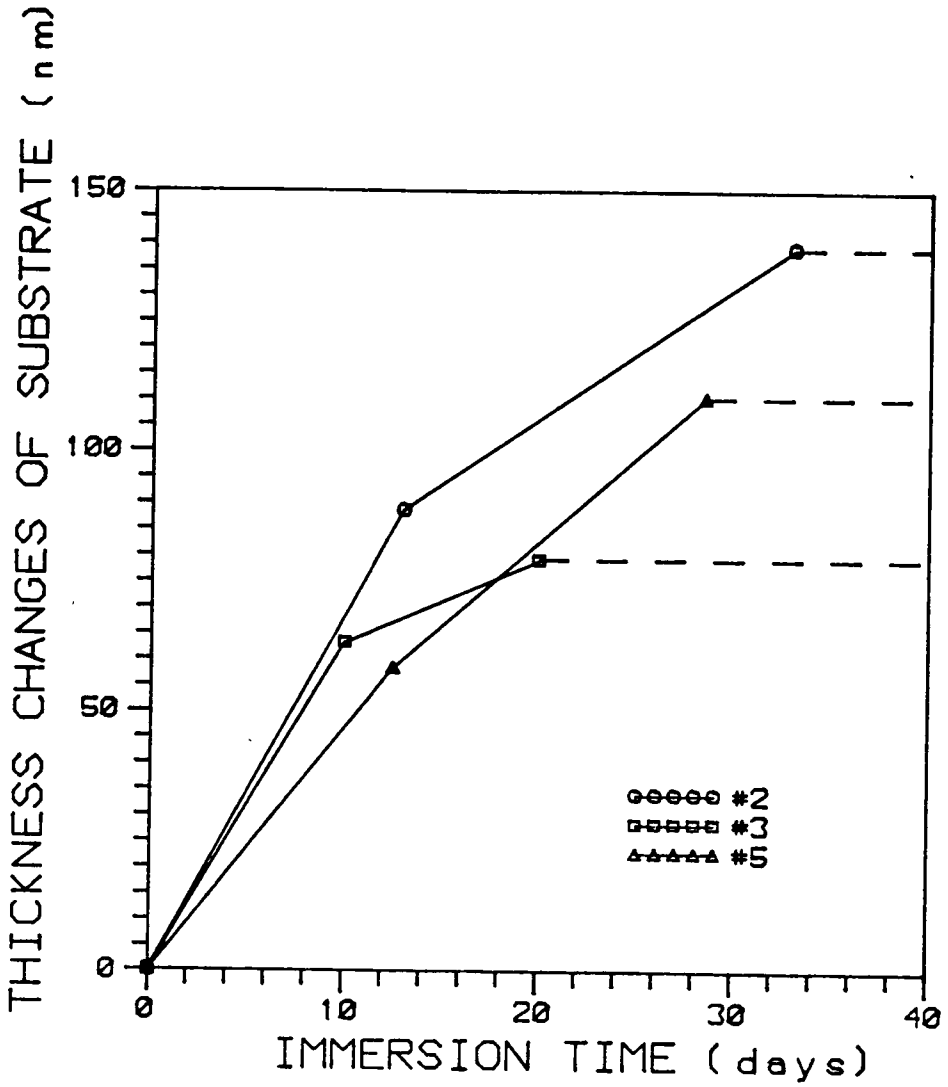


Figure 8.54 The thickness increase of the substrate during water immersion of samples #2, #3 and #5.

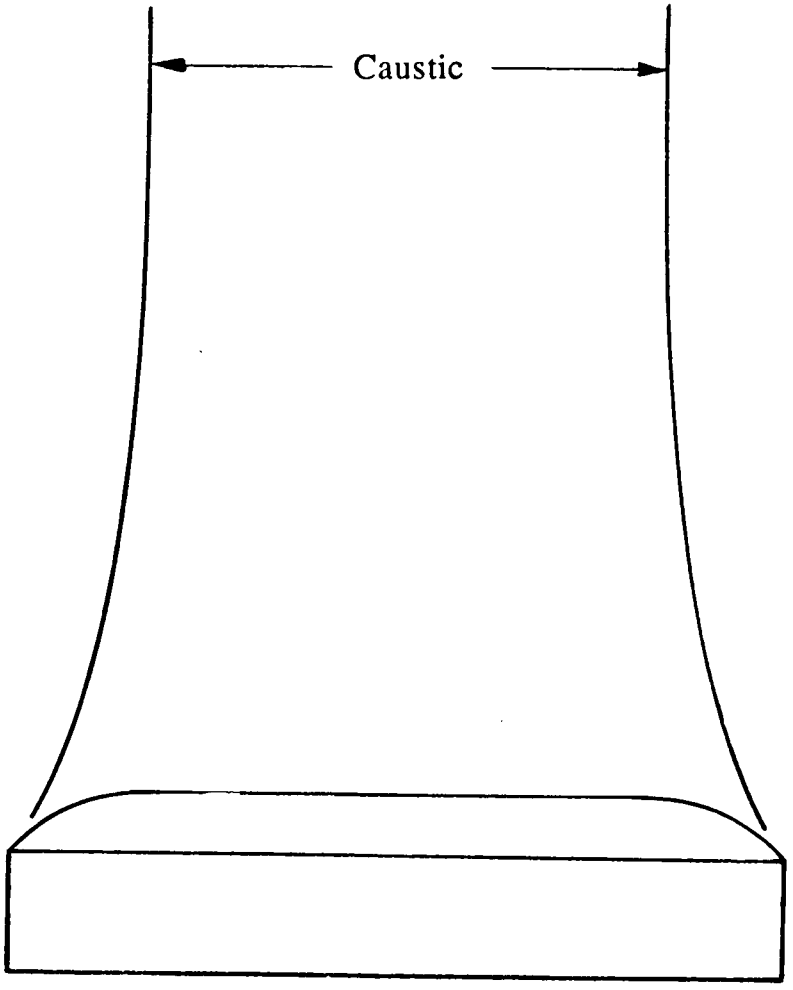


Figure 8.55 Schematic of caustic focus generated by the curved edges of the coating on the COB.

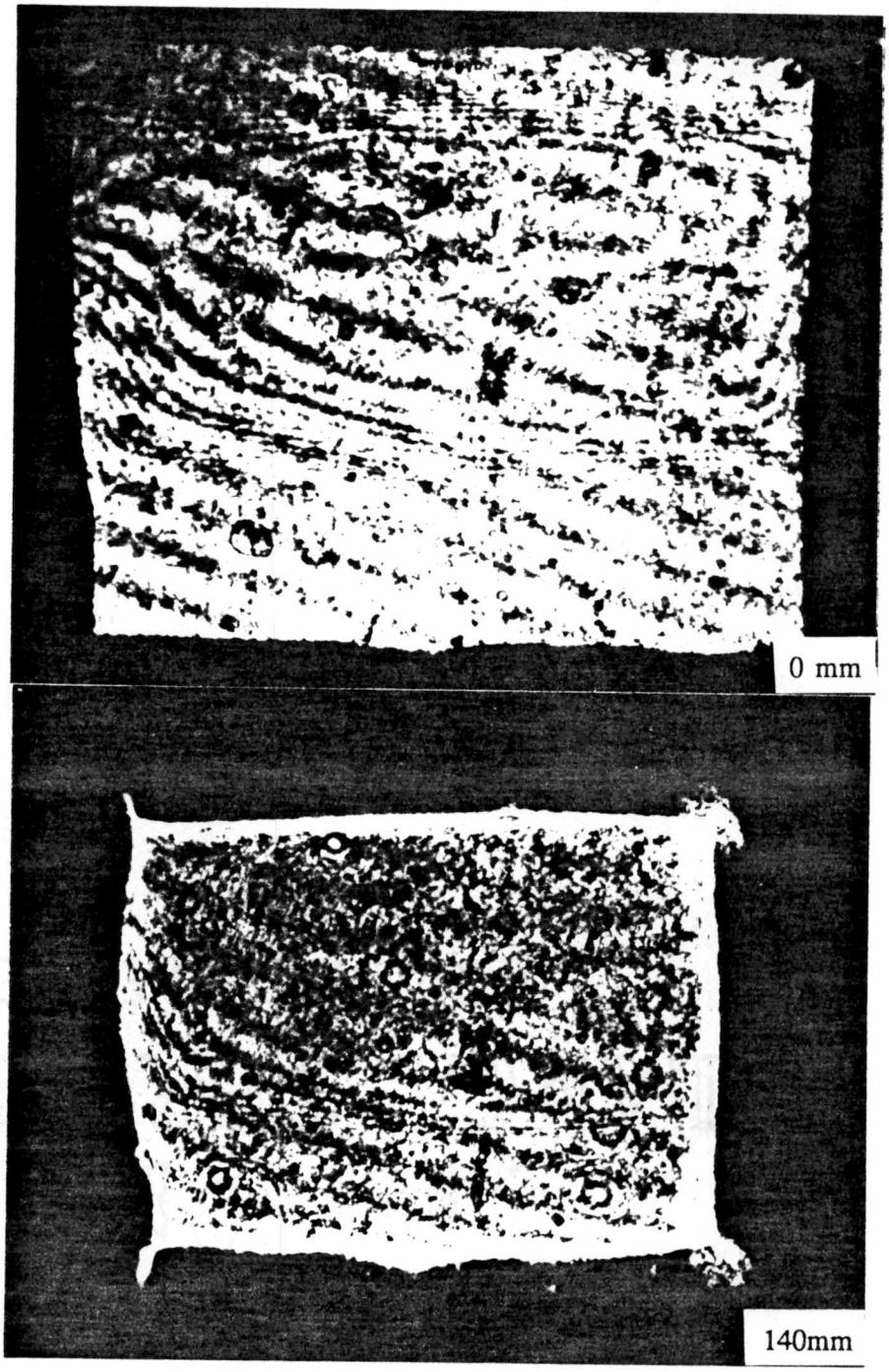


Figure 8.56 The caustic focus (bright "picture frame") generated by the curved edges of the polymer coating and observed at four different distances from the specimen surface.

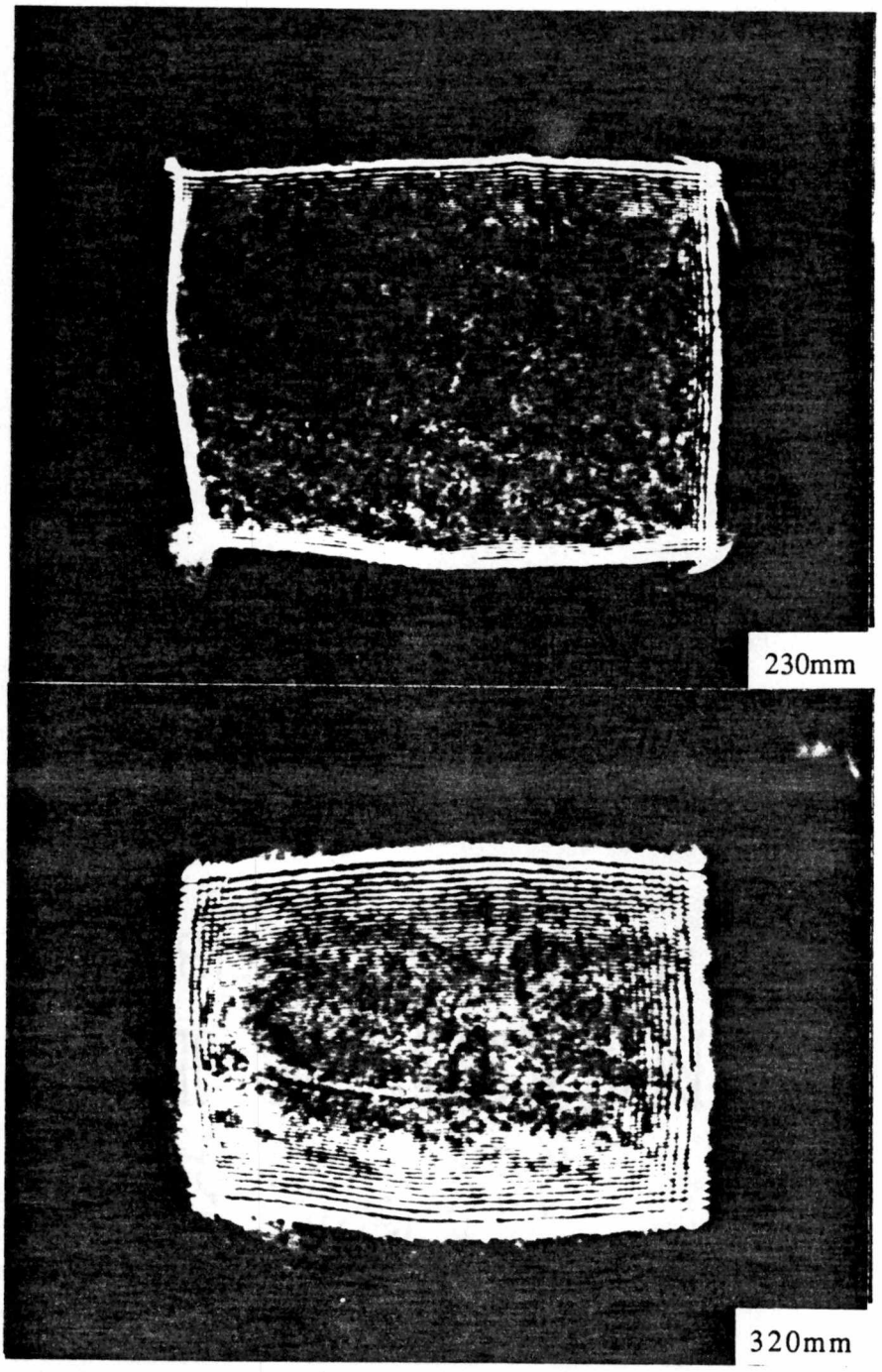


Figure 8.56 Continued.

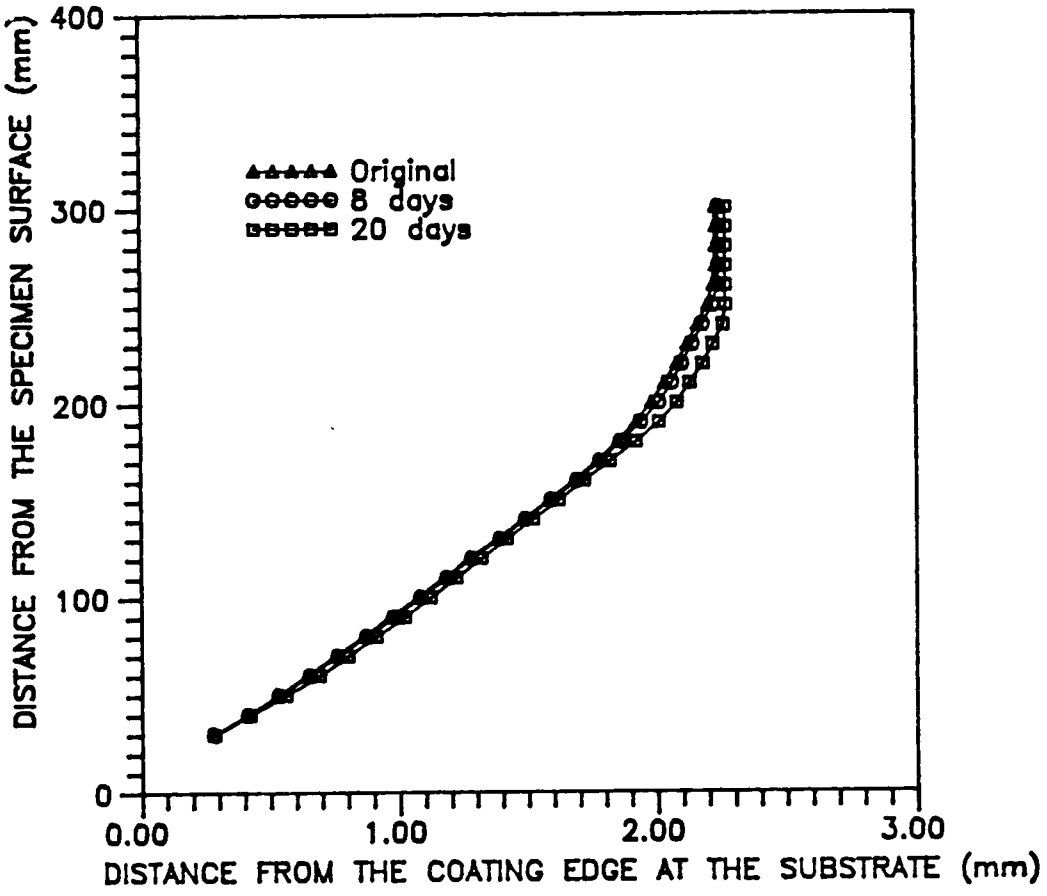


Figure 8.57 The measured caustic focus for sample #1 immersed in distilled water at 25°C.

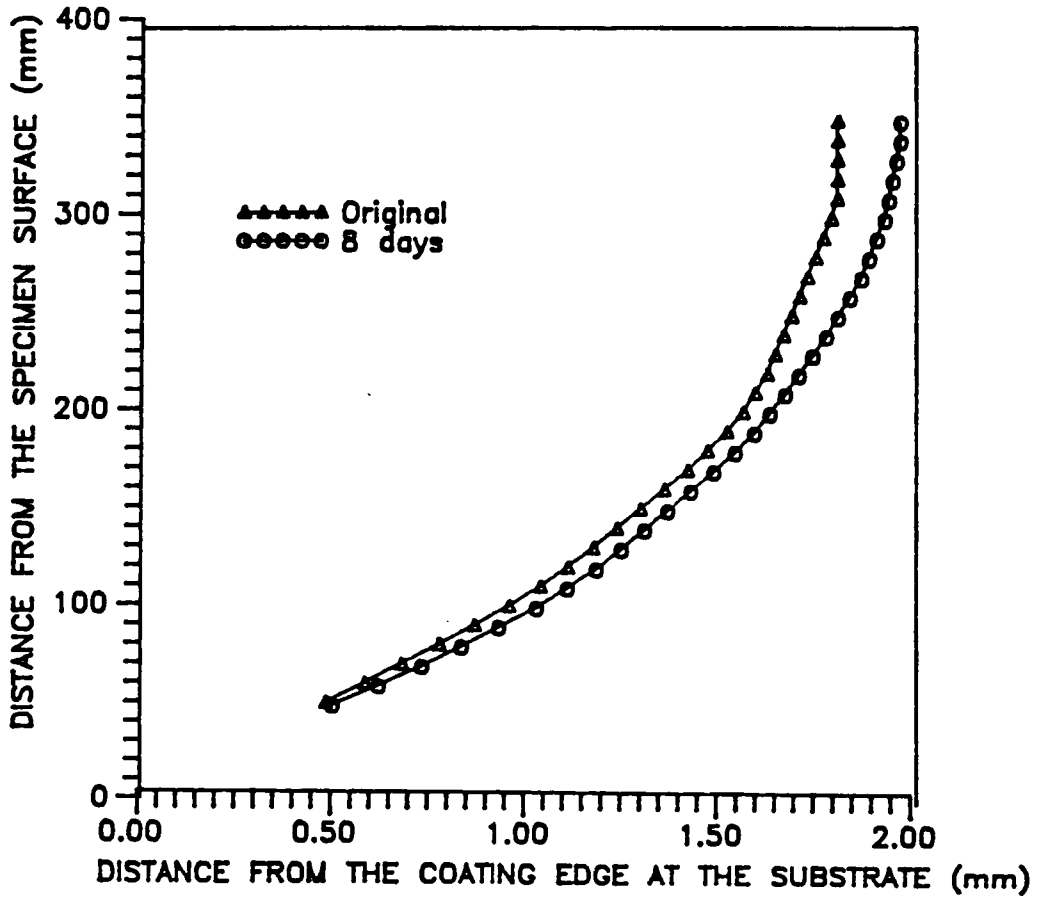


Figure 8.58 The measured caustic focus for sample #2 immersed in distilled water at 25°C.

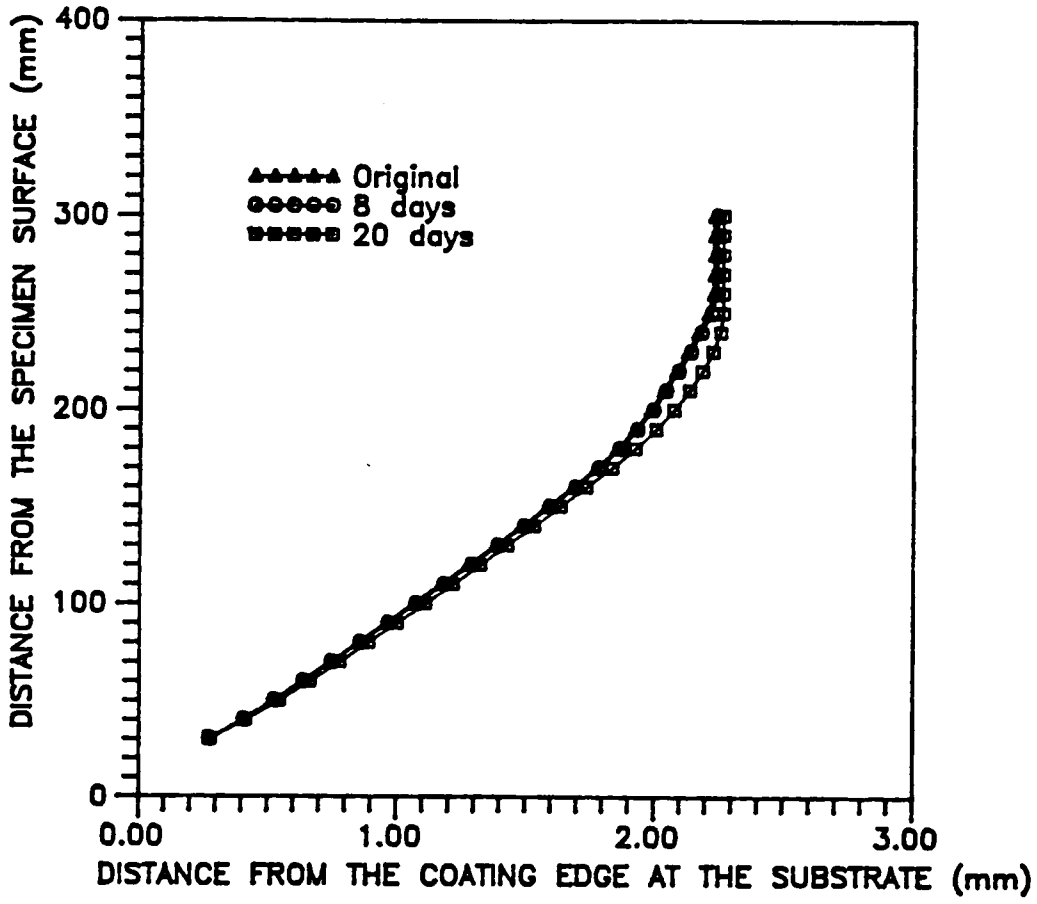


Figure 8.59 The measured caustic focus for sample #3 immersed in distilled water at 25°C.

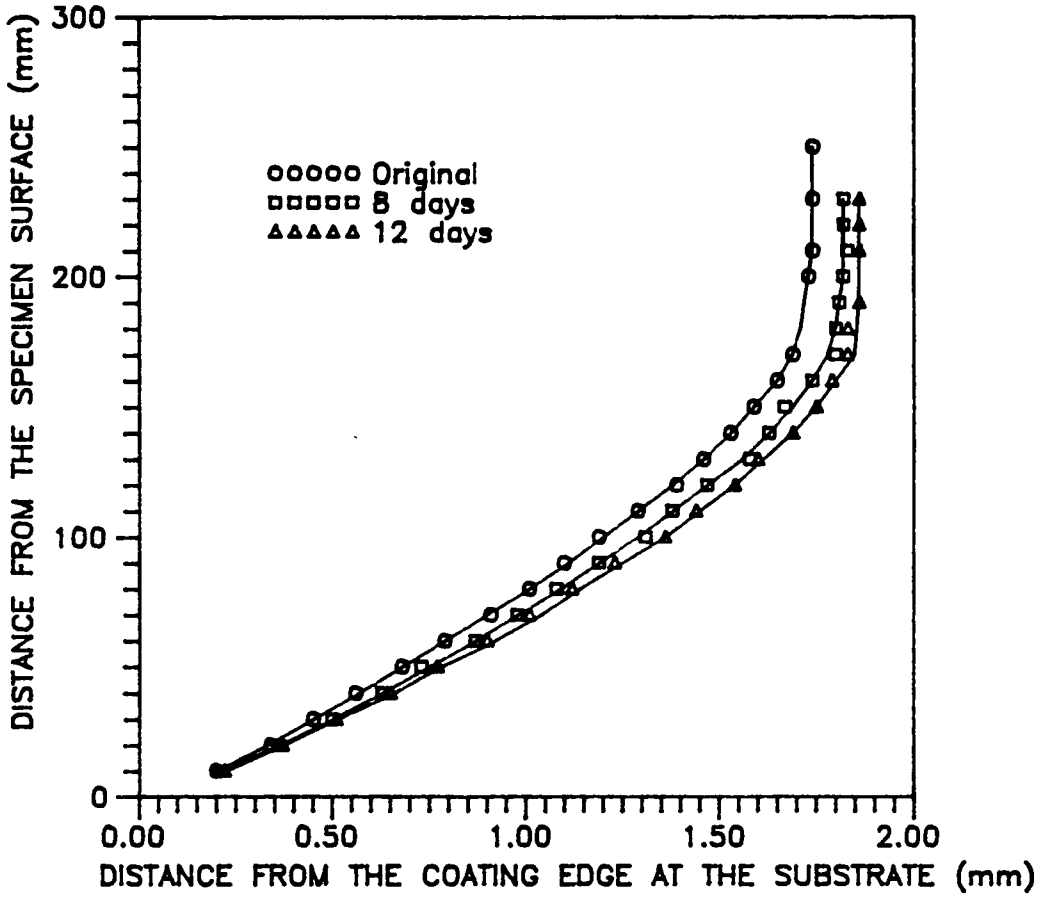


Figure 8.60 The measured caustic focus for sample #4 immersed in distilled water at 25°C.

presented in Figures 61-64. We note that the coatings on samples #1, #2, #3 and #4 appear to be of different as-received thickness. There are two possible explanations for this. Either the thickness is not well controlled by the coating process, or the reference point from which measurements are made is different for each sample. The absolute values for the increase in coating thickness attributable to water uptake, however, are reliable since these values are not changed significantly if the edge points of the surface profiles are extrapolated to a reasonable point in order to make the original coating thicknesses identical.

Since the samples have been treated under different conditions, see Table 5.1, the coatings are expected to exhibit different responses to water immersion tests. These differences have been demonstrated by comparing the normal displacement well within the uniformly flat region of surface coating, as shown in Figure 65. Sample #3, which had been subjected to 11 days salt spray, has lowest swelling rate, i.e., smallest slope in Figure 8.65, and lowest saturated value of water uptake. Sample #1, which had been exposed for 11 days in a humidity chamber, has lower swelling rate and lower saturated value of water uptake. Although samples #2 and #4 have almost identical swelling rates, the saturated water contents are different. This latter difference may be attributed to the effects of different post-curing treatments.

8.7.3 Failure modes of coating and substrate

In order to investigate the durability of the protection function of the coatings, an extended water exposure test was performed by

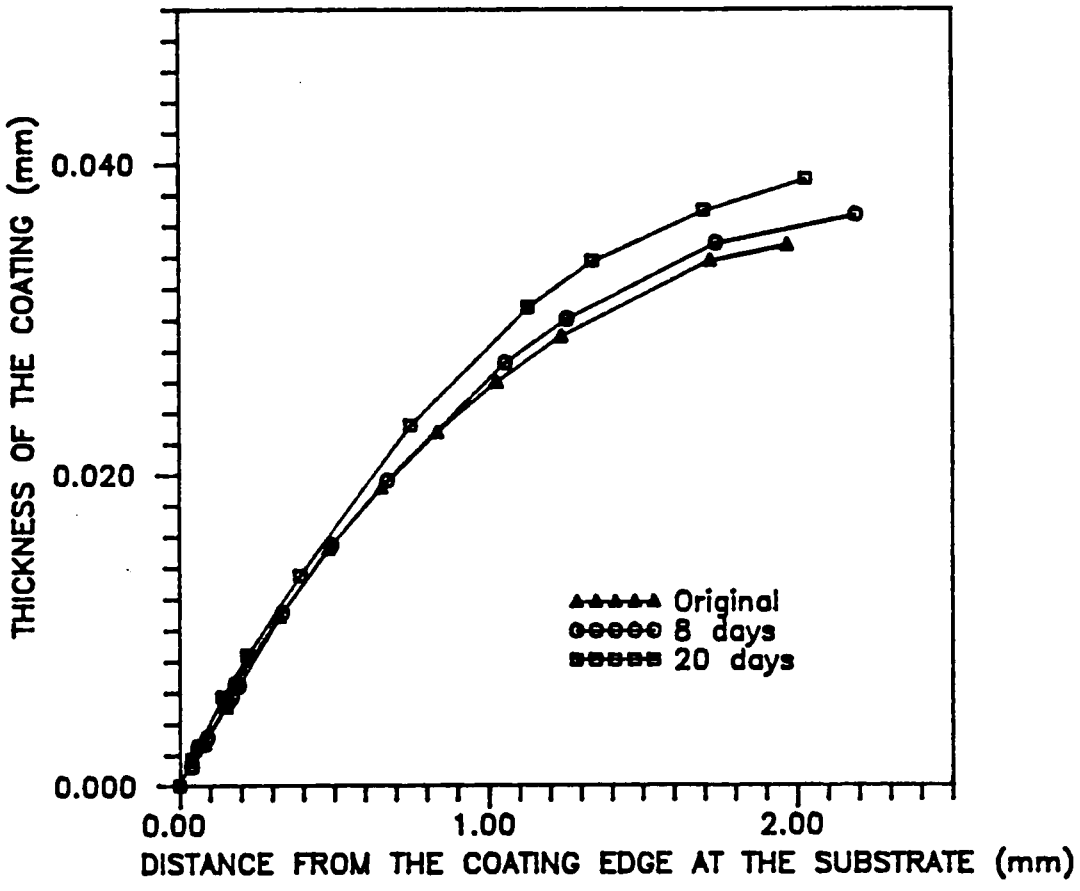


Figure 8.61 The coating surface profiles during water uptake obtained by inverting the data in Figure 8.57.

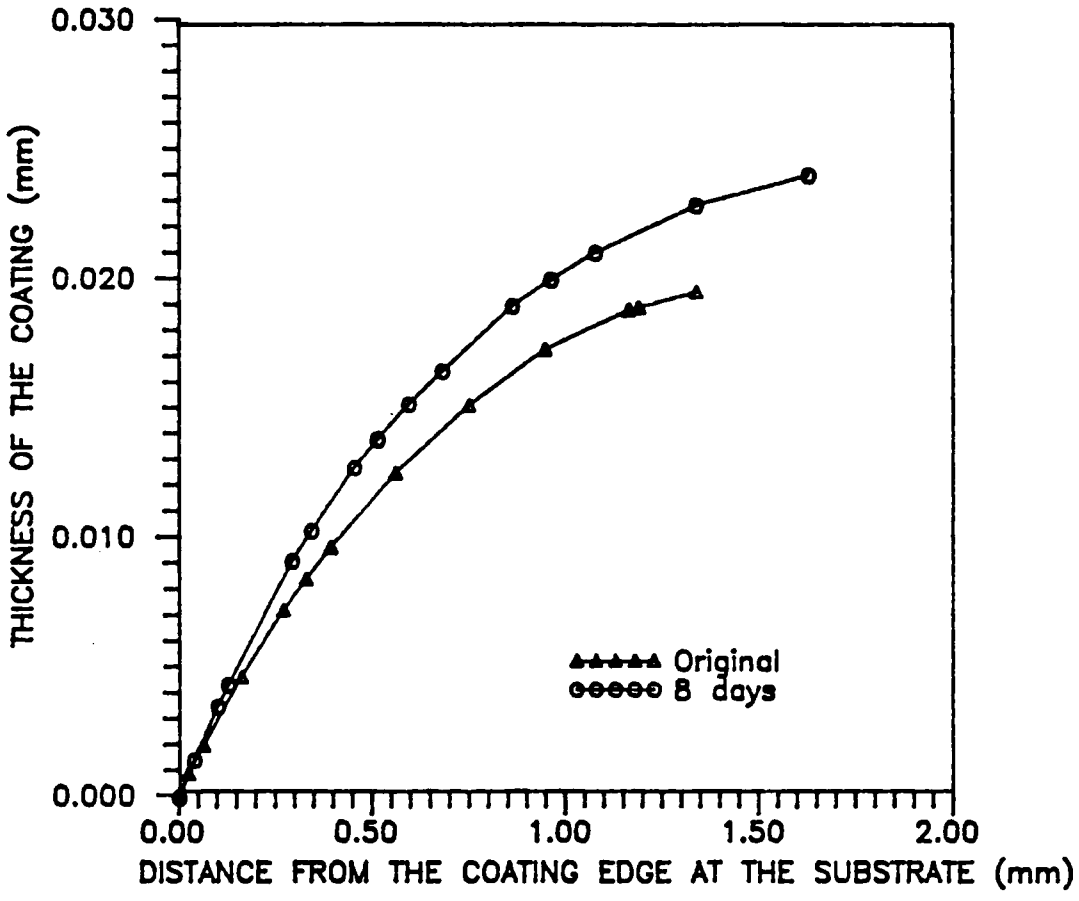


Figure 8.62 The coating surface profiles during water uptake obtained by inverting the data in Figure 8.58.

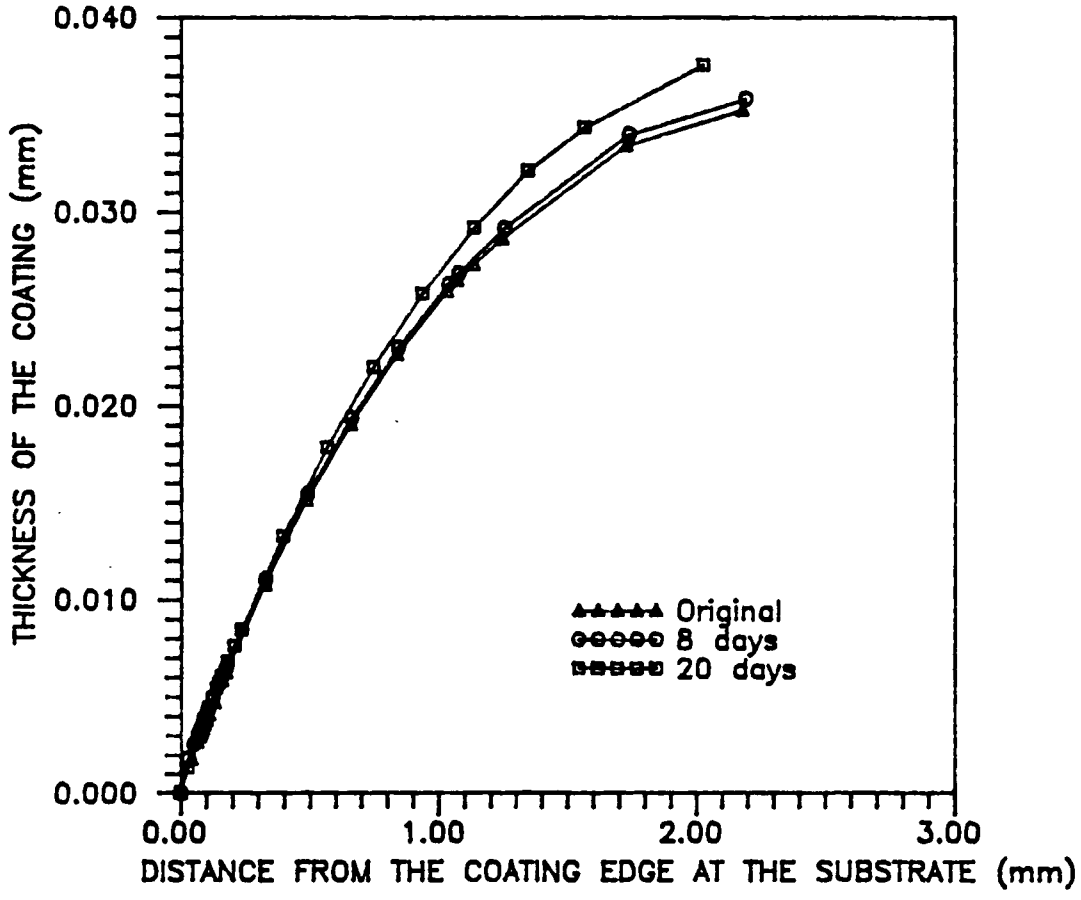


Figure 8.63 The coating surface profiles during water uptake obtained by inverting the data in Figure 8.59.

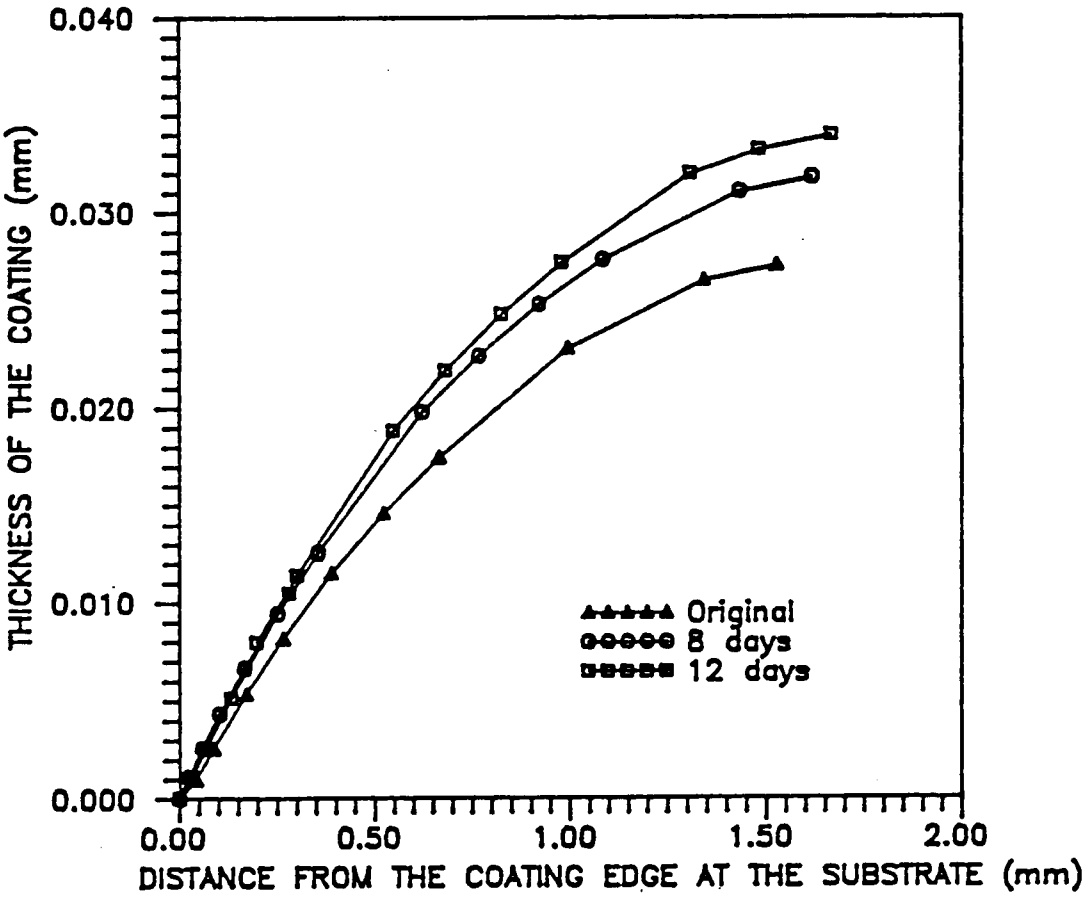


Figure 8.64 The coating surface profiles during water uptake obtained by inverting the data in Figure 8.60.

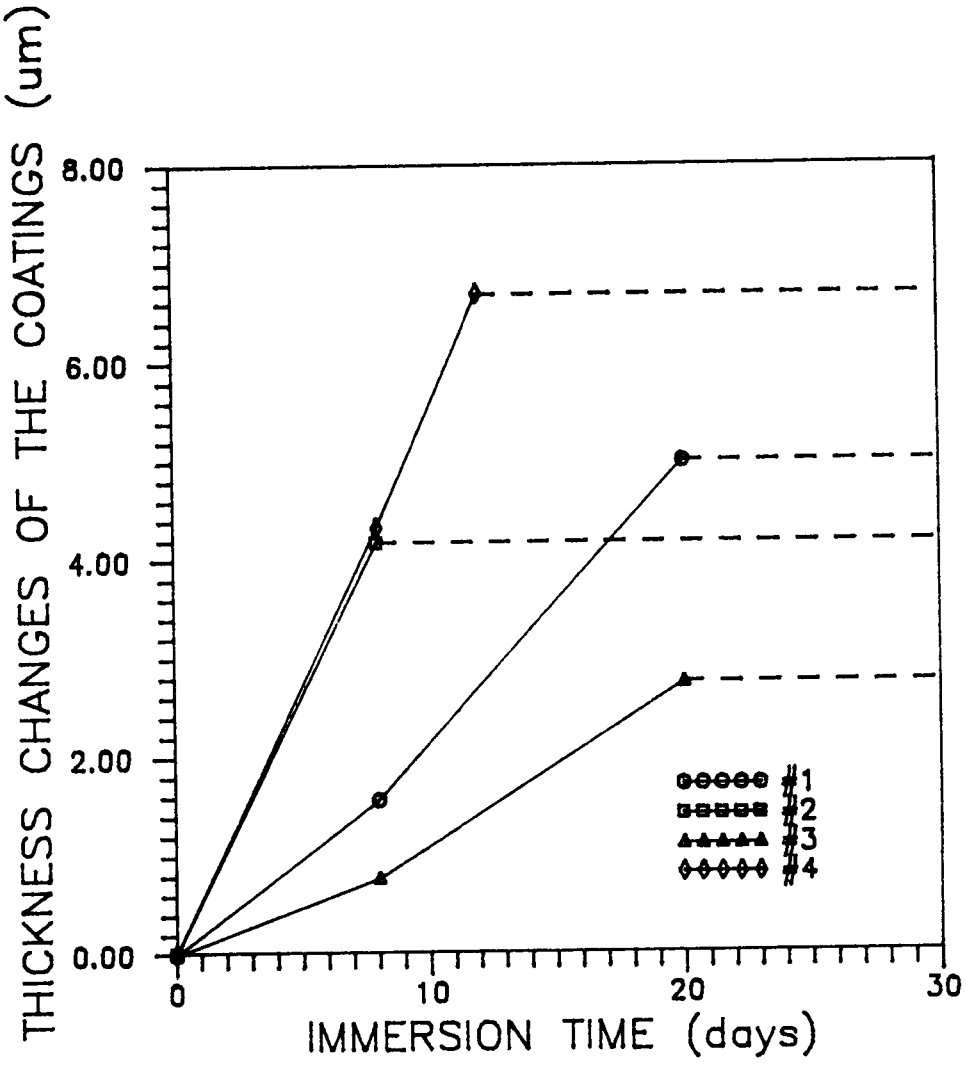


Figure 8.65 The coating thickness change due to water uptake for the different samples.

immersing samples in distilled water at 25°C. Figure 8.66 (a) shows the result for an as-received specimen. After 30 days immersion, some corrosion pits appear on that specimen, as seen in Figure 66 (b). Careful examination of the photograph of the as-received specimen reveals that there was some contrast at the corrosion pit sites. EDAX X-ray analysis in the SEM, Figure 8.67 (a), suggests that, near the corrosion pits, the coating has been damaged or destroyed since aluminum from the substrate interface can be detected. Elsewhere, where the coating is not damaged, only silicon is detected, see Figure 67 (b). Some bubbles exist within the coating, e.g. at **B** in Figure 66, but they do not initiate corrosion pits.

Another sample, Figure 8.68, shows no visible damage after 50 days under same conditions.

One other mechanism of degradation occasionally observed in the present work is peeling. Figure 8.69 shows a coating which, at the corner, has peeled away from the substrate. Some corrosion products can be seen at this corner.

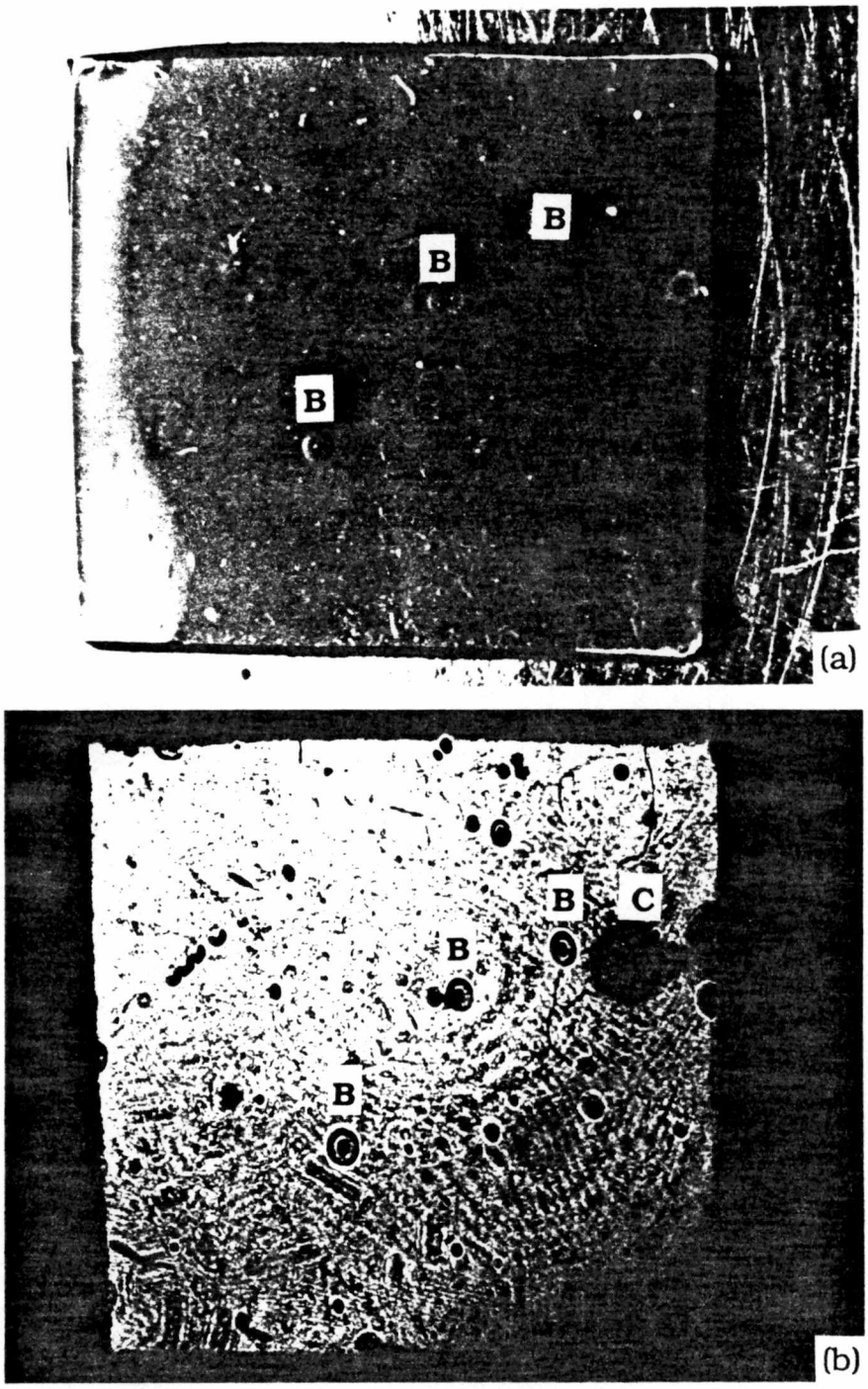
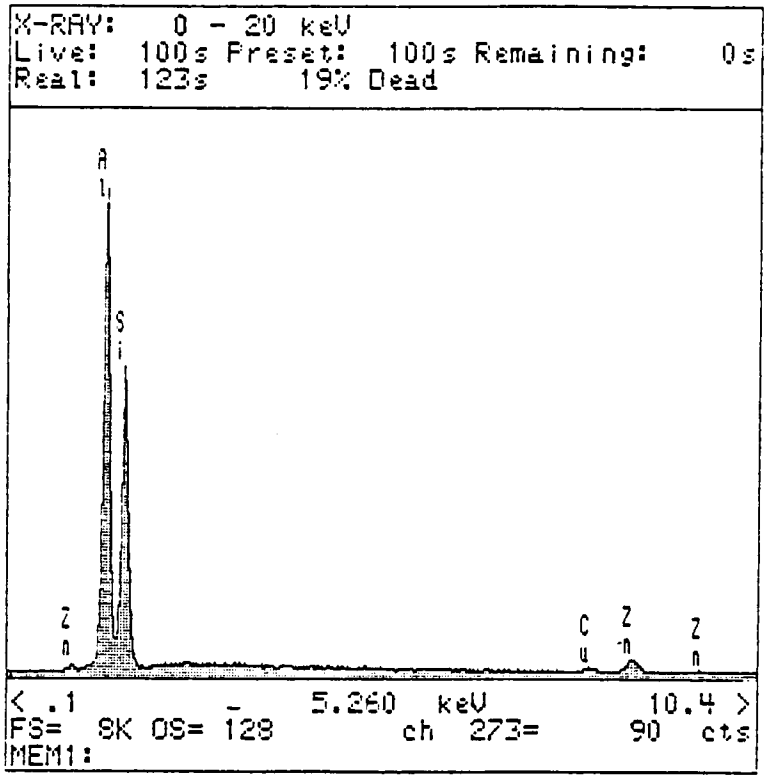
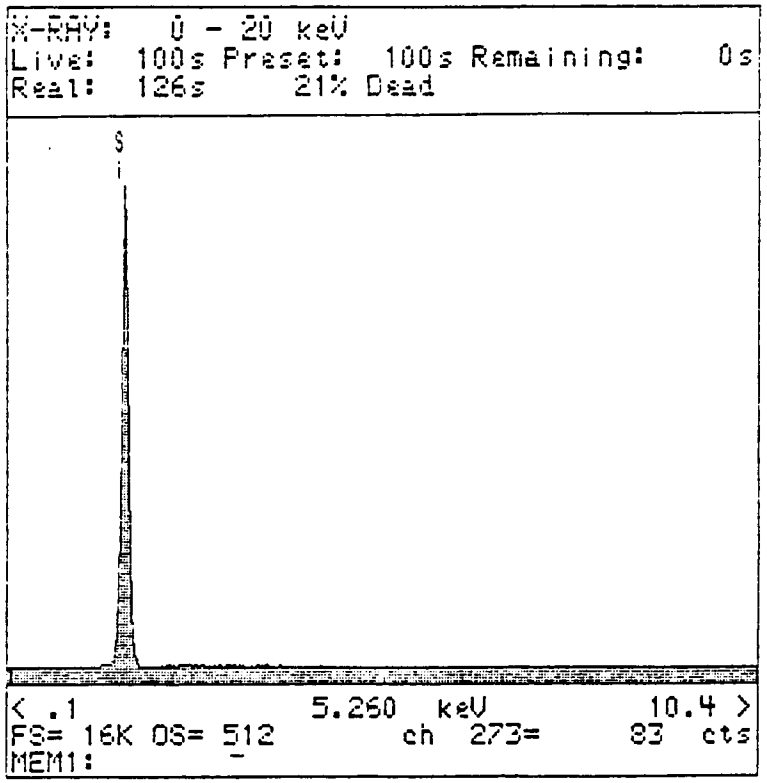


Figure 8.66 (a) As-received specimen, and (b) after 50 days immersion in distilled water at 25°C. **B**-bubble, **C**-corrosion pit.

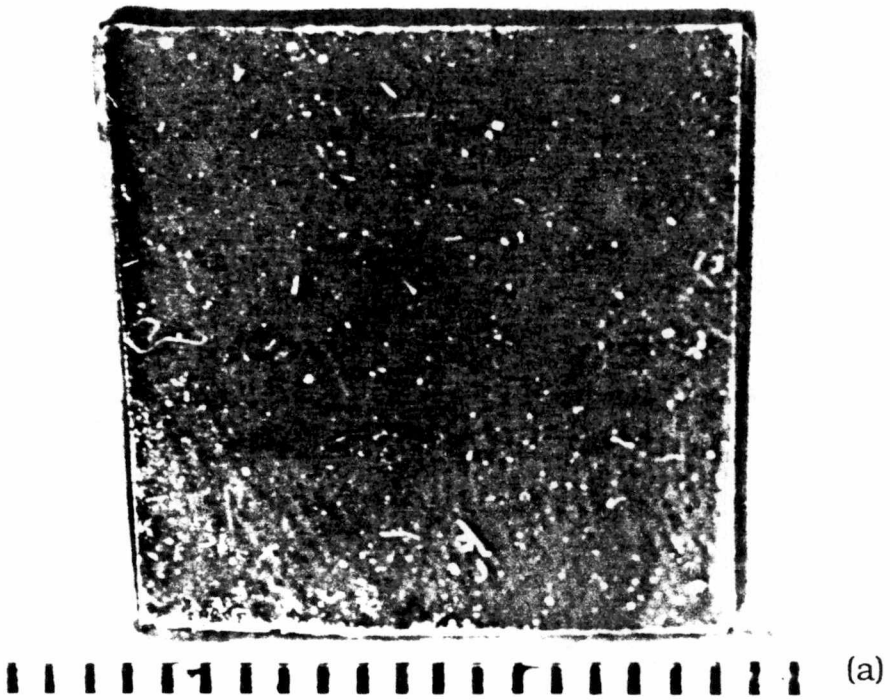


(a)

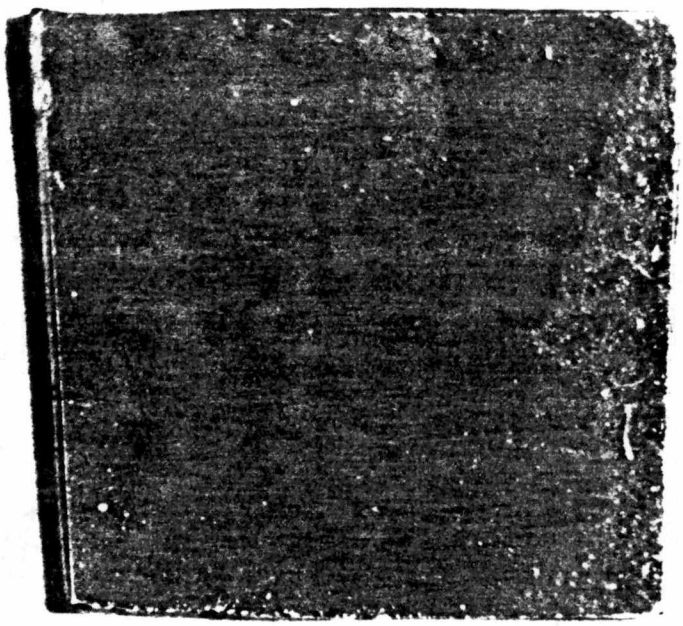


(b)

Figure 8.67 X-ray analysis, (a) at a corrosion pit, (Zn and Cu are present in the specimen holder), and (b) elsewhere on the coating.



(a)



(b)

Figure 8.68 No visible damage. (A) As-received specimen, and (b) after 50 days immersion in distilled water at 25°C.

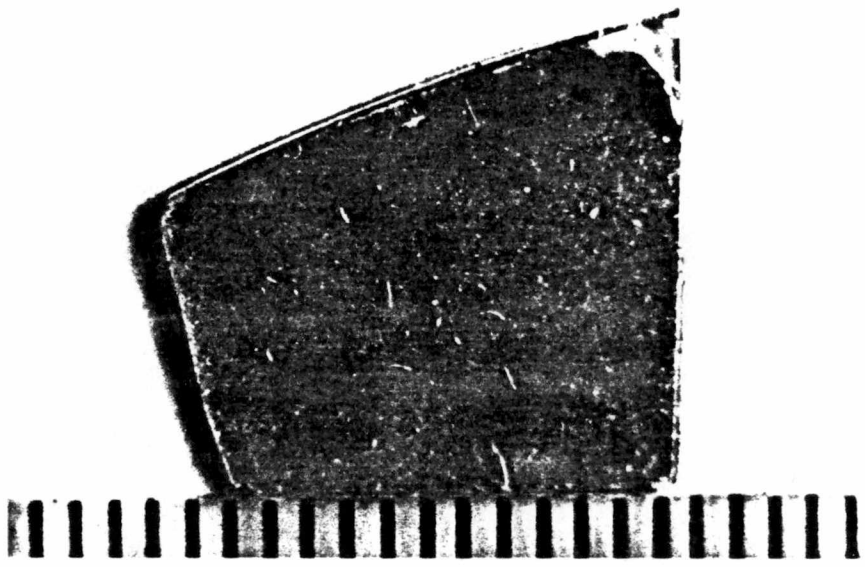


Figure 8.69 Polymer coating that has peeled away from the substrate.

CHAPTER IX

CONCLUSIONS

This dissertation has presented two new methods of characterizing the behavior of composites and electronic packages undergoing water uptake. From research conducted using these new methods, several features of moisture induced degradation of composites and electronic packages, have been discovered. This, in turn, has enabled the author to assess the capabilities of the methods as means for studying and measuring stress-induced birefringence and small displacements in materials science and engineering.

1. In its entirety, the response of a single fiber in a model resin matrix composite undergoing water uptake has been experimentally investigated. When water diffuses in, the matrix material swells and exceeds the shrinkage that resulted from curing and cool down from the resin cure temperature. The actual change from shrinkage to net swelling has been monitored by observation of the reversal in direction of optical fast and slow axes of the matrix resin. Swelling of the matrix is locally constrained by the rigid fiber and fiber/matrix interfacial stresses are generated. The magnitude and distribution of the resulting interfacial shear stresses have been observed by measurement of the associated stress-induced birefringence. The shear stresses near the fiber ends is large enough to initiate interfacial debonding, the extent of which has been detected by observation of where, along the fiber, the interfacial shear stress distribution

changes. The axial tension in the fiber, arising via the interfacial shear stress, causes the fiber to deform. The consequent Poisson's contraction of the fiber has been investigated by means of an interferometric "Strain Gage". Also, the strain corresponding to the axial tensile stress has been studied using moire interferometry and optical caustic foci measurements of displacement of a cover slip bonded to, and perpendicular to, the fiber. Finally, it has been demonstrated that the axial tensile stress in the fiber can be large enough to fracture the fiber. This previously unknown phenomenon has been investigated experimentally using photoelasticity and electron microscopy.

2. The effects of different proprietary surface treatments, applied to fibers, on the durability of interfacial bonding when the composite is exposure to moisture is of considerable technological interest. The advent of improved fiber surface preparations claimed by fiber manufacturers has been substantiated by our experiments with carbon fibers. We have shown that, for certain surface treatments, the durability of load transfer between matrix and fiber has been enhanced to such an extent that swelling deformations large enough to cause fiber fracture can be realized. That is, fiber fracture can occur due to environmental effects alone, there being no stress applied externally.

3. The radial distribution of axial stress around a single fiber in epoxy resin undergoing water uptake confirms that there exists a large axial tension inside the fiber.

4. Carbon fiber fractures caused by the axial tension resulting from moisture uptake, have been studied in some detail. Different

failure modes have been observed for different surface treatments. The better the durability of the interfacial bonding, the shorter the time for fiber fracture to occur in water immersion tests. Mechanical tests to investigate the incidence of fiber fracture, in tensile test-pieces containing a bundle of fibers, have confirmed our conclusions about the effects of different surface treatments.

5. Experimental results, on water uptake by polymer coating on the chip on board, have revealed the effects of post-curing treatment on the dimensional change rates, and hence on both water uptake rates and saturated values of water uptake. The results also reveal that a sample subjected to 11 days salt spray had lowest swelling rate and lowest value of saturated water uptake, and that a sample treated for 11 days in a humidity chamber had lower swelling rate and lower value of saturated water uptake, than samples which had not been previously exposed to an aqueous environment.

6. Two generic types of degradation attributable to the polymer coating have been identified. One is electrolytic corrosion of the underlying metallic substrate and the other is swelling and, in some cases, peeling of coating. Results obtained for prolonged immersion in water at 25^0C show that, if one takes the above two degradation mechanisms as sole failure criteria, the coating provides adequate protection for 50 days. The results also show that bubbles inside the coating do not lead to resovable damage after water immersion of up to 50 days. However, other damage to the coating itself can lead to corrosion pits in the metallic substrate.

7. Our method of using resin optical retardation measurements

to determine the sign and to estimate the magnitude of interfacial shear stress provides a semi-quantitative method by which the shear stress distribution can be studied. We have used this to monitor the occurrence of interfacial debonding at fiber ends. The results are consistent with the relative occurrence of fiber fractures for the various surface treatments reported in conclusion 4.

8. A moire multiple-beam interferometric technique has been successfully used to measure small deformation of the metallic substrate beneath the transparent polymer protective coating on the chip on board. Such deformation cannot be detected by moire two-beam interferometry.

9. A new technique to measure small changes in surface curvatures using optical caustic foci has been developed. Mathematical analysis for the technique predicts that the procedure, measuring the caustic surface and then inverting to obtain the reflecting surface profile, is reliable. The sensitivity of the method is about 10nm at the center of the reflecting surface. The accuracy claimed for this measurement is already great and could be further improved if, instead of the caustic focus itself, its diffraction pattern were to be analyzed.

This new technique has been successfully used to measure dimensional changes accompanying water uptake by model composites and by polymer coatings on COB components. Our moire optical interference technique cannot be used for this purpose owing to transparency of the coating material.

10. The second differential of the reflecting surface can be

obtained directly from the caustic focus. This, if it can be assumed to be differential of displacement of a thin plate, is a measure of the bending moment. By differentiating twice to get the 4th differential, the distribution of stresses normal to the plate can be obtained. This is a distinct advantage over stress estimation by differentiating measured displacements four times.

LIST OF REFERENCES

LIST OF REFERENCES

Adams, D.F.(1979), Second Annual Army Composite Materials Research Review, University of Massachusetts, p.18.1.

Agarwal B. D. and Bansal R. K.(1979), Fiber Sci. Tech., Vol. 12, p. 149.

Alfrey, T., Jr., Gunee, E.F. and Lloyd, W.G.(1966), "Diffusion in Glassy Polymers", J. Polymer Science: Part C, Vol.12, p.249.

Ashbee, K.H.G.(1989), "Fundamental Principles of Fiber Reinforced Composites," Technomic Publishing Co., Inc..

Ashbee, K.H.G., Frank, F.C. and Wyatt, R.C.(1967), Proc. Roy. Soc., A300, p.415

Ashbee, K.H.G. and Tossell, D.A.(1988), Final report to Martin Marietta Labs., Under contract: UTK-87-002c.

Ashbee, K.H.G. and Wyatt, R.C.(1969), Proc. Roy. Soc., A312, p.553.

Bert, C.W., and Kline, R.A.(1985), Polym, Compos., Vol.6, p.133.

Brewster, J.R.(1989), "Some Applications of Caustic Foci to Non-destructive Evaluation," M.Sc.Thesis, University of Tennesse, Knoxville.

Browning, C.E., Husman, G.E. and Whitney, J.M.(1977), ASTM STP 617, p.481.

Bueche, F.(1962), "Physical Properties of Polymers", Interscience Publishers, New York.

Carr, A.D.(1986), Polymer NDE, Ed. Ashbee, K.H.G., Technomic Publishing Co.,Inc., p.213.

Chang, Y.J., Chen, C.T. and Tobolsky, A.V.(1974), J. Polymer Sci. Polymer Phys. Ed., Vol.12, p.1.

Clerke, D. A. and Bader, M. G.(1986), J. Mat. Sci. Letters, p 903.

Cohen, A.C. Jr.(1978), Technometrics, Vol.7, p.579.

Cook, J. and Gordon, J.E.(1964), Proc. Roy. Soc. Lond., Vol.282, p508.

Cooper, G.A. and Kelly, A.(1967), J. Mech. Phys., Solids, Vol.15, p.279.

Cottrell, A.H.(1964), Proc. Roy. Soc. Lond., Vol.282, p.2.

Cox, H.L.(1952), J. Appl. Phys., Vol.3, p.72.

Crank, J.(1956), 'The Mathematics of Diffusion," Clarendon Press, Oxford.

Deanin, R.D.(1972), "Polymer Structure, Properties and Application", Cahners Book, Boston, Mass..

DeIasi, R.J.and Schulte, R.L.(1984), Environmental Effects om Composite Materials, Ed. Springer, G.S., Technomic Publishing Co., Inc., Vol.2, p.144.

Dewimill, D. and Bunsell, A.R.(1982), J. Phys. D. Appl. Phys., Vol.15, p.2079.

Drzal, L.T., Rich, M.J. and Lloyd, P.F.(1982), J. Adhesion, Vol.16, p.1.

Drzal, L.T., Rich, M.J., Koenig, M.F. and Lloyd, P.F.(1983), J. Adhesion, Vol.16, p.133.

Drzal, L.T., Rich, M.J. and Rayland, W.(1987), 42th Annual conference, Composites Institute, The Society of the Plastic Industry, Inc., 7A.

Ernsberger, F. M.(1968), J. American Ceramic Society, Vol.51, p.545.

Ferry, J.D.(1961), "Viscoelastic Properties of Polymers", Wiley, New York, London.

Flory, P.J.(1953), "Principles of Polymer chemistry", Cornell University Press, Ithaca.

Frank, F.C.(1970), Proc. R. Soc. Lond., A319, p.127.

Frank, F.C.(1973), J. Nucl. Mat., VOl. 48, p.199.

Garton, A. and Daly, J.H.(1985), Polymer Composites, Vol. 6, p.4.

Gillat, O. and Broutman, L.J.(1976), ASTM STP 658 (American Society for Testing and Materials, Philadelphia), p.2.

Hahn, H.T.(1976), "Residual Stresses In Polymer Matrix Composite Laminates", J. Composite Materials, Vol.10, p.266.

Harris, B., Moyley, J. and Philips, D.C.(1975), J. Mat. Sci., Vol.10, p.2050.

Hecht, E.(1987), "Optics", Addison-Wesley Publishing Co..

Henson, M.C. and Weitsman, Y.(1987), "Composites'86: Recent Advances in Japan and the United States; Proceedings of the Third Japan-U.S. Conference on Composite Materials; Kawata, Ikema, Kobayashi, Eds.; Japan Society of Composite Materials, Tokyo.

Holland, A.(1964), "The Properties of Glass Surface", New York, Wiley.

Hopfgarten, F.(1979), Fiber Sci. & Tech., Vol.12, p.283.

Hull, D.(1981), "An Introduction to Composite Materials," the University Press, Cambridge, Great Britain.

Kalthoff, J.F., Beinert, J. and Winkler, S.(1977), ASTM STP 627, p.167.

Kelly, A.(1970), Proc. Roy. Soc., A319, p. 95.

Kelly, A.(1972) Strong Solids. Clarendon Press, Oxford.

Kelly, A. and Davies, G.T.(1965), Metall. Rev., Vol.10, p.1.

Kelly, A. and Tyson W. R.(1965), J. Mech. Phys. Solids, Vol.13, p.329.

Kookootsedes, G.J.and Lockhart, F.J.(1967), Silicone Molding Compounds for Semiconductor Device, 135 Meeting Am.Chem.Soc., Miami, Fla.

Kuske, A. and Robertson, G.(1974), "Photoelastic Stress Analysis," John Wiley & Son.

Kwei, T.K.(1966), J. Appl. Polymer Sci., Vol.10, p.1647.

Laurities, K.N. and Sandoff, P.E.(1979), Technical report AFML-TR-794179, Material Laboratory, Wright Patterson Air Force Base, Dayton, Ohio.

LeFebvre, D.R., Dillard, D.A. and Ward, T.C.(1989), "A Model for the Diffusion of Moisture in Adhesive Joints. Part 1: Equations Governing Diffusion", J. Adhesion, Vol.27, p.1.

LeFebvre, D.R., Dillard, D.A. and Brinson, H.F.(1989), "A Model for the Diffusion of Adhesive Joints. Patr 2: Experimetnal", ibid, Vol.27, p.19.

Licari, J.J.(1970), Plastic Coatings for Electronics, McGraw-hill Book Co., New York.

Love, A.E.H.(1959), Treatise on the Mathematical Theory of Elasticity, Chap. XXII, Cambridge University Press, P.455.

Machenzie, J. D.(1965), Phys. Chem. Glasses, Vol.6, p.461.

Mandell, J.F., Grande, D.H. and McGarry, F.J.(1980), in Proceedings of 35th Conference of R.P./Composite Institute New Orleans 1980 (Society of the Plastics Industry, New York, 1980) Paper 26D.

Mandell, J.F., Grande, D.H., Tsaing, T.H. and McGarry, F.J.(1986), ASTM AST 893 (American Society for Testing and Materials, Philadelphia) p.87.

Manogg, P.(1964), Adwendung der Schattenoptik zur Untersuchung des ZerreiBvorgangs von Platten. Dissertation, Universitat Freiburg.

Marom, G.(1977), Polym. Eng.& Sci. Vol.17, p.799.

Marom, G and Broutmam, L.J.(1981), J. Adhesion, Vol.12 p.153.

Marston, T.U., Atkins, A.G. and Felbeck, D.K.(1974), J. Mat. Sci., Vol.9, p.447.

Mathes, K.N.(1967), Selection of an Insulation System in Product Design, Insulation, Ocotober.

Maxwell, J.C.(1853), Trans. Roy. Soc. Edinburgh, Vol.XX, Part I, p.87.

McKague, E.L.,Jr., Reynolds, J.D.and Halkias, J.E.(1978), J. Appl. Polymer Sci., Vol. 22, p.1643.

Miller, G. and Gaur, U.(1987), 5th International Joint Military/Goverment Industry Symposium on Structural Adhesive Bonding, p.280.

Miller, B., Muri, P. and Rebenfeld, L.(1987), Comp. Sci. Tech., Vol.28, p.17.

Mullin, J., Berry, J.M. and Gatti, A.(1968), J. Com. Mat. Vol. 2, p.82.

Mullin, J.U. and Mazzio, J.M.(1971), Basica Failure Mechanisms in Advanced Composites, Final report to NASA, Contrasct No. NASw-2093.

Outwater, J.O., Jr., and Murphy, M.C.(1969), Proc. of the 24th Ann. Tech. Conf. of the RPIC Div., The Society of the Plastics Industry, Inc., Washington, D.C., P.11c.

Paul, D.R.(1969), J. Polymer Sci., A, Vol.7, p.1811.

Penn, L. and Lee, S.M.(1982), Fibre Sci. Tech., Vol.17, p.91.

Piggott, M.R.(1980), "Load-Bearing Fiber Composites," Pergamon Press.

Piggott, M.R.(1987), Polymer Composites, Vol.8, p.291.

Poincaré, H.(1892), "Theorie Mathematique de la Lumiere", t.II,p.275 et suiv., Paris, Carne, Editeur.

Poritsky, H.(1934), Physics, Vol.5, p.406.

Predecki, P. and Barrett, C.S.(1984), Environmental Effects on Composite Materials, Ed. Springer, G.S., Technomic Publishing Co., Inc., Vol.2, p.136.

Raghava, R.S.(1987), 2th Technical Conference, The American Society for Composites, Tecnomic Publishing Co., p.281

Rehage, G. and Borchard, W.(1973), "The Physics of Glassy Polymers", edited by R.N. Haward (Wiley, New York), CH.1, pp.541.

Rosen B. W.(1965), Fiber Composite Materials (American Society for Metals, 1965).

Sargent, J.P. and Ashbee, K.H.G.(1980), J. Adhesion, Vol.11, p.175.

Sargent, J.P. and Ashbee, K.H.G.(1984), J. Appl. Polymer Sci., Vol.29, p.809.

Sargent, J.P. and Upstill, C.(1986), Polymer NDE, Ed. Ashbee, K.H.G., Technomic Publishing Co., Inc., pp.195.

Schwartz, M.M.(1984), "Composite Materials Handbook," McGraw-Hill, Inc..

Shelton, C.G.and Marks, P.R.(1988), J. Mat. Sci. Letters, Vol.7(6):673.

Shen, C.H. and Springer, G.S.(1976), J. Comp. Mater., Vol.2, p.2

Springer, G.S.(1977), J. Comp. Mater., Vol.11, p.107.

Springer, G.S. and Tsai, S.W.(1967), J. Comp. Mater., Vol.1, p.166.

Springer, G.S.(1980), Ed., "Environmental Effects on Composite Materials," Technomic Publishing Co., Inc., Vol.1.

Springer, G.S.(1984), Ed., "Environmental Effects on Composite Materials," Technomic Publishing Co., Inc., Vol.2.

Theocaris P.S.(1970), J. Appl. Mech. Vol.37, p.409.

Tolansky, S.(1973), "An Introduction to Interferometry," Longman Group Limited, Great Britain.

Tyson, W.R. and Davis, G.I.(1965), British J. Appl. Phys., Vol. 16, p.199.

Valentin, D., Paray, F. and Guetta, B.(1987), J. Mat. Sci., Vol. 22, p.46.

Vaudin, M.D. and Ashbee, K.H.G.(1982), J. Mat. Sci.,Vol.17, p.1329.

Vieht, W.R. and Sladek, K.J.(1965), J. Colloid Sci., Vol.20, p.1014.

Wake, W.C.(1978), "Theories of Adhesion and Uses of Adhasives: a review", Polymer, Vol.19, p.291.

Ward, I.M.(1971), "Mechanical Properties of Solid Polymers," Wiley-Interscience, London.

Weitsman, Y.(1977), J. Com. Mat., Vol. 11, p.378.

Whiteside, J.B., Delasi, R.J.and Schulte, R.L.(1983), ASTM STP 813, (American Society for Testing and Materials, Philadelphia), p.192.

Whitney, J.M. and Ashton, J.E.(1971), AIAA Journal, VOl. 9, p.1708.

Whitney, J.M. and Drzal, L.T.(1987), Toughened Composites, ASTM STP 937, p.179.

Whitney, J.M., Daniel, I.M. and Pipes, R.B.(1984), Experiemental Mechanics of Fiber Reinforced Composite Materials, The Society for Experimental Mechanics, Prentice-Hall, Inc., p.157.

Wiederhorn, S.M. and Bolz, L.H.(1970), J. Am. Ceram. Soc., Vol. 53, p.543.

Williams, J.G., Donnellan, M.E., James, M.R. and Morris, W.L.(1990), 5th Technical Conference of the American Society for Composites, Technomic Publishing Co.,Inc., p.127.

Wyatt, R.C. and Ashbee, K.H.G.(1969), Fib. Sci. Tec., Vol.2, p.29.

Yaniv, G. and Ishai, O.(1987), Polym. Eng. Sci., Vol. 27, p.731.

Yasuda, H., Lamaze, C.E. and Peterlin(1971), J. Polymer Sci., Vol.9, p.1117.

APPENDICES

Appendix A

Consider a case where $\mu_1 = \mu_2$ in order to avoid the need to introduce different reflection and transmission coefficients at each interface. The amplitudes of the reflected waves are given [Hecht 1987] by

$$\begin{aligned} E_{1r} &= E_o\, r\, e^{i\omega t} \\ E_{2r} &= E_o\, t\, r' t'\, e^{i(\omega t - d)} \\ E_{3r} &= E_o\, t\, r'^3 t'\, e^{i(\omega t - 2d)} \\ &\cdot \\ E_{Nr} &= E_o\, t\, r'^{(2N-3)} t'\, e^{i[\omega t - (N-1)d]} \end{aligned} \qquad \text{(A-1)}$$

where $E_o e^{i\omega t}$ is the incident wave, r and r' the amplitude-reflection coefficients, t and t' the amplitude-transmission coefficients, for different interfaces.

The terms δ, 2δ, ..., $(N-1)\delta$ are the contributions to the phase arising from an optical difference between adjacent rays ($\delta = 2\mu_f\, t \cos\theta$). There is an additional phase contribution arising from the optical distance traversed on reaching a point focus, but this is common to each ray and has been omitted. The relative phase shift undergone by the first ray as a result of the reflection is embodied in the quantity r'. The resultant reflected scalar wave is then

$$E_r = E_{1r} + E_{2r} + E_{3r} + \ldots + E_{Nr},$$

This can be rewritten from Eq.(A-1) as

$$E_r = E_o\, e^{i\omega t} \{ r + r'tt'e^{-i\delta}[1+(r'^2e^{-i\delta}) + (r'^2e^{-i\delta})^2 + \ldots + (r'^2e^{-i\delta})^{N-2}\ ]\} \qquad \text{(A-2)}$$

If $r'^2e^{-i\delta} < 1$, and if the number of terms in the series approaches infinity, the series converges. In the case of zero absorption, no energy being taken out of the waves, $r = r'$ and $tt' = 1-r^2$, the resultant wave becomes

$$E_r = E_o\, e^{i\omega t} \left[\frac{r(1-e^{-i\delta})}{1-r^2\, e^{-i\delta}} \right]$$

The reflected flux density at focus point is then $I_r = \frac{E_r E^*_r}{2}$, that is,

$$I_r = \frac{E_o{}^2 r^2 (1-e^{-i\delta})(1-e^{+i\delta})}{2(1-r^2e^{-i\delta})(1-r^2e^{+i\delta})}$$

which can be transformed into

$$I_r = I_i\, \frac{2r^2(1-\cos\delta)}{(1+r^4)-2r^2\cos\delta} \qquad \text{(A-3)}$$

The symbol $I_i = \frac{E_o{}^2}{2}$ represents the incident flux density. Using the trigonometric identity $\cos d = 1-2\sin^2(\frac{\delta}{2})$, Eq.(A-3) can be rewritten as

$$I_r = I_i \frac{[\frac{2r}{(1-r^2)}]^2 \sin^2 \frac{\delta}{2}}{1 + [\frac{2r}{(1-r^2)}]^2 \sin^2 \frac{\delta}{2}} \qquad \text{(A-4)}$$

Then a new quantity, the coefficient of finesse, F, is introduced,

$$F = \left(\frac{2r}{1-r^2}\right)^2 \qquad \text{(A-5)}$$

Eq.(A-4) can be written as

$$\frac{I_r}{I_i} = \frac{F \sin^2(\frac{\delta}{2})}{1 + F \sin^2(\frac{\delta}{2})} \qquad \text{(A-6)}$$

The term $[\ 1+ F \sin^2(\frac{\delta}{2})]^{-1} = \mathbf{A}(\theta)$ is known as the **Airy function**. Thus,

$$\frac{I_r}{I_i} = \frac{F \sin^2(\frac{\delta}{2})}{1 + F \sin^2(\frac{\delta}{2})} = \frac{1-\mathbf{A}(\theta)}{\mathbf{A}(\theta)} \quad \mathbf{A}(\theta) = 1- \mathbf{A}(\theta) \qquad \text{(A-7)}$$

The complementary function [1 - **A**(θ)] is Eq.(A-6). Thus the fringe intensity distribution in reflection is obtained by the complementary function, as shown in Figure 7.3. The fringes are now narrow dark fringes on a bright background.

Equation (7-35) can be derived as follows.

Since

$$U - X = (Z_1\text{-}S)\tan\alpha + Z_2\tan\beta + Z_3\tan\gamma \qquad (7\text{-}34)$$

where:

S = the thickness of the coating,

$Z_1 - S$ = the depth of immersion water,

Z_2 = the thickness of the optical plate,

Z_3 = the distance from the optical flat to the caustic focus,

α, β, γ = the reflected and refracted angles at the interfaces.

The conditions for formation of caustic once again are Eq.(7-17), which can, for this case, be written as,

$$\frac{dU}{dX} = 1 + (Z_1 - S)\frac{1}{\cos^2\gamma}\frac{d\gamma}{dX} + \left(-\frac{dS}{dX}\right)\tan\gamma + Z_2\frac{d\tan\beta}{dX} + Z_3\frac{d\tan\alpha}{dX} = 0 \qquad (B\text{-}1)$$

Since, from Figure 7.34,

$$\beta = \sin^{-1}(R_1 \sin\gamma)$$

$$\tan\beta = \frac{\sin\beta}{\cos\beta} = \frac{R_1 \sin\gamma}{\sqrt{1-(R_1 \sin\gamma)^2}}$$

and

$$\sin\alpha = (R_2 \sin\beta) = R_2 R_1 \sin\gamma$$

$$\tan\alpha = \frac{\sin\alpha}{\cos\alpha} = \frac{\sin\alpha}{\sqrt{1-\sin^2\alpha}} = \frac{R_2 R_1 \sin\gamma}{\sqrt{1-(R_2 R_1 \sin\gamma)^2}}$$

then,

$$\frac{d\tan\beta}{dX} = \frac{d}{dX}\left(\frac{R_1 \sin\gamma}{\sqrt{1-(R_1 \sin\gamma)^2}}\right)$$

$$= R_1 \frac{\sqrt{1-(R_1\sin\gamma)^2}\cos\gamma\frac{d\gamma}{dX} + \sin\gamma\frac{R_1 \sin\gamma\cos\gamma\frac{d\gamma}{dX}}{\sqrt{1-R_1\sin\gamma 2}}}{1-(R_1\sin\gamma)^2}$$

and

$$\frac{d\tan\alpha}{dX} = \frac{d}{dX}\left(\frac{R_2 R_1 \sin\gamma}{\sqrt{1-(R_2 R_1 \sin\gamma)^2}}\right)$$

$$= R_1 R_2 \frac{\sqrt{1-(R_1 R_2 \sin\gamma)^2}\cos\gamma\frac{d\gamma}{dX} + \sin\gamma\frac{R_1 R_2 \sin\gamma\cos\gamma\frac{d\gamma}{dX}}{\sqrt{1-(R_1 R_2 \sin\gamma)^2}}}{1-(R_1 R_2 \sin\gamma)^2}$$

Substituting these equations into Eq. (B-1), the relationship is given by

$$Z_3 = (-1 - (Z_1 - S)\frac{1}{\cos^2\gamma}\frac{d\gamma}{dx} + \frac{dS}{dx}\tan\gamma + Z_2 R_1 \frac{\sqrt{M}\frac{d\gamma}{dx}\cos\gamma + \frac{R_1 \sin^2\gamma \cos\gamma \frac{d\gamma}{dx}}{\sqrt{M}}}{M})/T \quad (7\text{-}35)$$

where:

$$T = R_1 R_2 \frac{\sqrt{N}\frac{d\gamma}{dx}\cos\gamma + \frac{R_1 R_2 \sin^2\gamma \cos\gamma \frac{d\gamma}{dx}}{\sqrt{N}}}{N}$$

$$M = 1 - (R_1 \sin\gamma)^2$$

$$N = 1 - (R_1 R_2 \sin\gamma)^2$$

$$R_1 = \frac{n_0}{n_1}$$

$$R_2 = \frac{n_1}{n_2}$$

$n_0 = 1.00$, $n_1 = 1.52$, and $n_2 = 1.30$ are the refractive indices for air, optical flat and water, respectively.

Appendix C

Some of the computer programs generated during the course of research are listed. The function of each program is indicated at the beginning of each program.

```
10 REM DRAW CAUSTIC FORMED IN A CUP OF COFFEE
20 SCREEN 9: WINDOW (-2.55,-2)-(2.55,2):CLS
30 PI=3.1415926#
40 FOR TT=0 TO 180 STEP 2
50 T=PI*TT/180
60 X=COS(T)
70 YY=(X-COS(T))*SIN(2*T)/COS(2*T)+SIN(T)
75 LINE (X,YY)-(X,YY)
76 LINE (X,-YY)-(X,-YY)
80 NEXT TT
90 FOR THETA=0 TO 90 STEP 1
100 A=PI*THETA/180
110 X=COS(A)-1/2*COS(A)*COS(2*A)
120 Y=SIN(A)-1/2*COS(A)*SIN(2*A)
130 LINE (X,Y)-(X,Y)
140 LINE (X,-Y)-(X,-Y)
150 NEXT
155 PRINT "155"
160 FOR YO=.9 TO 0 STEP -.03
170 XO=SQR(1-YO^2)
175 THETA=ATN(YO/XO)
176 IF THETA>PI/4 THEN ALPHA=PI-2*THETA:GOTO 210
180 ALPHA=2*THETA
190 X=XO-.8/SQR(1+(TAN(ALPHA))^2)
200 Y=TAN(ALPHA)*(X-XO)+YO:GOTO 230
210 X=XO+.8/SQR(1+(TAN(ALPHA))^2)
220 Y=YO-TAN(ALPHA)*(X-XO)
230 LINE (-1.5,YO)-(XO,YO)
235 LINE (-1.5,-YO)-(XO,-YO)
240 LINE (XO,YO)-(X,Y)
245 LINE (XO,-YO)-(X,-Y)
250 NEXT YO
```

```
10 REM CONVERT FOCI INTO THE PROFILE OF COATING SURFACE
20 N=77:W=1:L=.004:PI=3.1415926#
25 DIM X(N),U(N),Z(N),SLP(N),SS(N),XX(N),YY(N)
30 CLS:SCREEN 9: WINDOW (-W/10,-L/10)-(W,L)
35 LINE (0,0)-(0,L)
36 LINE (0,0)-(W,0)
40 OPEN "FOCI25.DAT" FOR INPUT AS #1
45 OPEN "PROFI.DAT" FOR OUTPUT AS #2
50 FOR I=1 TO N
60 INPUT#1, X(I),U(I),Z(I)
70 IF I=1 THEN GOTO 500
80 SLP(I)=(Z(I)-Z(I-1))/(U(I)-U(I-1))
81 'PRINT SLP(I);ATN(SLP(I))*180/PI
83 II=PI/2
85 FOR J=0 TO II STEP .001
90 GAMA=J:REM PRINT "J";GAMA;
100 X=1.3/1.5*SIN(GAMA):XX=X:REM PRINT "X";X;
110 GOSUB 5000
115 REM PRINT "XX1";XX
120 X=1.5/1.3*SIN(2*GAMA-XX):REM PRINT "X1";X;
130 XX=X
140 GOSUB 5000
145 REM PRINT "XX2";XX
150 D=ATN(SLP(I))-(PI/2-XX+GAMA)
160 IF ABS(D)<.001 THEN SS(I)=TAN(GAMA):GOTO 175
170 NEXT J
175 IF I<3 THEN GOTO 500
180 XX(1)=(SLP(I-1)*U(I-2)-Z(I-2))/SLP(I-1)
190 YY(1)=0:REM PRINT I;YY(I-2)
200 XX(I-1)=(-YY(I-2)+SS(I-1)*XX(I-2)+Z(I-1)-SLP(I)*U(I-1))
201 XX(I-1)=XX(I-1)/(SS(I-1)-SLP(I))
210 YY(I-1)=SS(I-1)*(XX(I-1)-XX(I-2))+YY(I-2)
220 LINE (XX(I-1),YY(I-1))-(XX(I-1),YY(I-1)),13
230 PRINT#2,XX(I-1),YY(I-1)
500 NEXT I
600 CLOSE #1:CLOSE #2
700 END
5000 REM ARCSIN(X)
5001 REM PRINT X;XX
5010 GA1=1:GA2=1
5030 FOR N=1 TO 8
5040 FEN1=GA1*N
5050 FEN2=GA2*(N*2)*(N*2-1)
5060 GA1=FEN1:GA2=FEN2
5070 DD=GA1/(2^(2*N)*GA2^2*(2*N+1))*X^(2*N+1)
5080 XX=XX+DD
5090 NEXT N
5100 RETURN
```

```
10 'ACCURACY OF REFFRACTION ANGLE WITH THE THICKNESS
15 'CHANGES OF COATING
20 PI=3.14159:DEGRE=360/(2*PI)
30 SCREEN 9:WINDOW (0,0)-(10,100):CLS
35 OPEN "ERROR.DAT" FOR OUTPUT AS #1
40 A=.1:B=2.3026:R=1.3/1.5:REM R=Na/Nb a-water&b-polymer
60 NRAYS=120:MAX=20:L=300
70 STP=MAX/NRAYS
80 FOR X=0 TO 8 STEP .1
90 Y=EXP(X-B)+A
94 NEXT X
95 FOR X=.1 TO 8 STEP .1
96 Y=EXP(X-B)+A
100 YD=EXP(X-B)
105 YDD1=EXP(X-B)
110 ALPHA1=PI/2-ATN(YD):REM INCIDENT ANGLE AT POINT 1
120 SIN1=SIN(ALPHA1)*R:REM SIN1=SIN(BETA1)
130 BETA1=ATN(SIN1/SQR(1-SIN1^2)):REM REFRACTION ANGLE
135 'AT POINT 1
140 THETA=ALPHA1-BETA1:REM INCIDENT ANGLE AT SUBSTRATE
145 Y1=X*TAN(THETA):REM PATHVECTOR IN COATING AT X DIRECTION
150 GOSUB 5000
155 Y3=Y+Y1+Y2
156 X3=LOG(Y3+A)+B
160 YD2=EXP(X3-B)
165 YDD2=EXP(X3-B)
170 BETA2=PI/2-ATN(YD2)+THETA:REM INCIDENT ANGLE AT POINT 2
180 SIN2=SIN(BETA2)/R:REM SIN2=SIN(ALPHA2)
185 IF SIN(BETA2)>1.3/1.5 THEN GOTO 330:REM CRITICAL ANGLE
190 ALPHA2=ATN(SIN2/SQR(1-SIN2^2)):REM TRANSMISSION ANGLE
195 'AT POINT 2
200 GAMMA=ALPHA2-(PI/2-ATN(YD2))
240 XX=X3+L*COS(GAMMA)
250 YY=Y3+L*SIN(GAMMA)
260 DX=.001
270 DBETA=-2*(YDD2*(X3*DX)/(1+(YD2)^2))
275 DBETA2=DBETA-COS(PI/2-ATN(YD1))*(-YDD1*(X*DX)/(1+(YD1)^2))*R
280 DA2=COS(BETA2)/COS(ALPHA2)*DBETA2/R
290 DGA=DA2+YDD2/(1+(YD2)^2)
300 RATIO=DGA/GAMMA
305 DANGLE=DEGRE*DGA
310 PRINT#1,X,DGA,GAMMA,RATIO
320 LINE (X,DANGLE)-(X,DANGLE)
330 NEXT X
340 CLOSE #1
350 END
5000 FOR Y2=0 TO 50 STEP .005
5100 DELTA=Y2-TAN(THETA)*(LOG(Y+Y1+Y2+A)+B)
5200 IF ABS(DELTA)<.005 THEN GOTO 5400
5300 NEXT Y2
5400 RETURN
```

```
10 REM SPLINE, FIRST DATA OF POINTS, THEN SOLVE LINEAR EQUAS. TO GET Ki
20 CLS:SCREEN 9: WINDOW (-.5,10)-(2,20)
21 LINE (0,12)-(1.5,12)
22 LINE (0,12)-(0,20)
23 N=3:C=12
25 DIM B(N,N+1)
26     DIM A(N,N+1),X(N)
30 X1=.0399:X2=.3074:X3=.7257
40 Y1=12.9632:Y2=15.9736:Y3=19.4388
50 M1=16.3355:MN=7.645:STP=.01
55 GOSUB 500
56 GOSUB 800
59 REM OPEN "SPLIN2.DAT" FOR OUTPUT AS #1
60 FOR X=X1 TO X2 STEP STP
70 S1=Y1+(Y2-Y1)/(X2-X1)*(X-X1)+1/6*(X-X1)*(X-X2)*(2*X(1)+X(2)+(X(2)-X(1))/(X2-X
1)*(X-X1))
80 LINE (X,S1)-(X,S1),C
85 REM PRINT#1, X,S1
90 NEXT X
100 FOR X=X2 TO X3 STEP STP
110 S2=Y2+(Y3-Y2)/(X3-X2)*(X-X2)+1/6*(X-X2)*(X-X2)*(2*X(2)+X(3)+(X(3)-X(2))/(X3-
X2)*(X-X2))
120 LINE (X,S2)-(X,S2),C
125 REM PRINT#1,X,S2
130 NEXT X
140 REM CLOSE #1
150 END
500 REM GENERATION OF A COEFFICIENT MATRIX FOR CALCULATION OF K1...Kn IN
510 REM SPLINE EQUATION
520 N=3
570 B(1,1)=2*(X2-X1)
580 B(1,2)=X2-X1:B(2,1)=B(1,2)
590 B(1,3)=0:B(3,1)=B(1,3)
600 B(1,4)=6*((Y2-Y1)/(X2-X1)-M1)
610 B(2,2)=2*((X2-X1)+(X3-X2))
620 B(2,3)=X3-X2:B(3,2)=B(2,3)
630 B(2,4)=6*((Y3-Y2)/(X3-X2)-(Y2-Y1)/(X2-X1))
640 B(3,3)=2*(X3-X2)
650 B(3,4)=6*(MN-(Y3-Y2)/(X3-X2))
660 OPEN "COEFF.DAT" FOR OUTPUT AS #1
670 FOR I=1 TO N
680 FOR J=1 TO N+1
690 PRINT#1,B(I,J)
700 NEXT J
710 NEXT I
720 CLOSE #1
730 RETURN
800 REM SOLUTION OF LINEAR EQUATIONS BY ITERATIONS
801 REM INPUT THE DATA FILE, THE NUMBER OF UNKNOWNS,N, THE MAX ITERATIONS,M
802 REM AND THE ALLOWED ERROR, D.
805     OPEN "COEFF.DAT" FOR INPUT AS #1 :REM INPUT THE COEEFICIENT MATRIX
810     N=3:REM THE NUMBER OF UNKNOWNS
820     M=100: REM MAX ITERATIONS
825     D=.001: REM ALLOWED ERROR
840     FOR I=1 TO N
850     FOR J=1 TO N+1
860     INPUT#1,A(I,J)
870     NEXT J
```

```
880     X(I)=A(I,N+1)
890     NEXT I
895     CLOSE #1
900     FOR K=1 TO M
910     T=0
920     FOR I=1 TO N
930     S=0
940     FOR J=1 TO N
955     S=S+A(I,J)*X(J)
960     NEXT J
970     B=X(I)
980     X(I)=B+(A(I,N+1)-S)/A(I,I)
990     IF ABS(X(I)-B)=<D THEN GOTO 1010
1000    T=T+1
1010    NEXT I
1020    IF T=0 THEN GOTO 1040
1030    NEXT K
1035    PRINT "CONVERGENCE TOO SLOW.USING LAST VALUES COMPUTED OR INCREASING
1036    PRINT "ITERATION TIMES"
1040    PRINT X(1),X(2),X(3)
```

```
10      REM CALCULATION OF AXIAL STRESS DISTRIBUTION IN A
15      'CIRCULAR STRESS FILED OR A CYLINDRICAL COMPOSITE
20      'SPECIMEN OF A SINGLE FIBER
30      'INPUT THE RADIUS, R, OF THE CIRCULAR STRESS FIELD,
40      'THE DIVIDENCE, N, OF THE RADIUS, AND THE MEASURED
50      'RETARDATIONS
60      DIM R(100), T(100), S(100), RE(100)
65      INPUT " THE STRESS-OPTIC COEFFICIENT OF THE MATERIAL?
66      (NM/UM.PSI)";B
67      PRINT
68      PRINT "THE STRESS-OPTIC COEFF.(nm/um.Psi):  ";B
69      PRINT
70      INPUT "INPUT THE RADIUS OF THE STRESS FIELD? (um)"; RA
80      PRINT
90      INPUT "INPUT THE NUMBEROF OF RETARDATION MEASUREMENTS=";M
100     PRINT
110     PRINT "INPUT THE MEASURED RETARDATION Re(N)? (nm)"
115     PRINT
116     N=M-1
120     FOR I=0 TO M-1
130     PRINT "Re(";I;")="
140     INPUT RE(I)
150     NEXT I
160     REM RE(I)=2B(S(1)T(1)+S(2)T(2)+...+S(I)T(I))
170     R(0)=RA
180     FOR I=1 TO N
190     R(I)=SQR((RA*(N-I+1)/N)^2-(RA*(N-I)/N)^2)
200     NEXT I
205     PRINT "DISTANCE","RETARDATION","AXIAL STRESS(Psi)"
206     PRINT "DISTANCE(um)","RETARDATION(nm)","AXIAL STRESS(Psi)"
207     PRINT RA,RE(0),0
210     FOR I=1 TO N
215     SIGMA=0
216     IF I=1 GOTO 250
220     FOR J=1 TO I-1
222     TJ=SQR((RA*(N-J+1)/N)^2-(RA*(N-I)/N)^2)
225     T(J)=TJ-SQR((RA*(N-J)/N)^2-(RA*(N-I)/N)^2)
230     SIGMA=SIGMA+S(J)*T(J)
240     NEXT J
250     S(I)=(RE(I)-2*B*SIGMA)/(2*B*R(I))
255     D=RA*(N-I)/N
260     PRINT D,RE(I),S(I)
265     PRINT D,RE(I),,S(I)
270     NEXT I
300 END
```

VITA

(許正榮)

Zheng Rong Xu was born and grown in Shanghai, China. He received a Bachelors degree in Metallurgical Engineering with the highest honor from Kunming Institute of Technology in January 1982. After working eight months as an associate engineer at Meishan Metallurgy Company, Nanjing, China, he entered the graduate school in Peking University of Iron and Steel Technology (now, University of Science and Technology, Beijing), where he received his Master degree in Metallurgical Engineering in July 1985. Before he came to the University of Tennessee, Knoxville in January 1987, he worked as a research engineer and group leader in Shanghai Iron and Steel Research Institute.

He is a member of ASM international, ASC, SAMPE, SPE, and TSM.